



TECHNISCHE
UNIVERSITÄT
WIEN
Vienna University of Technology

DISSERTATION

Investigation of Block Phenomena in Pyramidal, Cochlear, and Retinal Neurons

Ausgeführt zum Zwecke der Erlangung des akademischen Grades einer
Doktorin der technischen Wissenschaften

unter der Leitung von
Prof. DDDr. Frank Rattay
Institut für Analysis und Scientific Computing (E101)

eingereicht an der Technischen Universität Wien
Fakultät für Mathematik und Geoinformation

von
Sogand Sadat Sajedi
Matrikelnummer: 01225220



Wien am 13. Dezember 2021

Acknowledgments

I am incredibly grateful to my advisor Prof. Frank Rattay for supporting me during these years. Prof. Rattay, I was the luckiest student to have a great person like you as my advisor, and I admire your lovely personality, enthusiasm, knowledge, and wisdom. I would like to express my deepest thanks to my colleagues and friends, Dr. Andreas Fellner and Dr. Paul Werginz, for their help and support and for providing many valuable comments that improved this work.

I must also thank the Austrian Science Fund (FWF) for the financial support of this project. I would like to give my regards to Prof. Eugenijus Kaniusas and Prof. Winfried Mayr for their support and acceptance of being members of my dissertation committee.

This work would not have been possible without my husband's, Amirreza Heshmat, assistance. Amirreza was also my colleague and provided valuable insight into this research. Thank you for believing in me and supporting me. No words can express my gratitude and love to you.

Last but not least, I would like to express my deepest gratitude and love to my parents and my sister for their endless and unconditional love, help, and support. I am forever grateful to my parents for giving me the opportunities and experiences that made me who I am today. I am thankful to my sister for being a warm and caring person and ensuring that I always had the love I needed.

Abstract

Selective stimulation with microelectrodes of individual neurons is a major challenge in neuroprosthetics. Active propagation of action potential (AP) is possible within a stimulation window with a lower (LT) and an upper (UT) threshold. An anodal surround block inhibits AP propagation during an intensive cathodic stimulus by hyperpolarizing the flanks in the axonal membrane. A somatic block, in contrast, stops generating AP in the soma caused by a reversal sodium current at strong depolarizations. An interval between stimulating and blocking states is of concern in neuronal excitation.

Here, the threshold window and block phenomena of pyramidal (PC), cochlear (SGC), retinal (RGC) neurons, as well as myelinated and non-myelinated axons were analyzed. 3D models of neurons were simulated as cable models leading to large systems of ordinary differential equations, solved with numerical solutions, e.g., backward Euler, MATLAB ODE, and CVODE in Neuron. The point source approach was applied to calculate the extracellular voltage in most parts except the first part, which employs a finite element method. In most calculations (with some exceptions), a monophasic cathodic pulse with a duration of 100 μ s was used to investigate the threshold windows.

In the first part, 3D human cochlear neurons were investigated; the main findings were: (i) 3D pathways irregularities caused significant changes in excitation profiles compared with previous 2D investigations concerning AP initiation sites and latencies which might be of interest for cochlear implant users, and (ii) increasing degeneration level caused lower anodic thresholds or anodic sensitivity.

In the second part, the comparison of excitation and blockage of 2D models of PC, SGC, and RGC showed the following key results: (i) Due to low sodium conductivity in the PC model, the soma was not excitable for short pulse durations. (ii) Profoundly degenerated SGC (soma with one layer of myelin) was not excitable at the electrode to soma distances less than 4 μ m. (iii) Stimulation in close distances to soma was ruled by the somatic region, and the cell UT was due to somatic block, whereas at distant stimulation, axons governed the cell excitability, and UT was due to anodal surround block. (iv) In the whole-cell experiment, the highest UTs and threshold ratios were found in the PC model for both pulse durations.

In the next step, stimulation windows and block were studied in detailed reconstructed 3D morphologies of PCs (n=8), including the complex structure of axon collaterals and RGCs

(n=34) for an increasing range of electrode to cell distances for positions in the soma vicinity. The main findings were: (i) Soma played almost no role in PC excitation. In contrast, for stimulating RGCs in the soma vicinity, soma may mostly rule the cell excitation, and at these distances, UT occurs due to somatic block in RGC. (ii) At LT levels, APs always initiated at axon initiation segment (AIS) in both cell types; in cells with short AIS, the AP site was close to the distal part of AIS, whereas, in cells with longer AIS, the initiation site shifted towards the center of AIS. (iii) PCs possessed extremely high UTs, and (iv) no complete block was observed in PCs. (v) The arrangement of axon collaterals in PCs significantly impacted UTs while almost no impact on LTs.

The last chapter was a pure axon study comparing thin vs. thick and myelinated vs. non-myelinated fibers. For myelinated fibers, the main findings were: (i) Highest UTs were observed in thin and thick Mainen model (which was used in 3D PC myelinated axons) and MRG model. (ii) Increasing fiber diameter decreased UTs and threshold ratios in the investigated axon models. (iii) Increasing the pulse duration caused decreasing the UTs and threshold ratios and most significantly in thin fibers. In non-myelinated fibers, important findings were: (i) Highest UTs and threshold ratios were found for thin fibers, and UTs and threshold ratios decreased by increasing the diameter. (ii) Increasing pulse duration decreased UTs and threshold ratios as previously observed in myelinated fibers.

In summary, as previously found, axons are the most excitable parts of the cell that rule the cell excitation except for electrode positions very close to the soma. Although stimulating thick fibers are easier, it is rather challenging because of small threshold windows due to lower UTs and may lead to easier blockage situation.

Zusammenfassung

Die selektive Stimulation mit Mikroelektroden einzelner Neuronen ist eine große Herausforderung in der Neuroprothetik. Eine aktive Ausbreitung des Aktionspotentials (AP) ist innerhalb eines Stimulationsfensters mit einer unteren (LT) und einer oberen (UT) Schwelle möglich. Ein anodischer Surround-Block hemmt die AP-Ausbreitung während eines intensiven kathodischen Stimulus durch Hyperpolarisierung der Flanken in der axonalen Membran. Im Gegensatz dazu stoppt ein somatischer Block die AP-Erzeugung im Soma, die durch einen Natriumumkehrstrom bei starken Depolarisationen verursacht wird. Ein Intervall zwischen stimulierenden und blockierenden Zuständen ist bei der neuronalen Erregung von Bedeutung.

Hier wurden das Schwellenfenster und Blockphänomene von pyramidalen (PC), cochlearen (SGC), retinalen (RGC) Neuronen sowie myelinisierten und nicht-myelinisierten Axonen analysiert. 3D-Modelle von Neuronen wurden als Kabelmodelle simuliert, die zu großen Systemen gewöhnlicher Differentialgleichungen führten, die mit numerischen Lösungen gelöst wurden, z. B. Rückwärts-Euler, MATLAB ODE und CVODE in Neuron. Zur Berechnung der extrazellulären Spannungsverteilung wurde in den meisten Teilen der Punktquellenansatz verwendet, mit Ausnahme des ersten Teils, der eine Finite-Elemente-Methode verwendet. In den meisten Berechnungen (mit einigen Ausnahmen) wurde ein monophasischer kathodischer Puls mit einer Dauer von 100 μ s verwendet, um die Schwellenfenster zu untersuchen.

Im ersten Teil wurden menschliche 3D-Cochlea-Neuronen untersucht; Die wichtigsten Ergebnisse waren: (i) Unregelmäßigkeiten der 3D-Pfade verursachten signifikante Veränderungen der Erregungsprofile im Vergleich zu früheren 2D-Untersuchungen in Bezug auf AP-Initiierungsstellen und -Latenzen, die für Benutzer von Cochlea-Implantaten von Interesse sein könnten, und (ii) zunehmender Degenerationsgrad verursachte niedrigere anodische Schwellenwerte oder anodische Empfindlichkeit.

Im zweiten Teil zeigte der Vergleich von Anregung und Blockade von 2D-Modellen von PC, SGC und RGC die folgenden wesentlichen Ergebnisse: (i) Aufgrund der geringen Natriumleitfähigkeit im PC-Modell war das Soma für kurze Pulsdauern nicht erregbar. (ii) Stark degeneriertes SGC (Soma mit einer Myelinschicht) war an der Elektrode bis zu Soma-Abständen von weniger als 4 μ m nicht erregbar. (iii) Die Stimulation in unmittelbarer Nähe zum Soma wurde durch die somatische Region bestimmt, und der UT der Zelle war auf eine somatische Blockierung zurückzuführen, während bei einer Fernstimulation Axone die Erregbarkeit der Zelle regelten und der UT auf einen anodischen Surround-Block

zurückzuführen war. (iv) Im Ganzzellexperiment wurden die höchsten UTs und Schwellenverhältnisse im PC-Modell für beide Pulsdauern gefunden.

Im nächsten Schritt wurden Stimulationsfenster und -block in detailliert rekonstruierten 3D-Morphologien von PCs (n=8) untersucht, einschließlich der komplexen Struktur von Axonkollateralen und RGCs (n=34) für einen zunehmenden Elektroden-Zell-Abstand für Positionen in die Soma-Nähe. Die wichtigsten Ergebnisse waren: (i) Soma spielte fast keine Rolle bei der PC-Erregung. Im Gegensatz dazu kann bei der Stimulation von RGCs in der Nähe des Somas das Soma hauptsächlich die Zellerregung bestimmen, und in diesen Abständen tritt UT aufgrund einer somatischen Blockierung in RGC auf. (ii) Auf LT-Spiegeln werden APs in beiden Zelltypen immer am Axon-Initiationssegment (AIS) initiiert; in Zellen mit kurzem AIS lag die AP-Stelle nahe dem distalen Teil von AIS, während sich in Zellen mit längerem AIS die Initiationsstelle zum Zentrum von AIS hin verlagerte. (iii) PCs besaßen extrem hohe UTs, und (iv) bei PCs wurde kein vollständiger Block beobachtet. (v) Die Anordnung der Axon-Kollateralen in PCs hatte einen signifikanten Einfluss auf UTs, während er fast keinen Einfluss auf LTs hatte.

Das letzte Kapitel war eine reine Axonstudie, in der dünne vs. dicke und myelinisierte vs. nicht myelinisierte Fasern verglichen wurden. Für myelinisierte Fasern waren die wichtigsten Ergebnisse: (i) Die höchsten UTs wurden im dünnen und dicken Mainen-Modell (das in 3D-PC-myelinisierten Axonen verwendet wurde) und im MRG-Modell beobachtet. (ii) Zunehmender Faserdurchmesser verringerte UTs und Schwellenverhältnisse in den untersuchten Axonmodellen. (iii) Die Erhöhung der Pulsdauer verursachte eine Verringerung der UTs und der Schwellenverhältnisse und am deutlichsten in dünnen Fasern. Bei nicht-myelinisierten Fasern waren folgende wichtige Erkenntnisse: (i) Die höchsten UTs und Schwellenverhältnisse wurden für dünne Fasern gefunden, und UTs und Schwellenverhältnisse nahmen durch Vergrößerung des Durchmessers ab. (ii) Eine Erhöhung der Pulsdauer verringerte UTs und Schwellenverhältnisse, wie zuvor bei myelinisierten Fasern beobachtet. Zusammenfassend lässt sich sagen, dass Axone, wie bereits festgestellt, die am stärksten erregbaren Teile der Zelle sind, die die Zellerregung steuern, mit Ausnahme der Elektrodenpositionen sehr nahe am Soma. Obwohl die Stimulation dicker Fasern einfacher ist, ist dies aufgrund der kleinen Schwellenfenster aufgrund niedrigerer UTs eine ziemliche Herausforderung und kann zu einer einfacheren Blockadesituation führen.

Contents

Acknowledgments.....	ii
Abstract.....	iii
Zusammenfassung.....	v
List of Figures.....	x
List of Tables.....	xiii
Abbreviations.....	xiv
Chapter 1.....	1
1.1 Excitation of neurons.....	1
1.1.1 Cochlear implant (CI).....	3
1.1.2 Retinal implants.....	4
1.1.3 Brain stimulation.....	6
1.2 Anatomy and electrophysiology of neurons.....	7
1.2.1 Cell membrane.....	9
1.2.2 Electric properties of the passive membrane.....	10
1.2.3 Active properties of the membrane.....	10
1.2.4 Action potential initiation and propagation.....	12
1.2.5 Synaptic excitation, natural signaling of neuron.....	14
1.2.6 Electric stimulation.....	15
1.2.7 Threshold window and block phenomena.....	16
1.3 Anatomy, electrophysiology, and modeling of SGC, RGC, and PC.....	20
1.3.1 Spiral ganglion cells.....	21
1.3.2 Retinal ganglion cells.....	24
1.3.3 Pyramidal cells.....	27
1.4 Comparison between three investigated cells: SGC, RGC, and PC.....	32
1.4.1 Geometrical differences and similarities.....	32
1.4.2 Ion channels.....	34
1.5 Overview and limitations.....	36
1.6 Outlines.....	39
Chapter 2.....	40
2.1 Membrane models.....	40

2.2	Hodgkin-Huxley membrane model (HH model)	42
2.3	Multi-Compartment model.....	46
2.4	Solving differential equation.....	48
2.4.1	Euler Method	49
2.5	Extracellular stimulation	50
2.5.1	Activating function	53
2.6	Implementations	55
Chapter 3	56
3.1	Data preparation and computational modeling	56
3.2	SGC 3D pathways	60
3.3	Extracellular voltage	63
3.4	Excitation profiles in healthy target neurons.....	67
3.5	Suprathreshold excitation.....	72
3.6	Excitation of fibers without peripheral process.....	74
3.7	Discussion	76
Chapter 4	78
4.1	Model neurons.....	78
4.2	Biophysical properties.....	80
4.2.1	RGC	80
4.2.2	PC.....	82
4.2.3	SGC.....	84
4.3	Comparison of threshold windows.....	84
4.4	Evaluation of threshold ratios	88
4.5	The effect of pulse duration on threshold ratios.....	90
4.6	Discussion	93
Chapter 5	95
5.1	Model neurons.....	95
5.2	Biophysical properties.....	99
5.2.1	PC.....	99
5.2.2	RGC	104
5.3	PC model validation.....	105
5.4	Soma impact on thresholds	107
5.5	AP initiation sites	112

5.6	Partial upper threshold in PCs.....	114
5.7	Impact of stimulus parameters on threshold	116
5.7.1	PCs.....	116
5.7.2	RGCs.....	118
5.8	Discussion	119
Chapter 6	123
6.1	Axon models	123
6.1.1	The CRRSS model.....	124
6.1.2	The MRG model	125
6.2	Threshold windows in myelinated fibers	129
6.3	Threshold ratios in myelinated fibers.....	131
6.3.1	The MRG model	132
6.3.2	10HH model.....	132
6.3.3	The CRRSS model.....	132
6.3.4	The Mainen model	133
6.4	Threshold windows in non-myelinated fibers.....	135
6.5	Threshold ratios in non-myelinated fibers	136
6.6	Discussion	139
6.6.1	Myelinated fibers	139
6.6.2	Non-myelinated fibers	140
Chapter 7	142
References	146
Curriculum Vitae	161

List of Figures

Figure 1.1. Stimulation level vs. damage level in neural implants. Figure and caption from (Cogan et al., 2016).	2
Figure 1.2. Elements of a cochlear implant system. Figure taken from (Wilson and Dorman, 2008).	4
Figure 1.3. Schematic from retina components and retinal prostheses. Figure taken from (Tong et al., 2020).	5
Figure 1.4. A schematic representing deep brain stimulator (DBS) and the human brain. Figures adapted from (Rosa and Lisanby, 2012).	7
Figure 1.5. Neuron anatomy. Figure and caption adapted from (Castagnola, 2014; Leterrier, 2018).	9
Figure 1.6. Schematic illustration of a cell membrane. Figures are slightly adapted from (Learning, 2021).	12
Figure 1.7. Action potential.	13
Figure 1.8. Synaptic activity. Figure adapted from (Pereda, 2014).	15
Figure 1.9. In-vitro recording of RGCs. Figure and caption adapted from (Boinagrov et al., 2012).	18
Figure 1.10. Somatic and axonal recording of a 2D modeled RGC. Figure and caption from (Rattay, 2014).	19
Figure 1.11. Spiral ganglion cells (SGC). (A) Figure adapted from (Wan and Corfas, 2017). (B) Figure from Chester Chia / Harvard Medical School. (C) Figure from (Rattay et al., 2001b).	22
Figure 1.12. Mouse retina with RGC schematic morphologies. Figure is taken from (Sanes and Masland, 2015).	25
Figure 1.13. Three typical types of pyramidal neurons in mouse. Figure and caption adapted from (Guo et al., 2017).	28
Figure 1.14. RGC vs. PC. (A1) Figure from (Morgan and Wong, 2007). (A2) Figure from (Morgan and Wong, 2007) (A3) Figure from (Mazzoni et al., 2008). (B1) Figure and caption from (Guo et al., 2017).	33
Figure 2.1. Passive membrane model. Figure adapted from (Kaniusas, 2012).	40
Figure 2.2. Active membrane model in HH-style. Figure adapted from (Kaniusas, 2012).	42
Figure 2.3. Action potential in a HH model.	45
Figure 2.4. Schematic of the multi-compartment model in a part of a non-myelinated neurite.	47
Figure 2.5. Surface and resistance in a spherical soma.	48
Figure 2.6. Finite element model of a point source electrode vs. spherical electrode (3 μm). Figure from (Fellner et al., 2019).	52
Figure 2.7. FE model of cochlear extracellular stimulation.	53
Figure 2.8. Activating function of a straight myelinated axon from the SGC axon model.	54

Figure 3.1. Schematic drawing of the compartment model of a human type I SGC. Figure and caption adapted from (Potrusil et al., 2020)..... 58

Figure 3.2. FE model of the human cochlea with 30 traced nerve fiber bundles. Figure adapted from (Potrusil et al., 2020)..... 61

Figure 3.3. Length measurements of 30 reconstructed SGCs. Figure adapted from (Potrusil et al., 2020). 62

Figure 3.4. Extracellular voltage for the selected active electrode, L4, from the lateral system. Figure adapted from (Potrusil et al., 2020)..... 63

Figure 3.5. Extracellular voltage for the selected active electrode C5 from the perimodiolar system. Figure adapted from (Potrusil et al., 2020). 65

Figure 3.6. Extracellular voltage for the selected active electrode L11 from the lateral system. Figure adapted from (Potrusil et al., 2020)..... 66

Figure 3.7. Extracellular voltage for the selected active electrode C21 from the perimodiolar system. Figure adapted from (Potrusil et al., 2020). 67

Figure 3.8. Stimulation of intact target fiber basal11 at threshold level with the lateral electrode of L4. Figure adapted from (Potrusil et al., 2020). 69

Figure 3.9. Stimulation of intact target fiber basal11 at threshold level with the perimodiolar electrode of C5. Figure adapted from (Potrusil et al., 2020). 70

Figure 3.10. Stimulation of intact target fiber middle 5 at threshold level with the lateral electrode of L11. Figure adapted from (Potrusil et al., 2020)..... 71

Figure 3.11. Threshold stimulation of intact target fiber middle 5 with the perimodiolar electrode of C21. Figure adapted from (Potrusil et al., 2020). 72

Figure 3.12. Suprathreshold stimulation of middle5 with L11. Figure adapted from (Potrusil et al., 2020). 73

Figure 3.13. Stimulation of degenerated target fibers basal11 (top) and middle5 (bottom) at threshold level. Figure slightly adapted from (Potrusil et al., 2020). 74

Figure 3.14. ANO/CAT threshold ratios are plotted for the target fibers and the selected electrodes. Figure from (Potrusil et al., 2020)..... 75

Figure 4.1. The linear geometry dendrite-soma-axon. 80

Figure 4.2. Examples of traced RGCs. Figure adapted from (Fohlmeister et al., 2010)..... 81

Figure 4.3. The lower (LT) and upper threshold (UT) of the single soma stimulation in RGC, SGC, and a PC. Figure adapted from (Sajedi et al., 2020)..... 85

Figure 4.4. The lower (LT) and upper thresholds (UT) of the axon experiment in RGC, SGC, and a PC. Figure adapted from (Sajedi et al., 2020)..... 86

Figure 4.5. The lower (LT) and upper thresholds (UT) of the whole-cell experiments in the RGC, SGC, and a PC. Figure adapted from (Sajedi et al., 2020). 87

Figure 4.6. The lower (LT) and upper thresholds (UT) of the single soma and axon, and whole-cell experiments. Figure adapted from (Sajedi et al., 2020). 87

Figure 4.7. Threshold ratios versus electrode distance. 89

Figure 4.8. Threshold ratios (100 μ s vs. 1 ms)..... 92

Figure 5.1. Realistic model neurons. Figure from (Sajedi et al., 2021). 97

Figure 5.2. Investigated PC model neurons (PC1-PC8)..... 98

Figure 5.3. Reproducing backpropagation activated Ca^{2+} spikes. 106

Figure 5.4. The lower and upper thresholds in RGC and PC models. Figure adapted from (Sajedi et al., 2021). 109

Figure 5.5. Lower threshold (LT) in PC models vs. dendrite diameter. 110

Figure 5.6. AIS is the AP initiation site in RGCs and PCs. Figure adapted from (Sajedi et al., 2021). 114

Figure 5.7. PC excitation during various amplitude. Figure adapted from (Sajedi et al., 2021)..... 115

Figure 5.8. Spiking nodes percentage. Figure adapted from (Sajedi et al., 2021). 116

Figure 5.9. Thresholds for different electrode positions around the PC soma. Figure adapted from (Sajedi et al., 2021). 117

Figure 5.10. Effect of electrode diameter and pulse shape on threshold ratios in RGC model neurons. Figure adapted from (Sajedi et al., 2021)..... 119

Figure 6.1. Multi-compartment double cable model of MRG axon. Figure and caption from (McIntyre et al., 2002). 128

Figure 6.2. Lower (LT) and upper thresholds (UT) for myelinated axon models. 131

Figure 6.3. Threshold ratios (UT/LT) of the investigated myelinated axon models. 134

Figure 6.4. Lower (LT) and upper thresholds (UT) for non-myelinated axon models. 136

Figure 6.5. Threshold ratios (UT/LT) of the investigated non-myelinated axon models..... 138

List of Tables

Table 3.1. Human SGC model parameters with slight adaptations (Rattay et al., 2001b).	59
Table 4.1. Geometric and electrophysiological parameters used in the investigated cell models.....	79
Table 4.2. G-bar conductances (mS/cm ²) for modeled RGC. From (Fohlmeister et al., 2010)	82
Table 4.3. G-bar conductances (mS/cm ²) for modeled PC. From (Rattay and Wenger, 2010).	84
Table 4.4. Threshold ratios (UT/LT) for the investigated cells and distances for a cathodic pulse with 100 μ s and 1 ms duration.	91
Table 5.1. Parameter values were obtained from (Almog and Korngreen, 2014).....	103
Table 5.2. Maximum conductivities in RGC models based on data from (Fohlmeister et al., 2010; Werginz et al., 2020).....	104
Table 5.3. r^2 values for correlations between multiple geometric parameters and LT, UT, as well as threshold ratio (UT/LT).	112
Table 6.1. Biophysical parameters used in the CRRSS model, based on (Chiu et al., 1979; Sweeney et al., 1987).	125
Table 6.2. Biophysical parameters used in the MRG model. All parameter values were based on the original study (McIntyre et al., 2002) with slight adaptation in *.....	126

Abbreviations

2D	Two Dimensional
3D	Three Dimensional
AP	Action Potential
AF	Activating Function
ANO	Anodic
AIS	Axon Initial Segment
CAT	Cathodic
CRRSS	Chiu-Ritchie-Rogart-Stagg-Sweeney (model)
CI	Cochlear Implant
DBS	Deep Brain Stimulation
FE	Finite Element
FCM	Fohlmeister-Coleman-Miller (model)
FH	Frankenhaeuser-Huxley (model)
HVA	High Voltage Activated (ion channel)
HH	Hodgkin and Huxley (model)
L5	Layer Five
LT	Lower Threshold
MRG	McIntyre-Richardson-Grill (model)
MVA	Medium Voltage Activated (ion channel)
NoR	Nodes of Ranvier
ODE	Ordinary Differential Equation
PC	Pyramidal Cell
RGC	Retinal Ganglion Cell
SE	Schwarz-Eikhof (model)
SSI	Spike Site Initiation
SGC	Spiral Ganglion Cell
UT	Upper Threshold

Chapter 1

General Introduction

This chapter aims to provide the required background from an anatomical and electrophysiological point of view. To fulfill this goal, first, the anatomy of the three organs of interest, which are crucial for understanding the result section, are described and introduced briefly to the reader. In the next step, the anatomy and electrophysiology of neurons and their cell membrane features, in general, are addressed. In addition, section 1.3 is devoted to more specific descriptions and enlightenment on the anatomy and neuron electrophysiology of the investigated neuron types, and the next section compares these three cells from an anatomical and electrophysiological aspect. The last section discusses the limitations of the field and the goal of the study.

1.1 Excitation of neurons

A stimulus elicits action potentials (APs) in a neuron. In the brain, as an example, natural excitation is commonly caused by chemical synapses (see section 2.4). However, excitation can also occur by applying electric or magnetic fields. Neuroprosthetics bypass a damaged part to restore the lost sense or function. These devices serve either as surface stimulators, such as training muscles, or implantable devices such as cochlear implants (CI), retinal implants, cortical and deep brain stimulators.

An implant delivers electric charges to the tissue by the electrode and depolarizes the excitable cell membrane to elicit neural responses. The amount of charge delivered to the tissue is calculated by the time integral of the current ($I_{stim} \times T_{stim}$). The overall charge needs to be zero to prevent charge accumulation and, consequently, avoid tissue damage (Brummer and Turner, 1977). This is done mainly by applying biphasic pulses that include cathodic and anodic phases, with the same amount of charge that can be symmetric or asymmetric. Another important objective of using charge-balanced pulses is to preserve the electrode potential within a range to prevent irreversible reduction and oxidation that destroy the electrode.

Electrodes used in neural implantations are usually divided into macro- and microelectrodes. The macroelectrodes use high charge/ phase threshold and low charge density thresholds placed on the tissue surface with a surface area larger than 0.001 cm^2 . Microelectrodes can be used to penetrate the target with a surface area smaller than 0.0001 cm^2 , and they use low charge/phase thresholds and high charge density thresholds (Cogan, 2008). Microelectrodes are mostly used in small and dense neural tissues, improving selectivity and spatial resolution. Several studies reported that by using penetrating microelectrode in the brain, about 1 nC/phase threshold could be sufficient for stimulating neural tissue (McCreery et al., 1994, 2000, 2002). The damage, however, is expected at four times larger than this threshold (Cogan, 2008). In contrast, macroelectrodes are effective at smaller than $10 \text{ } \mu\text{C/cm}^2$ thresholds, which is below their tissue damage range ($30 \text{ } \mu\text{C/cm}^2$ for electrode with a surface area of 0.06 cm^2), reported by Kuncel and Grill, who reviewed functional and tissue damage thresholds of various studies using clinically deep brain stimulation (Kuncel and Grill, 2004). Figure 1.1 shows neural stimulation and damage levels for various implants, including electrodes with surface area $< 0.01 \text{ cm}^2$ and larger electrodes.

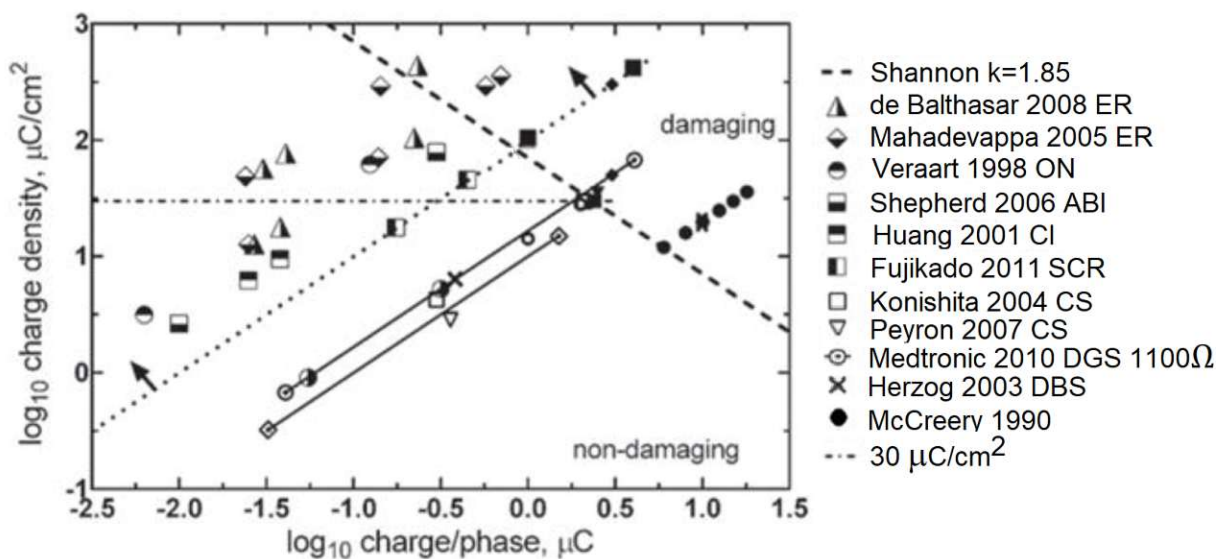


Figure 1.1. Stimulation level vs. damage level in neural implants having an electrode with geometric surface area $< 0.01 \text{ cm}^2$ (region above and to the left of the dotted line as indicated by the arrows) compared with larger electrodes. ER, ON, CI, and SCR represent epiretinal surface, optic nerve surface, cochlear implants, and suprachoroidal placement targeting the retina. ABI, CS, and DBS represent auditory brain stem surface, cortical surface stimulation, and deep brain stimulation. $k = 1.85$ is chosen

from the Shannon equation (McCreery et al., 1990) to define the boundary between damaging and non-damaging stimulation. Figure and caption from (Cogan et al., 2016).

Moreover, another important factor that limits the maximum charge densities applied to the electrodes is the electrode material as well as the charge-injection mechanism. There are two charge-injection mechanisms, the capacitive charging that forms an electrode-electrolyte double layer and the faradaic charging in which the electrode surface will oxidize and reduce (Cogan, 2008). Some materials can benefit from both injection mechanisms, such as electrodes from platinum and platinum-iridium alloys with a maximum charge density of 0.05-0.15 mC/cm² (Rose and Robblee, 1990). Whereas materials such as titanium nitride can only use capacitive charging, and its maximum charge density is about 1 mC/cm² (Weiland et al., 2002). More details on electrode limitations and safety parameters for neural implants can be found in (Cogan, 2008; Cogan et al., 2016).

However, one crucial factor in neural prostheses such as epiretinal and cochlear implants is selectivity and spatial resolution. In epiretinal implants, the application of microelectrode arrays requires narrow intensity ranges for each electrode, because every electrode should only activate nearby cells to elicit a small visual phosphene needed to restore vision. Thus, long stimulation pulse width (25 ms/phase) with lower stimulus intensity is often considered in epiretinal prosthesis (Weitz et al., 2015). In CIs, channel interactions occur due to using high-intensity range pulses. Channel interaction refers to a situation in which different regions of the cochlea are excited simultaneously by a single electrode that associates with poor speech understanding (Bierer and Faulkner, 2010; Bierer and Litvak, 2016). The following sections address some related implant devices as well as the interfaced anatomy regions.

1.1.1 Cochlear implant (CI)

The ear is divided into three sections: external, middle, and inner ears (see Figure 1.2). The external ear consists of the pinna that catches the sound waves and conducts them to the external acoustic meatus that ends at the tympanic membrane or eardrum. The middle ear is located between the temporal bone and the inner ear lateral wall. The middle ear amplifies and transmits the eardrum's vibrations to the inner ear, which is achieved by the auditory ossicles. The deepest part of the ear, the inner ear, contains the vestibular and cochlear organs. Cochlea transforms mechanical movements received from the middle ear into electric signals via inner and outer hair cells and sends them to the spiral ganglion cells (SGCs), also called cochlear neurons, to carry the signals to the brain.

Cochlear implants are commercial devices and the most successful neuroprosthetics used by 800000 persons worldwide (Boisvert et al., 2020). A CI aims to use electric stimulation of residue hearing path to restore the sense of hearing in people with severe hearing loss problems. A CI, shown in Figure 1.2, contains a microphone to select the sound and transfer it to the external processor. In the external processor, the sound is converted first into digital signals. Signals are delivered to an antenna located in a headpiece, a transmitter, attracted to an internal unit by a magnet. The internal unit, inserted behind the impaired ear under the skin, consists of a receiver that collects the signals and a stimulator that generates a set of stimuli and sends them to the implanted electrode array inside the cochlea (Wilson and Dorman, 2008).

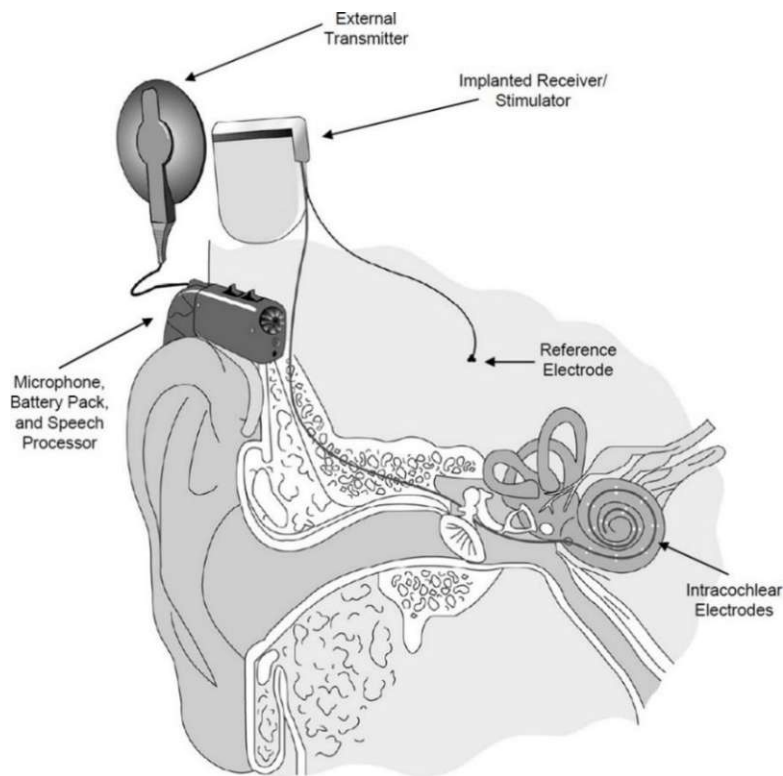


Figure 1.2. Elements of a cochlear implant system. Figure is taken from (Wilson and Dorman, 2008).

1.1.2 Retinal implants

Light enters the cornea at the front window of the eye and gets transmitted and focused into the backside (Figure 1.3A). The iris is the colored part that regulates the amount of light before transmitting and getting focused by the lens, surrounded by the white outer coat, the sclera. The retina is located in the back of the eye and consists of the nerve layers of retinal ganglion cells (RGC), bipolar, amacrine and horizontal cells, and photoreceptors. After sensing the light, the retina creates electric pulses (usually in scale of graded potentials or small spikes) through

the nerves, which then generate APs (large spikes) in the last neural layer (axons of retina ganglion cells) and travels to the brain through the optic nerve.

The primary reasons for blindness and low vision are age-related eye diseases, e.g., age-related macular degeneration and common eye disorders, including amblyopia and strabismus (CDC, 2020). Despite an advanced degeneration of the retinal architecture, the inner retinal neurons are mostly preserved (Humayun et al., 1996, 1999).

Retinal prostheses can be placed either intraocular or extraocular and stimulate the remaining neural pathway to restore the vision sense partially (Werginz and Rattay, 2014). Figure 1.3 shows a schematic of the retinal anatomy and the electrode array positions in the three most common approaches:

- i) Epiretinal implants place the electrodes on the top side of the retina, where the ganglion cells are located (Eckmiller, 1997; Rizzo III and Wyatt, 1997).
- ii) Subretinal implants with electrodes located under the retina close to damaged photoreceptors (Chow and Chow, 1997; Zrenner et al., 1997).
- iii) Suprachoroidal implants with electrodes placed between choroid and sclera (Tong et al., 2020).

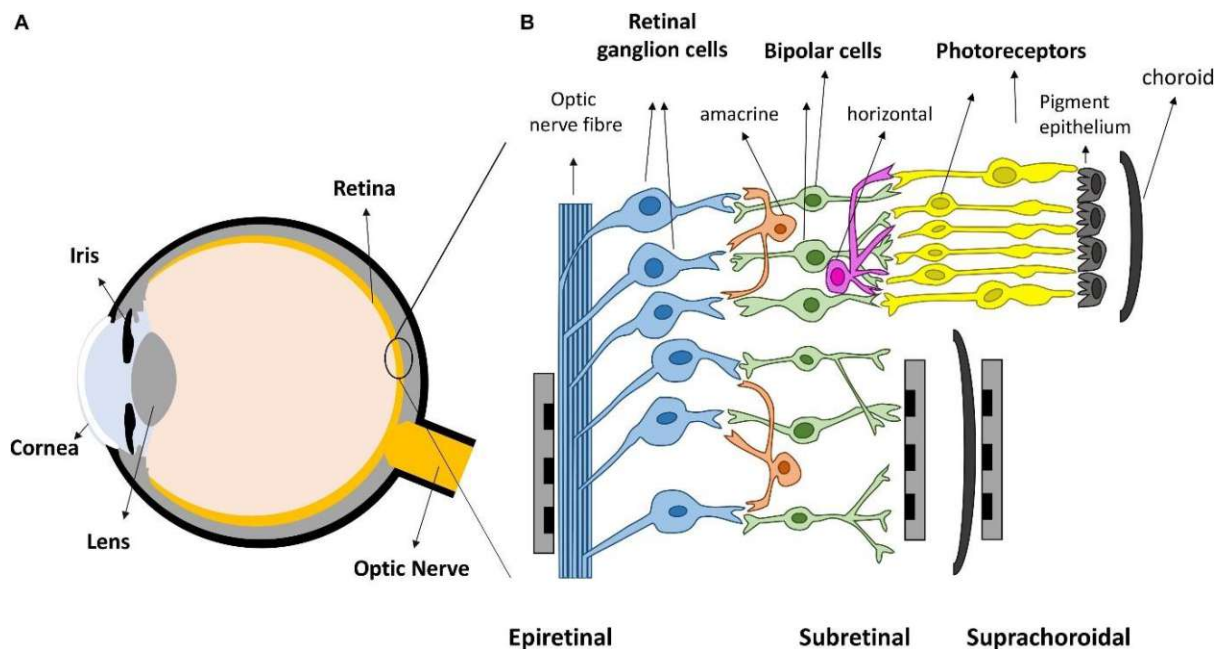


Figure 1.3. Schematic from retina components and retinal prostheses. (A) Eye diagram description. (B) Three layers of neurons build the retina: photoreceptors, bipolar cells and retinal ganglion cells (RGCs), horizontal and amacrine cells located in-between. Three possible locations of retinal prostheses: Epiretinal arrays make contact with the RGCs; subretinal located connect with bipolar cells,

and suprachoroidal implants inserted between the choroid and sclera. Figure is taken from (Tong et al., 2020).

1.1.3 Brain stimulation

About 100 billion neurons build the human brain with a highly complicated structure. The brain divides into the left and right lobes dedicated to specific series of functions. The cerebral cortex is the most outer layer of the brain, which associates with higher thinking skills. For the sake of simplicity, the current section addresses the anatomy of some cerebral cortical parts of the brain limited to the content of this thesis; the auditory, visual, and somatosensory cortex (Figure 1.4).

The auditory cortex, located in the temporal lobe, processes the auditory information coming from the central site of the SGCs. It is mainly responsible for spectrotemporal, involving time and frequency information, analyzing the auditory pathway's signals, and sending them to the following processing unit for speech processing.

The visual cortex processes visual information such as form, pattern, and motion coming from the visual pathway. Visual cortex neurons elicit signals when visual stimuli arise within their receptive field. The receptive field is the area of the entire visual field that evokes electric signals.

Somatosensory is the section of the cortex subjected to receiving and processing sensory information such as touch, pressure, temperature, and pain from the entire body. It is located within the postcentral gyrus of the parietal lobe and behind the motor cortex of the frontal lobe. Somatosensory then sends the sensory signal to the other parts of the brain for further processing.

Deep brain and cortical stimulations have provided substantial clinical benefits worldwide. They have been used for neurological disorders such as Parkinson's disease, dystonia, Tourette Syndrome, pain, depression and obsessive-compulsive disorder, etc. The complete mechanisms of cortical prostheses' function are still undiscovered. It is known that a variety of mechanisms associated with neural function are affected by the electrical stimulation of the brain, and many factors such as the amplitude and characteristic of the stimulation, physiology, and geometry of different cells, the geometry of the electric field, etc., are involved. However, the neurons of the central nervous system possess different anatomical and electrophysiological properties that may lead to the various effects of brain stimulation (Perlmutter and Mink, 2006).

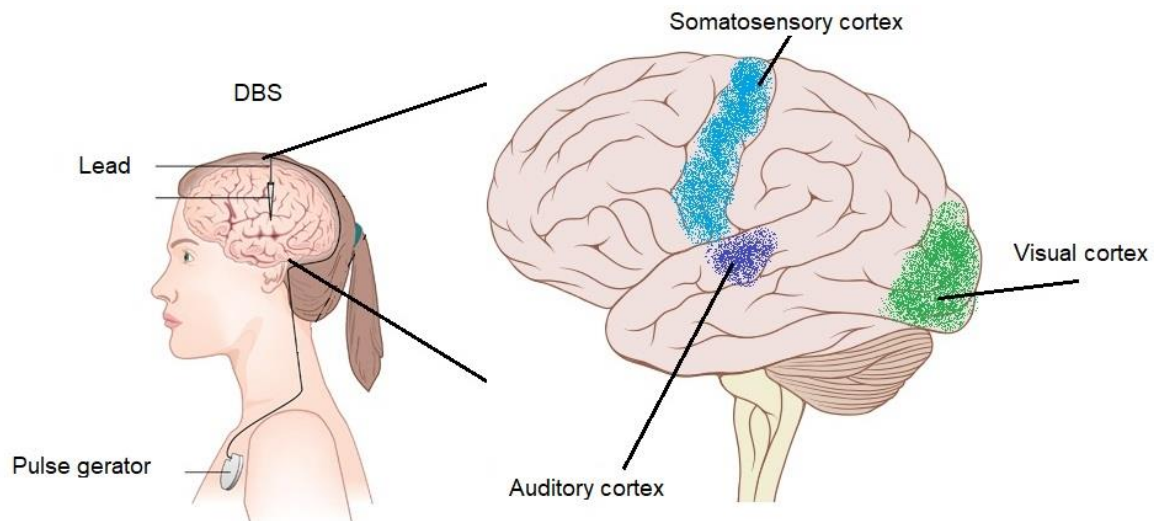


Figure 1.4. A schematic representing deep brain stimulator (DBS) and the human brain. Figures adapted from (Rosa and Lisanby, 2012).

1.2 Anatomy and electrophysiology of neurons

The anatomical basis of this section is taken from (Fundamental Neuroscience for basic and clinical applications and fundamental Neuroscience, chapter 2). Neurons, in general, process the information inside the body. Their essential role is to receive information as electrical signals from their neighbor processing units, usually other neurons. This information is usually sent to the next unit by a combination of electrical and chemical events. In brief words, neurons consist of the cell body or soma, the processes, dendrite, and axons (Figure 1.5). Neurons are in close contact with glial cells, which together build the nervous system from a histological point of view. Glial cells do not propagate signals and exist on central and peripheral nervous systems. However, they support neurons structurally and functionally, such as transporting nutrients to neurons and removing the waste products; they also preserve the electrochemical neuron surrounding. An important type of glial cells is Schwann cells, which are myelin sheaths around axons in the peripheral nervous system. Glia cells isolate the propagating signal through sheets of a membrane (myelin) to preserve energy and facilitate propagation.

Figure 1.5 demonstrates the essential components of a typical neuron. Soma is the central part of the neuron from which neurites (processes) grow. Soma includes the nucleus structure for protein synthesis and metabolic purposes, also known as the metabolic center of neurons. The general types of neurons, indicated by the shape of the soma, are multipolar (99% of neurons), pseudounipolar, and finally, bipolar cells. Soma in the multipolar neuron can have different shapes such as triangular, polygonal, etc., leading to multiple dendrites, and typically one main

axon develops from the soma. Multipolar neurons are mostly present in the central nervous system, such as pyramidal cells (PCs). Pseudounipolar neurons have a spherical-shaped soma with a single process that usually bifurcates in the vicinity of the soma to a long central process (axon) and a long peripheral process (dendrite). Bipolar neurons usually have round or elliptical-shaped somata, and the two processes, dendrite, and axon originate from each end of the soma. They can be found in the retina or the cochlea, such as SGCs.

Dendrites are the receiver sites of the neurons usually located in the vicinity of the axonal terminals of other neurons where they have synaptic contacts. Dendrites fork widely around the soma with a larger diameter in proximal sites (primary dendrites) and form thinner bifurcations in the distal site of soma (secondary dendrites)

Axons are the most extended components of neurons and often reach large distances before bifurcating and terminating. They exit from the soma with a small portion called axon hillock and an adjacent axon initial segment (AIS) that forms the few dozen micrometers of the axon beginning (see Figure 1.5C). Most axons are wrapped in myelin sheaths. The myelination of an axon is not continuous but is interrupted by sections of the axon called nodes of Ranvier (NoR). The length of the myelin sheath is related to the diameter of the axon, usually $100 \times$ axon diameter (Rushton, 1951). Myelin facilitates signal propagation through the long axon, and the NoR amplifies the neural signals.

Axon terminal arbors located at the end of the axon are the points of contact between the cells. The terminal is usually capped with so-called synaptic boutons. Synapses are the communication sites of an axon with the dendrites or soma of the adjacent neurons. More details on synaptic activity are given in section 1.2.5.

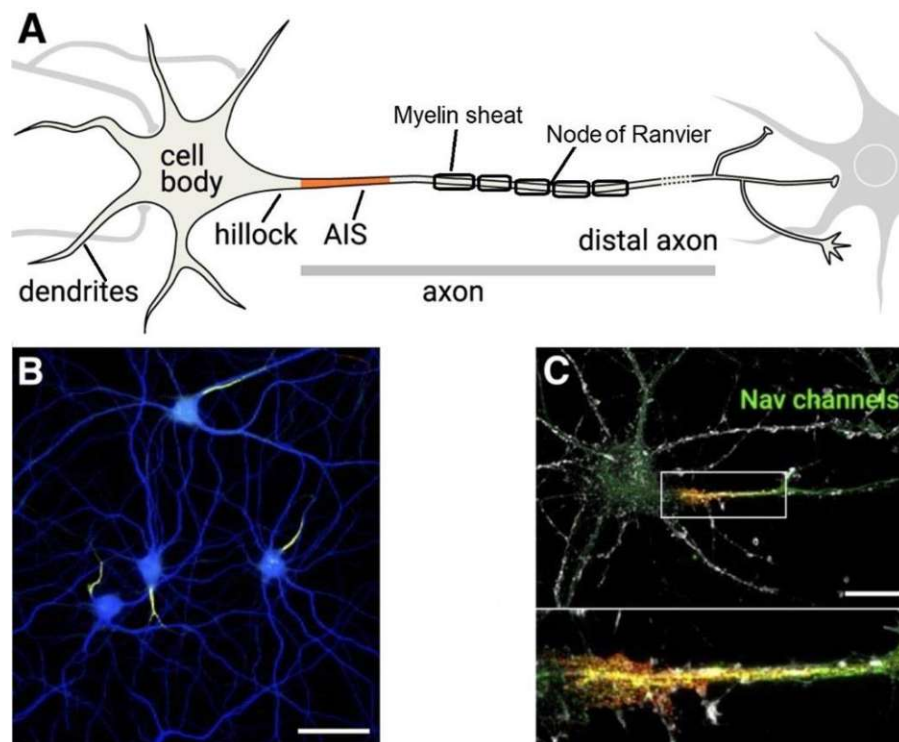


Figure 1.5. Neuron anatomy. **(A)** Neuron schematic. **(B)** Neurons from the hippocampus (a major section in the brain) after 22 days in a culture labeled for axon initial segment (AIS). The somatodendritic compartment is labeled using an antibody (blue). Scale bar, 50 μm . **(C)** Hippocampal neuron after 14 days in culture labeled (gray and red) and Na_v channels (green). Bottom, The zoomed image represents the AIS. Scale bar, 20 μm . Figure and caption adapted from (Castagnola, 2014; Leterrier, 2018).

1.2.1 Cell membrane

The basic content of the following sections is based on (Rattay, 1990; Kaniusas, 2012). A neuron membrane has a bilipid structure and is therefore excitable. The intra- and extracellular environments on a neuron are usually filled by charged and polar molecules such as ions and amino acids. Subsequently, a neuron membrane covered by pores, pumps, and channels accommodates the passage of the molecules and ions inside and outside the cell. The electrical properties of neurons originate from the membrane features and induce a potential differentiation between the outside and inside the cell that is time and spatial dependent. Usually, if no stimulus exists, a cell is in a resting state and processes a stationary potential known as resting potential. The membrane potential will change by receiving information in terms of chemical changes in and outside the cell. These changes can be either imbalance of the membrane resting potential or as strong as APs. Either way, these local changes, and fluctuations will propagate through the cell, usually to the end of the axon terminals leading to

chemical interactions for transferring the information to the next unit, and this is how neurons exchange information.

1.2.2 Electric properties of the passive membrane

The cell membrane is permeable only for specific ions and molecules that cross the membrane either by gradient forces or electric forces. The unequal concentration of ionic substances in and outside the membrane generates a concentration gradient. Passages by gradient forces are according to simple diffusion law through some mechanisms that facilitate their passage. Passages by electric forces are according to Kirchhoff's law which equalizes the net electric currents inside and outside the cell to bring the voltage back to its resting state. Figure 1.6A shows a simple illustration of the passive membrane.

Different channels and transfer proteins cover the membrane, e.g., carrier and (resting) channel proteins. Carrier proteins and channel proteins or pores facilitate the passage of the ions and molecules from the side with a higher concentration to the side with a lower concentration (diffusion law). Carrier proteins bind to specific molecules, change their conformation and carry them to the intracellular medium whereas, resting channel proteins are always open and specified to particular ions such as sodium (Na^+), potassium (K^+), and chloride (Cl^-) according to their size, charge, and the amount of the surrounding water molecules.

Moreover, when charged ions and molecules pass the membrane, the membrane resting potential changes, generating a current between the two sides of the membrane to equalize the voltage difference and bring back the membrane voltage to the resting value. As long as the potential changes are small, they provoke no AP, which refers to the subthreshold behavior of the cell. However, in the case of AP propagation, the passive properties and behavior of the cell determine the propagation speed of AP along the cell membrane. According to these electrophysiological features, a passive cell membrane can be modeled with a cable model discussed in section 2.1.

1.2.3 Active properties of the membrane

Two important mechanisms mainly regulate the membrane's active properties: regulatory membrane mechanisms and active transport. Figure 1.6B displays a schematic of both mechanisms.

Gated channel proteins generate the regulatory mechanisms. Gated channel proteins are only open when: (i) the membrane potential exceeds the resting value (usually an increase), (ii)

chemical substances bind to the receptor site, or (iii) when mechanical/thermal forces are involved. Gated channels can be either open or close, but after a particular time, they become nonactivated and take some time to activate again.

Different types of voltage-gated channels are known, such as voltage-gated Na^+ , voltage-gated K^+ , voltage-gated Ca^{2+} , and voltage-gated Cl^- . The density and type of these channels mainly depend on the neuron type and anatomy. About 500 per μm^2 voltage-gated Na^+ channels exist in the non-myelinated axon, while in the myelinated axon, they are mostly accumulated in the nodes of Ranvier with a much higher density.

The second type of gated-channels involved in the active properties of the membrane is the transmitter-gated channels. When a chemical messenger binds to the receptor site, the channel opens, and specific ions pass the membrane. For example, the acetylcholine-gated channel opens when a neurotransmitter, acetylcholine, binds to the receptor and Na^+ and K^+ ions pass the postsynaptic membrane.

Another type of gated-channels is the stress-sensitive channel named stretch-gated channel. In case of applying stretching or thermal forces on the membrane, the stretch-gated channels open and lead to an inflow of Na^+ and outflow of K^+ ions. In addition, it is worth mentioning that some channels react to specific ions, such as the Ca^{2+} -activated K^+ channel that their opening probability increases with intracellular Ca^{2+} concentration.

Active transport is the second mechanism that governs the active properties of the membrane. Their structure is similar to the diffusion mechanism, with a clear difference; these channels need energy such as adenosine triphosphate (ATP) or electrostatic energy to overcome the gradient and work against it. One example of these highly specified active transporters is the sodium-potassium pump. These pumps generate an outflow of Na^+ and an inflow of K^+ ions to bring the membrane potential back to the resting state and compensate for the work of voltage-gated channels. By this mechanism, the membrane potential reaches a hyperpolarizing stage (the last stage on an AP) that is a bit more negative than the resting potential.

In the early 1950s, Andrew Fielding Huxley and Alan Lloyd Hodgkin proposed the most famous active membrane model (HH model) based on a cable model considered as one of the excellent accomplishments of 20th-century biophysics (Hodgkin and Huxley, 1952). The model describes how an AP initiates and propagates in a squid axon. A brief description of the AP in their model is discussed in the following section. Detailed insight into the model, however, will be given later in section 2.2.

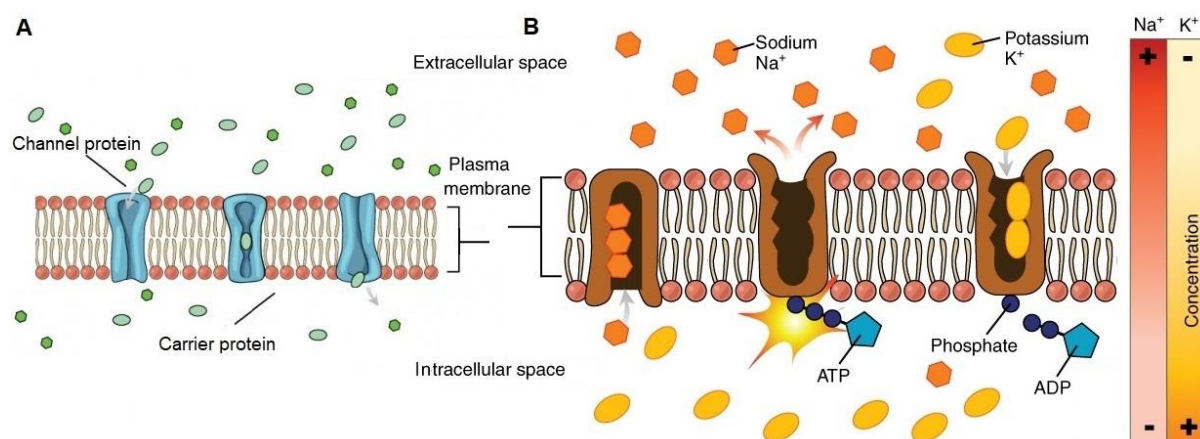


Figure 1.6. Schematic illustration of a cell membrane. **(A)** Passive diffusion by channel proteins and carrier proteins. **(B)** Active pump and gated channels. Figures are slightly adapted from (Learning, 2021).

1.2.4 Action potential initiation and propagation

Electrophysiological properties of a neuron membrane allow it to possess a stationary potential, known as resting potential. A stimulus can be naturally produced by chemical, thermal, mechanical changes or by employing electrical stimulation. Either way, it changes the amount of charged molecules and ions inside and outside the membrane and leads to local changes first as subthreshold behavior, and if the stimulus is large enough to develop an active cell response, then as an AP. After the Noble prize-winning work of Hodgkin and Huxley, AP initiation and propagation along the cell can be explained mathematically by modeling the biophysical properties of the membrane to electric components, which is called a cable model. More insight into the mathematical point of view is given in section 2.2, but it will be very briefly discussed in the following.

HH introduced gating variables as m and n for activating channel opening of sodium and potassium ions, respectively, and h as the inactivating factor for sodium. Figure 1.7A shows voltage changes in the AP scale against the time in a patch of a squid cell membrane. After stimulus onset (red square, red vertical line), membrane potential increases (depolarizes) to a certain level (purple vertical line). A closer look at the ion current densities and their gating performance demonstrate a continuous membrane voltage change (Figure 1.7B-C). When the membrane potential crosses a threshold level, voltage-gated Na^+ channels open (sodium activation gate probability of m , increases) and leads to an inflow of Na^+ into the cell, consequently resulting in a rise in the membrane potential. With a delay and lower speed, voltage-gated K^+ channels open (n increases), resulting in an outflow of K^+ ions that decreases

(repolarizes) the membrane potential (Figure 1.7B). In addition, at some point close to the end of depolarization phase, inactivation of the voltage-gated Na^+ channels occurs (inactivating gate probability of h drops to values close to 0), which stops the passage of Na^+ ions (Figure 1.7C). Although AP starts locally, it consists of actuating or sensory information. The information should be carried to the central nervous system for further processing or to peripheral units such as muscles to act accordingly. However, delivering the signal to the following processing units is done mainly by a combination of chemical and electric activities, known as synaptic excitation (see next section).

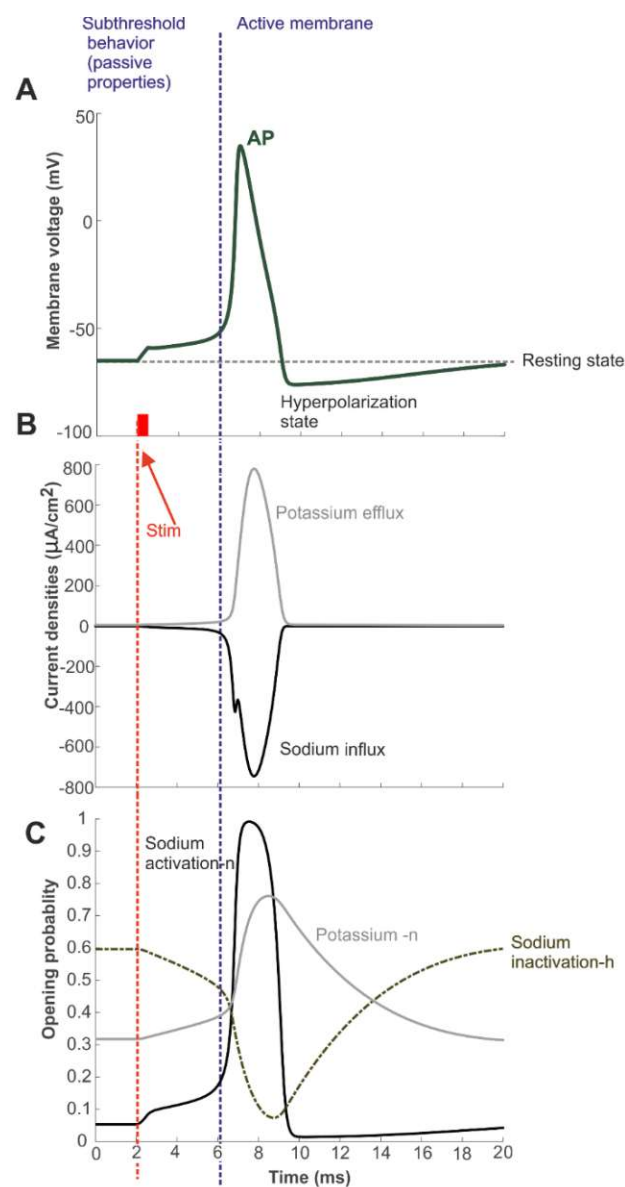


Figure 1.7. Action potential. (A) Transmembrane voltage (mV) against time (ms) in a single compartment with Hodgkin and Huxley model (calculated with the original parameters at 6.3°C). (B)

Na^+ and K^+ Current densities, and (C) sodium and potassium gating probabilities. More insight into gating kinetics is given in section 2.2.

1.2.5 Synaptic excitation, natural signaling of neuron

Synaptic activity in neurons can be either chemical or electrical (Figure 1.8). A chemical synapse includes chemical substances (neurotransmitters) and has three sites: (i) a presynaptic site, typically an axonal bouton. Axon bouton contains vesicles, and vesicles contain the neurotransmitters released during the process. Vesicles are usually close to the presynaptic membrane, so-called active sites. (ii) A postsynaptic site directly across the cleft, mostly a dendrite or soma of another cell. (iii) A cavity is the synaptic cleft between two sites involved in the synaptic process. The synaptic cleft is an area in which the neurotransmitters are free.

When an AP propagates along the axon and arrives at the presynaptic terminal, it depolarizes the presynaptic membrane potential, leading calcium channels to open. Calcium influx causes vesicles to fuse, which then causes the release of neurotransmitters into the cleft. Free neurotransmitters can then bind to specific receptors in the postsynaptic membrane and cause an excitation (depolarizing) effect leading to AP initiation in the postsynaptic membrane called excitatory synapse or an inhibition (hyperpolarizing) effect that reduces the postsynaptic cell activity called an inhibitory synapse. The type of synapse depends on the type of the involved neurotransmitters.

In electrical synapses, mostly between muscle cells, two neurons are connected by tiny gap junctions, narrower than the cleft, including no chemical components. Gap junction facilitates the signal transmission between the connected cells that transmits directly between the membranes (Figure 1.8B).

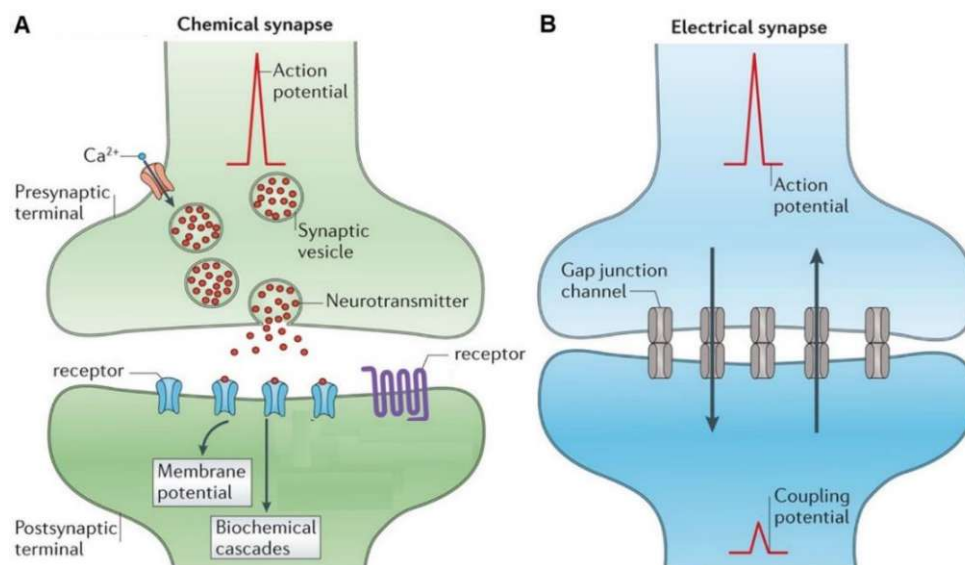


Figure 1.8. Synaptic activity. **(A)** Chemical vs. **(B)** electrical transmission. Figure adapted from (Pereda, 2014).

1.2.6 Electric stimulation

Electric stimulation of the nerves is applicable in two ways: intracellular and extracellular approaches. The extracellular approach is used in clinical applications where an electrode or an electrode array is placed on the skin surface or within the body.

Extracellular stimulation of neurons goes back to almost 2000 years ago by discovering the electric impulses of an electric catfish used to treat pain. In the middle of the 18th century, electric shocks were generated with electro static machines for paralyzed patients. Altus Kratzstein, a German physician, wrote the first book in 1745 on electric therapy, supporting that muscle can be manipulated through electric current. An interesting finding was published by an Italian physician, Luigi Galvani, a century later. He used a bimetallic rod to pass an electric current through a frog's spine to investigate muscle interactions in the legs. These investigations were followed by other scientists, who tried to explain the phenomena. Many conflicting hypotheses were proposed until the work of Hodgkin and Huxley was published and answered the most fundamental questions in the field. However, by understanding the concept and the origin of the electric behavior of neurons, the clinical application of electric stimulation was developed.

An intracellular recording is mostly used to understand and investigate the electrophysiological properties of neurons. In the intracellular approach, an electrode is placed at the membrane

surface or inside a neuron. An important application of this approach is the patch-clamp technique introduced by (Sakmann and Neher, 1984).

In intracellular stimulation, if a positive (anodic) current is applied to the electrode, the membrane potential locally increases until it reaches the threshold level, and finally, an AP elicits and propagates. In comparison, a negative (cathodic) stimulus causes the membrane potential to drop to a more negative value than the resting potential.

In extracellular stimulation, however, the situation becomes more complicated. Every electrode generates an electric field spreading by isopotential lines (or surfaces) that reflect on the cell membrane. Consequently, the initiation and propagation of the AP become less predictable and more sophisticated, which depend on many factors such as the type and shape of the pulse.

In 1986, Rattay introduced the concept of activating function (AF). The AF is the second derivative of the extracellular potential and the driving force in neural extracellular stimulation for a homogeneous fiber. AF predicts the initiation AP site in the stimulated nerve by calculating the response of the membrane compartments to the extracellular stimulus at the beginning of the stimulation (Rattay, 1986, 1999). The concept was validated and used in many computational and experimental studies (Butson et al., 2007; Eickenscheidt and Zeck, 2014); more insight into extracellular stimulation and AF is given in section 2.5.

1.2.7 Threshold window and block phenomena

A threshold window refers to an intensity interval with a lower and an upper limit that actively propagates APs during extracellular stimulation. The lower threshold (limit) is the smallest current amplitude of the electrode that causes active responses of the cell. The upper threshold is the stimulation level above which no AP is elicited. However, a block is when an AP cannot be generated or propagated. Depending on the type, a block may depend on several parameters such as amplitude, electrode distance, and temperature.

By increasing the temperature of the stimulated cell, the AP propagation can be inhibited, which is called heat or thermal block. Heat block has been studied in recent years for controlling the excitability of the region of interest. This technique can be accomplished by delivering infrared lights into the concerned nerve tissue. Several studies have used infrared lights in peripheral nerves to inhibit the small-diameter axons in mammalian and nonmammalian specimens (Wells et al., 2005; Duke et al., 2012, 2013; Matic et al., 2013; Cayce et al., 2014; Lothet et al., 2017). Successful and selective control of small-diameter axons of sensory fibers can have many clinical applications in the future, such as treating pain, hypertension, and chronic nausea.

Collision block happens if two APs initiated at the same neurite propagate against each other, and when the APs confront, they both stop propagating, and the membrane potential goes back to the resting state. The collision block naturally occurs due to absolute refractory time. Absolute refractory time refers to when an AP is rising to its peak value. Regardless of the stimulus intensity, no further AP can be elicited during this period. Therefore, when two collided AP reach each other at this point, both get suppressed.

An anodal surrounding block occurs due to increasing cathodic stimulus, producing anodic surrounding flanks in the stimulated membrane. The two induced hyperpolarized regions (flanks) stop the initiated AP from further propagation in the depolarized area (Katz and Miledi, 1965; Jankowska and Roberts, 1972; Roberts and Smith, 1973; Rattay and Aberham, 1993). To understand the nature of this phenomenon, one can imagine an electrode above a straight axon. When a cathodic stimulus (minus V_e values) is applied, the transmembrane potential ($V_m = V_i - V_e$) below the electrodes becomes depolarized. Since the sum of all currents through a closed area needs to be zero (first Kirchhoff's law), the depolarized current must be compensated, and this is done by flanks becoming hyperpolarized by opposing currents.

The somatic block was introduced by (Boinagrov et al., 2012). The group used a microelectrode close to RGC somata and reported an upper stimulation threshold by increasing the amplitude at a specific value below the cellular damage, where the somata stopped generating AP (Figure 1.9). Depending on pulse duration, the upper to the lower threshold ratio ranged from 1.7 to 7.6 in a somatic block (Boinagrov et al., 2012). This short interval between stimulating and blocking state is of concern in electrical micro-stimulation of tiny dense tissues, such as retina, when the electrodes are close to each other and impact cells from various regions.

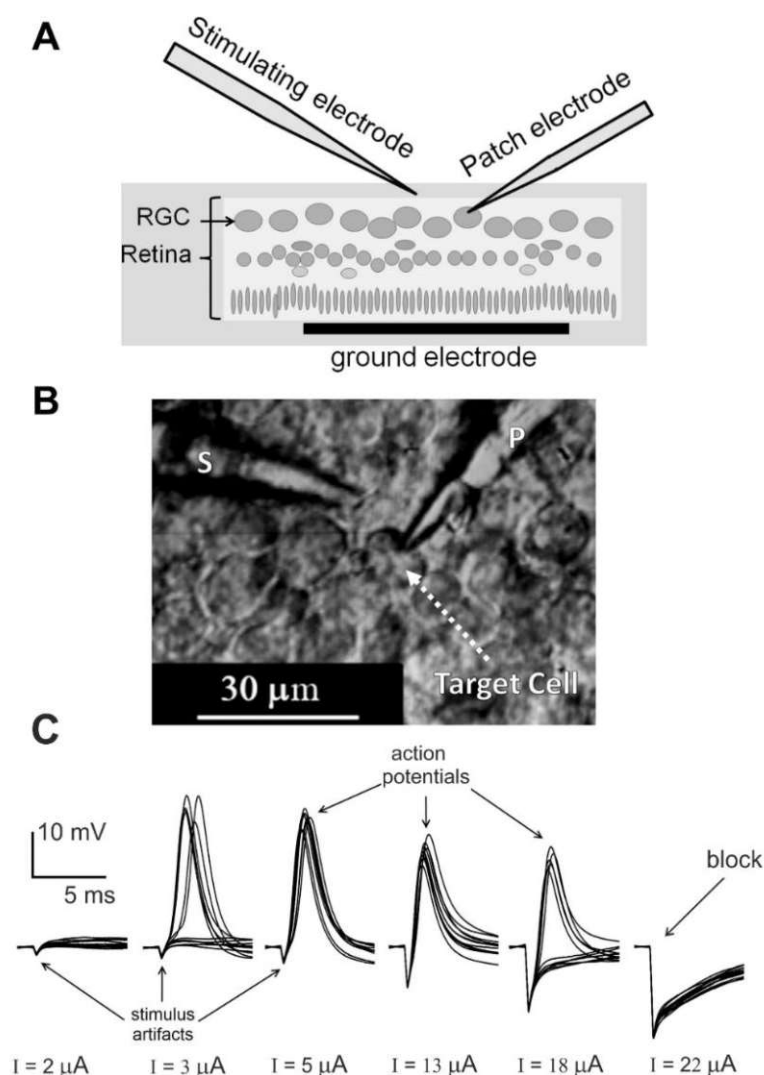


Figure 1.9. In-vitro recording of RGCs. **(A)** Schematic diagram of patch-clamp recording and stimulating. **(B)** Microscope image of isolated RGCs with a patch pipette (p) attached to the target cell and a stimulating electrode (s) holding close to the target cell. **(C)** Voltage membrane against the time for increasing cathodic stimulus with a duration of 0.2 ms. AP is generated for current intensities from 5 to 13 μA , and for 3 and 18 μA , AP was only elicited in half of the experiments. No AP below 2 μA and above 22 μA . Figure and caption adapted from (Boinagrov et al., 2012).

In a computational model of a RGC soma, the group studied the reason behind this block, and they found a reversal sodium current occurs due to high depolarized forces. An AP happens due to the inflow of sodium inside the cell, so this force is equal to $F_{Na} = (E_{Na} - V_m)$ where the E_{Na} and V_m represent the sodium Nernst potential and membrane potential (see section 2.1). As long as F_{Na} is a positive value, the sodium flows inside, and membrane voltage depolarizes. If the stimulus is intensely high where the V_m exceeds the E_{Na} , the sodium flow direction reverses, and sodium now exits the cell and leads to strong hyperpolarization in the membrane

potential (see Figure 1.9C). As a consequence of strong hyperpolarization, the AP cannot be generated. One important difference between an anodal surrounding block and a soma block is the generation of the AP. As mentioned above, an AP is generated in the depolarized region in anodal surrounding block, yet the strong hyperpolarized flanks do not propagate. Whereas, in soma block, because of strong hyperpolarization, AP cannot be elicited in the first place.

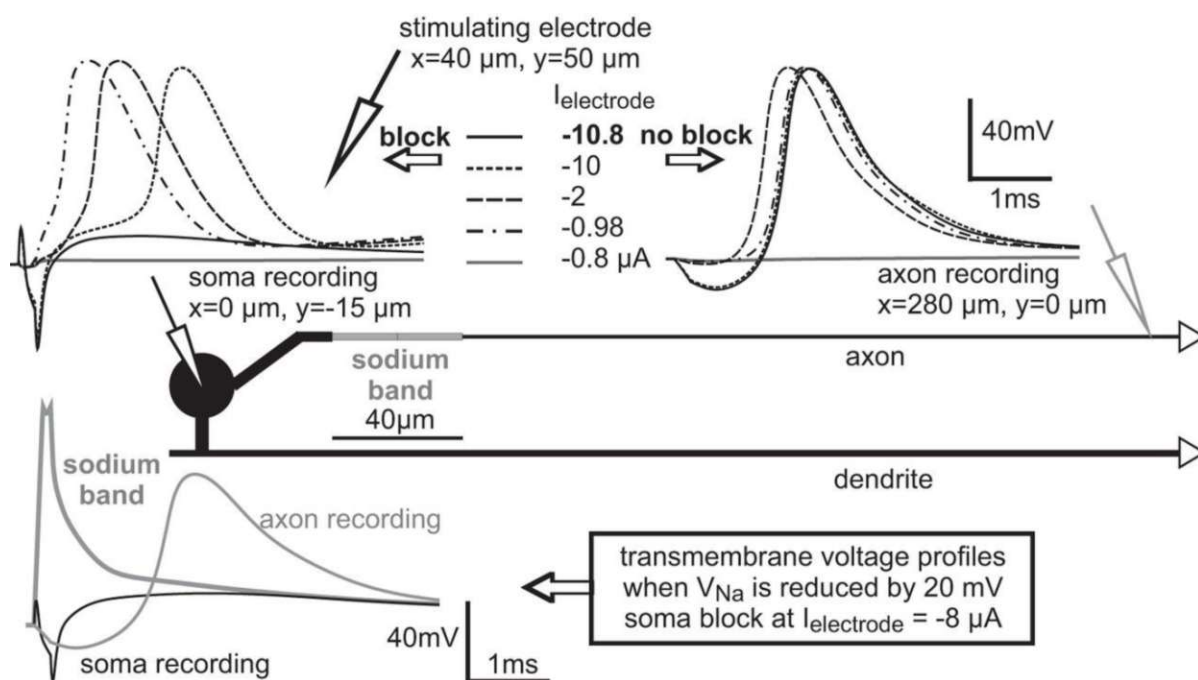


Figure 1.10. Somatic and axonal recording of a 2D modeled RGC. The model geometry is shown in the middle trace. Stimulating electrode is placed above the axon hillock while two recording sites are at soma center and distanced axon. Upper traces show transmembrane voltages from soma and axon while increasing a cathodic stimulus. Bottom traces demonstrate membrane voltage of soma and axon versus time for reduced external sodium concentration stimulated with a cathodic pulse of $8 \mu\text{A}$. Model diameter and length in μm , soma (20), axon hillock (3 and 40), axon initial segment (2, 40), thin axon (1, 170), vertical dendrite (4 and 10), and dendrite (2 and 300). Pulse duration 0.2 ms. Figure and caption from (Rattay, 2014).

Afterward, Rattay simulated a RGC cell with a 2D compartment model including the dendrite and axon (Figure 1.10, middle trace). He showed that the electrode position plays an essential role in the somatic upper threshold phenomenon, and if the axons are located in the active (depolarized) area, they can generate a propagating AP while the soma is in block (Figure 1.10 upper and bottom traces). Moreover, this situation mainly occurs when extracellular stimulation with high intensity is applied, which mostly leads to AP initiation in the axonal part, as frequently observed and reported. The AP generation in axons during somatic upper threshold was also reported by (Meng et al., 2018). In another computational study, the somatic

upper threshold phenomenon has been investigated on spherical soma, and they identified two additional mechanisms causing the somatic upper threshold: the strong potassium currents and the inactivating sodium ion channels (Fellner et al., 2019).

In summary, heat and collision blocks can be generated deliberately to inhibit or deactivate an undesirable neural activity; anodal and somatic blocks, on the other hand, may occur unpleasantly. However, the undesirable block situations are worth studying deeper, especially in micro-stimulation such as retinal and cortical implants.

One important term frequently used in current work is "upper threshold," which refers to the highest excitable amplitude after which either a somatic block or an anodal surround block occurs.

1.3 Anatomy, electrophysiology, and modeling of SGC, RGC, and PC

The permeability of the neuron cell membrane appears from pores and channel proteins across the membrane that contribute to the electric properties of the cell membrane. Studying membrane channel functions is feasible by applying different methods to understand the electrophysiology of neurons. In this category, one can mention clamping techniques and anatomical-biochemical approaches. The following content mentions some of these techniques based on (Cullinan et al., 1995; Mohs et al., 2000).

The patch-clamp technique for recording single-ion channel is one of the essential methods discovered by (Sakmann and Neher, 1984) and used in vitro investigations. The patch-clamp technique gives insight into the cell electrophysiology, such as the types and quantity of ions and channels in the cell. The characteristic responses of the channels, such as activation, inactivation, and closing states, can also be studied with this technique. In this method, a specific glass micropipette with a sharp tip forms a high-resistance seal that allows a current with low noise to pass through the single-channel and enables the recording of the induced voltage. Patch-clamping is achievable in different configurations such as cell-attached patch, inside-out, and outside-out patch. A whole-cell clamp is a cell-attached configuration that enables recording the whole currents passing through the whole-cell membrane. Other electrophysiological methods in patch-clamping are current and voltage-clamp recording.

In a current clamping technique, the voltage across the membrane is measured while the injected current into the cell is under the experimenter's control. In contrast, the examiner measures the current needed to hold a specific voltage in a voltage-clamp method. In vivo single-cell, electrophysiology is another method that allows us to investigate neurons in

functioning brain environments. In this method, microelectrodes are inserted into the brain of an anesthetized animal. The animal is then placed in a stereotaxic instrument (an instrument used to locate precisely area of interest in the brain by means of coordinates) that allows recording the cellular activity. X-ray or magnetic resonance imaging methods in humans can be used. In this approach, the physical activity of neurons can be recorded extracellularly. This method has many uses, such as local drug application, stimulation recordings, local synaptic decoupling. Although most investigations on channels and ion types involved in the neuron cell membrane are obtained in vitro, it is worth mentioning that the vivo investigations are highly correlated with anatomical findings.

Moreover, other crucial methods to study neurons and their cell membrane features are anatomical-biochemical approaches such as immunocytochemistry, in situ hybridization, and neuroanatomical tract-tracing. Immunocytochemistry uses specific antibodies to target antigens to mark specific types and locations of proteins that can be substances such as ion channels and neurotransmitters. Furthermore, depending on the type of analysis, the detection system used in this technique can be either peroxidase histochemistry or fluorescence.

In situ hybridization is a similar method to immunocytochemistry, with the difference that it uses mRNAs to bind and generate labeled RNA or DNA probes. Furthermore, neuroanatomical tract-tracing is a method that is mainly used to understand the connectivity and projections of neural networks. In recent years, the techniques mentioned above provided essential information to understand neural microcircuitry characteristics that help scientists to understand underlying mechanisms in neurons and brain functioning.

1.3.1 Spiral ganglion cells

SGCs innervate the hair cells of the organ of Corti in the cochlea. The organ of Corti includes three rows of outer hair and one row of inner hair cells. SGCs receive information from hair cells through synaptic activities and pass them to the brainstem through their central processes or axons. There are two types of SGCs; type I SGCs form 90-95% of the auditory nerve population (Spoendlin, 1972). Type I cells are bipolar neurons with larger non-myelinated somata, about 20 μm in humans (Ota and Kimura, 1980; Potrusil et al., 2012). The axon and dendrite of SGCs type I are myelinated and connect the inner hair cells with the brainstem. Each inner hair cell contacts 10 to 15 SGCs type I (Liberman, 2020). The type II SGCs are about 5-10% of the auditory neuron population (Spoendlin, 1972; Ota and Kimura, 1980). Type II neurons are pseudounipolar neurons with non-myelinated processes, and each type II cell innervates several outer hair cells. Figure 1.11A shows a schematic illustration of SGC type I

and their innervation, the distal part of the axons builds the auditory nerve (not shown). As the numerous type I neurons are responsible for encoding the sound, type I SGCs are studied in this work and referred to as SGCs.

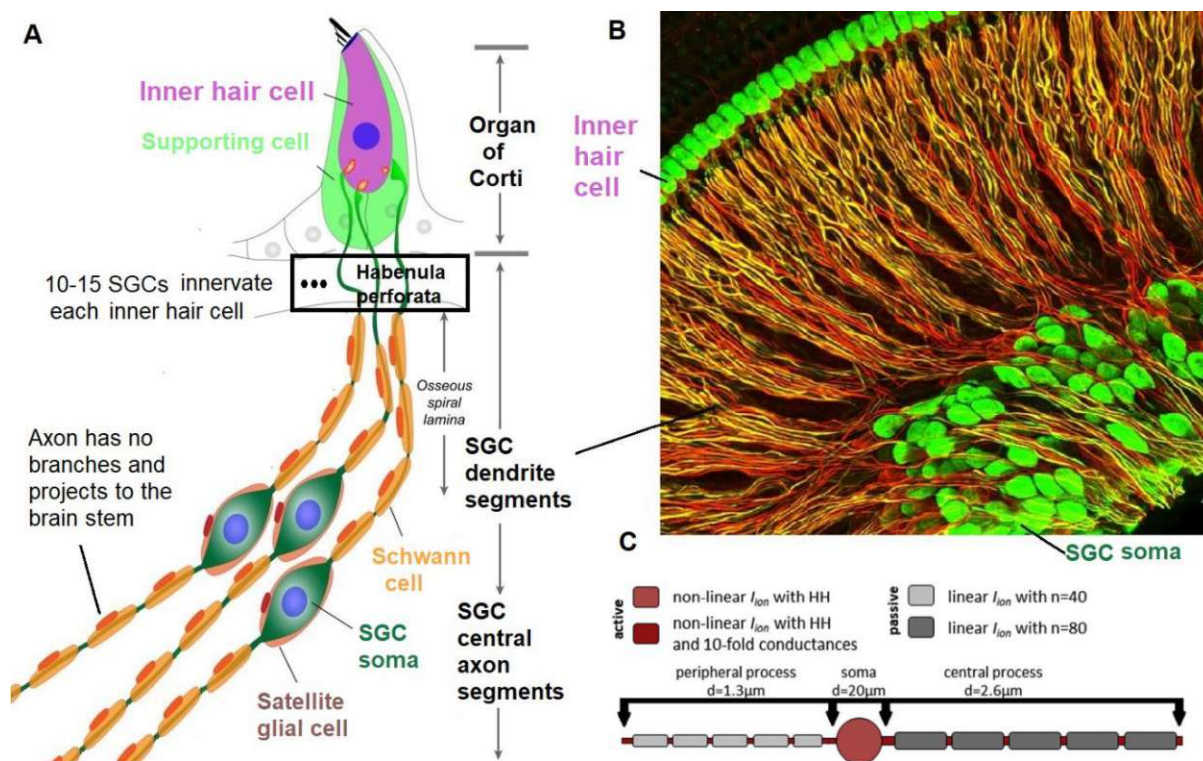


Figure 1.11. Spiral ganglion cells (SGC). **(A)** Schematic illustration of three examples SGCs from connecting to an inner hair cell in the habenula perforate and project via branchless myelinated dendrite and axon to the brain stem. Figure adapted from (Wan and Corfas, 2017). **(B)** Microscopy image of spiral ganglion cells from Chester Chia / Harvard Medical School. **(C)** Rattay's compartment model in SGC fibers was used in this study (Rattay et al., 2001b).

Encoding the auditory signals by afferent SGCs includes temporal features, and therefore these cells can be classified due to their spontaneous discharge rate (Liberman and Oliver, 1984). This point gives rise to the heterogeneity of their threshold sensitivity and their spontaneous firing rates, which is not understood, yet it has been proved that pre- and post-synaptic properties are involved in this mechanism, and this can also be seen in the distribution and quantity of the voltage-gated ion channels known in these cells. However, the electrophysiology of SGCs in humans is poorly investigated and understood, and most available data are from mice, cats, and guinea pigs. Nevertheless, some studies documented the available information pretty well (Rusznák and Szűcs, 2009; Davis and Liu, 2011; Oak and Yi, 2014; Reijntjes and Pyott, 2016). The voltage-gated channels in SGCs are mostly known from patch-clamp, immunofluorescence, electrophysiology, pharmacology, and RNA sequencing

techniques. Sodium voltage-gated channels generally provide the AP initiation in neurons, and there are nine classified types of voltage-gated sodium channels, $Na_{v1.1}$ to $Na_{v1.9}$ (Catterall et al., 2005). The most valuable information about voltage-gated sodium channels was revealed by two studies that reported the existence of Na_v channels in both somata and processes of SGCs. Hossain et al. reported the presence of Na_v , particularly $Na_{v1.6}$ (except $Na_{v1.2}$) in the initial segments of the processes and nodal region in adult mice (Hossain et al., 2005). Another study has found $Na_{v1.6}$ and $Na_{v1.7}$ in somata and SGCs processes (Fryatt et al., 2009).

Potassium voltage-gated channels are classified into the group of K_{v1} to K_{v12} channels (Gutman et al., 2003). Potassium channels are mostly responsible for restoring the membrane potential. The type and identification of potassium voltage-gated channels in SGCs have been well-reviewed (Rusznák and Szűcs, 2009; Oak and Yi, 2014). However, most identified potassium voltage-gated channels in SGCs are $K_{v1.1}$, $K_{v1.2}$, $K_{v1.4}$, $K_{v1.6}$, $K_{v3.1}$, $K_{v3.3}$, $K_{v3.4}$, $K_{v4.2}$, $K_{v4.3}$, $K_{v7.2}$, $K_{v7.3}$, $K_{v7.4}$, and $K_{v11.1}$. There is also a type of non-selective cation channels, known as HCN channels, which are permeable to sodium and potassium, and has been identified in SGCs (Chen, 1997; Bakondi et al., 2009; Yi et al., 2010; Kim and Holt, 2013; Liu et al., 2014a, 2014b). It has been reported that they have a significant role in setting the resting potential in SGCs. Evidence from immunofluorescence, electrophysiology, and pharmacology studies suggests the existence of other channels such as voltage-sensitive Ca^{2+} channels (Lopez et al., 2003; Roehm et al., 2008; Chen et al., 2011; Lv et al., 2012, 2014).

Modeling auditory fibers or SGCs combined with detailed cochlear models facilitated the comprehension of hearing phenomena. Up to now, various compartment models have been introduced to mimic the function of human auditory neurons. Three successful models (Rattay et al., 2001b; Briaire and Frijns, 2005; Smit et al., 2008) have been compared and reviewed in a recent study (Bachmaier et al. 2019). The morphological features were similar and followed the human SGC morphology. Sodium and potassium channels were presented and used in all three models. The gating properties, though, were different. Briaire and Frijns used the Schwarz-Eikhof or SE model in the NoRs (Schwarz and Eikhof, 1987). In contrast, the other two models resembled the gating properties and equations as in the HH model with some modifications. To model the ion channel activity in the NoR, Rattay used 10-fold HH membrane conductance at 28.9° C, which fits the AP shapes recorded at cat 37°C. Moreover, the HH model was in good agreement with the discrimination sensitivity of double-pulse experiments in CI users (Motz and Rattay, 1986).

Although the models could mimic some characteristics of SGCs compared with experimental studies, such as pulse ratios for single pulse stimulations, they may fail to replicate the long-term effects. The most significant barrier for a precise imitation can be the result of a lack of

information on both the morphology and kinetics of SGCs. However, the current study considered only single pulses, and no long-term effect was studied. The SGCs are modeled based on the compartment model from Rattay et al., 2001b, with the slight morphological improvement that has been revealed during this work by (Heshmat et al., 2020; Potrusil et al., 2020)

1.3.2 Retinal ganglion cells

The retina consists of nine main layers: (i) nerve fiber layer, (ii) ganglion cell layer, (iii) inner plexiform, (iv) inner nuclear layer, (v) outer plexiform layer, (vi) outer nuclear layer, (vii) outer limiting membrane, (viii) photoreceptor inner segments, and (ix) pigment epithelium. RGCs are the last processing units from the retina nerve layer. RGCs have non-myelinated axons until they leave the eye and form the optic nerve, where they develop myelination sheaths. RGC somata are located in the ganglion cell layer, and their dendrite arborizations are in the inner plexiform layer. Despite many morphological similarities, yet in many ways, RGCs are divergent, and this heterogeneity leads to their features and sensitivities. According to different criteria, there are various types of RGCs.

Four criteria have been described to distinguish RGCs (Sanes and Masland, 2015): (i) morphological differences, (ii) gene expression, (iii) spacing regularities (Wässle and Riemann, 1978; Kay et al., 2012), and finally (iv) physiological properties.

In response to light intensity variations, important discrimination revealed differences between ON- and Off-center RGCs (Kuffler, 1953). Further investigations exposed that the ON and OFF dendrites arborize in different layers, which leads to functional variations (Famiglietti and Kolb, 1976; Famiglietti et al., 1977).

Over past decades studies on the RGC types have been carried out mainly in mice, cats, and monkeys. At least 25 types of RGC are known in mouse retina (Roska and Meister, 2014). Some types are briefly mentioned in this part, with a baseline taken from a review paper (Sanes and Masland, 2015).

Figure 1.12, the upper panel, depicts mouse retinal cells in the different lamina, and the bottom panel shows top views of some RGC types of the mouse retina. Additionally, the cell types used in chapter 5 are shown in the red square.

One RGC group is the *ON-OFF directionally selective ganglion cells*, classified into four types. They are discovered first in rabbits (Barlow et al., 1964; Barlow and Levick, 1965) and

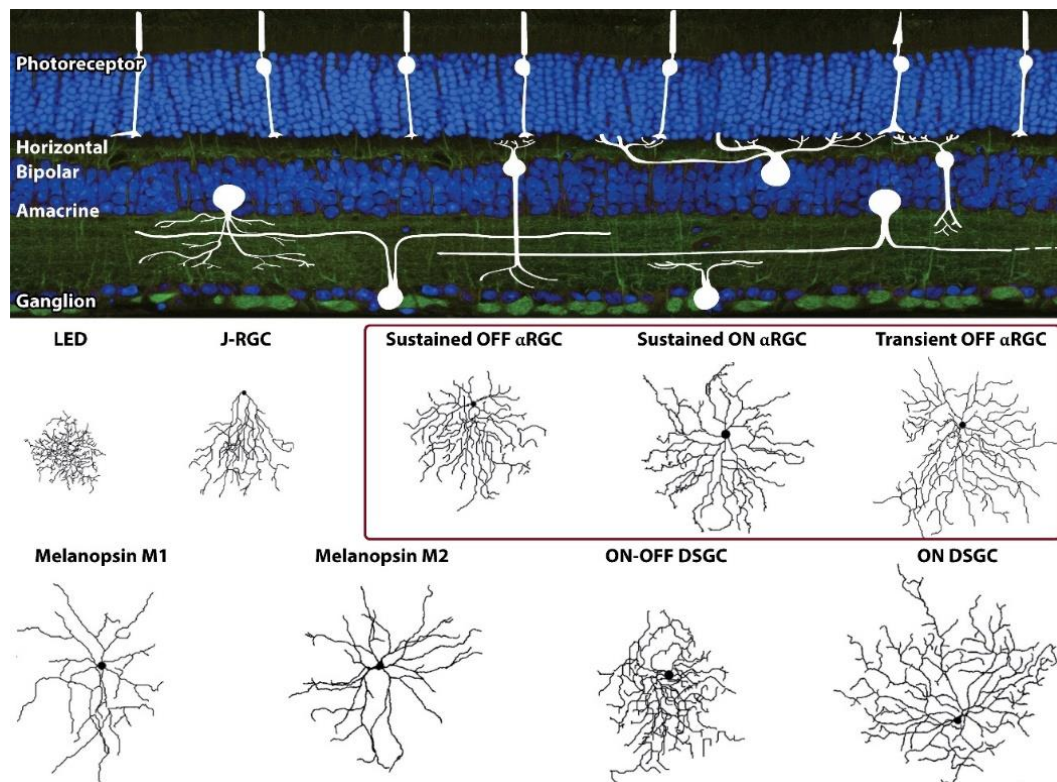


Figure 1.12. Mouse retina with RGC schematic morphologies from local edge detector (LED), J-RGCs, α RGCs, intrinsically photosensitive melanopsin-containing RGCs, On and ON-OFF directionally selective RGCs (DSGC). Figure is taken from (Sanes and Masland, 2015).

later in mice (Weng et al., 2005). As their name suggests, they respond to the increase and decrease of stimulus intensity and the motion of the stimulus in a specific direction.

The second group is three types of *ON directionally selective ganglion cells*, initially known in rabbits and first introduced by (Barlow et al., 1964; Barlow and Levick, 1965). Similar to the former introduced groups, they are also direction-selective but only respond to ON stimuli. Their types and directional tuning have been investigated (Sun et al., 2006; Yonehara et al., 2009; Dhande et al., 2013).

Another group is the *alpha retinal ganglion cells* (α RGCs), divided into three main types. Wassel and colleagues first discovered α RGCs in the cat retina (Wässle et al., 1981). α RGCs mostly have large somata and dichotomously branching dendrites divided into two independently functioning axes. Furthermore, in mice, three groups of α RGCs have been introduced (Pang et al., 2003): sustained ON, sustained OFF, and transient OFF α RGCs. α RGCs differ in physiologic features and laminar locations. Their dendrites laminate about 70%, 50%, and 30% of the depth of the inner plexiform layer in sustained ON, sustained OFF,

and transient OFF, respectively. These are the ganglion types that have been investigated in chapter 5.

Moreover, there are five types of *intrinsically photosensitive melanopsin-containing RGCs* with large dendritic arbors and inherent light sensitivity, and various studies have comprehensively investigated their role (Panda et al., 2002; Hattar et al., 2002, 2003; Qiu et al., 2005; Do and Yau, 2010). Another RGC type is the *local edge detectors* were first described and named in a study by (Levick, 1967) employed in rabbits and cats. The physiology and morphology of these cells have been vastly investigated by (Amthor et al., 1989; Van Wyk et al., 2006; Baccus et al., 2008; Russell and Werblin, 2010). As their names imply, these cells get excited only if the stimuli fall within the center of their receptive field and do not exceed the borders. *J-RGCs* are other types that are divided into three groups. They have been distinguished by (Yamagata and Sanes, 2008, 2012). J-RGCs are OFF-type RGCs with asymmetric dendritic arbors. J-RGGCs detect upward motion in the visual field and have explicit different directional behavior than ON-OFF and ON directionally selective ganglion cells.

There is another classification of RGCs based on their response to stimuli and their firing rate mostly used for the mammalian retina. This classification has two major groups for almost all RGCs: the well-studied brisk RGCs, about 50% of all RGCs. Brisk RGCs respond rapidly at the beginning of the stimulus with a high firing rate, and they are also susceptible to stimulus contrast (Cleland and Levick, 1974; Stone and Fukuda, 1974). As a subgroup in the brisk cell, one can name beta RGCs and α RGCs. However, the rest of the RGCs in this classification are sluggish RGCs. The sluggish RGCs respond slowly at the beginning, and their rate is low. Sluggish cells are more selective to spatial features such as local edge, motion. (Cleland and Levick, 1974; Caldwell and Daw, 1978; Amthor et al., 1989).

However, when it comes to the electrophysiology of RGCs, controversial information on the type and location of the ion channels can be found in the literature. The two most essential ions found in most RGC cells, independent of their types, are Na^+ and K^+ . First, Kaneda and Kaneko discovered sodium channels with different densities in sluggish and brisk cells (Kaneda and Kaneko, 1991). Furthermore, various studies using immunohistochemistry analysis have found sodium channels type $Na_{v1.2}$ to $Na_{v1.3}$ and $Na_{v1.6}$ in the RGC layer of the vertebrate retina (Caldwell et al., 2000; Boiko et al., 2001; Craner et al., 2003; Khaliq et al., 2003; Kaneko and Watanabe, 2007). In addition, there are many disagreements on the locations of these channels and the types of channels present in each cell. Boiko groups (Boiko et al., 2001) reported sodium channels such as $Na_{v1.2}$ and $Na_{v1.6}$ in the RGC axon. In contrast,

several groups have found sodium channels in both axon and soma (Craner et al., 2003; Kaneko and Watanabe, 2007).

In the case of potassium voltage-gated channels in RGC, there is not enough information about the exact location or type. Some studies, however, reported $K_{v1.1}$ to $K_{v1.6}$ mostly presented in these cells (Henne et al., 2000; Pollock et al., 2002; Höltje et al., 2007). In addition to potassium and sodium channels, studies using patch-clamp techniques discovered the presence of other currents in RGCs such as T-type, low-voltage-activated Ca^{2+} currents, and hyperpolarization-activated current (Pape, 1996; Lee et al., 2003; Henderson and Miller, 2007).

Various models have been established for retina cells to help computational studies understand retina function, and more details of retina cell models can be found in a review study by the Guo group (Guo et al., 2014). RGCs were the first retina cells modeled with ionic gating kinetic, modified based on HH kinetic type. Some of the famous retina cell models are: the Fohlmeister-Coleman-Miller (FCM), the Sheasby-Fohlmeister model, Schachter model, and Jeng sodium-channel-band model (Fohlmeister and Miller, 1997; Sheasby and Fohlmeister, 1999; Schachter et al., 2010; Jeng et al., 2011). FCM is one of the primary models established first in a single compartment model (Fohlmeister et al., 1990; Fohlmeister and Miller, 1997).

The FCM model includes four nonlinear voltage gate channels and one linear channel, Na^+ , Ca^{2+} , non-inactivating K^+ , inactivating K^+ , Ca^{2+} activated K^+ and leakage. Additionally, FCM includes intracellular calcium flux [Ca^{2+}]. The FCM model is also applicable in more realistic RGC geometries, including soma, dendrite, AIS, axon hillock, and distal axon (Fohlmeister et al., 2010). The FCM model provides computational studies investigating many dynamic phenomena, e.g., subthreshold activities, burst firing, spike-frequency adaptation, etc. (Fohlmeister and Miller, 1997; Kameneva et al., 2011). More insight into the gating properties and details in the model is given in section 4.2.1.

1.3.3 Pyramidal cells

The basic concept of this section is written based on (Feldmeyer, 2015). PCs, the prevalent neurons in the cortex and hippocampus in vertebrates, were first described by (y Cajal, 1888). They play essential roles in sensory perception, motion, and learning at single-cell and network connection levels.

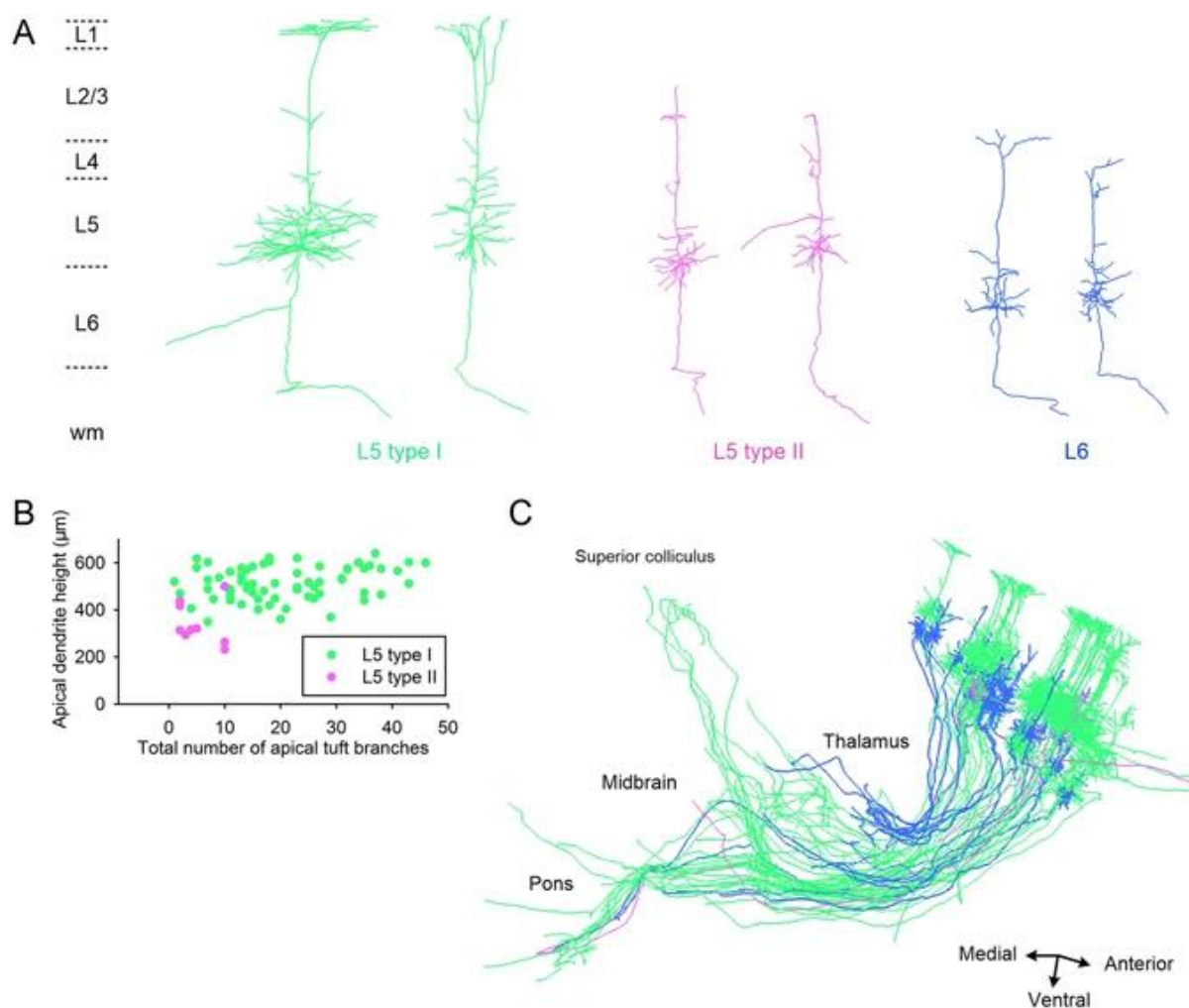


Figure 1.13. Three typical types of pyramidal neurons in mouse. (A) reconstructed geometries. (B) Branch number of the apical tuft vs. apical dendrite height in L5 type I and II. (C) Spatial projection of 65 pyramidal neurons from the same hemisphere of one brain dataset. L5 type I: green, $n = 39$; L5 type II: purple, $n = 5$; L6: blue, $n = 21$. Figure and caption adapted from (Guo et al., 2017).

As their name implies, they have pyramid-shaped soma, their short basal dendrites emerge from the soma, and in the cortex, the apical dendrites extend from the top of the soma toward the pia mater (Figure 1.13). Both dendrites have small outgrowths called dendritic spines that are sites of excitatory presynaptic activations. On the other hand, inhibitory synaptic is at dendritic shafts and soma. Neocortical PCs are the major output neurons of the neocortex and usually have very long axons (up to 1 m in mammals) with two domains: local and long-range. The local axonal domain projects and extends within the same cortical layer. The long-range axon, on the other hand, extends to the intra- or subcortical target units. Axonal terminals make synaptic connections that can be either excitatory or inhibitory. The PC long-term connections are very different depending on the cell types and their axonal domains. For instance,

neocortical layer 5 (L5) PCs with thin apical tuft have different axon domains and, therefore, different projections than flattened apical tuft (Kampa et al., 2007).

Vast arborization in PC dendrites allows them to receive synaptic inputs from various neurons and add up in the dendrites, also known as synaptic integration. Synaptic integration mainly occurs in the basal and apical dendrites, and it can be either passive such as subthreshold behaviors or as strong as AP since dendrite contains voltage-gated channels such as Ca^{2+} , K^+ , and Na^+ , studies frequently demonstrated that the PC dendrites generate Ca^{2+} and Na^+ spikes (Schiller et al., 1997; Magee, 1999; Martina et al., 2000; Migliore and Shepherd, 2002; Johnston et al., 2003).

Synaptic plasticity is the shape changes of neural connection, and if the synaptic activity is strengthening and increases the postsynaptic membrane voltage, it is called long-term potentiation. Whereas, if the synaptic activity is weakening, it decreases the voltage in the postsynaptic region called long-term depression, both types are fundamental mechanisms in learning and memory.

However, in the neocortical PCs, synaptic plasticity changes according to the synaptic activities and the time of AP firing in the pre- and post-synaptic areas. In PCs, when the AP initiates in the soma or the axon due to an active synaptic, it actively backpropagates to the dendrites (Stuart and Sakmann, 1994). It is reported that the AP backpropagation and the Ca^{2+} spikes may play an essential role in providing necessary changes to induce either long-term potentiation or depression (Kampa et al., 2007).

In addition to wide variation in the morphology, the distribution and type of ion channels are different in PCs (Talley et al., 1999; Häusser et al., 2000). As a result of this complexity, it is hard to understand the properties of different cells. However, the focus of the current work is only on neocortical PCs of L5, and from now on, these PC types will be only discussed and referred to as PCs.

However, understandings of electrophysiology of neurons, including most presented kinetics on ion channels, are based on the kinetic of the HH model. Experimental investigations using electrophysiological techniques such as patch-clamping have detected various types of ions presented heterogeneously in different parts of PCs: (i) Intracellular calcium flux [Ca^{2+}], (ii) voltage-gated Na^+ channel, (iii-iv) slow and fast inactivating K^+ channels, (v) the hyperpolarization-activated channel, (vi-vii) the high- and medium voltage-activated Ca^{2+} channel, (viii-ix) and finally small- and large conductance Ca^{2+} gated K^+ channels (Jansen, 1984; Deschênes et al., 1984; Pollard and Crunelli, 1988; McCormick and Pape, 1990; Soltesz et al., 1991; Huguenard and Prince, 1991, 1992; Foehring et al., 2000; Magistretti et al., 2000;

Khaliq et al., 2003; Sun et al., 2003; Akemann and Knöpfel, 2006; Almog and Korngreen, 2009; Deister et al., 2009). Details on the gating kinetics of each presented ion channel and pump are given in chapter 5.

Compartment models proposed for PCs are mainly based on observations from experimental investigations that are rough approximations of PCs. However, by multiple recordings of cell behavior, numerical simulation can define more accurate compartment models in PCs. Several studies have shown that methods based on searching parameters can be very successful in obtaining matches between models and recorded data from actual cells (West, 1996; Vanier and Bower, 1999). Among parameter search methods, two algorithms are more productive in constraining compartment models for a single PC, the stochastic algorithms, such as simulated annealing (Kirkpatrick et al., 1983), and the genetic algorithms, which is an optimization algorithm based on Darwinian evolution mechanisms and is known as the most effective method (Mitchell, 1998).

For the three-dimensional (3D) PCs, we used the biophysical properties of the soma and dendrites, such as ion channel kinetics and densities, based on experimental data from Almog and Korngreen (Almog and Korngreen, 2014). They used a pharmacological peeling procedure based on the somatosensory cortex in rats and a genetic optimization algorithm. Their model has succeeded in mimicking many electrophysiological features in PC dendrites, such as AP backpropagation, reproducing Ca^{2+} and Na^+ spikes, alternations in intracellular calcium concentration detected from experimental studies (Stuart and Sakmann, 1994; Stuart et al., 1997). In addition, the two-dimensional (2D) PC was modeled based on a compartment model from (Rattay and Wenger, 2010).

In contrast to the valuable information on conductance densities in the soma and apical dendrites, inferior information on basal dendrites as well as on axons is available (Keren et al., 2005). The available morphological information about the PC axons based on numerous experimental studies are as follows: (i) axon emerges from the soma through a truncate-shaped area called axon hillock of about 0-2 μm , (ii) extend to about 35-40 μm section that consists of a high density of voltage-gated Na^+ channels. (ii) Up to 300 μm away from the hillock, axon extends into a non-myelinated part (Shu et al., 2007; Hu et al., 2009), and finally (iii) at the end of the non-myelinated axon, first NoR starts, and from there myelinated axon starts.

However, there is contradictory information about the sodium channels density between soma and AIS. For instance, slight differences in sodium density were observed between soma and AIS in the patch-clamp experiment (Colbert and Johnston, 1996; Colbert and Pan, 2002; Ruben et al., 2003). In contrast, antibody studies reported a high density of sodium channels in AIS (Wollner and Catterall, 1986; Komada and Soriano, 2002; Boiko et al., 2003). Additional

studies in PCs have indicated that the AP initiates at the distal side of the AIS, a particular subcellular domain targeted by specific types of K^+ channels (Inda et al., 2006; Kole et al., 2007; Shu et al., 2007b; Van Wart et al., 2007).

One of the very primary axon compartment models for PCs was established by (Mainen and Sejnowski, 1996). The group used independent constraints from anatomical and physiological data on PCs to accomplish their primary goals, such as explaining the contradictory capability of dendritic Na^+ channels to support the propagation and not initiation of spikes in dendrites, examining the role of the AIS in spike initiation and AP backpropagation to dendrites. Fifteen years later, a group reported additional information about sodium channel types and integration gained in an experimental study and proposed their corresponding compartment model (Hu et al., 2009). Their immunostaining and patch-clamp investigations revealed high- and low-threshold Na^+ channel subtypes of $Na_{v1.2}$ and $Na_{v1.6}$, respectively. According to their findings, $Na_{v1.6}$ presented in axon hillock, AIS, non-myelinated axon, and nodes of Ranvier. Whereas, $Na_{v1.2}$ presented in soma and AIS.

However, their proposed axon model was similar to the Mainen model with slight improvements such as smaller Na^+ density channel ratios between soma and AIS, adding a non-myelinated part into the model, and considering two different types of Na^+ channels in different parts of the axon (see Hu et al., 2009 for more detail). Yet, the myelinated part in both models was more or less the same and based on the cable model and kinetics provided by Hodgkin and Huxley. Besides conductance-based or HH-style compartment models, other axon models can describe the properties of myelinated axons in mammalian.

Three milestones in axonal models are:

1. The McNeal model is the first compartment model for extracellular stimulation of a myelinated axon (McNeal, 1976). In the McNeal model following assumptions were used (i) infinite length of the fiber, (ii) equally spaced NoR, (iii) nodal length was considered constant for all fiber diameter whereas internodal length was proportional to fiber diameter, and finally (iv) myelin sections were considered as a perfect isolator. The active membrane was simulated with the Frankenhaeuser Huxley or FH model based on frog data.
2. The model of Chiu-Ritchie-Rogart-Stagg-Sweeney, CRRSS model (Sweeney et al., 1987; Chiu et al., 1979; Rattay, 1990) is based on the fact that in axons of warm-blooded animals, the NoR has potassium currents only of insignificant magnitude. Sodium and leakage currents dominate the active membrane.
3. The McIntyre-Richardson-Grill or MRG model (McIntyre et al., 2002) has a double-cable structure for the axon, and its myelin sheath and a current can flow in

between. MRG model data is available only for fiber diameter ranging from 5.7 to 16 μm .

Moreover, PC axons used in chapter 5 are based on real traced cells in the experimental studies with a 3D shape and numerous axonal collaterals. Therefore, for simplicity, the compartment model used in our PCs was based on HH-style models (Mainen and Sejnowski, 1996; Hu et al., 2009; Almog and Korngreen, 2014). More details on the geometry and kinetics of the models can be found in section 5.2. Additionally, the most famous myelinated axon models and non-myelinated axons will be compared and discussed in the last chapter.

1.4 Comparison between three investigated cells: SGC, RGC, and PC

In the following, the three investigated cells are discussed and compared in two ways. First, their geometry is compared according to their synaptic activities and roles, and next, their ion channels are discussed briefly for different parts of the cells. However, more details on geometry and kinetic features are given in sections 3.1 and 5.2.

1.4.1 Geometrical differences and similarities

As previously mentioned, SGCs are bipolar cells, have one non-branching dendrite and one non-branching axon with no branches (Figure 1.11). The SGCs (type I) receive their synapses from inner hair cells. There are several SGCs innervate a single inner hair cell. Therefore, a single neuron only reacts with the lowest threshold at a specific frequency called characteristic frequency. After a deflection of about 0.003° of stereocilia at the top of hair cells (Hudspeth, 1989), by releasing neurotransmitters, they increase the hair cell voltage membrane by about 0.1 mV (Crawford and Fettiplace, 1985), which causes neurotransmitter release and AP initiation at the beginning part of the SGCs (terminal). The AP propagates from the terminal through the axon to the brain stem. Due to the frequency nature of the sound and directional excitation of hair cells, the firing time of the SGCs is synchronized with the acoustic signal up to about 3 kHz.

The multiple innervations of each hair cell lead to the cooperation of all fibers in one group representing the phase synchronized signal. The cooperating phenomenon can be explained by the volley principle. Assuming five fibers have a spontaneous rate synchronized with comprising frequencies in a tone, each fiber then will be excited at one frequency and fires with that frequency, so the compound of all five will build up the whole tone. Taken together, timing

is crucial in the spiking pattern of SGCs, and therefore both dendrite (after passing the habenula perforate, about 10 μm) and axons (5 μm after emerging from the soma) are myelinated.

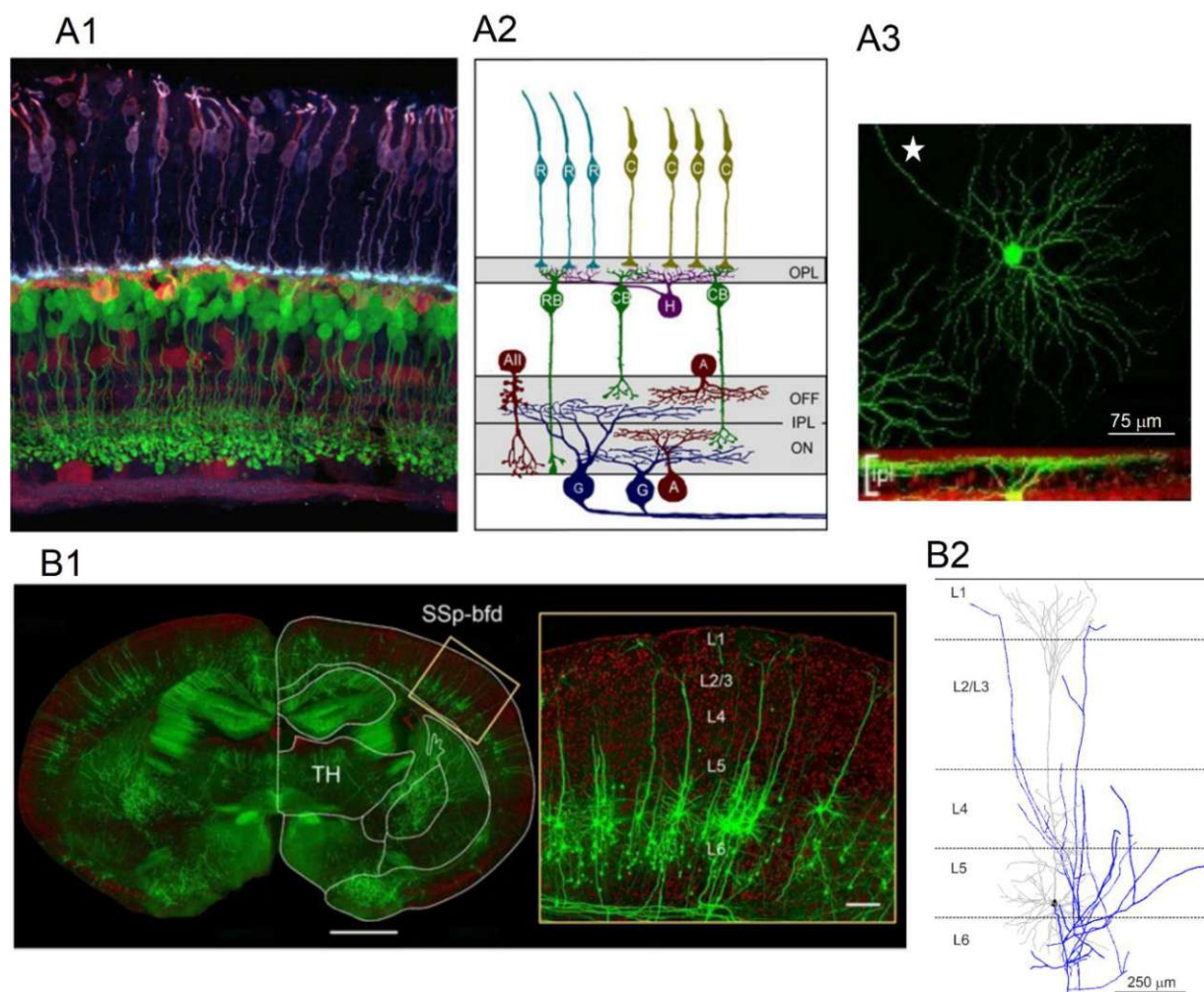


Figure 1.14. RGC vs. PC. **(A1)** A cross-section from immunostained mature mouse retina, photoreceptors in purple, amacrine and ganglion cells in red and bipolar cells in green Figure from (Morgan and Wong, 2007). **(A2)** Schematic diagram of retina major cell components and their projection patterns. Figure from (Morgan and Wong, 2007) **(A3)** a whole-mount view of an individual RGC from mouse, with dendrites projected in a single plane, the axon is depicted by a star. Figure from (Mazzoni et al., 2008). **(B1)** SSp-bfd and TH represent barrel-related primary somatosensory cortex and the thalamus in mouse, respectively. Scale Bar is 1 mm. The inset illustrates the cortical cytoarchitecture and the fine morphology of pyramidal neurons. Scale Bar is 100 μm . Figure and caption from (Guo et al., 2017). **(B2)** Reconstructed morphology from a model PC L5 in mouse somatosensory region, dendrites in gray, soma in black, axon in blue.

RGC dendrites obtain their input through synapses from bipolar and amacrine cells located in the inner plexiform layer (Figure 1.14A1-A2). After integrating and processing the information received from synapses, the long straight axon of RGCs sends them to the visual cortex through

the optic nerve (Schiller, 2010; Masland, 2012). RGC axons leave the eye at lamina cribrosa (a hole in the sclera, white region, occupied by a mesh-like structure), developing myelin sheaths in the post laminar region.

As mentioned before, RGCs are highly divergent due to various connections and roles in visual processing. However, to accomplish their functional specificity, their dendrites must be lamina restricted (Figure 1.14A3, bottom), meaning it is confined to a particular sublamina of the inner plexiform layer in a planar form to build synapses with subtypes of bipolar and amacrine cells (Wässle, 2004). PCs (L5), on the other hand, have extended dendrites that usually project up to layer 1 of somatosensory cortex (Figure 1.14B1-B2), which is about 1341 μm in rats and up to 600 μm in mice (Ledergerber and Larkum, 2010; Guo et al., 2017). However, neurons with arborized dendrites, e.g., PCs, and RGCs, usually collect synaptic inputs spread among their dendritic trees; it is known that these inputs are mainly in the form of subthreshold changes rather than AP and pioneering work indicated the AP is generated in the AIS (See Figure 1.5) or probably the first nodes of Ranvier in these neurons (Coombs et al., 1957; Fatt, 1957; Fuortes et al., 1957; Palmer and Stuart, 2006; Kole et al., 2008).

1.4.2 Ion channels

While different channels and ions are considered in each model cell, the three most effective ions in AP generation, Na^+ , K^+ , and Ca^{2+} are compared in three investigated kinetics in the following.

According to Rattay's model, ion channels presented in soma SGCs are chosen based original HH model. The sodium and potassium conductivities are set to values from the HH model as 120 and 36 mS/cm^2 , respectively. In NoR, presomatic and postsomatic regions in both dendrite and axon, these conductivities are set to 10-fold HH. Finally, no Ca^+ channels exist in our SGC model.

However, in the 3D RGC model (based on Fohlmeister et al., 2010; Werginz et al., 2020), the sodium channel ($\text{Na}_{v1.2}$) is present in soma and dendrites, and besides $\text{Na}_{v1.2}$, one additional type of sodium channel ($\text{Na}_{v1.6}$) is considered in the axon. The sodium conductivity is set to 65 mS/cm^2 in soma and dendrite for RGCs; in contrast, the values go up to 2.5 and 1.5 times larger in the hillock and distal parts of AIS respectively. On the other hand, potassium channels exist in one type ($\text{K}_{v1.2}$) in all parts except in the AIS. In the soma and dendrite potassium conductivity is set to 35 mS/cm^2 and up to 1.8 and 2 times increased in hillock, proximal AIS, respectively. In addition, the potassium channel $\text{K}_{v1.6}$ is considered at distal AIS with a

conductivity of 62.5 mS/cm^2 . The Ca^{2+} and Ca^{2+} activated K^+ channel are assumed 1.5 and 0.15 mS/cm^2 with the same conductivities in soma, dendrite, and axons.

In contrast, in 3D PCs (based on Almog and Korngreen, 2014), the sodium conductivity in the soma and basal dendrite is assumed to be about 35 mS/cm^2 , about 53% smaller than the sodium value in RGC soma and dendrite. In the apical site, this value decreases by increasing the distance to the soma to a value of 5.6 mS/cm^2 . In addition, in axons of PCs, sodium conductivities increase up to 17, 2.8, and 85 times in hillock, non-myelinated axon, and AIS (as well as NoRs), respectively. The myelin sheaths are considered with the same conductivities as in the soma except for the leakage (passive) channel. Furthermore, two types of potassium channels are assumed: a slow and a fast inactivating K^+ channels, with conductivities of about 20 and 33, respectively, in soma, non-myelinated and internodes of myelinated axon. The conductivities increase up to 7.5-fold (for slow channel) and 3-fold (for fast channels) in hillock, AIS, and NoR.

Calcium has an essential role in the AP backpropagation in PCs, and it is responsible mainly for generating calcium spikes in the dendrites of cortical neurons, which, as previously mentioned, has a crucial role in providing necessary changes for synaptic plasticity. It exists in five forms of channels in both soma and dendrites in 3D PCs: an intracellular $[\text{Ca}^{2+}]_i$ concentration, two voltage-gated Ca^+ channels as well as two Ca^{2+} -gated K^+ channels. In contrast to RGCs, calcium ions are not presented in the PC axon.

In 3D PCs, the Ca^{2+} conductivities for each channel are considered constant in the soma and basal dendrites, whereas these channels decrease from soma to the apical dendrites with a nonlinear gradient which is given in the related method section (chapter 5). The large-conductance Ca^{2+} gated- K^+ channel has a conductivity of 0.06 and 0.12 in soma and dendrites, whereas the calcium conductivity for the small-conductance channel is about 0.3 and 0.05 in soma and dendrites, respectively. For a high and a medium voltage-gated Ca^{2+} channels, the maximum calcium permeabilities are set to 0.9×10^{-6} and 0.003 cm/s , respectively, in soma and dendrites.

1.5 Overview and limitations

Neuroprosthetics are successful medical devices that include electrodes for stimulation or recording neural tissue. Neural stimulation is accomplished by injecting electrode currents that generates an extracellular potential that polarizes the target neuron's membrane and elicits neural responses. The recording electrode, in contrast, monitors neural activities by measuring the membrane potential of the region of interest (Kilgore, 2015).

During the last decades, neuroprosthetics had many applications for treating and restoring lost functions in stimulating the central nervous system, such as brain-stimulating devices that are used to treat motor symptoms in essential tremor, Parkinson's disease (Limousin et al., 1999; Montgomery Jr, 1999), brain stimulation for treating epilepsy (Velasco et al., 2001; Hodaie et al., 2002), psychiatric disorders (Mayberg et al., 2005; Kuhn et al., 2010), treating chronic pain with brain stimulation (Coffey, 2001) and spinal cord stimulation (Cameron, 2004), cochlear and brainstem stimulation for restoring the sense of hearing (Shannon, 2012), retina and visual cortex stimulation for restoring the sense of vision (Rizzo III and Wyatt, 1997). In addition, neuroprosthetics is applied to stimulate the peripheral nervous system, such as vagus nerve stimulation for treating epilepsy (Schachter and Saper, 1998), depression (Sackeim et al., 2001), sacral nerve stimulation for treating bladder dysfunction (Jezernik et al., 2002) and many other examples that can be found in (Kilgore, 2015).

One of the biggest challenges in neural prosthetics is the selective and arbitrary stimulation of a small group of cells while the neighbor cells remain calm. It is more demanding and even more challenging to stimulate only a part of the cell, such as stimulation only the soma, AIS, or the axonal terminals. During past years, micro-fabrication of electronic components allows more effective stimulation of individual cells; as an example, one can mention the high-density microelectrode arrays for retinal prostheses (Mathieson et al., 2012). However, It has been reported that the penetrating electrodes are more successful in focal stimulation, such as in the retina (Chen et al., 2020), visual cortex, or other brain structures (Schmidt et al., 1996; Middlebrooks and Snyder, 2008; Nguyen et al., 2016).

One inevitable reason for failure in selective stimulation is that a minimum electrode distance from the neural tissue is required. For instance, CI makes selectivity hard to accomplish. The large distance between electrodes in CIs leads to a wide distributed electric field that eventually disturbs selective stimulation. However, an opposite problem occurs when the electrode is very close to the neural tissue, such as epiretinal implants, where the electrode should directly impact RGCs. This situation can lead to an undesirable blocking state in the region of interest or, again, stimulate non-target neurons that eventually disturb the resolution. Another common

failure usually occurs due to electrode replacement during surgery, such as suboptimal electrode placement as a common reason for failure in deep brain stimulation (Okun et al., 2005, 2008; Ellis et al., 2008) and spinal cord stimulation (Cameron, 2004), which can generate problematic side effect that causes from nontarget region stimulation (Cameron, 2004; Okun et al., 2008). Taken together, selective stimulation is a crucial factor and difficult to achieve in most cases.

Another important factor in extracellular stimulation is the pulse shape. In most cases, cathodic stimulation needs a smaller amplitude than anodic pulse for spike initiation in the target cell ((Ranck, 1975; Rattay, 1986, 1999); see Figure 2.8). Hence, cathodic pulses are more likely to use in electric stimulation. However, monophasic pulses cannot be applied in neuroprosthetics because charge accumulation within the tissue leads to tissue damages. To avoid this problem, cathodic leading pseudo-monophasic pulses with second charge balancing (long and weak) phase of opposite polarity are often used.

However, in extracellular stimulation, a stimulus window appears with a lower and upper limit (threshold) for initiation and active propagation of an AP. The existence of an upper limit is due to high-intensity stimulation, which causes strong hyperpolarization in the flank regions and blocks the AP propagation in axon as a so-called anodal surround block or cathodic block (Katz and Miledi, 1965; Jankowska and Roberts, 1972; Roberts and Smith, 1973; Rattay and Aberham, 1993). Besides a cathodic block, a somatic block resulting from high-intensity stimulation was also observed when stimulating cultured RGC somata (before growing neurites) (Buitenweg et al., 2002). More recently, another study showed somatic UT during high-amplitude stimulation of RGCs with cathodic pulses (Boinagrov et al., 2012). Various computational studies investigated the problem with simplifications on geometry and kinetics (Rattay, 2014; Meng et al., 2018; Fellner et al., 2019).

The distinction between anodal surround block and somatic UT is challenging when complicated geometries are involved. However, this study aims to investigate different kinetics and geometries, which could help distinguish two UTs. Discrimination of somatic vs. axonal UT might be of great interest in micro-stimulation since, in the case of a somatic upper threshold, the spike can still generate in the axonal site and further propagate one-sided along the nerve fiber (Rattay, 2014; Meng et al., 2018). In comparison, the axonal UT (cathodic UT) prevents AP propagation along the most essential part of the cell, the axon, and is thought to block the cell completely.

The first part of this thesis investigates the realist micro-stimulation of SGCs with 3D pathways for LT and suprathreshold stimulations, the spike initiation site, and the excitation profiles. One of the limitations was investigating the UT and spike blockage in this part as the cochlea's

nature and the cochlear arrays' design does not allow the stimulation of fibers in the close vicinity of the cellular membrane.

For the second step, simplified 2D cell geometries were used to study the effect of different biophysical properties and channel densities on threshold window and threshold ratios in most three typical cells: SGCs and RGCs, and PCs. Our most important limitation in this step was simplifying the geometry, considering a point source approach and homogeneous neural tissue. However, by applying these simplifications and eliminating complicated geometrical differences, we investigated the effect of kinetic and biophysics of each cell on AP initiation and inhibition.

In the next step, more advanced models from realistic traced RGC and PC neurons were used to investigate AP generation at LT and blockage conditions during micro-stimulation in the soma vicinity in light of complicated geometrical features. However, again some limitations were considered in this step; for instance, the extracellular medium was assumed homogeneous, whereas neural tissue is heterogeneous, and this heterogeneity leads to a deformed electric field (Figure 2.7). However, we believe heterogeneity has no substantial effects on the small electrode to cell distances. Moreover, the point source approach might not be an accurate approximation for neural tissue such as the retina and cortex. However, in a computational study by (Rattay, 1989), it has been demonstrated that within an electrode distance range from 5 μm to 5 mm, the point source approach meets the current thresholds from data collected by an experimental study (Ranck, 1975). This investigation aimed to extend the previous results to more realistic conditions eliminated in the last chapter, such as the effect of highly branched dendrites in RGC and PC and the complex axonal structures, including collaterals.

In the final part, four myelinated (a 10-fold HH, a CRRSS, a Mainen, and a MRG), as well as two non-myelinated axon models (a RGC and a classical HH), were used to investigate threshold window and anodal surround block in thin and thick fibers using a 100 μs and a doubled cathodic rectangular pulses. Again point source approach was applied to compute the extracellular potentials, and the medium was considered homogeneous. The final investigation on axons was encouraged by the findings in the previous chapters and comparison of the 2D and 3D models and different fundamental behaviors between RGCs and PCs.

1.6 Outlines

Chapter 2 aims to explain all general methods and materials used in this thesis to produce the presented results.

Chapter 3 is a study of spiral ganglion cells with reconstructed 3D pathways. Excitation profiles and spike initiation sites in the case of LT and suprathreshold were studied and compared for a CI environment.

Chapter 4 investigates threshold windows and threshold ratios (UT/LT) in 2D SGC, RGC, and PC models.

Chapter 5 investigates the threshold windows, and block phenomena in 3D reconstructed RGCs and PCs. In addition, thresholds and ratios have been investigated by considering more realistic stimulation factors.

Chapter 6 investigates anodal blocks, thresholds, and threshold ratios for different myelinated and non-myelinated axon models.

Chapter 2

General Methods

This chapter introduces the general mathematic, biophysics, and computing approaches employed to produce the main results in the following chapters. More specific methods such as particular models and gating kinetics used in each chapter are discussed in the related chapter separately. The basic concept of the following sections is adapted from (Rattay, 1990; Kaniusas, 2012).

2.1 Membrane models

The cable model was first developed by William Thomson in the 1850s to simulate the signal decays in submarine telegraphic cables (Thomson, 1856). Afterward, Hodgkin and Rushton used a reduced form of this model to investigate the passive properties of the axon (Hodgkin and Rushton, 1946). In cable theory, a neurite is divided into segments modeled with electric components such as resistance and capacitance but without inductivity (Figure 2.1). The resistance in the model is defined by the number of ions passing through the membrane passive structure, and the capacitance models the bilipid behavior of the cell membrane (See section 1.2).

According to Kirchhoff's law, the current passing through a passive membrane can be calculated by equation (2.3).

$$I_c = C_m \frac{dV_m}{dt} \quad (2.1)$$

$$I_{ion} = \frac{V_R}{R_m} \quad (2.2)$$

$$I_m = C_m \frac{dV_m}{dt} + \frac{V_R}{R_m} \quad (2.3)$$

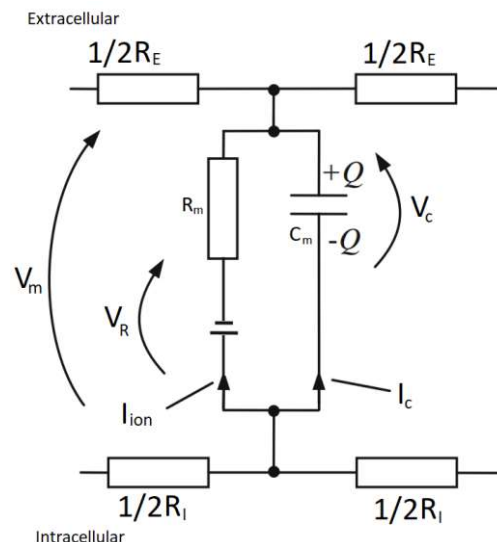


Figure 2.1. Passive membrane model. Figure adapted from (Kaniusas, 2012).

where, I_m , I_c , I_{ion} , and V_m depict the membrane, capacitance, resistance currents in μA and membrane potential in mV, respectively. The passive equation can define the subthreshold behavior of the cell while no AP generates.

However, the ionic transmission in the active membrane is determined by including the voltage-gated channels (See section 1.2.3). Because of different ion concentrations inside and outside the membrane, an electric field is generated, which induces an electrical driving force towards the field. On the other hand, an opposite diffusion force is produced to compensate for the ionic passage through the membrane. Equilibrium is achieved when the net current is zero, which is accomplished at a specific equilibrium voltage defined by the Nernst equation (Nernst, 1888).

$$E_x = \frac{RT}{ZF} \cdot \ln \frac{C_e^x}{C_i^x} \quad (2.4)$$

Where E_x , R , T , Z , and F denote the Nernst potential of ion x in mV, gas constant (8.314 J/kmol), the temperature in Kelvin, the valence of ion x , and the Faraday's constant (96485.33 C/mol). The C_e^x and C_i^x represent the specific ion concentration inside and outside the cell.

As discussed before, the membrane is permeable to specific ions such as K^+ , Na^+ , and Cl^- . Each ion has a particular equilibrium voltage; thus, the net flux of the ions needs to be zero, which implies a steady-state potential across the membrane when no external changes are applied, known as resting potential.

The membrane potential at steady state (resting potential) can be calculated with Goldman-Hodgkin-Katz (Goldman, 1943), and depending on the type of the cell, it usually ranges between -50 mV and -100 mV (Silbernagl and Despopoulos, 2007).

$$V_{rest} = \frac{RT}{ZF} \cdot \ln \frac{p_K C_e^K + p_{Na} C_e^{Na} + p_{Cl} C_i^{Cl}}{p_K C_i^K + p_{Na} C_i^{Na} + p_{Cl} C_e^{Cl}} \quad (2.5)$$

The active membrane can be modeled as follows (Figure 2.2).

$$I_C + I_{ion} - I_{stim} = 0 \quad (2.6)$$

$$\frac{dV_m}{dt} = \frac{(I_{stim} - I_{ion})}{C_m} \quad (2.7)$$

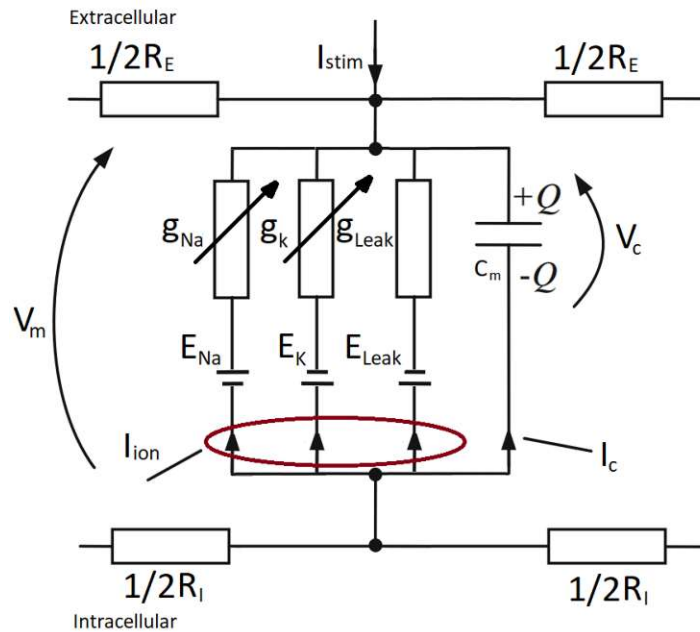


Figure 2.2. Active membrane model in HH-style. Figure adapted from (Kaniusas, 2012).

where, I_{ion} and I_{stim} represent the ionic currents in an active membrane and the stimulus current induced by an electrode, both in μA . The ionic currents in an active membrane consist of linear leakage channels from passive membrane properties and non-linear voltage-gated channels. Different membrane models have been proposed depending on the cell type and consequently presented ion channels. The electrophysiology of non-linear channels is studied for the first time by Hodgkin and Huxley in a squid axon, and most available kinetics are adapted from the HH model.

2.2 Hodgkin-Huxley membrane model (HH model)

Using the voltage-clamp technique, Hodgkin and Huxley studied the ion currents across the membrane of a squid axon. They described the opening and closing of the voltage-gated channels with a probability of the gates a channel possesses. They considered sodium channels having two types of gates: the activation (m) and inactivation (h) gates. The maximum sodium conductance of \bar{g}_{Na} is only achieved when both gate probabilities are 1, or in other words, both gates are entirely open.

Potassium, on the other hand, in their model, has only one type of gate, n , and its maximum conductance \bar{g}_K is achieved when $n = 1$. The current densities of ions ($\mu A/cm^2$) crossing the cell can therefore be determined by

$$i_{Na} = \bar{g}_{Na} m^3 h (V_m - V_{Na}) \quad (2.8)$$

$$i_K = \bar{g}_K n^3 (V_m - V_K) \quad (2.9)$$

$$i_{Leak} = g_{Leak} (V_m - V_{Leak}) \quad (2.10)$$

where $V_{ion} = E_{ion} - V_{rest}$, and conductivities are defined in (mS/cm²).

To describe the gating mechanisms in more detail, if x is the opening probability of a specific gate type (e.g., n , m , h), the gating process can be determined by $x(t, v)$ that describes the gating behavior of a high number of that specific gate type in a particular channel.

Gating rates (α_x and β_x) define the state of the gates at a specific membrane voltage within a time unit. More specifically, the α_x or opening rate describes the state of all closed gates being open with $\alpha_x (1 - x)$, and the β or closing rate describes the state of the opened gates that are getting close with $\beta_x x$. Thus the probabilities of the gates being open are calculated with the following differential equations.

$$\frac{dm}{dt} = [\alpha_m(1 - m) - \beta_m m] \times k \quad (2.11)$$

$$\frac{dh}{dt} = [\alpha_h(1 - h) - \beta_h h] \times k \quad (2.12)$$

$$\frac{dn}{dt} = [\alpha_n(1 - n) - \beta_n n] \times k \quad (2.13)$$

With k being the coefficient parameter to adapt the operating temperature T (in °C) to the original experiment temperature (6.3 °C) used in the HH model, and can be calculated by Equation (2.13).

$$k = Q_{10}^{\frac{T-6.3}{10}} \quad (2.14)$$

The suggested Q_{10} in the original HH model is 3. However, in the SGC model based on Rattay et al., 2001b, Q_{10} is used at $T = 28.9$ °C resulting in $k = 12$ that resembles the AP dynamics recorded in feline SGC (Motz and Rattay, 1986; Rattay and Danner, 2014).

The gating rates used to fit conductances to the experimental data in the HH model can be calculated by the following equations.

$$\alpha_m = \frac{2.5 - 0.1(V_m - V_{rest})}{e^{2.5 - 0.1(V_m - V_{rest})} - 1} \quad (2.14)$$

$$\beta_m = 4 e^{-\frac{(V_m - V_{rest})}{18}} \quad (2.15)$$

$$\alpha_h = 0.07 e^{-\frac{(V_m - V_{rest})}{20}} \quad (2.16)$$

$$\beta_h = \frac{1}{e^{3 - 0.1(V_m - V_{rest})} + 1} \quad (2.17)$$

$$\alpha_n = \frac{1 - 0.1(V_m - V_{rest})}{10 (e^{1 - 0.1(V_m - V_{rest})} - 1)} \quad (2.18)$$

$$\beta_n = 0.125 e^{-\frac{(V_m - V_{rest})}{80}} \quad (2.19)$$

with the resting conditions of $V_m(0) = V_{rest}$ (in mV), 0.05, 0.6, and 0.32 for $m(0)$, $h(0)$, and $n(0)$, respectively. However, the gating rates at the steady-state ($t \rightarrow \infty$), as well as the required time to reach this state (τ) can be computed by

$$x_{inf} = \frac{\alpha_x}{\alpha_x + \beta_x} \quad (2.20)$$

$$\tau = \frac{1}{\alpha_x + \beta_x} \quad (2.21)$$

and finally, the membrane potential is calculated by Equation (2.22).

$$\frac{dV_m}{dt} = \frac{-g_{Na} m^3 h (V_m - V_{Na}) - g_K n^4 (V_m - V_K) - g_L (V_m - V_{Leak}) + i_{Stim}}{c_m} \quad (2.22)$$

where the i_{Stim} is the current stimulus density in $\mu A/cm^2$, and c_m is the capacity of the membrane per cm^2 .

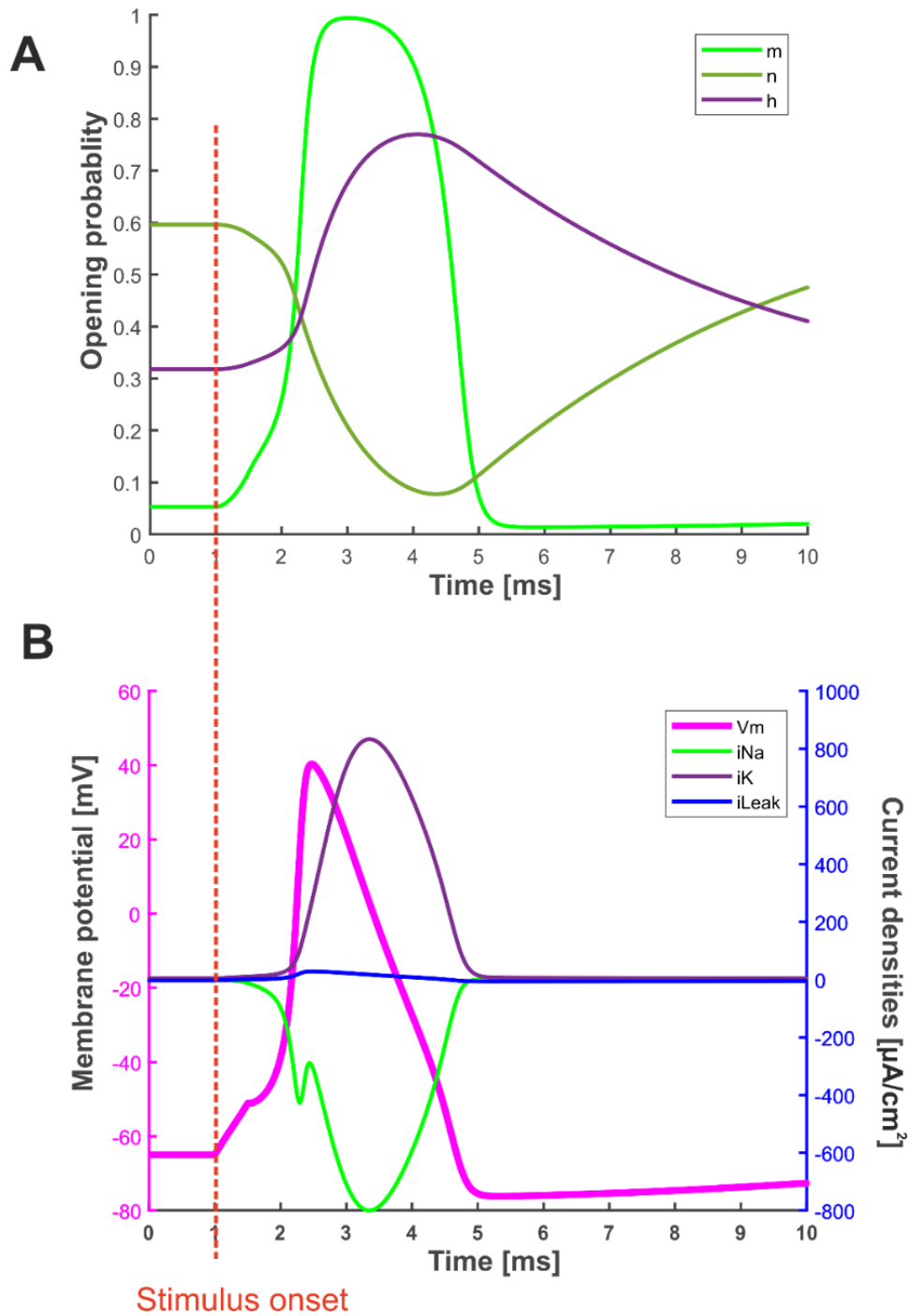


Figure 2.3. Action potential in a HH model. (A) Gating probabilities of sodium and potassium channels. (B) ionic membrane current densities compared with membrane potential. Note that the sodium current has a different direction (green curve). The highest sodium current is reached only if both activating and inactivating gates in the sodium channel are open. Additionally, the falling phase of the membrane potential occurs by the two repolarizing forces of the potassium activation and sodium inactivation mechanisms that lead the potassium efflux and stop the sodium influx, respectively.

Figure 2.3 shows gating probabilities for each gate type in sodium and potassium channels and the ion currents passing through a HH membrane model. Most cell kinetic models used in the following chapters, such as PC, RGC, and axon models (except for MRG and CRRSS), are based on the original HH model and called HH-style kinetics; details on the kinetics used in each model are given in the related sections. In addition, the original HH model with some adaptations was employed to simulate the excitation of SGCs fibers, according to Rattay et al. 2001. More detail about the SGC model is given in section 3.1.

2.3 Multi-Compartment model

A complex neural structure can be approximated by a multi-compartment model. Such model contains mostly cylindrical or spherical subunits with isopotential properties within them. A complete geometry and biophysical features of a neuron can be equivalented by a multi-compartment model consisting of thousands of subunits.

Figure 2.4 demonstrates a multi-compartment equivalent of a part of a non-myelinated axon with active compartments and nonlinear conductances of G_m . As a consequence of changing potential and membrane resistivity from one subunit to the adjacent units, a current is generated between neighboring compartments in the axial direction. Horizontal arrows represent the axial current. By adding the stimulus, Equation (2.6) can be developed and used for calculating the membrane potential in compartment n^{th} as follows

$$I_{C,n} + I_{ion,n} + I_{ax,n} - I_{Stim,n} = 0 \quad (2.23)$$

$$\frac{dV_m}{dt} = (-I_{ion} + \frac{V_{i,n-1} - V_{i,n}}{\frac{R_{n-1}}{2} + \frac{R_n}{2}} + \frac{V_{i,n+1} - V_{i,n}}{\frac{R_{n+1}}{2} + \frac{R_n}{2}} + I_{Stim})/C_m \quad (2.24)$$

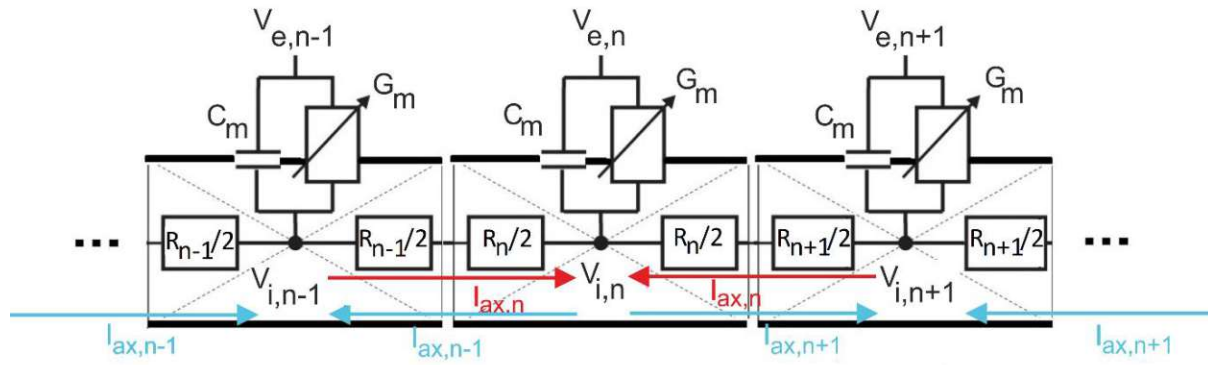


Figure 2.4. Schematic of the multi-compartment model in a part of a non-myelinated neurite.

In Equation (2.24), $R_n/2$ represents the resistance from the middle compartment n to the adjacent compartment. In a cylinder compartment n with a length and a radius of l_n and r_n both in cm, the circular cross-sectional area is equal to πr_n^2 (cm^2); thus, the R can be calculated from Equation (2.25).

$$\frac{R_n}{2} = \rho_i \frac{l_n}{2\pi r_n^2} \quad (2.25)$$

where ρ_i is the intracellular resistivity (in $\text{k}\Omega\text{cm}$), and the unit of R_n is $\text{k}\Omega$.

However, if the intended compartment is a sphere such as a single compartment soma connecting to n processes, the resistivity is then calculated by:

$$A_{soma} = 4\pi r^2 - \sum_n 2\pi r_{soma} h_n \quad (2.26)$$

with $h_n = r_{soma} - z_n$ (2.28) and $z_n = \sqrt{r_{soma}^2 - \left(\frac{d_n}{2}\right)^2}$ (2.27)

Finally, soma half radius can be driven from:

$$\frac{R_2}{2} = \frac{\rho_i}{2\pi r_{soma}} \ln\left(\frac{r_{soma} + z_n}{r_{soma} - z_n}\right) \quad (2.29)$$

However, it should be mentioned that in a multi-compartment soma with the compartments in the direction toward the electrode axis, the resistance of each compartment is computed with Equation 2.25.

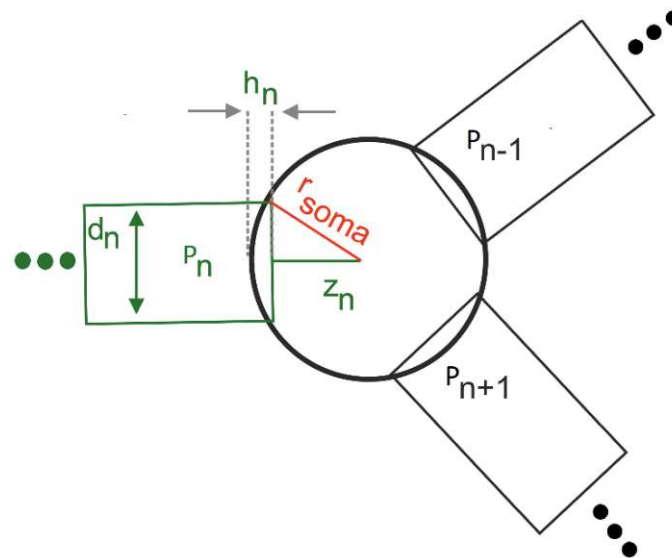


Figure 2.5. Surface and resistance in a spherical soma. The surface of a spherical soma, with one compartment and $n+1$ process connections, is calculated concerning the connecting processes. The half resistivity from the soma to the adjacent compartment of each process is calculated with a formula from (Rattay et al., 2003) shown in Equation 2.29.

However, it should be mentioned that in a multi-compartment soma with the compartments in the direction of the electrical field, the resistance of each compartment is computed with Equation 2.25.

2.4 Solving differential equation

The ordinary differential equation (ODE) driven from a multi-compartment model can be solved with numerical methods to analyze the cell responses to a stimulus. One of the frequently used methods is the Euler methods (Crank and Nicolson, 1947), such as forward (explicit) and backward (implicit) Euler. MATLAB (version R2020a, <https://mathworks.com>) also offers several solvers such as ODE15s variable order solvers based on backward differentiation formulas (Curtiss and Hirschfelder, 1952). Another possibility that provides a stable and efficient method for stiff problems is CVODE, which again uses the backward differentiation formula and is written in C-language by Cohen and Hindmarsh (Cohen and Hindmarsh 1994, 1996). In the following sections, the most frequently used solvers were the implicit backward Euler by implementing in MATLAB, and Python (version 3.8, <https://www.python.org/>), the ODE15s, and CVODE, which was used in NEURON.

However, ODE15s, as well as the CVODE solvers, were automatically applied by using the corresponding packages in the related programs. On the other hand, Backward Euler needs to be implemented by the user. In the following, the backward Euler method is described.

2.4.1 Euler Method

The Euler method is a numerical method that can estimate the solution of ODEs, and specifically, by using the implicit method, an extra equation needs to be solved. Thus, if $y(t)$ is a time-dependent system, e.g., a gate probability (m, n, h) or an ionic current, the driven ODE, $f(t, y)$ is then solved as follows.

$$\frac{dy}{dt} = f(y, t) \quad \text{where } y(0) = y_0 \quad (2.30)$$

So the forward Euler solution

$$y_{n+1} = y_n + f(y_n, t_n)\Delta t \quad (2.31)$$

and the backward Euler solution

$$y_{n+1} = y_n + f(y_{n+1}, t_{n+1})\Delta t \quad (2.32)$$

with n and Δt indicating the step and the step size ($t_{n+1} - t_n$) respectively. The i_x is taken as an example for an ionic current of channel x , with a gating probability j (m, n, h), so the current will be computed with:

From Equation (2.11-13)

$$\frac{dj}{dt} = \alpha_j(1 - j) - \beta_j j \quad (2.33)$$

using Equation (2.31)

$$j_{t+\Delta t} = j_t + (\alpha_j(1 - j_t) - \beta_j j_t)\Delta t \quad (2.34)$$

and from Equation (2.32)

$$j_{t+\Delta t} = j_t + (\alpha_j(1 - j_{t+\Delta t}) - \beta_j j_{t+\Delta t})\Delta t \quad (2.35)$$

$$j_{t+dt} = \frac{(j_t + dt \alpha_j)}{1 + dt (\alpha_j + \beta_j)} \quad (2.36)$$

where dt denotes the timestep mostly considered in a few (μ s), and finally, by replacing the driven gate probabilities in the corresponding ionic equations such as Equation (2.8-10), the ionic current is calculated for every step of the time.

2.5 Extracellular stimulation

An electrode placed outside of the cell generates an electric field that reflects on the cell membrane and changes the membrane potential. Various methods estimate the extracellular voltage (V_e) that an electrode induces. The following chapters have used three methods in this discipline: the point source, disk electrodes, and finite element (FE) methods.

The point source method is an analytical approximation of V_e . The electrode is considered a perfect point that induces a homogenous field. Thus the voltage induced in each compartment can be calculated by following the formula from (Rattay, 1990).

$$V_e = \frac{\rho_e I_{el}}{4\pi r} \quad (2.37)$$

Here, ρ_e indicates the resistivity of the extracellular medium ($k\Omega$ cm). The I_{el} is the electrode current (μ A), introduced by (McNeal, 1976), and r is the Euclidian distance of the electrode to the compartment center (cm). In this study, ρ_e is considered 0.3Ω cm for cochlear and cortical neurons, as well as axon models, and $1 k\Omega$ cm for retinal neurons (Rattay and Wenger, 2010; Werginz and Rattay, 2016).

The disk electrode approach was used in one set of experiments in chapter 5 to stimulate the RGCs excitation in epiretinal implants. Electrical field distribution under the application of disk electrodes was first studied by Newmann (Newman, 1966). Overmyer then studied the field distribution on these electrodes in a finite slab from a conductive material by numerical integration of the Laplace equation (Overmyer et al., 1979). Wiley and Webster (Wiley and Webster, 1982) gave an analytical solution to the problem, which was a good approximation of the one introduced by Overmyer in a simpler way. Thus, the extracellular voltage induced by a disk electrode can be driven from the following Equation.

$$V_e = \frac{\rho_e I_{el}}{2\pi a} \arcsin\left(\frac{2a}{\sqrt{(r-a)^2 + z^2} + \sqrt{(r+a)^2 + z^2}}\right) \quad (2.38)$$

with a , r , and z representing the electrode radius, the radial, and the axial distance to the electrode (in cm), respectively.

Finally, the third approach, employed in chapter 3, uses a numerical solution applying the FE method. In contrast to the two former introduced methods, the finite element model is a more realistic representation of the electrical field distribution since it considers the cell geometry and the electrode geometry in a realistic way, as well as the geometry of an inhomogeneous medium in which the electrode and cell are presented.

FE calculates the electric field and corresponding potential reflected on the cell in sophisticated 3D structures, such as the cochlea. In this method, the whole structure, such as the medium, electrode, and the cell, is divided into small tiny components and uses the partial differential equations and boundary limitations to calculate the V_e at each element.

The electrical potential ϕ in a volume conductor can be driven based on a reduced form of Maxwell's equation

$$\nabla\left(\sigma\nabla\phi + \epsilon\nabla\frac{\partial\phi}{\partial t}\right) = 0 \quad (2.39)$$

with σ and ϵ being conductivity and the permittivity of the medium, respectively. In simulations, the ϕ is the membrane potential ($V_m = V_i - V_e$). At this step, the intracellular current flow is not included (for simplicity and reducing the computational time). Therefore, Equation (2.39) can be written as

$$\nabla\left(\sigma\nabla V_e + \epsilon\nabla\frac{\partial V_e}{\partial t}\right) = 0 \quad (2.40)$$

and in the quasi-static condition, the ϵ is considered zero (Rattay et al., 2014).

Finally, by replacing the calculated V_e in Equation (2.24), the differential equation of the membrane potential of the n^{th} compartment can be written as

$$\frac{dV_m}{dt} = (-I_{ion} + \frac{V_{i,n-1} - V_{i,n}}{\frac{R_{n-1}}{2} + \frac{R_n}{2}} + \frac{V_{i,n+1} - V_{i,n}}{\frac{R_{n+1}}{2} + \frac{R_n}{2}} + \frac{V_{e,n-1} - V_{e,n}}{\frac{R_{n-1}}{2} + \frac{R_n}{2}} + \frac{V_{e,n+1} - V_{e,n}}{\frac{R_{n+1}}{2} + \frac{R_n}{2}})/C_m \quad (2.41)$$

Figure 2.6 compares the applied electric field on a spherical soma of a point source (left) and a spherical electrode (right) with the FE method. The electrode is located at a 20 μm distance from the soma center. However, in this example, the soma kinetic and intracellular flow is also considered in the model (Fellner et al., 2019). Inhomogeneity of the field in the model with realistic electrode geometry (right panel) can be observed, which induces slightly different impacts on the cell response.

However, in more complicated structures, such as inside a cochlea, the electrical field is further heterogeneous and distorted; thus, the point source approach is not a close approximation as in the example demonstrated in Figure 2.6, in which the medium is considered homogeneous and always possessing a single conductivity. Figure 2.7, in contrast, demonstrates the electric field distribution of a sphere electrode with a radius of 100 μm placed in a 3D FE model of the human cochlea, which has a heterogeneous structure.

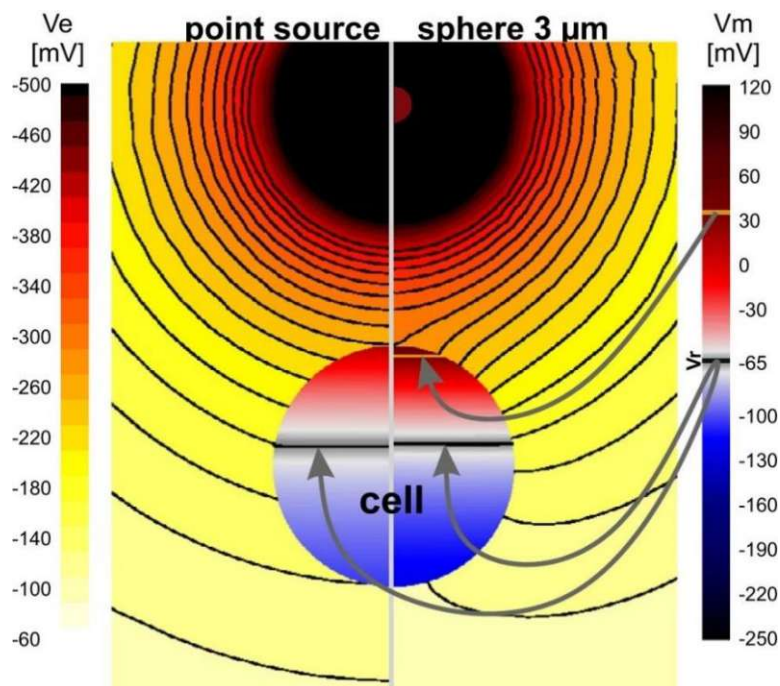


Figure 2.6. Finite element model of a point source electrode vs. spherical electrode (3 μm). The V_m and V_e (in mV) are shown for a point source (left panel) and spherical electrode (right panel) stimulating a spherical soma ($r = 20 \mu\text{m}$). Figure from (Fellner et al., 2019).

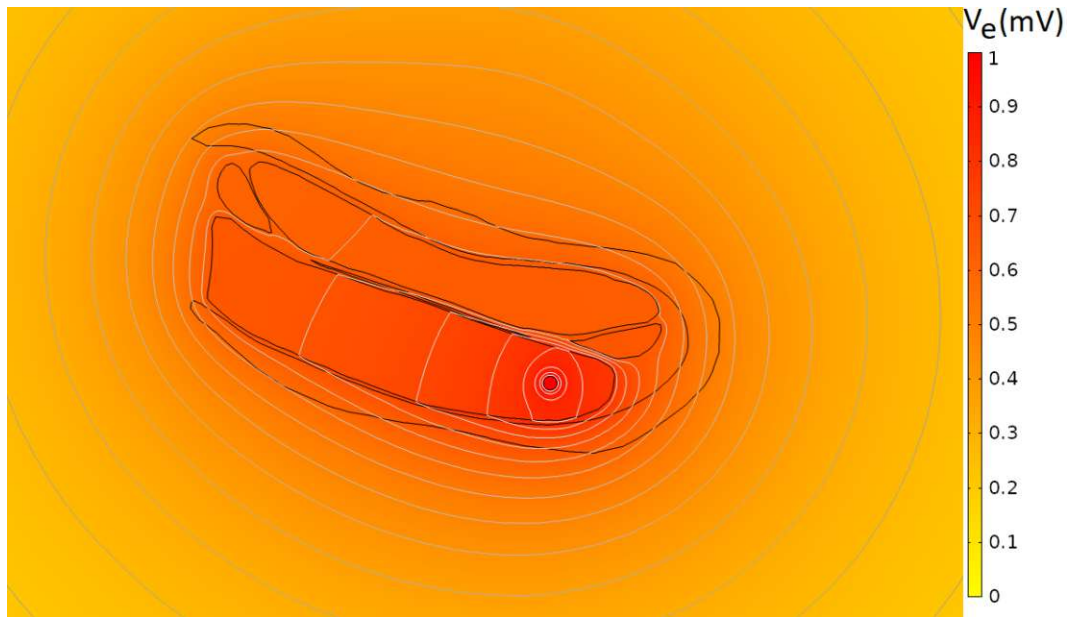


Figure 2.7. FE model of cochlear extracellular stimulation. The extracellular field is induced by a spherical electrode inside the scala tympani. The isopotential lines and cochlear structure borders are gray and black, respectively.

2.5.1 Activating function

The term activating function (AF) was introduced by Rattay (Rattay, 1999) for neurons of arbitrary shape, which is a strong tool to understand the effect of stimuli on the target cell (Garnhamt et al., 1995; Rattay, 1986, 1989, 1999). The impact of extracellular potential from equation (2.41) describes the term activating function in the n^{th} compartment.

$$f_n = \left(\frac{V_{e,n-1} - V_{e,n}}{\frac{R_{n-1}}{2} + \frac{R_n}{2}} + \frac{V_{e,n+1} - V_{e,n}}{\frac{R_{n+1}}{2} + \frac{R_n}{2}} \right) \frac{1}{C_m} \quad (2.42)$$

At the beginning of a stimulus, AF represents the changes in membrane potential influenced by the stimulus in each compartment. Regions with positive AF are depolarized at stimulus onset, making them strong candidates for AP initiation. In contrast, compartments with negative AF are mostly hyperpolarized at stimulus onset.

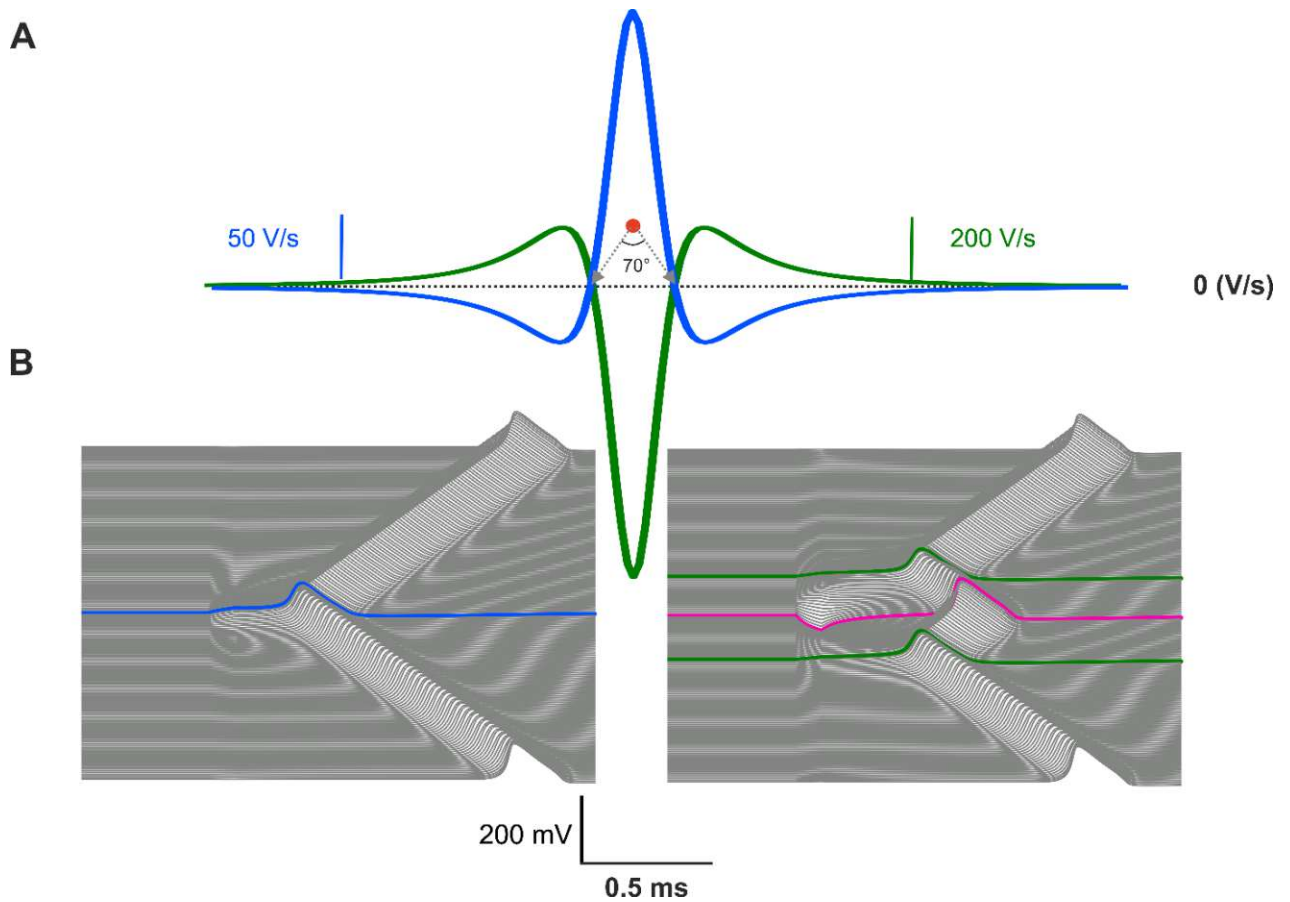


Figure 2.8. Activating function of a straight myelinated axon from the SGC axon model. **(A)** Comparing activating functions induced by a cathodic (blue) and an anodic stimulus (green) along the axonal membrane, with an anodic/cathodic threshold ratio of about 3.6. **(B)** Membrane voltage versus time, every line represents a single compartment. The compartment below the electrode position is shown in pink. Note that with a cathodic stimulus (left), the AP starts at the compartment below the electrode (blue) whereas, with an anodic pulse, it starts at the sides. The stimulus was a monophasic pulse with a duration of 100 μs set to 665 μA (anodic) and 180 (cathodic); for model properties, see section 3.1.

2.6 Implementations

Simulations in this study were performed in the following ways:

For SGC simulations, the extracellular potentials elicited by an electrode inside a scala tympani were first calculated in the FE model. The target cells were modeled with a compartment model in a second step. The suitable kinetics was implemented to the model in MATLAB. In the next step, COMSOL-MATLAB-interface was used for importing calculated V_e into MATLAB. For this step, the potential values were interpolated at the compartment midpoints. By assuming a quasi-static condition and a voltage value of 1 V, the outcomes could be adapted by multiplying the default electrode voltage value to a desirable value at compartment midpoints.

In addition, MATLAB and Python were used to calculate the differential equations in the self-implemented multi-compartment models such as 2D structures, to simulate intra- and extracellular stimulations and compute the membrane voltage, current, etc.

However, in some parts of the study, NEURON was used to create geometry, such as an axon, or import a real cell geometry from online databases (in this case, SWC files were converted to HOC). In this approach, a second step was to set the biophysical mechanisms available in NEURON in MOD files that were inserted into the cell according to the desired model. Intracellular stimulation and the voltage-clamp mechanism available in NEURON were used to test baseline functions of the cell, such as AP (back)propagation in PCs. The extracellular mechanism was supplied in NEURON, which interpolates the central points of each compartment. This can be done by inserting “xtra.mod” mechanisms at each compartment that calculates the corresponding V_e (mV) with a point source approach. In addition, all implementations in NEURON were controlled by the Python environment, and Python was used for further analysis and visualization purposes.

Chapter 3

Extracellular stimulation of spiral ganglion cells with three-dimensional pathways using ball electrodes

The following section aims to analyze the excitation of spiral ganglion cells with ball electrodes placed inside the scala tympani to mimic and study the micro-stimulation of 3D SGCs. This study benefits from a detailed FE model of the human cochlea, and 3D pathways of 30 tonotopically organized fiber reconstructed from manually segmented nerve bundles (bundle diameter of 15 μm). The cochlear FE model and reconstructed nerve pathways represented in this chapter are carried out by (Potrusil, 2013; Potrusil et al., 2020). The results performed in this chapter are first published in (Potrusil et al., 2020). The original study can provide more information on the preparation, imaging, and data processing, and spatial measurements.

3.1 Data preparation and computational modeling

In the original study (Potrusil et al., 2020), a primary method is presented for developing a computational framework that included an accurate and well-detailed FE model of a human cochlea as well as 30 reconstructed 3D pathways of cochlear nerves. The reconstructed auditory nerve bundles were tonotopically organized, including seven, nine, and fourteen auditory nerve bundles from the apical, middle, and basal turns, respectively. Fibers angles were measured from the round window with respect to the modiolus axis. For creating the FE human cochlea, two temporal bones from cadavers were used and analyzed following ethical guidelines corresponding to the Division of Clinical and Functional Anatomy of the Innsbruck Medical University (McHanwell et al., 2008; Riederer et al., 2012).

The isotropic spatial resolution of the micro-CT images of specimens 1 and 2 were 3 and 10 μm , respectively. The high spatial resolution of specimen 1 enabled to use of this specimen as the basis for the model. However, during the preparation process of specimen 1, the internal auditory canal was cut. Therefore the second cochlea with similar anatomical geometry was

used for further extrapolation of the central processes (axons) in the direction of the cochlear axis. Subsequently, the high-resolution data of specimen one was used for segmenting all three scalae and auditory nerve bundles along the cochlea. The segmentation data created a meshed surface model in Amira software (Thermo Fisher Scientific, <https://www.thermofisher.com>). In the next step, generated surfaces were exported as STL files for conversion into volume in SolidWorks, which was required for the following fine mesh creation, and applied the needed information such as conductivity in COMSOL Multiphysics (versions 5.4, <https://www.comsol.com>)

In the subsequent step, the electrodes were added to the model as spheres with a diameter of 0.2 mm. Electrode geometry and positions were chosen from two cochlear arrays: a lateral array of *FLEX SOFT*, MED-EL, Innsbruck, Austria (L1-L12), and a perimodiolar array of *CI24RE* Contour Advance, Cochlear, Sydney, Australia (C1-C22). For this purpose, a point was extracted from the original array data using the gap between the beginning of the array and the scala tympani. The XYZ coordinate of this point was set as the center of the first electrode. Other electrode locations were determined based on the array's total length and electrode distances.

Electrical conductivities (S/m) for materials used in the model were based on (Rattay et al., 2001a) and set as follows: 1.43 for scala tympani and scala vestibuli. 1.67 in scala media, 0.0334 in the modiolus, 0.016 for the cochlear outer surface (the compact bone) and the surrounding area, and finally 1000 for the electrodes.

A monopolar stimulation was chosen for this study in which a ground electrode is required, and monophasic pulses with a duration of 100 μs in both phase cathodic (CAT) and anodic (ANO) were applied to the active electrode to study the excitation of the investigated auditory nerves. A cuboid was used to set the ground electrode and placed the model within it, with a 0.4 mm distance from the upper surface and a distance of 7 mm to the other surfaces. Additionally, the outer surface was extended to a sphere with a radius of 100 mm to study the changes of the boundary size on the extracellular potentials. A linear shift appeared in the extracellular potentials, which could not affect the final results since the extracellular potentials are calculated from differences between neighboring compartments (see section 2.5, Equation (2.41)).

AC/DC module from COMSOL was chosen, and a quasistatic condition was considered. The surface of an active electrode was set to a fixed potential of 1 V (Rattay et al., 2001a). The current was then calculated for each electrode ranging between 321 and 384 μA that was in line with previous studies (Rattay et al., 2001a, 2001b; Kalkman et al., 2014; Mangado et al., 2018). At the final step in COMSOL, the extracellular potentials induced by the active

electrode were computed for several points from the bundle pathways depending on each nerve's length (60 to 70 points were extracted). By applying a spline interpolation, the V_e values were interpolated to the center of the compartment model of the target fiber.

In the last step, we modeled the SGCs with Rattay's multi-compartment model (Rattay et al., 2001b) to compute the excitation profiles induced by extracellular stimulation. The model consists of (i) a peripheral part including terminal, nodes of Ranvier, internode, and a presomatic region, (ii) a soma, and (iii) a central part including a postsomatic region, nodes of Ranvier and internodes. Figure 3.1 and Table 3.1 display all geometric and kinetic channel parameters used in the model. In addition, to resemble the degenerated conditions, the peripheral part was eliminated, and further deteriorations were considered by decreasing the soma layers gradually from $n=3$ in a healthy state to $n=2$ and $n=1$ as degenerated cases.

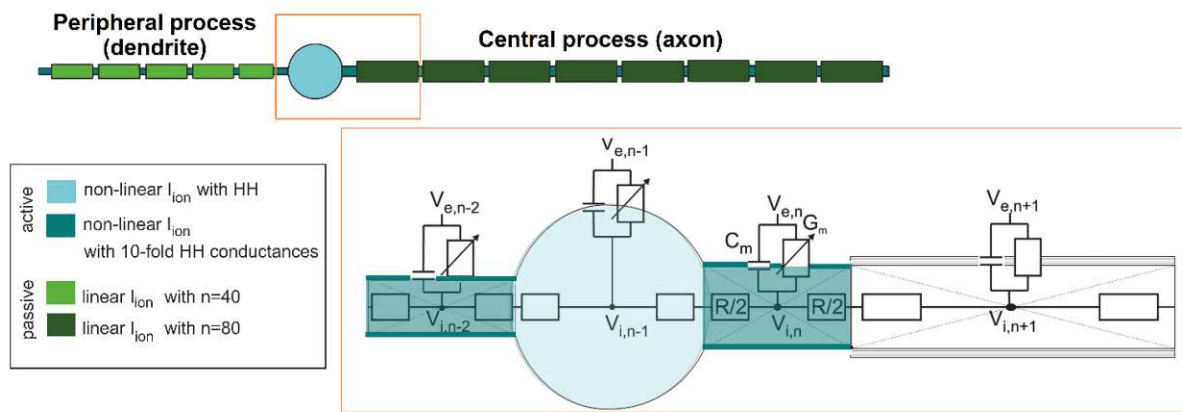


Figure 3.1. Schematic drawing of the compartment model of a human type I SGC. The colors describe the membrane models. The currents are defined by extracellular potential V_e , intracellular potential V_i , membrane capacitance C_m , membrane conductance G_m , and intracellular resistance R . Figure and caption adapted from (Potrusil et al., 2020).

Human SGC model parameter	
Length (μm)	
Non-myelinated terminal	10×10^{-4}
Presomatic region	100×10^{-4}
Postsomatic region	5×10^{-4}
Peripheral internode (except for the last one)	250×10^{-4}
Central internode	500×10^{-4}
Node of Ranvier	2.5×10^{-4}
Diameter (μm)	
Peripheral process	1.3×10^{-4}
Central process	2.6×10^{-4}
Soma	20×10^{-4}
Resistivity ($\text{k}\Omega\text{cm}$)	
Intracellular	0.1
Extracellular	0.3
Cell membrane kinetics	
Internode	Passive
Node of Ranvier	10-fold HH
Pre and post-somatic	10-fold HH
Terminal	10-fold HH
Soma	HH model
Myelin layer (N)	
Peripheral internode	40
Central internode	80
Soma	3
Membrane capacitance ($\mu\text{F}/\text{cm}^2$) *	1
Adjusted temperature ($^{\circ}\text{C}$)	
For all parts in the cell	28.9

Table 3.1. Human SGC model parameters with slight adaptations (Rattay et al., 2001b). * C_m was set to 1 ($\mu\text{F}/\text{cm}^2$) in active area and C_m/N in internods and soma.

3.2 SGC 3D pathways

Seven reconstructed apical fibers covered the angles (see section 3.1) from 928° (apical1, most apical fiber) to 620° (apical7); nine middle fibers were traced from 592° (middle9) to 327° (middle1), and the basal fibers covered cochlear angles from 298° in basal14 to 28° in basal1. Figure 3.2 demonstrates the FE model and the top view of the reconstructed pathways in each cochlear region. The human cochlear structure can be observed in panel A in a mid-modiolar slice. Modiolus and the Rosenthal's canal house the cochlear nerve tissue and the somata. Typically, a cochlear implant (or ball electrodes in this case) is inserted inside the scala tympani (Figure 3.2B).

More details on the 3D pathways of the reconstructed auditory nerve bundles can be seen in Figure 3.2C for three cochlear turns. Apical fibers represented a spiral pathway in both peripheral and central processes, with apical1 possessing the most spiraled pathways with an overall rotation of about 900° , covering the whole cochlea (2.5 turns). However, this spirality reduced systematically until the last apical fiber (apical7), whose peripheral rotation decreased to 45° (Figure 3.2C, left panel). Still, the first part of central processes in all apical fibers has a high spiral form (about 540° rotation) until they leave the internal acoustic fundus region. Middle fibers showed a low spirality (30° and 45°) only in middle1 and 2 in the peripheral process, and the rest have a straight peripheral pathway. The central process of the middle fibers, on the other hand, has turned from 270° to 360° until the internal acoustic region (Figure 3.2C, middle panel). The basal fibers displayed straight pathways until the distal part of their central processes, where they had a fan-shaped pathway with a maximum spirality up to 180° in some cases (basal1-6).

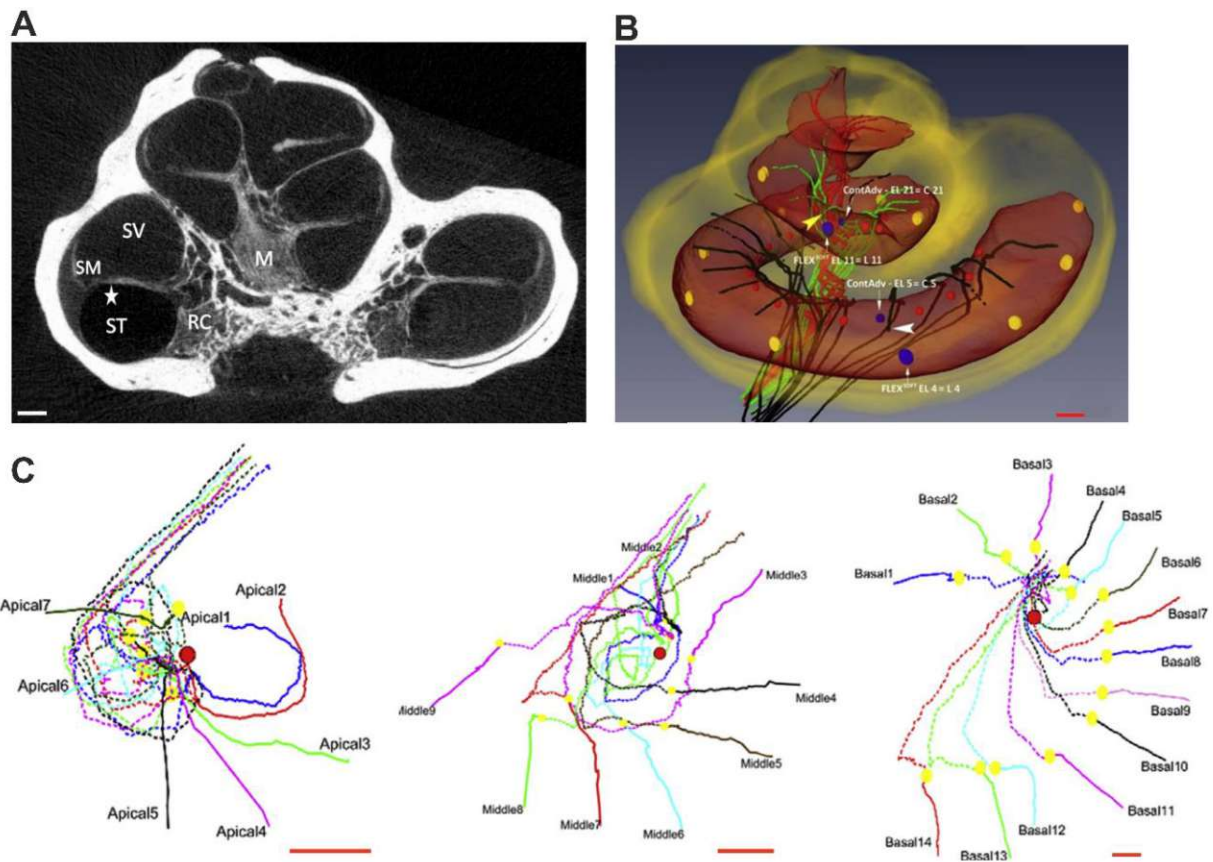


Figure 3.2. FE model of the human cochlea with 30 traced nerve fiber bundles. **(A)** A mid-modiolar slice through the cochlea. SV, SM, and ST represent the three scalae: scala tympani, scala media, and scala vestibuli, respectively. M and RC show the modiolum and Rosenthal's canal that house the SGCs and somata. The star depicts the location of the organ of Corti where the hair cells are located. **(B)** 3D view of 30 differently colored fibers from the basal (black), middle (green), and apical (red) cochlea turns together with the scala tympani. Additionally, the electrodes of both modeled CI systems are indicated; CI *FLEX SOFT* (yellow spheres), Contour Advance array (red spheres). The two electrodes in each system selected for analysis are depicted in blue. Reconstructed fiber bundles are displayed in **(C)**; the left panel shows seven apical SGCs, the middle panel: nine SGCs from the middle turn, and the right panel: 14 basal bundles. The top views in each panel indicate the soma (yellow spheres), the center of modiolum (red sphere), the peripheral processes (solid lines), and the central processes (the dashed lines). Figure adapted from (Potrusil et al., 2020).

Figure 3.3A demonstrates the total length of the reconstructed fibers and their corresponding distance to the apex. Mean values of the total length were 10.4, 8.4, and 8.6 mm, indicated by crosses for apical, middle, and basal turns in red, green, and blue, respectively.

Boxplots of peripheral process, central process, and total lengths are compared for all three cochlear turns (basal, middle, and apical) in Figure 3.3B. Boxplots demonstrate the first, second, and third quartile, the minimum and maximum values (whisker length), and mean \pm SD (black points). In the peripheral processes (Figure 3.3B, left panel), the peripheral lengths of the middle fibers were significantly different from apical ($p < 0.05$) and basal ($p < 0.001$) fibers. For both central and total fiber lengths, apical fibers were significantly different from middle fibers with $p < 0.05$ in central length and $p < 0.001$ in total length (Figure 3.3B, middle panel). The reconstructed apical fibers were also significantly different from basal fibers with $p < 0.001$ in total and central lengths (Figure 3.3B, middle and right panels).

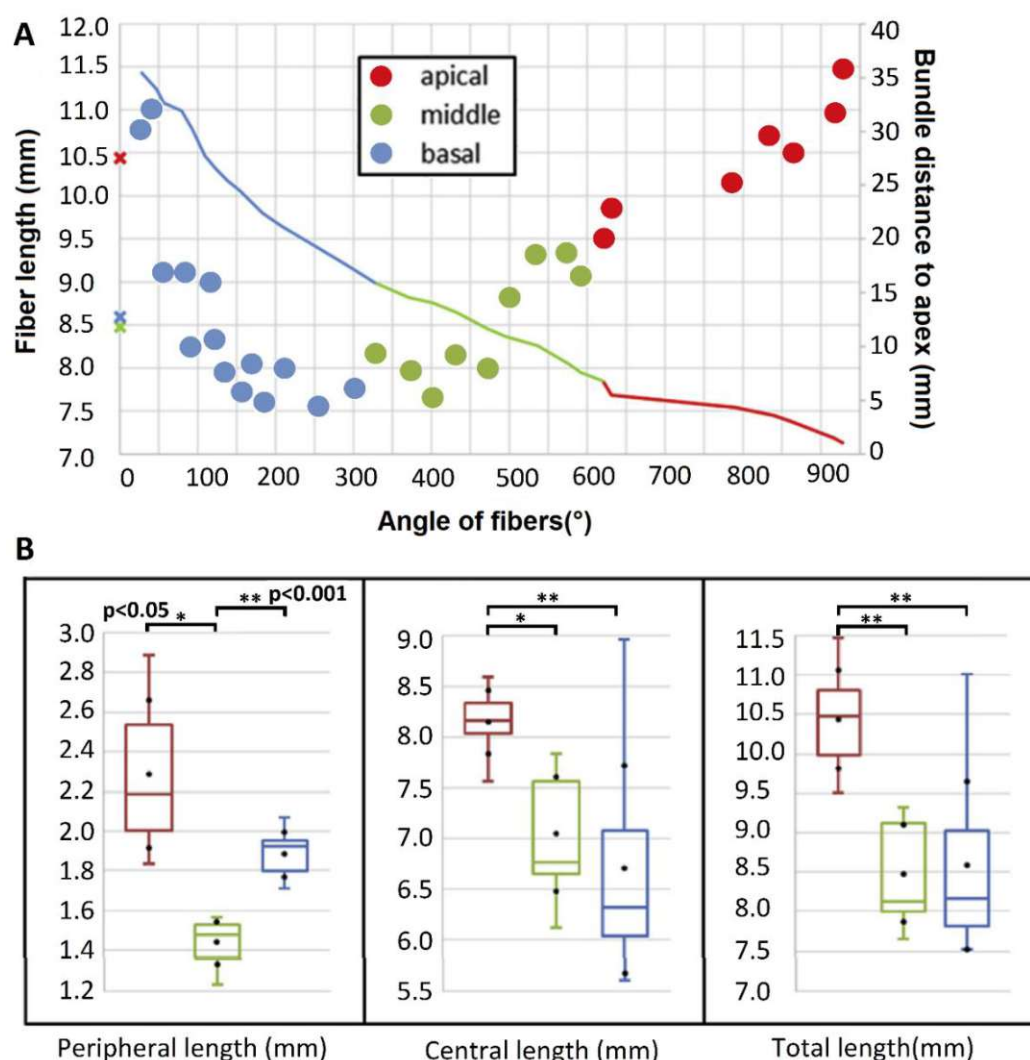


Figure 3.3. Length measurements of 30 reconstructed SGCs. **(A)** The total fiber length for each SGC is shown on the primary left axis, and mean values are indicated as crosses with the same color code. The corresponding distance to the apex (solid line) is plotted with respect to the right axis. The same colors indicate the range of each turn as the fibers. **(B)** Box plots for peripheral (left), central (middle)

processes, and total (right) lengths comparing apical (red), middle (green), and basal (blue) fibers. Boxes represent 1st, second (median), and third quartile, whiskers maximum and minimum values, black dots mean \pm SD. The statistical difference is indicated for $p < 0.05$ (*) and $p < 0.001$ (**). Figure adapted from (Potrusil et al., 2020).

3.3 Extracellular voltage

The extracellular voltage along selected SGCs induced by four selected electrode positions of L4 (73°) and L11 (457°) from the lateral system, C5 (76°) and C21 (430°) from the perimodiolar system are shown in Figure 3.4-3.7. The isosurface plot in the top panels demonstrates the extracellular potential in a slice through the electrode center with a voltage of 1V. The V_e along the neuron length are compared for the interested fibers with electrode distances to the fibers in the bottom panels. Target neurons with the closest distance from their peripheral terminals possessed the highest V_e values in the first part of the peripheral processes.

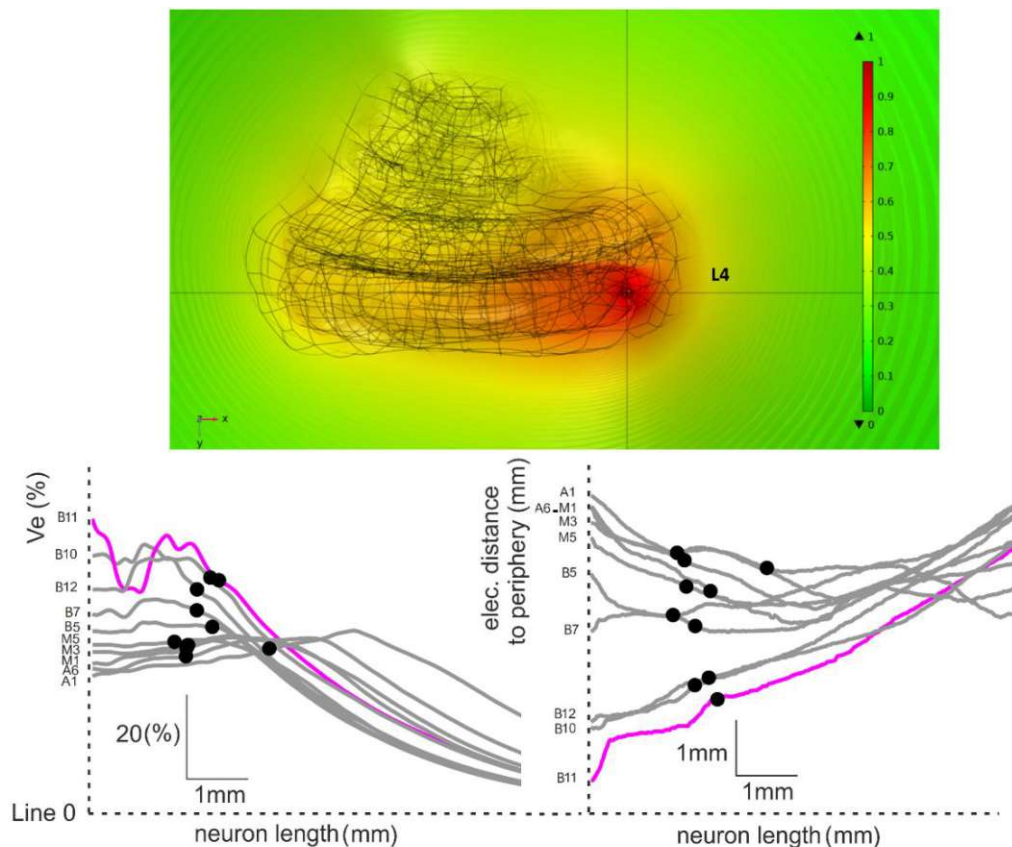


Figure 3.4. Extracellular voltage for the selected active electrode, L4, from the lateral system. The top panel shows the induced electric potential of the finite element model in a slice through the active electrode with the highest value of 1V in red. The wireframe rendering illustrates the segmented human

cochlea. The bottom panels show the corresponding extracellular voltage V_e (left) and electrode distance to the fiber (right) as a function of fiber length for the selected SGCs (close to the active electrode). Fiber with the highest V_e values (basal11) was chosen as target fiber (pink) and possessed the smallest electrode distance. B, M, and A represent the basal, middle, and apical fibers. Soma positions are shown with black circles. Figure adapted from (Potrusil et al., 2020).

Figure 3.4 shows that by activating the basal electrode L4, the target neuron of basal11 (B11) possessed the highest voltage of 70.4% of the electrode, with the lowest distance of 0.6 mm to the electrode at its terminal side. The following two closest basal fibers (basal10 and 12) had the peak value of V_e around the soma area (black circles) with an electrode distance of about 2 mm to their somata. Middle turn fiber bundles placed at the opposing side showed a maximum V_e value of about 40%, with fewer fluctuations in V_e values and electrode distances from 3.5 to 5 mm to peripheral sites. The apical fibers (apical6 and 1) received a maximum V_e of about 43% at their central parts at the closest distance to the electrode, below 4 mm, compared to their peripheral site with an electrode distance of about 6 mm.

Figure 3.5 demonstrates the same trend as Figure 3.4 but for active electrode C5, located close to the Rosenthal's canal at almost the same degree as L4 (76° vs. 73°). The maximum V_e of 77.2% was generated in the peripheral process of the target fiber, basal11 (B11), at about 1.5 mm away from the terminal with the closest distance to the electrode of about 0.38 mm. A closer distance from C5 to the peripheral processes caused an increase of about 7% compared with the corresponding lateral electrode L4. The V_e was reduced significantly for increased distance to the electrode. Yet again, the second and third closest basal fibers are the basal10, 12 with maximum V_e of about 62% and 69%, respectively, at their peripheral process with electrode distances of 0.7 and 1.2 mm, respectively. Once again, apical1 had a maximum V_e of 44.5% in the central process with a distance of 2.19 mm to the active electrode of C5. The excitation profiles of the majority of auditory nerves were comparable in corresponding electrode positions of L4 and C5.

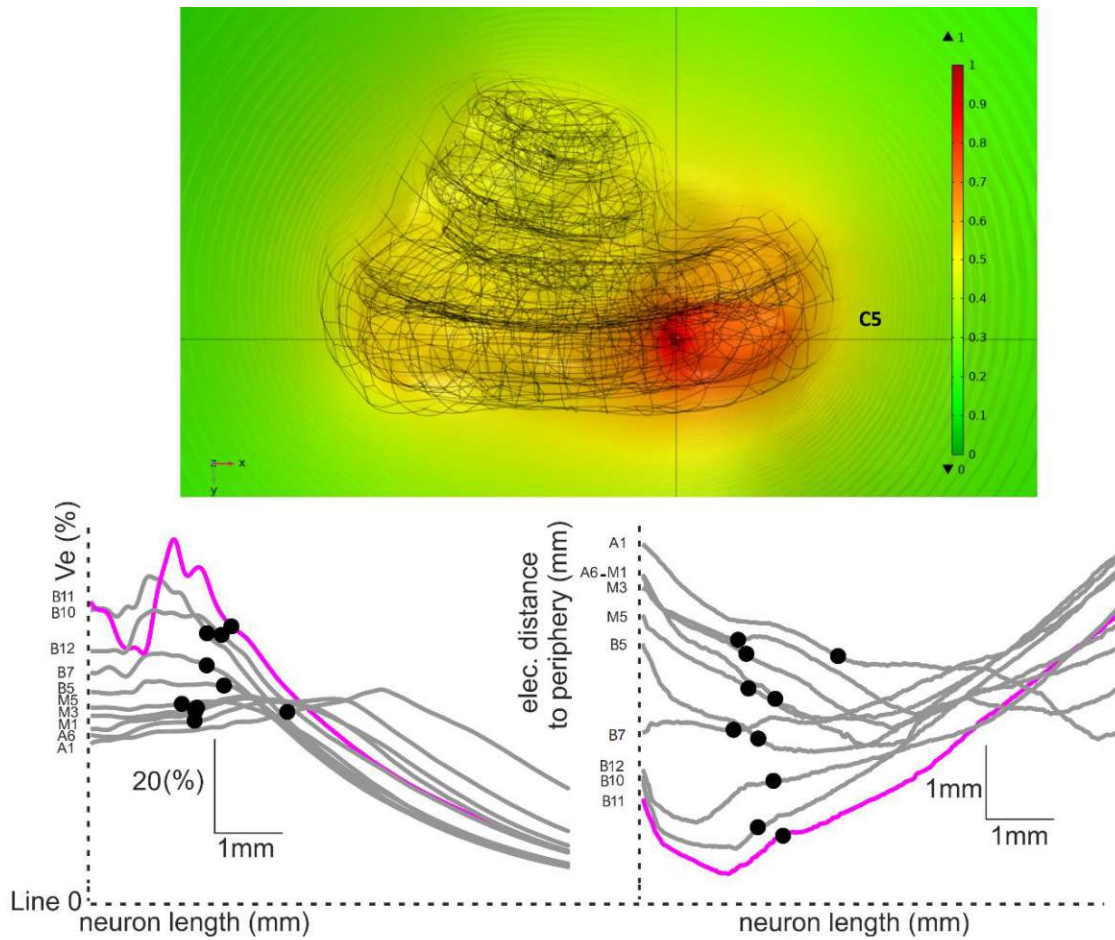


Figure 3.5. Extracellular voltage for the selected active electrode C5 from the perimodiolar system. Same layout as Figure 3.4 with the same target fiber of basal11, B11 (pink). Figure adapted from (Potrusil et al., 2020).

Figure 3.6 displays stimulation of the target neuron, middle5, M5 (pink), with the active electrode (L11) from the lateral system. The electrode generated the highest V_e of 80.9% in middle5 with an electrode distance of 0.35 mm to its peripheral terminal. Fibers from lower-frequency regions exhibited spiral pathways with spirality enhanced by reducing the distance to the apex, leading to a close distance to the active electrode L11. For instance, middle3 exhibited a maximum V_e of 61.8% that appeared at its soma. Moreover, by activating the L11, the basal fibers obtain the highest V_e values of about 40% at their central processes.

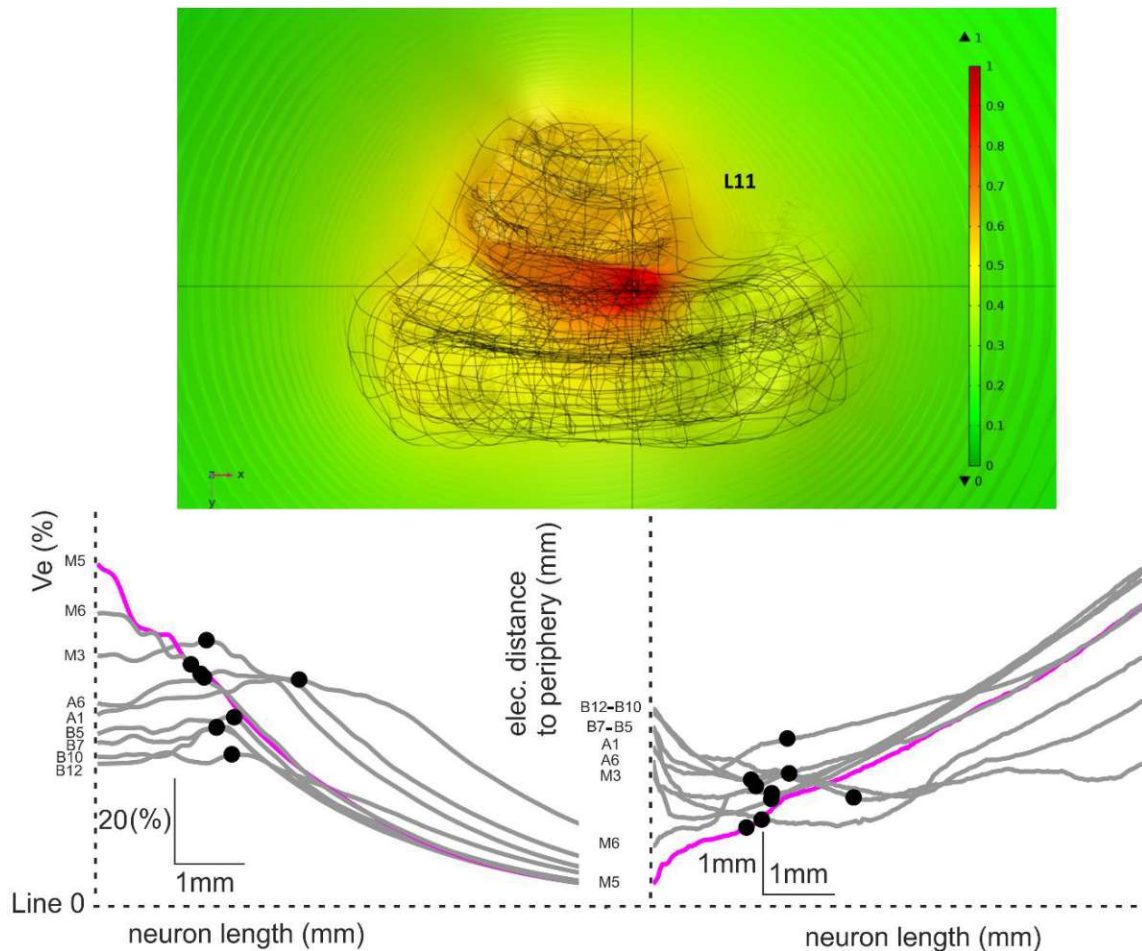


Figure 3.6. Extracellular voltage for the selected active electrode L11 from the lateral system. Same layout as Figure 3.4 with the target fiber of Middle5, M5 (pink). Figure adapted from (Potrusil et al., 2020).

Figure 3.7 illustrates excitation of the region of interest by C21 from the perimodiolar system that induces maximum V_e of 81.9% (located at 0.82 mm on the peripheral process) at the target neuron of middle5 with a minimum distance of 0.25 mm to the active electrode of C21. Again the voltage profiles of most neurons are similar in corresponding electrode positions of L11 and C21.

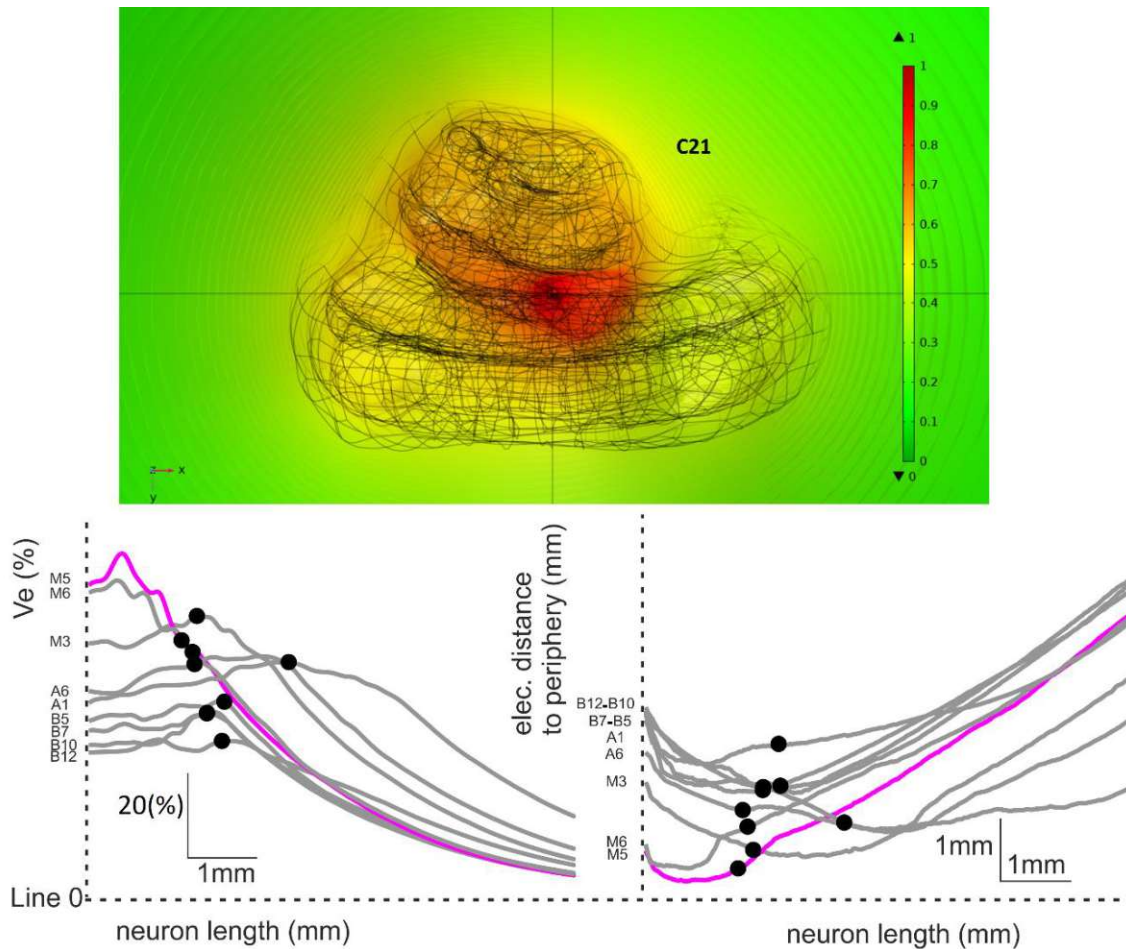


Figure 3.7. Extracellular voltage for the selected active electrode C21 from the perimodiolar system. Same layout as Figure 3.4 with the target fiber of Middle5 (pink). Figure adapted from (Potrusil et al., 2020).

3.4 Excitation profiles in healthy target neurons

The excitation profiles of the target neurons (basal11 and middle 5) with an intact (healthy) morphology are demonstrated in Figures 3.8-11. In each figure, panel A shows the V_e (orange) for CAT pulse along the first part of the target neuron (green box). In comparison, the black curve shows the distances of the compartment centers to the active electrode. The closest point to the active electrode, indicated by the gray arrowheads, always corresponds to the highest (most negative) V_e value.

On top of the B and C panels, the snapshots of times with a time step of 0.1 ms are shown for all four cases. The red, purple, and black thick curves indicate the pulse offset, AP initiation sites, and AP at the soma, respectively. On the bottom panel B and C, voltage membrane (in

V_e is plotted versus the time for peripheral active compartments (nodes of Ranvier), presomatic region, soma, and central nodes in green, orange, black, and pink, respectively, for CAT (B) and ANO (C) pulses and the AP initiation sites are shown in thick purple.

Comparing the orange and black curves, positions with the smallest distance to the electrode (gray arrowhead) possess the highest negative V_e values for all cases (Figure 3.8-11). In all investigated cases, CAT needs a lower threshold than the ANO pulse; however, the threshold ratio ANO/CAT is always essentially lower than four as previously reported by several computer simulation studies (Ranck, 1975; Rattay, 1986, 1999), which assumes microelectrode stimulation of long straight fibers with a constant diameter in a large homogenous medium (Rattay, 1986). The estimated ANO/CAT ratios were 2.38 and 2.6 in middle5 stimulated by L1 and C21, respectively; 1.05 and 1.3 in basal11 stimulated by L4 and C5, respectively. The irregular 3D pathways caused more fluctuations in V_e along the fiber that resulted in lower threshold ratios and their large variations. This result demonstrates that 3D pathway irregularities caused a more complex fiber-electrode distance relation than assumed in previous computer simulation studies.

AP did not always initiate at the positions with the highest V_e value since the driving force for membrane potential variations in every compartment is not directly its V_e value, but the corresponding AF explains the AP initiation sites. For compartments with two neighbors, the AF is proportional to the second derivative of V_e (curvature) and inversely proportional to its intracellular resistance and capacitance (Rattay, 1986, 1999).

Consequently, an area will be depolarized when the AF is positive, marked by upward arrows in the orange V_e curve in Figure 3.8-3.11, panel A. On the other hand, a negative AF (downward arrows in the orange V_e curve) denotes hyperpolarizations. The positive and negative AFs are also detectable at the beginning of the corresponding green traces during the pulse onset (Figure 3.8-11, bottom of the panel B) as depolarization and hyperpolarization areas, respectively. For ANO pulses, the same area is reversely polarized, so the hyperpolarized area becomes depolarized, and hence it is a candidate for AP initiation, as shown in Figure 3.8-3.11, panel C.

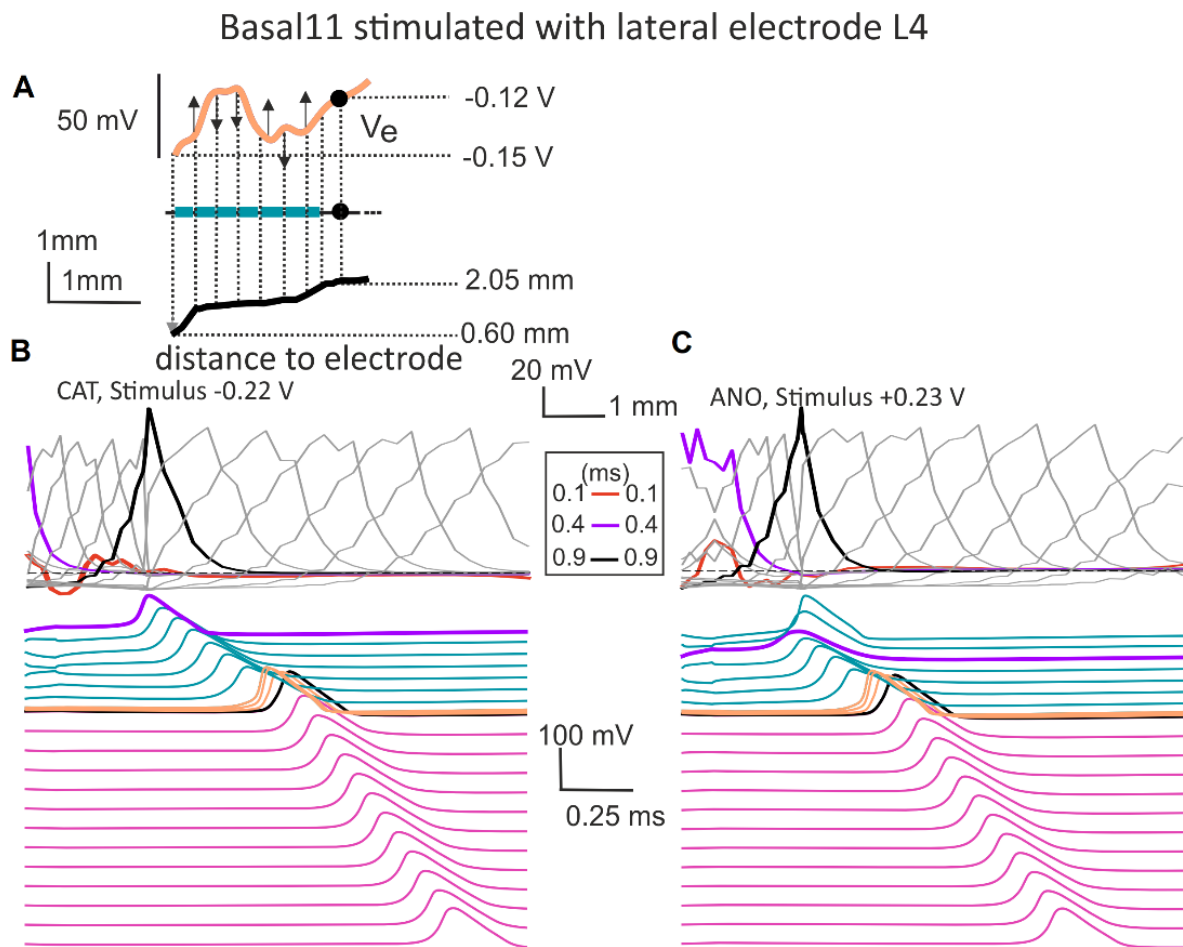


Figure 3.8. Stimulation of intact target fiber basal11 at threshold level with the lateral electrode of L4. **(A)** The top curve (orange) shows the extracellular potential V_e for cathodic pulse (CAT) along the peripheral part, the soma positions (black circles), the largest (negative) V_e , and the somatic V_e value are shown with horizontal black dashed lines; the vertical black dashed lines indicate the positions of nodes of Ranvier, and the black curve shows the distances of the compartment centers to the electrode. A schematic illustration between the curves shows the compartments with internodes in green. **(B-C)** Top: Voltage along the fiber at different times (gray) are plotted for CAT **(B)** and ANO **(C)** pulses. Snapshots are shown at every 0.1 ms. The stimulus offset (0.1 ms), AP initiation, and AP at soma are represented in red, purple, and black thick lines, respectively. Bottom: membrane voltage against time is plotted for CAT **(B)** and ANO **(C)** pulses; the traces represent selected compartments. The green, orange, black, and pink lines represent peripheral nodes, presomatic region, soma, and central nodes, respectively. AP initiation sites are shown in purple. Corresponding threshold values are displayed on the top. Figure adapted from (Potrusil et al., 2020).

Basal11 stimulated with central electrode C5

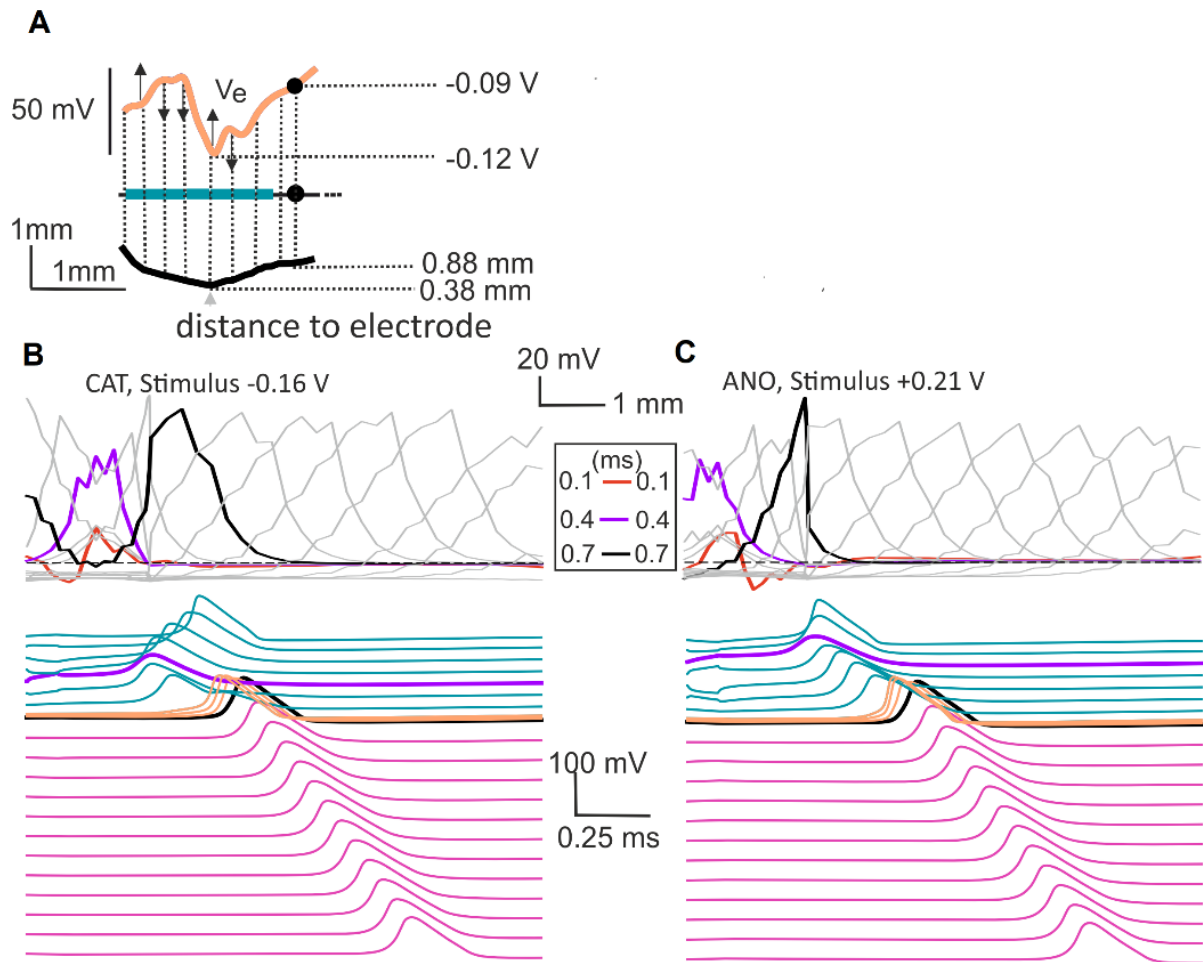


Figure 3.9. Stimulation of intact target fiber basal11 at threshold level with the perimodiolar electrode of C5. Same layout as in Figure 3.8. Figure adapted from (Potrusil et al., 2020).

Furthermore, by stimulating at threshold levels, the AP was mostly initiated in the dendrite except in middle5 stimulated by C21 with ANO pulse (Figure 3.11C), where the AP was first elicited in the axon. Although the axons are rather far away, the small electric field is compensated by a large axonal diameter according to the rule that thick fibers are easier to stimulate than thin ones (Ranck, 1975; Rattay, 1986, 1999).

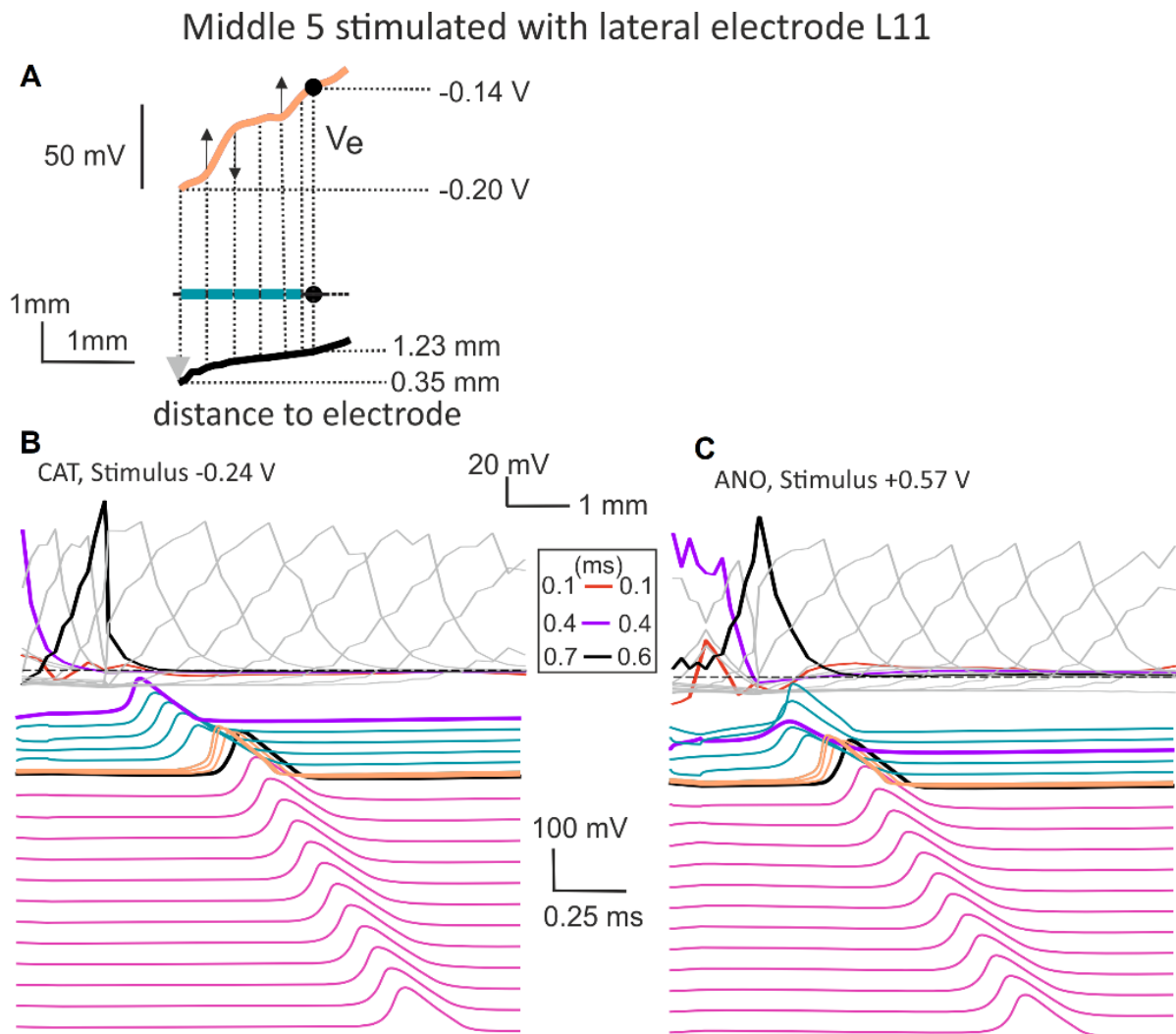


Figure 3.10. Stimulation of intact target fiber middle 5 at threshold level with the lateral electrode of L11. Same layout as in Figure 3.8. Figure adapted from (Potrusil et al., 2020).

Middle 5 stimulated with central electrode C21

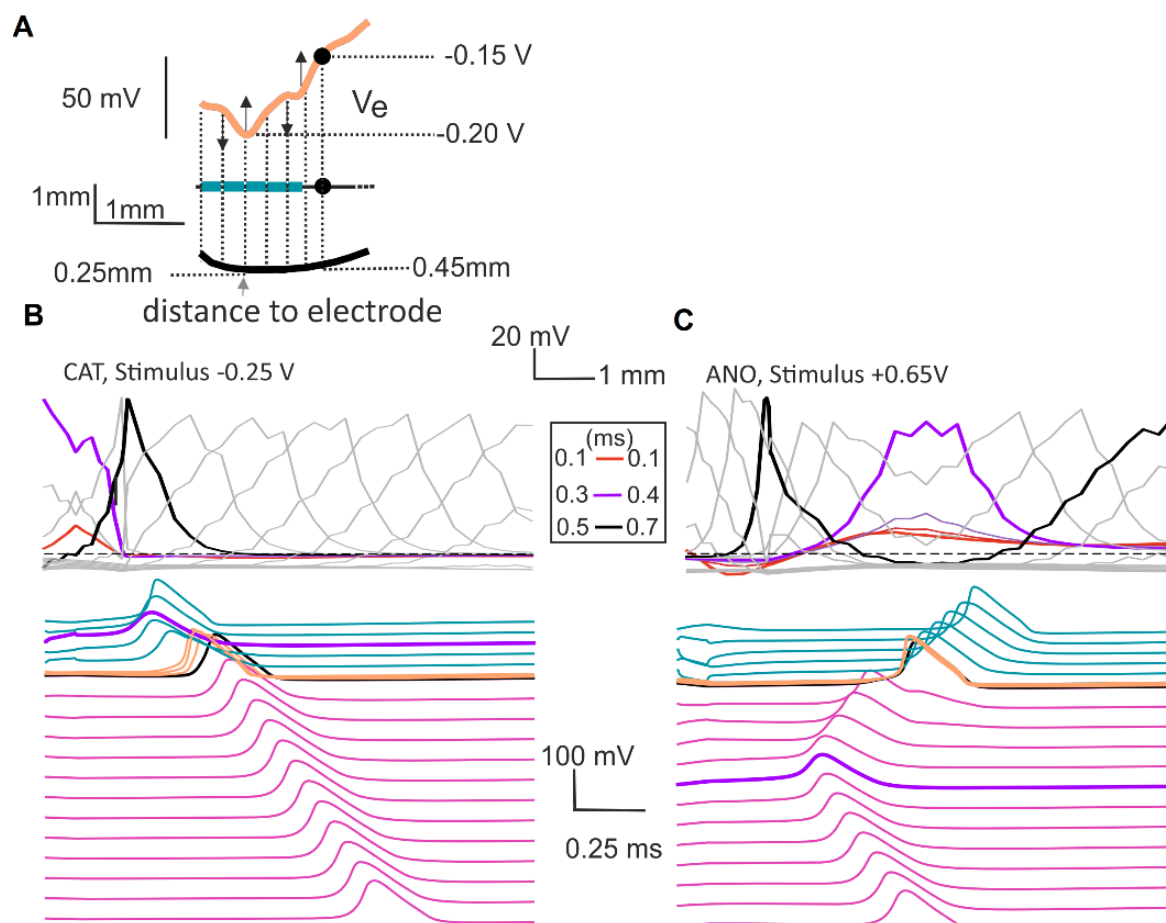


Figure 3.11. Threshold stimulation of intact target fiber middle 5 with the perimodiolar electrode of C21. Same layout as in Figure 3.8. Figure adapted from (Potrusil et al., 2020).

3.5 Suprathreshold excitation

With increasing the stimulus, V_e fluctuations increased further, and the AP initiated in more than one position in the stimulated fibers. Figure 3.12 shows the suprathreshold stimulation of middle5 by electrode L11. The membrane voltages against time have been plotted for CAT and ANO pulses in Figure 3.12A and Figure 3.12C, respectively. CAT stimulation started AP in two sites in the peripheral process, at the first and fourth node of Ranvier (thick purple) simultaneously and AP at the fourth node of Ranvier dominated and stopped propagation of the distal AP by collision block, causing 0.5 ms faster conduction of the AP to the central end compared with stimulation at the threshold.

Figure 3.12B displays the corresponding AF with depolarized and hyperpolarized regions for CAT stimulation. Two peaks at the first and fourth nodes in the peripheral process (purple stars) predicted the AP initiation sites. The stronger ANO stimulation caused one AP initiation in the third node of the peripheral process (thick purple), as previously occurred at threshold level stimulation (Figure 3.10C). Interestingly, another AP was generated at the fifth node of the central process (thick purple), which significantly increased the AP conduction velocity to the terminal end, decreased the AP arrival time to 0.3 ms, back-propagated the AP to the soma, and blocked AP conduction of the distal site.

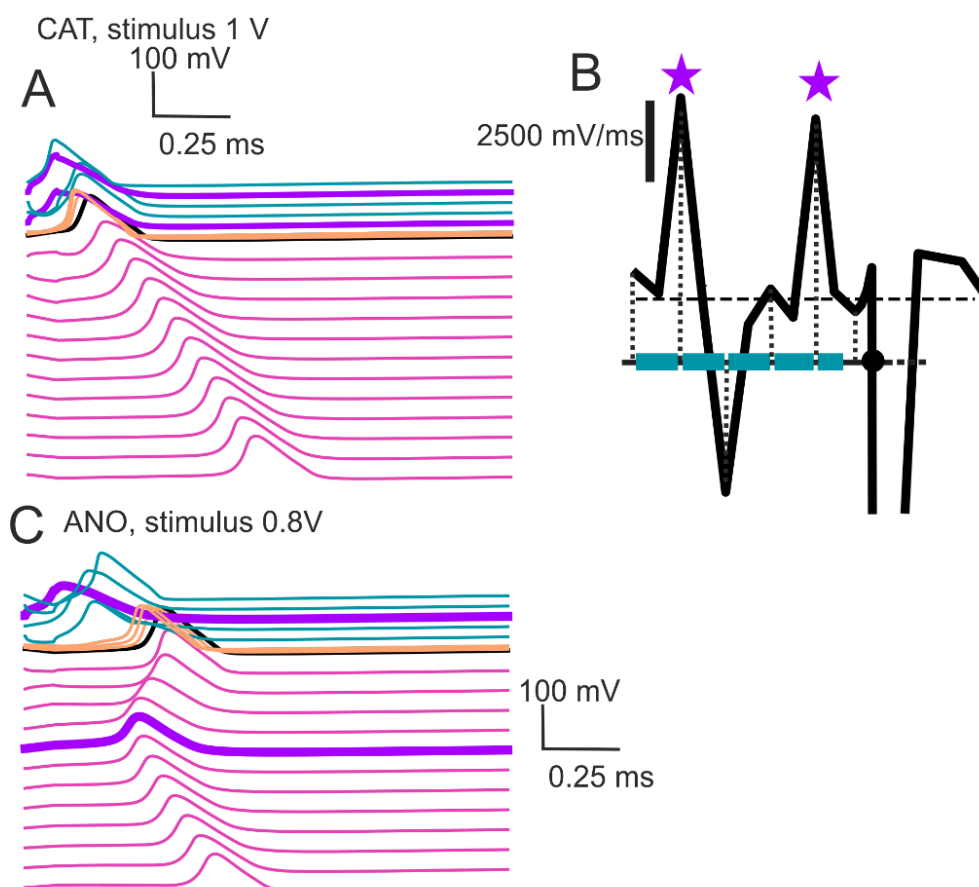


Figure 3.12. Suprathreshold stimulation of middle5 with L11. **(A)** Stronger CAT stimulation elicits two spatially separated APs in the peripheral process (purple lines). **(B)** The corresponding activating function (AF) (black curve) is reproduced with its zero line (horizontal black dashed line) parallel to the peripheral process. The vertical black dashed line marks node positions and the corresponding AF value. The green rectangles represent the compartment model for internodes and the black sphere for the soma position. The purple stars show the highest values of the AF, indicating AP generation. **(C)** Stronger ANO stimulation also elicits two APs in the target fiber. The initiation of an AP in the central process reduces conduction time to the last compartment. Figure adapted from (Potrusil et al., 2020).

3.6 Excitation of fibers without peripheral process

The stimulation thresholds were computed for degenerated target fibers in the next step. It is reported that the peripheral process is often lost in prolonged severe and profound hearing impairment (Spoendlin and Schrott, 1988). Therefore, we considered no peripheral part in our degeneration model with soma surrounded by three layers for this step of calculations (Potrusil et al., 2012). This part is shown in Figure 3.13 for both investigated fibers and electrodes.

However, losing the peripheral site usually leads to the smallest electrode-fiber distance at the soma and, therefore, the highest V_e . In the case of CAT pulses, this usually results in AP initiation at the soma (Figure 3.13 left panels). Consequently, higher thresholds were needed to load the large capacity of the soma compared with highly excitable nodes of Ranvier in healthy fibers.

On the other hand, ANO pulses generated APs at the central process (see Figure 3.13, right panels). In Middle5, the corresponding thresholds were only slightly increased (3% and 33% when stimulated by C5 and L11, respectively). However, in basal 11, the ANO threshold increased more than four times. The significant ANO threshold rise can originate from longer peripheral processes in the basal than middle fibers (Figure 3.3B), which causes a larger electrode distance to soma, and therefore higher thresholds were needed.

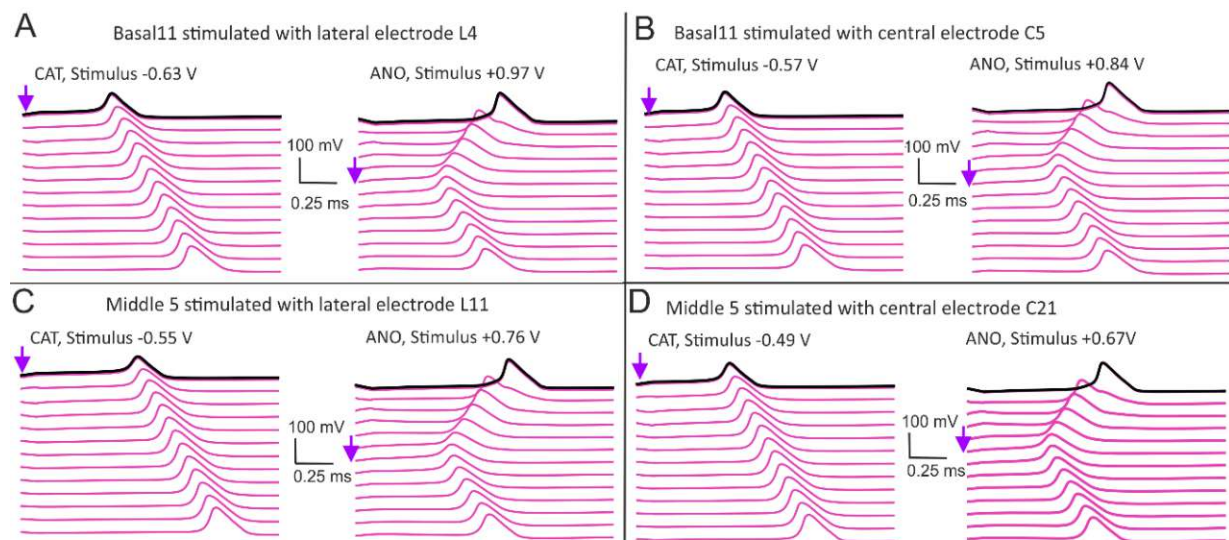


Figure 3.13. Stimulation of degenerated target fibers basal11 (top) and middle5 (bottom) at threshold level. The same layout as Figure 3.8B-C bottom panels without peripheral processes. Arrows depict AP initiation sites. For CAT, APs are generated in the soma. For ANO, the third line (central node C2) is most excited at stimulus offset, but the AP is initiated more distant because loading the soma

capacitance consumes much of the current passing the membrane at node C2. Figure slightly adapted from (Potrusil et al., 2020).

In a final set of experiments, the number of soma layers was gradually decreased (from $n=3$ to $n=1$) to replicate the soma degeneration pattern. The results of this part are demonstrated in Figure 3.14. The concentration of the degenerated cases with $n=2$ and $n=1$ above the black line ($\text{ANO}/\text{CAT} = 1$) shows more sensitivity to ANO pulses than the CAT in these fibers (Figure 3.14, top panel), which is in line with findings presented previously (Macherey et al., 2008; Undurraga et al., 2012; Jahn and Arenberg, 2019). Figure 3.14, bottom panel, shows that decreasing the soma layers does not influence the ANO threshold, whereas the CAT threshold increased significantly, leading to a sensitivity of most degenerated fibers to ANO pulses.

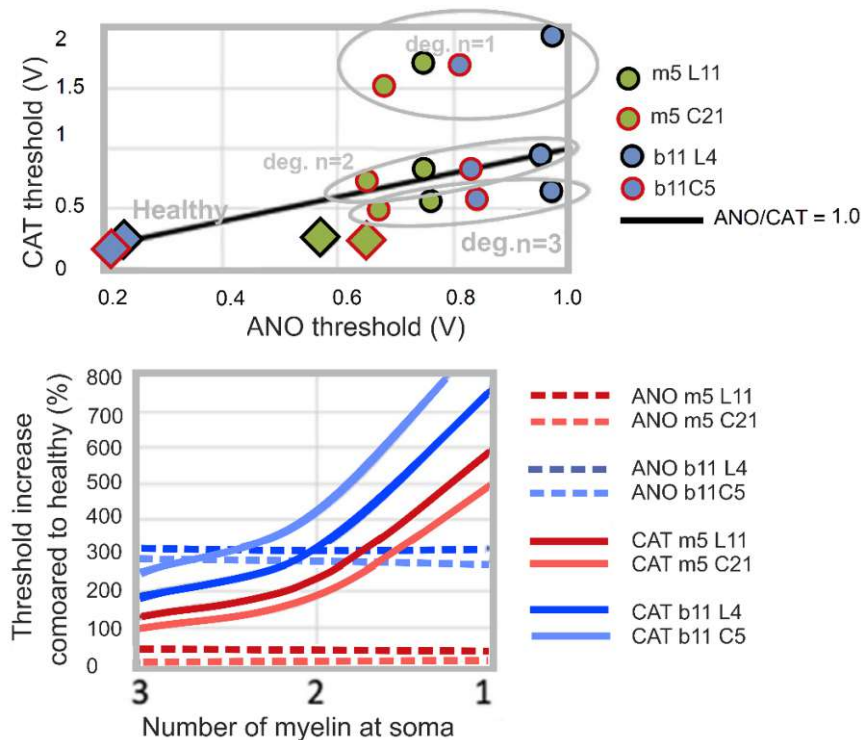


Figure 3.14. ANO/CAT threshold ratios are plotted for the target fibers and the selected electrodes. Top panel: The healthy SGCs are displayed as diamonds and the degenerated fibers as circles. The number of myelin layers at the soma is indicated inside the grey ellipses. Marks above the solid black line indicate a threshold ratio $\text{ANO}/\text{CAT} < 1$ and thus higher sensitivity to anodic stimulation. Bottom panel: For the degenerated fibers, the threshold increase compared with the healthy values is plotted for the decreasing number of myelin layers at the soma (increasing soma capacitance). Figure from (Potrusil et al., 2020).

3.7 Discussion

Investigation on SGC excitation profiles induced by neuroprosthetics is difficult and ethically impossible (van den Honert and Stypulkowski, 1987; Javel and Shepherd, 2000; Rattay et al., 2001a, 2001b; Long et al., 2014; Hochmair et al., 2015). On the other hand, by investigating the electrode position, stimuli configurations, and the resulted neural excitation pattern, computational studies aim to shed more light on single fiber and spiking behavior (Black et al., 1983; Spelman et al., 1980; Suesserman and Spelman, 1993; Cohen et al., 1996; Frijns et al., 1995; Hanekom, 2001; Rattay et al., 2001a; Briaire and Frijns, 2005; Finley et al., 2011).

A recent study used a mathematical method to reconstruct spiral pathways from finite element model of the cochlea with a constant rotation of 45° and constant length at the peripheral process and reported that considering a complex model and subsequently spiraled fibers have a significant impact on AP initiation sites which consequently leads to different latencies (Bai et al., 2019). Another computational study of the human cochlea employed oblique fiber trajectories for the apical turn (Kalkman et al., 2014). However, most computational studies use complicated cochlear geometry without incorporating the 3D cochlear neuron pathway.

In contrast, this chapter uses a detailed human cochlear finite element model from high-resolution micro-CT and 30 tonotopically organized (28° - 928°) reconstructed 3D pathways from the manually traced fiber bundles presented in (Potrusil et al., 2020). Including the 3D pathway in the FE model led to a more complicated fluctuating potential along the fibers (Figure 3.4 - Figure 3.7). As previously investigated and reported, stimulation of long straight homogeneous structures such as an axon with cathodic pulses usually results in depolarizations of the regions close to electrodes, whereas, for anodic pulses, this region is hyperpolarized while two flanks on both sides are depolarized, and therefore usually, an ANO/CAT threshold ratio of 4 is reported in the literature (Ranck, 1975; Rattay, 1986). In addition, in some cases, due to an edge effect (AP from the end of the fiber), the peripheral terminal may win if the electrode is close enough to the peripheral end (Rubinstein and Rubinstein, 1993; Rattay, 2008; Rattay et al., 2017). However, our results demonstrated that when pathway spirality is included, oscillations in extracellular potentials are expected (Figure 3.8-11), which makes the situation more complicated than previously observed in studies with more simplifications of auditory fibers (Rattay et al., 2001b). Due to pathway irregularities and spirality, various polarizing forces occurred at the positions indicated by black arrows resulting in several candidates for AP initiation (Figure 3.8-11, panel A).

The presented results may also be of interest for bilateral CI users as it has been shown that delay in AP arrival time may increase the interaural time differences that are a crucial factor

for sound localization as well as speech understanding in noisy environments (Litovsky et al., 2009; Laback et al., 2015). We demonstrated that with increasing the threshold of the active electrode, in addition to one AP site at the periphery, a second AP initiation site appeared close to soma which won the AP propagation as the earlier AP sites were suppressed by a collision block (Figure 3.12). As a result, we can expect that fibers from the same frequency regions can initiate AP from different sites and therefore have different AP arrival times (latency) because the distant AP at the site with weaker extracellular potential may reach the axonal end a few milliseconds later.

Clinical studies demonstrated that the number of peripheral processes is lower than central processes (Spoendlin and Schrott, 1988, 1989; Felder et al., 1997). In addition, a recent study showed that the peripheral fibers appeared thinner and less myelinated in people with severe and profound hearing status and the severity of the peripheral degeneration is significantly variable between people with hearing loss problems (Heshmat et al., 2020). Several clinical and computational studies reported anodic sensitivity (less ANO thresholds) for degenerated investigated SGCs (Rattay et al., 2001b; Macherey et al., 2008; Undurraga et al., 2013; Jahn and Arenberg, 2019), and a recent study investigated the effect of various parameters such as pulse shape, CI array, and stimulation strategy on the polarity sensitivity (Heshmat et al., 2021). Here, the thresholds for both polarities were calculated and compared for the closest neuron to the active electrode (target neuron) in intact fibers and different degenerated cases without peripheral process when the soma layers decreased from three to one. Decreasing the soma layers increased the soma capacitance and made the soma less excitable. The ANO polarity resulted in more axonal excitability in contrast to soma excitability in CAT (see Figure 3.13) in the case of peripheral loss. Therefore, by increasing the somatic degeneration, the ANO threshold remained almost constant whereas, CAT thresholds increased significantly, up to 8-fold (Figure 3.14, lower panel), and consequently caused up to 70% smaller ANO/CAT ratios in cases with fully degenerated soma ($n=1$) compared with the degenerated case with three myelinated layers around the soma.

In summary, this result demonstrated that detailed and accurate models are essential for realistic representations of the cochlea and CIs. Moreover, it is worth mentioning that understanding single neuron behavior, when realistic pathways are incorporated, enables us to understand more complicated behaviors of multiple neurons recordings from clinical experiments.

Chapter 4

Investigation on upper threshold in spiral ganglion, retinal ganglion, and pyramidal cells with linear geometry

In this chapter, stimulation windows are evaluated and compared for three cells: SGC, RGC, and PC with a 2D geometry. Cell geometries were simplified to investigate the effect of cell kinetics on the threshold windows and ratios. The RGC and PC threshold computations of this chapter were performed by Andreas Fellner and Isabel Stienon. Part of the results in this section was published first in (Sajedi et al., 2020).

4.1 Model neurons

The somatic upper threshold was reported as a limit for spike generation in the soma of RGCs for close electrode distances ($\sim 30 \mu\text{m}$) (Boinagrov et al., 2012). However, several computational studies have shown that this limit cannot hinder AP generation and propagation in the axonal part, and UT block depends strongly on electrode distance and position as well as cell geometry and kinetics (Rattay, 2014; Meng et al., 2018). Here, the AP initiation and blockage in the axon and soma were investigated for three different cell types with linear geometry: (i) a SGC modeled with Rattay's multi-compartment model (chapter 3, Figure 3.1 and Table 3.1), (ii) a RGC modeled based on (Fohlmeister et al., 2010) and finally (iii) a PC modeled according to (Rattay and Wenger, 2010). As shown in Figure 4.1C, the soma was divided into several compartments aligned in the z-axis direction where the point source was located. The multi-compartment soma consisted of 51 compartments for the electrode to soma distances $< 10 \mu\text{m}$ and 21 compartments for distances $> 10 \mu\text{m}$. Details on geometric and electric parameters can be found in Table 4.1. More information on RGC and PC model kinetics is discussed in the following sections.

In all experiments, the lower and upper thresholds were calculated for eight different electrode distances from 1 to 200 μm (1, 2, 5, 10, 20, 50, 100, and 200 μm). The electrode was always located along the z-axis, and electrode distance was considered the distance between the electrode center and the cell's surface (to soma surface in the single soma and whole-cell experiments or the middle of axon in the axon experiment). However, thresholds were not calculated in some cases because either the cell was not excitable (close electrode to cell distances) or the AP initiated at the axonal end.

Experiments were performed in three ways for each model cell: (i) the single soma experiment: stimulation above the single soma with a multi-compartment configuration (no axon or dendrite included), (ii) the axon experiment: stimulation above the middle of a single axon (in myelinated fiber, the electrode was set above a node of Ranvier), and finally (iii) the whole-cell experiment: stimulation of above the multi-compartment soma in a complete cell (dendrite-soma-axon). Monophasic cathodic pulses with durations of 100 μs and 1 ms were applied in all experiments.

Parameter	RGC	SGC	PC
Soma diameter (μm)	20	20	20
Dendrite diameter (μm)	4/2	1.3	4
Dendrite length (μm)	160	2000	2100
Axon diameter (μm)	~ 1	2.6	1
Axon length (μm)	3170	10000	1170
Extracellular resistivity ($\Omega\cdot\text{cm}$)	300	300	300
Intracellular resistivity ($\Omega\cdot\text{cm}$)	100	100	100
Membrane capacitance ($\mu\text{F}/\text{cm}^2$)	1	1	1
Temperature ($^{\circ}\text{C}$)	35	29	37
Resting potential (mV)	-67	-70	-72

Table 4.1. Geometric and electrophysiological parameters used in the investigated cell models.

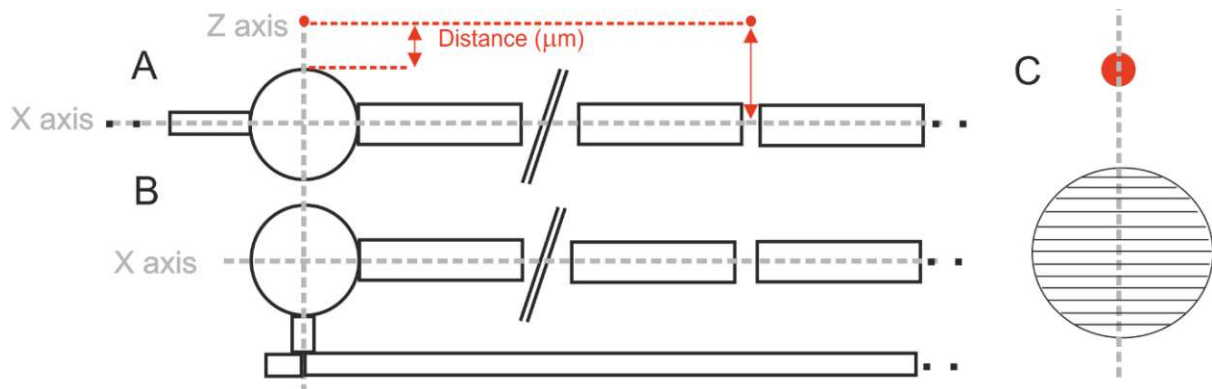


Figure 4.1. The linear geometry dendrite-soma-axon for (A) SGC, PC, and (B) RGC. The red circles represent the electrode position. The red dashed lines with arrows mark the distance between the electrode and the surface of the soma and the axon. (C) Multi-compartment soma used in single soma and whole-cell experiments. The soma consists of 21 compartments (for distances $> 10 \mu\text{m}$) and 51 compartments (for distances $\leq 10 \mu\text{m}$) along the z-axis.

4.2 Biophysical properties

4.2.1 RGC

The RGC was modeled based on data from the cat (Fohlmeister et al., 2010). They proposed four RGC models, cat alpha, cat beta, rat type I, and rat type II, and each model consisted of the same channels and differed in the maximum ion channel conductances along the neural membrane. The model has the same channels as the previously investigated model of tiger salamander RGC by Fohlmeister and Miller (Fohlmeister and Miller, 1997) except for the potassium inactivation current that was excluded in this model.

This thesis used the cat beta (current chapter) and rat type II (chapter 5) to model the investigated RGCs. Differences in geometries between two cells can be observed in Figure 4.2

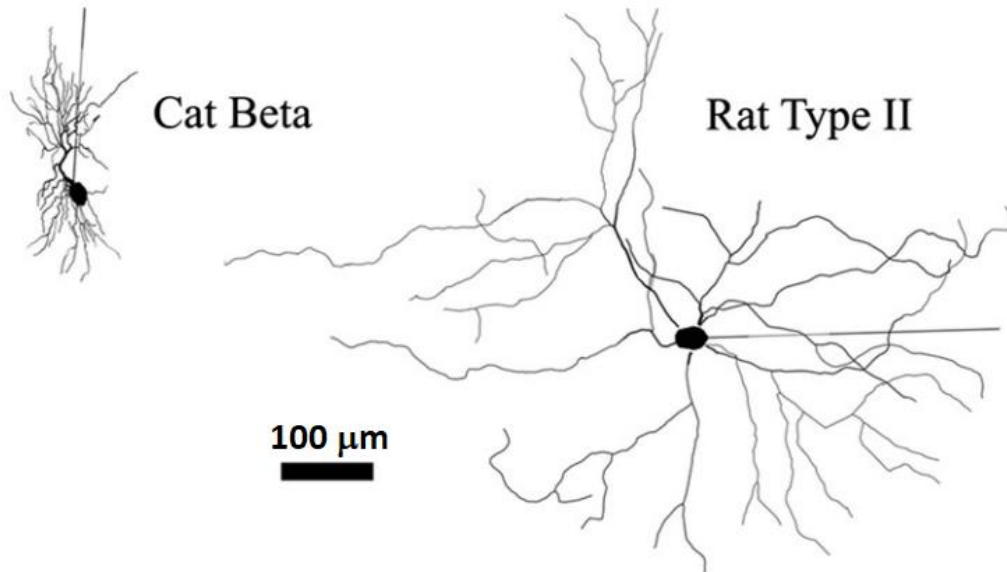


Figure 4.2. Examples of traced RGCs from the cat beta (left), and rat type II (right). Figure adapted from (Fohlmeister et al., 2010).

The gating rate equations ($T > 30^\circ\text{C}$) used for the cat beta model follow:

Sodium

$$\alpha_m(V) = \frac{-2.725(V + 35)}{\exp[-0.1(V + 35)] - 1} \quad \beta_m(V) = 90.83 \exp\left[\frac{-(V + 60)}{20}\right] \quad (4.1)$$

Sodium inactivation

$$\alpha_h(V) = 1.817 \exp\left[\frac{-(V + 52)}{20}\right] \quad \beta_h(V) = \frac{27.25}{1 + \exp[-0.1(V + 22)]} \quad (4.2)$$

Potassium activation (delayed rectifier)

$$\alpha_n(V) = \frac{-0.09575(V + 37)}{\exp[-0.1(V + 37)] - 1} \quad \beta_n(V) = 1.915 \exp\left[\frac{-(V + 47)}{80}\right] \quad (4.3)$$

Calcium activation

$$\alpha_c(V) = \frac{-1.362(V + 13)}{\exp[-0.1(V + 13)] - 1} \quad \beta_c(V) = 45.41 \exp\left[\frac{-(V + 38)}{18}\right] \quad (4.4)$$

Furthermore, according to Fohlmeister et al., 2010, a H-type non-inactivating calcium current is added to the RGC model, which has a similar parametrization as sodium activation and with a variable Nernst potential depending on intracellular calcium concentration ($[Ca^{2+}]_i$, see Equation (5.1)). The Ca^{2+} activated K^+ ($I_{K,Ca}$) is formulated as follows

$$g(K, Ca) = G - bar(K, Ca) \frac{([Ca^{2+}]_i / Ca_{diss})^2}{1 + ([Ca^{2+}]_i / Ca_{diss})^2} \quad (4.5)$$

with $Ca_{diss} = 10^{-6}$ molar and $[Ca^{2+}]_i = 10^{-7}$ molar.

The conductivities used in the RGC model are based on whole-cell recording experiments in the original study and are shown in Table 4.2. Additionally, a linear leakage current with maximum conductance of 0.1 mS/cm² is included in the model.

Channel	Dendrites	Soma	IS	TS	Axon
Cat Beta RGC					
Na	63.90	69.40	100.00	244.5	124
K	13.40	32.00	50.10	50.1	50
Ca	1.39	1.39	0.836	0.0	04

Table 4.2. G-bar conductances (mS/cm²) for modeled RGC. IS and TS represent the Initial Segment and Trigger Segment, respectively (Fohlmeister et al., 2010)

4.2.2 PC

The PC was a simplified model from (Rattay and Wenger, 2010). This model incorporates sodium channel kinetics from (Hu et al., 2009), who investigated the sodium distribution in PC L5 from rat prefrontal cortex using the patch-clamp technique. They found an accumulation of high-threshold $Na_{v1.2}$ in soma, dendrite, hillock, and proximal AIS and low-threshold $Na_{v1.6}$ at distal AIS, non-myelinated axon, and nodes of Ranvier. The fast potassium channel followed the kinetics from (Mainen and Sejnowski, 1996).

Na_{v1.2} activation

$$\alpha_{m_{12}}(V) = \frac{0.182(V + 28)}{1 - \exp\left[\frac{-(V + 28)}{7}\right]} \quad \beta_{m_{12}}(V) = \frac{-0.124(V + 28)}{1 - \exp\left[\frac{(V + 28)}{7}\right]} \quad (4.6)$$

Na_{v1.2} inactivation

$$\alpha_{h_{12}}(V) = \frac{0.024(V + 35)}{1 - \exp\left[\frac{-(V + 35)}{5}\right]} \quad \beta_{h_{12}}(V) = \frac{-0.0091(V + 60)}{1 - \exp\left[\frac{(V + 60)}{5}\right]} \quad (4.7)$$

Na_{v1.6} activation

$$\alpha_{m_{16}}(V) = \frac{0.182(V + 41)}{1 - \exp\left[\frac{-(V + 41)}{6}\right]} \quad \beta_{m_{16}}(V) = \frac{-0.124(V + 41)}{1 - \exp\left[\frac{(V + 41)}{6}\right]} \quad (4.8)$$

Na_{v1.6} inactivation

$$\alpha_{h_{16}}(V) = \frac{0.024(V + 48)}{1 - \exp\left[\frac{-(V + 48)}{5}\right]} \quad \beta_{h_{16}}(V) = \frac{-0.0091(V + 73)}{1 - \exp\left[\frac{(V + 73)}{5}\right]} \quad (4.9)$$

Potassium-fast activation

$$\alpha_{n_v}(V) = \frac{0.02(V - 25)}{-\exp\left[\frac{-(V - 25)}{9}\right]} \quad \beta_{n_v}(V) = \frac{-0.002(V - 25)}{1 - \exp\left[\frac{(V - 25)}{9}\right]} \quad (4.10)$$

Table 4.3 represents all conductivities used in the model PC. The myelination in the axon was simulated by considering a passive state with a reduced capacity of 0.02 $\mu\text{F}/\text{cm}^2$. Additionally, a linear leakage current with maximum conductance of 0.33 mS/cm^2 is employed throughout the PC.

Channel	Dendrites	Soma	Hillock	AIS	Non-my.	NoR
Na_{12}	8	8	320	100	0	0
Na_{16}	0	0	0	320	300	160
K_v	10	10	100	100	150	20

Table 4.3. G-bar conductances (mS/cm^2) for modeled PC. AIS, Non-my., and NoR represent the AIS, the non-myelinated axon, and nodes or Ranvier, respectively (Rattay and Wenger, 2010).

4.2.3 SGC

Biophysical properties of SGC were based on Rattay's multi-compartment model (Rattay et al., 2001b), which was used to compute the LTs, UTs, and threshold ratios induced by the point source approach. Model details can be found in Figure 3.1 and Table 3.1.

4.3 Comparison of threshold windows

Figure 4.3 demonstrates stimulation of single soma experiments for pulse durations of 100 μs (panel A) and 1 ms (panel B). Stimulating the PC soma was not possible with 100 μs pulses resulting from the low sodium conductance ($8 mS/cm^2$) in the PC soma against the 8.7 and 15 times larger sodium conductances in RGC and SGC models, respectively. A SGC soma covered with three glial cell layers was excitable at the smallest electrode distance of 1 μm (black), whereas decreasing the layers to 1, an AP could only be generated for electrode distances larger than 4 μm (blue traces, and black arrow). The LTs and UTs increased in the investigated cells by increasing the electrode distance. The arrow shows the $LT = UT$ at the smallest possible distance (4.6 μm) for the degenerated SGC with one glial cell layer.

However, by increasing the pulse duration to 1 ms, the PC soma became excitable from electrode distances $> 5 \mu m$ (blue traces in Figure 4.3B). The RGC soma was not excitable for electrode distances $< 5 \mu m$ when a longer pulse was applied (red traces in Figure 4.3A-B).

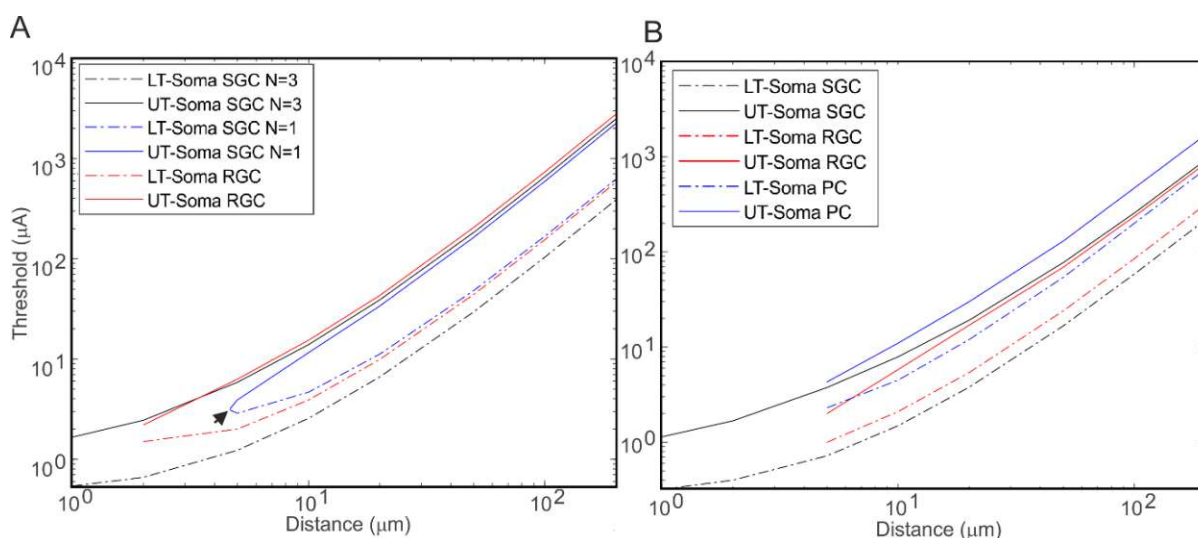


Figure 4.3. The lower (LT) and upper threshold (UT) of the single soma stimulation in RGC, SGC, and a PC for a monophasic cathodic pulse with a duration of **(A)** 100 µs and **(B)** 1ms. N represents the number of myelin layers of the SGC soma covered by glial cells. The arrow shows the start point where the LT and UT (N=1) are met. Figure adapted from (Sajedi et al., 2020).

In the next set of experiments, the LTs and UTs were calculated and compared for the three investigated axon models (SGC, RGC, and PC). By applying a 100 µs pulse (Figure 4.4A), the LT trend was similar in both myelinated fibers (SGC and PC, black and blue, respectively), with SGC axon possessing smaller LT values that may result from longer nodes of Ranvier (2.5 vs. 1 µm) and thicker axonal diameter (2.6 vs. 1 µm) in the model leading to a higher sodium conductivity in nodal area. UTs showed the same trend in all three cells for small electrode distances (1 and 2 µm).

However, the trends for RGC and PC axons were close in all electrode distances compared to the SGC axon, which possessed smaller UTs. In addition, in the PC axon, UT increased with increasing the distance up to 100 µm and decreased for the largest electrode distance (200 µm).

When the pulse duration was increased to 1 ms (Figure 4.4B), the LT values in all three axons were close regardless of electrode distance. The same trend was also observed for UTs in RGC and PC axons. The SGC axon, on the other hand, possessed larger UTs for close electrode distances (< 10 µm), and UTs decreased in larger electrode distances.

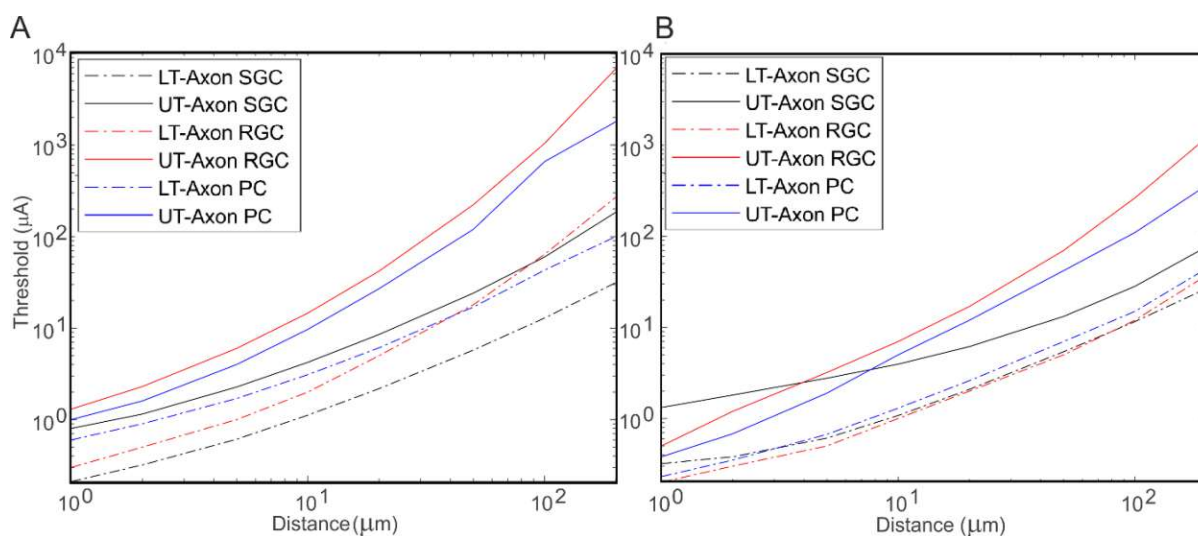


Figure 4.4. The lower (LT) and upper thresholds (UT) of the axon experiment in RGC, SGC, and a PC for a monophasic cathodic pulse with a duration of (A) 100 μs and (B) 1ms. Same layout as Figure 4.3. Figure adapted from (Sajedi et al., 2020).

In the final experiment, the complete cells were investigated with the electrode above their soma (Figure 4.5). Panel A shows the stimulation with a 100 μs pulse. For close electrode distances ($<10 \mu\text{m}$), in the PC model, LTs and UTs were up to 10 and 100-folds, respectively, higher than those in SGC and RGC. In all cells, the threshold windows increased monotonically with increasing the electrode distance, except in SGC, at an electrode distance of about 40 μm , the UTs started to decrease (purple circle). More analysis revealed that the complete SGC upper limit followed the single soma UTs in close electrode distances, whereas, at this point (electrode distance $\sim 40 \mu\text{m}$), UTs in the whole cells started to follow the axonal UT trend (Figure 4.6).

By applying a 1 ms pulse (Figure 4.5B), the LT and UT trends became linear for SGC (black), whereas the RGC and PC followed the same trend as in the shorter pulse duration (red and blue). LTs and UTs were smaller in all cell types when a longer pulse is applied.

Comparison of threshold windows

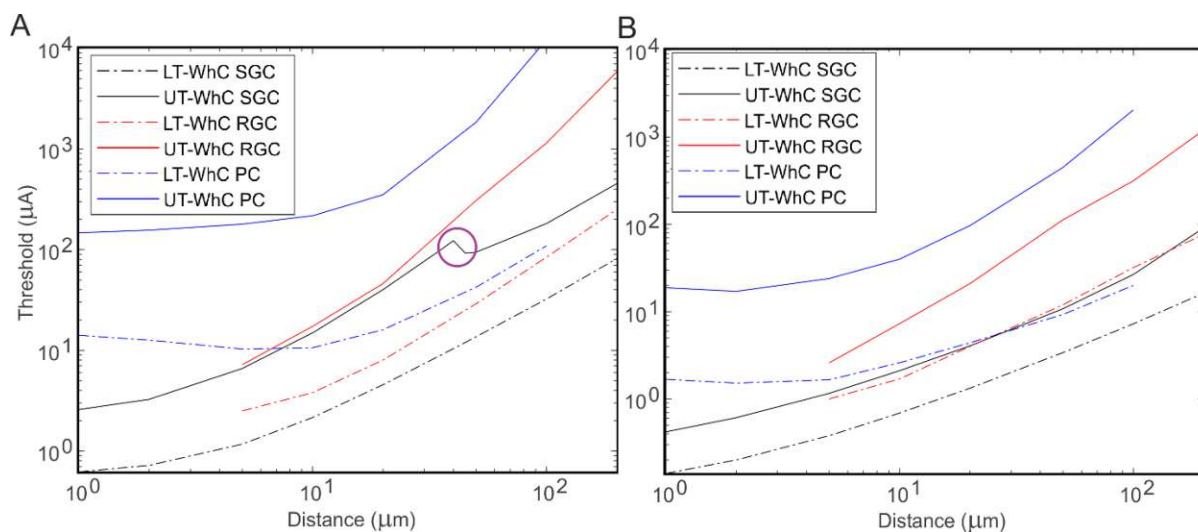


Figure 4.5. The lower (LT) and upper thresholds (UT) of the whole-cell experiments in the RGC, SGC, and a PC for a monophasic cathodic pulse with a duration of **(A)** 100 μs and **(B)** 1 ms. Same configuration as Figure 4.3. The purple circle shows at an electrode distance of about 40 μm UT trend changes abruptly to a narrower threshold window. Figure adapted from (Sajedi et al., 2020).

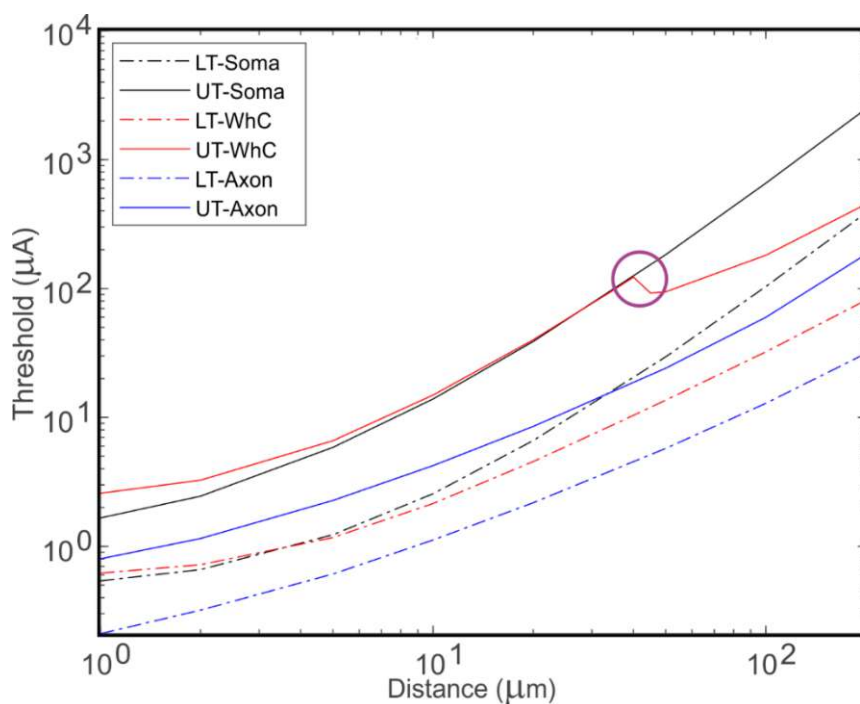


Figure 4.6. The lower (LT) and upper thresholds (UT) of the single soma and axon, and whole-cell experiments for SGC, with 100 μs a monophasic cathodic pulse. Not that for electrode distances below 40 μm (purple circle), the UT follows the soma trend, and for larger electrode distances, the SGC UTs become close to axonal upper threshold values. Figure adapted from (Sajedi et al., 2020).

4.4 Evaluation of threshold ratios

A more detailed analysis of threshold ratios (UT/LT) for a 100 μs pulse is performed in this section. The investigation revealed that threshold ratios of the soma and axon experiments followed the same trends in the investigated cells: a non-linear trend in the single soma experiments (Figure 4.7A) and a linear trend for the axons investigation (Figure 4.7B).

On the other hand, the ratios demonstrated two different trends for the whole-cell experiment. For close electrode distances (up to 20 μm in RGC and up to 40 μm in SGC), the trend followed the behavior of the single soma case in the corresponding distances (Compare Figure 4.7A & Figure 4.7C). However, the comparison was not possible in the PC case because the soma was not excitable with a pulse duration of 100 μs .

The ratio changed to a similar trend in larger electrode distances as in the axonal stimulation (compare Figure 4.7B & Figure 4.7C) in the three investigated cells, which means that soma significantly impacted threshold ratios for close electrodes to soma distances (except in PC). In contrast, the axon governed the cell excitation by increasing the electrode distance. Similar investigations have been done for the larger pulse duration (data not shown), and no correlation was found between whole-cell and soma and axon thresholds.

Additionally, threshold ratios have been compared for whole-cell stimulation with a pulse duration of 100 μs (Figure 5.7D). PC possessed the highest ratios, particularly in larger electrode distances, and the ratios increased dramatically by increasing the electrode distance. RGC ratios increased slightly with increasing electrode to cell distance. In SGC, on the other hand, the ratios remained in similar ranges for all electrode to cell distances.

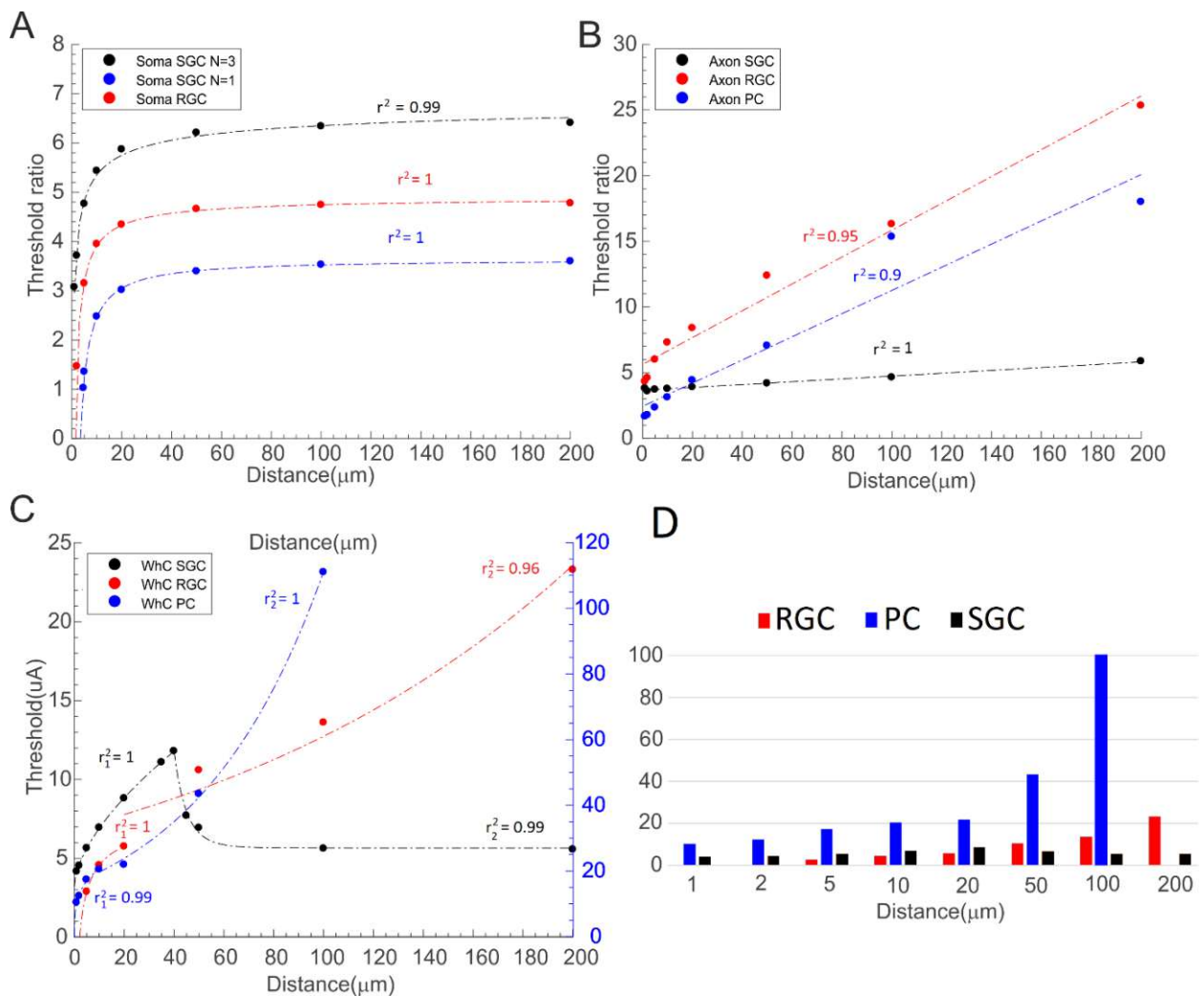


Figure 4.7. Threshold ratios versus electrode distance. **(A)** UT to LT ratios were shown for comparing the stimulation of single soma in SGC (N=3 vs. N=1) and RGC with 100 μs monophasic cathodic pulse. The data in all three cell models were fitted with logarithmic regression with the same color code as for the cell types. **(B)** Same layout as **(A)** for stimulating SGC, RGC, and PC axon alone. Data were fitted with a linear regression (dashed line) with the same color code as the cells. **(C)** Same layout as in **(A)** for stimulation of complete cells. Each cell data was fitted with two different regressions: a logarithmic regression, an exponential growth (in RGC and PC), and decay (in SGC). The right axis represents threshold ratio ranges for PCs. **(D)** Threshold ratios vs. the electrode to cell distance for stimulation of complete model cells with 100 μs monophasic cathodic pulse.

4.5 The effect of pulse duration on threshold ratios

In the last step, threshold ratios were compared for two pulse durations (100 μs and 1 ms). Figure 4.8 represents all ratios in the three investigated cells for both pulse durations for the investigated distances in single soma, axon, and whole-cell experiments. Ratios for the short (100 μs) and the long pulse (1 ms) have been compared, and the data for the whole-cell experiment is demonstrated in bar charts in Figure 4.8.

In the case of SGC (Figure 4.8A), threshold ratios are almost constant until the last two distances when the longer pulse was applied. By applying 100 μs pulse, the ratios increased until the electrode distance of 20 μm and decreased for further distances. However, the ratios decreased significantly by increasing the pulse duration and remained almost constant, except for the largest investigated electrode distance (200 μm).

In the case of RGC (Figure 4.8B), threshold ratios increased by increasing the electrode distance in both pulse durations. Similarly, as in SGC, threshold ratios were significantly higher in 100 μs pulse duration, particularly for larger electrode distances (>50 μm)

In the case of PC (Figure 4.8C), Similar to RGC, threshold ratios increased by increasing the electrode to soma distance in both pulse durations. In contrast to the last two cells, ratios were in close ranges for the investigated pulse durations (100 μs vs. 1 ms). Overall, the threshold ratios were significantly higher in PC than RGC and SGC.

100 μs				1 ms		
SGC				SGC		
Distance (μm)	Soma	Axon	Whole-Cell	Soma	Axon	Whole-Cell
1	3.0741	3.8095	4.1613	3.5625	4.125	3
2	3.7121	3.5937	4.5278	4.2	4.7632	3.05
5	4.7642	3.7213	5.641	5.2222	4.541	3.0526
10	5.4336	3.7768	6.9395	5.3087	3.6574	3.058
20	5.8701	3.9083	8.8022	5.0607	2.9474	3.0526
50	6.2077	4.1913	6.9273	4.62	2.4399	3.1794
100	6.3375	4.6467	5.6142	4.3794	2.4387	3.6777

The effect of pulse duration on threshold ratios

200	6.4077	5.8717	5.5597	4.2453	2.8729	5.5897
RGC				RGC		
Distance (µm)	Soma	Axon	Whole-Cell	Soma	Axon	Whole-Cell
1	-	4.3333	-	-	2.5	-
2	1.4667	4.6	-	-	4	-
5	3.15	6	2.88	2	6.4	2.6
10	3.9487	7.3	4.5526	2.7619	7	4.2941
20	4.3434	8.4	5.75	3.1481	8.5	5.25
50	4.6591	12.3889	10.5862	2.875	14	9.4167
100	4.7419	16.3125	13.6071	2.7765	22	9.875
200	4.7759	25.3333	23.3	2.6984	32.4324	15.6494
PC				PC		
Distance (µm)	Soma	Axon	Whole-Cell	Soma	Axon	Whole-Cell
1	-	1.6667	10.4255	-	1.6522	11.1905
2	-	1.7778	12.381	-	1.9429	11.25
5	-	2.3529	17.3786	1.8696	2.8358	14.4578
10	-	3.129	20.4717	2.4444	3.8462	15.3846
20	-	4.4262	21.9375	2.5	4.6154	22.0455
50	-	7.0588	43.4988	2.4074	6	48.3871
100	-	15.3488	111.0092	2.35	7.3333	102.5
200	-	18	-	2.2973	8.1818	-

Table 4.4. Threshold ratios (UT/LT) for the investigated cells and distances for a cathodic pulse with 100 µs and 1 ms duration.

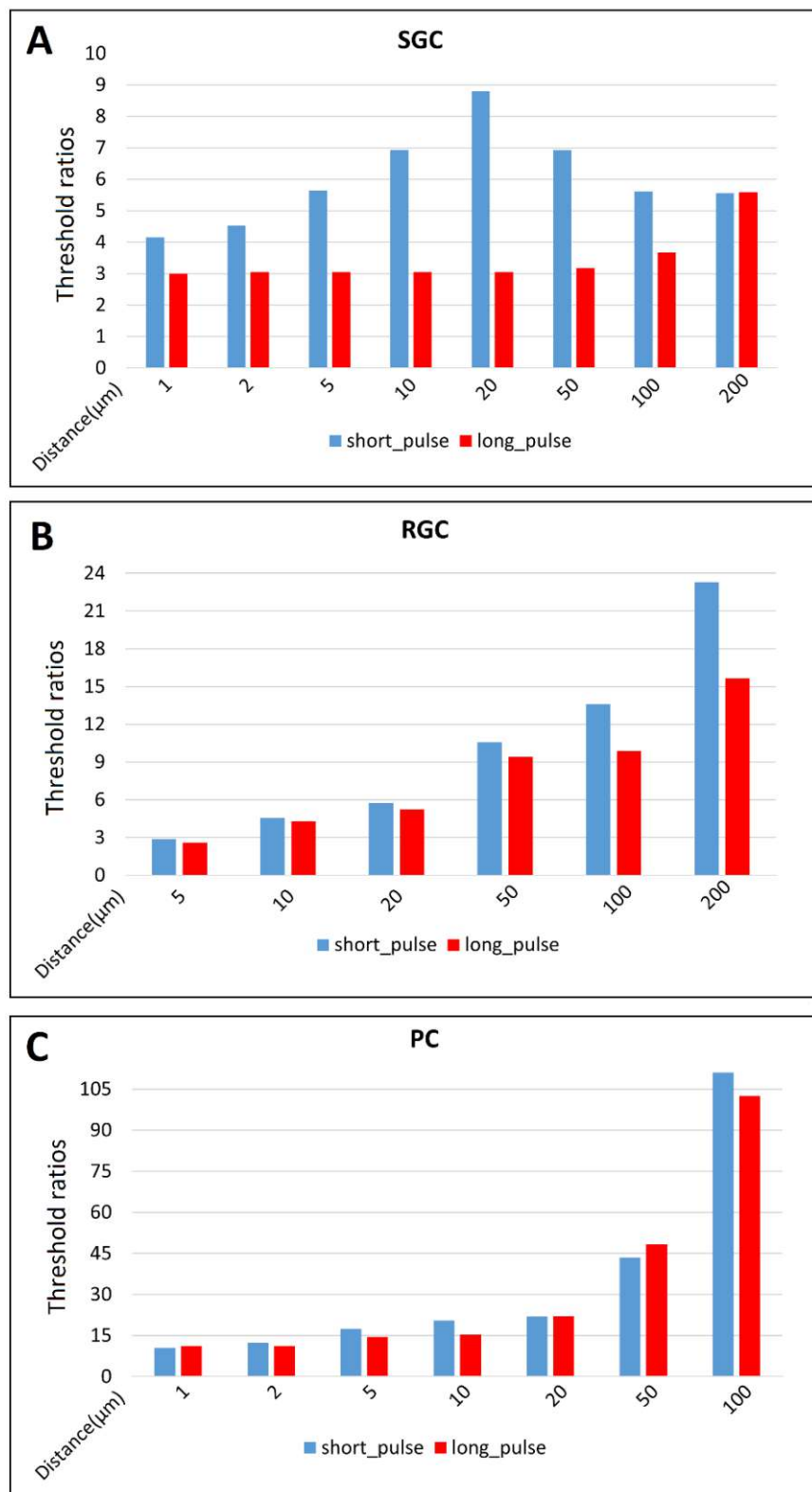


Figure 4.8. Threshold ratios (100 μs vs. 1 ms). Threshold ratios are compared for 100 μs and 1 ms pulse duration in (A) SGC, (B) RGC, and (C) PC.

4.6 Discussion

Using tiny devices in highly dense neural tissues such as the retina or layers of the brain causes undesirable excitation in the non-target area and blockage of target cells. Block phenomena such as anodal surround and somatic block have been investigated and discussed frequently (Ranck, 1975; Boinagrov et al., 2012; Rattay, 2014; Meng et al., 2018). Electrodes close to soma create hyperpolarization and depolarization areas at the same time. For cathodic pulses, the hemisphere close to the electrode becomes depolarized, whereas the other hemisphere is hyperpolarized (see Figure 2.6).

For an anodic pulse, the behavior is inverted. A somatic upper threshold occurs at high stimulus strength due to several mechanisms (Fellner et al., 2019): (i) potassium current that leads potassium leaving the cell in order to compensate the depolarization of membrane voltage caused by sodium influx, (ii) sodium inactivation that controls the sodium influx, and finally (iii) the sodium reversal current happens on the depolarized side of the cell membrane.

Anodal surround (or cathodic) block, on the other hand, occurs in the axonal membrane of the cell. In an anodal surround block, AP is generated at the depolarized area close to the electrode, yet AP cannot propagate due to hyperpolarized flanks on the two opposing sides. Therefore, an upper limit can originate either from a somatic UT, particularly for close electrode distances (Boinagrov et al., 2012; Rattay, 2014; Meng et al., 2018; Fellner et al., 2019) or from the cathodic block when electrodes are located in distant.

UTs and LTs with a point source approach were investigated for three cell mechanisms with a linear geometry in three ways: stimulation of a single soma, axon, and whole-cell. In the single soma experiment, the PC soma was not excitable with the short pulse duration of 100 μ s due to low sodium conductance of 8 in PC, vs. 69.4 and 120 mS/cm^2 in RGC and SGC, respectively. Profoundly degenerated SGC soma was not excitable for electrode distance closer than 4 μm , while in the healthy case (soma layer = 3), excitation was possible at the smallest investigated electrode distance of 1 μm .

PC possessed the highest UT values compared with RGC and SGC. Investigating cell excitations with 100 μ s pulse revealed that for electrode distances close to the soma, the whole-cell excitability was governed by the soma (except in PC), whereas, at larger electrode distances, the excitability of the whole-cell was governed by the axon, in the three cells.

The effect of pulse duration on UT/LT ratios was previously studied by Boinagrov et al., 2012, which reported a variation from 1.7 to 7.6 in their computational model of RGC somata. The group suggested that such variation in stimulus windows could originate from soma size and

shapes and the effect of the extracellular field. Here, threshold ratios for increasing electrode distance were compared for two pulse durations (100 μ s vs. 1 ms). Threshold ratios in RGC and SGC were similar and comparable, whereas PC possessed the highest threshold ratios, particularly in large electrode distances. Generally, threshold ratios were smaller when the longer pulse was applied in all three investigated cells (Figure 4.8A-C, red vs. blue bars).

However, in this investigation, the cell geometry was limited to a linear 2D configuration where the effect of the dendritic tree (in RGC and PC) and axonal collaterals (for PC) on thresholds was neglected. Therefore, the next chapter aims to investigate more realistic cell models and kinetics for the two most important types of cells in micro-stimulation: RGC and PCs.

Chapter 5

Block phenomena during electric micro-stimulation of pyramidal cells and retinal ganglion cells

In this chapter, a similar investigation to the previous chapter was extended by using 3D geometries from a group of PCs (n=8) RGCs (n=34). The simulations aim to identify the contribution of soma to AP generation and blockage during micro-stimulation. Here, the spike initiation and propagation were examined incorporating complex axon collateral structures. Additionally, realistic electrode and pulse properties in RGCs, as well as electrode positioning effects on PCs, were studied. Results presented in this chapter were first published in (Sajedi et al., 2021); Paul Werginz carried out the RGC results and analysis.

5.1 Model neurons

Eight reconstructed morphologies from L5 pyramidal neurons of rat somatosensory cortex were taken from an online database (<http://neuromorpho.org/>, (Ascoli, 2006; Hay et al., 2013; Cohen et al., 2020)). Figure 5.1A shows a model PC. PCs can have various complex arrangements of axon collaterals, which are important for extracellular stimulation studies. The investigated model PCs are demonstrated in Figure 5.2, with dendrite and axon indicated in gray and blue, respectively. In the PC models, the soma was replaced with a spherical soma with a diameter of 20 μm .

In the second step, the axonal tree was reconstructed from the originally traced axon, which was accomplished based on a decision tree algorithm. The axonal tree was divided into (i) the hillock, i.e., the first 0-2 μm of the main axon branch, and followed by (ii) the AIS (L=35-48 μm), (iii) the non-myelinated axon (100-150 μm) until branching starts which was modeled as (iv) the first node of Ranvier (0.5-1 μm) and all branches followed by (v) internodes (100 \times sectional diameters (Rushton, 1951)) and (vi) nodes of Ranvier (0.5-1 μm). The nodal length depended on the adjacent compartment length and was placed at the beginning of the branches

and the end of the myelin sections except at the terminal to prevent self-spiking originating from the large nodal area.

34 reconstructed morphologies from alpha RGC of mouse retina were used from an earlier study (Werginz et al., 2020). A model neuron is represented in Figure 5.1B. Model neurons were split into (i) dendritic trees, (ii) the spherical soma with a diameter ranging from 14 - 24 μm , (iii) hillock ($L = 10 - 47 \mu\text{m}$), (iv) AIS ($L = 12 - 33 \mu\text{m}$), and (v) distal non-myelinated axon ($L \sim 1000 \mu\text{m}$).

For each cell in both groups (PCs and RGCs), the spherical soma was either model as a single or a multi-compartment soma with 41 truncated cones with the compartment axis always pointing toward the stimulating electrode (Figure 5.1C) in order to study the gradient of the electric field on the soma (Fellner et al., 2019). Additionally, the Kruskal-Wallis test was used for two soma groups comparisons with significance levels setting: $p < 0.05$ * , $p < 0.01$ ** , $p < 0.001$ ***. Boxplots use the standard notation (1st Quartile, Median, 3rd Quartile).

Neuron 7.8 (Carnevale and Hines, 2006); and Python 3.8 (<https://www.python.org>) were used to investigate intra- and extracellular responses in both cell types. Compartment length was set to 1-2 μm in the axons and less than 10 μm in dendrites. In most experiments, a monophasic cathodic pulse with a duration of 0.1 ms was applied except for one set of experiments where the effect of pulse shape was studied.

The point source approach (see section 2.5) is used in all experiments except for one stimulation set for RGCs, where the effect of disk electrode (see section 2.5) diameter was investigated. Figure 5.1D shows a segmented soma (5 compartments). The main axis of the soma compartments pointed toward the electrode (vertical dashed line). The Euclidian distance from the electrode and compartment center on the sphere surface (r) is used to calculate the extracellular potential at the soma.

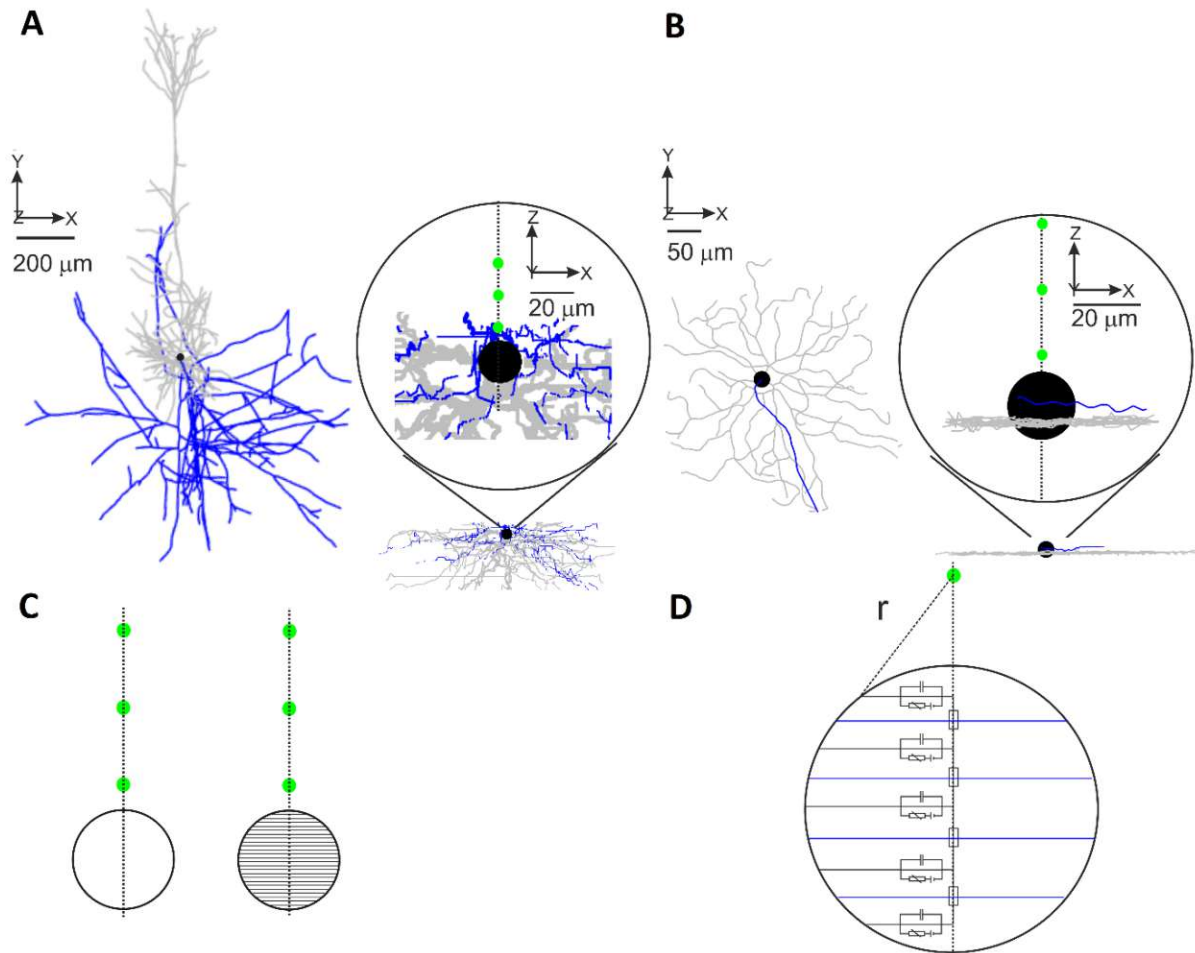


Figure 5.1. Realistic model neurons. Characteristic (A) PC and (B) RGC model geometries. Green circles in the inset show the first three investigated electrode positions (15, 30, and 45 μm). Dendrites in gray, axon in blue, and soma in black. (C) The soma was modeled either as a single compartment (left) or was divided into 41 compartments (right). The multi-compartment soma axis pointed toward the electrode (vertical dashed line). The green circles display the first three investigated electrode positions. (D) Schematic illustration of segmented soma (only five compartments are shown) with the Euclidian distance (r) to the electrode (green) used to calculate the extracellular potential in multi-compartment soma. Figure from (Sajedi et al., 2021).

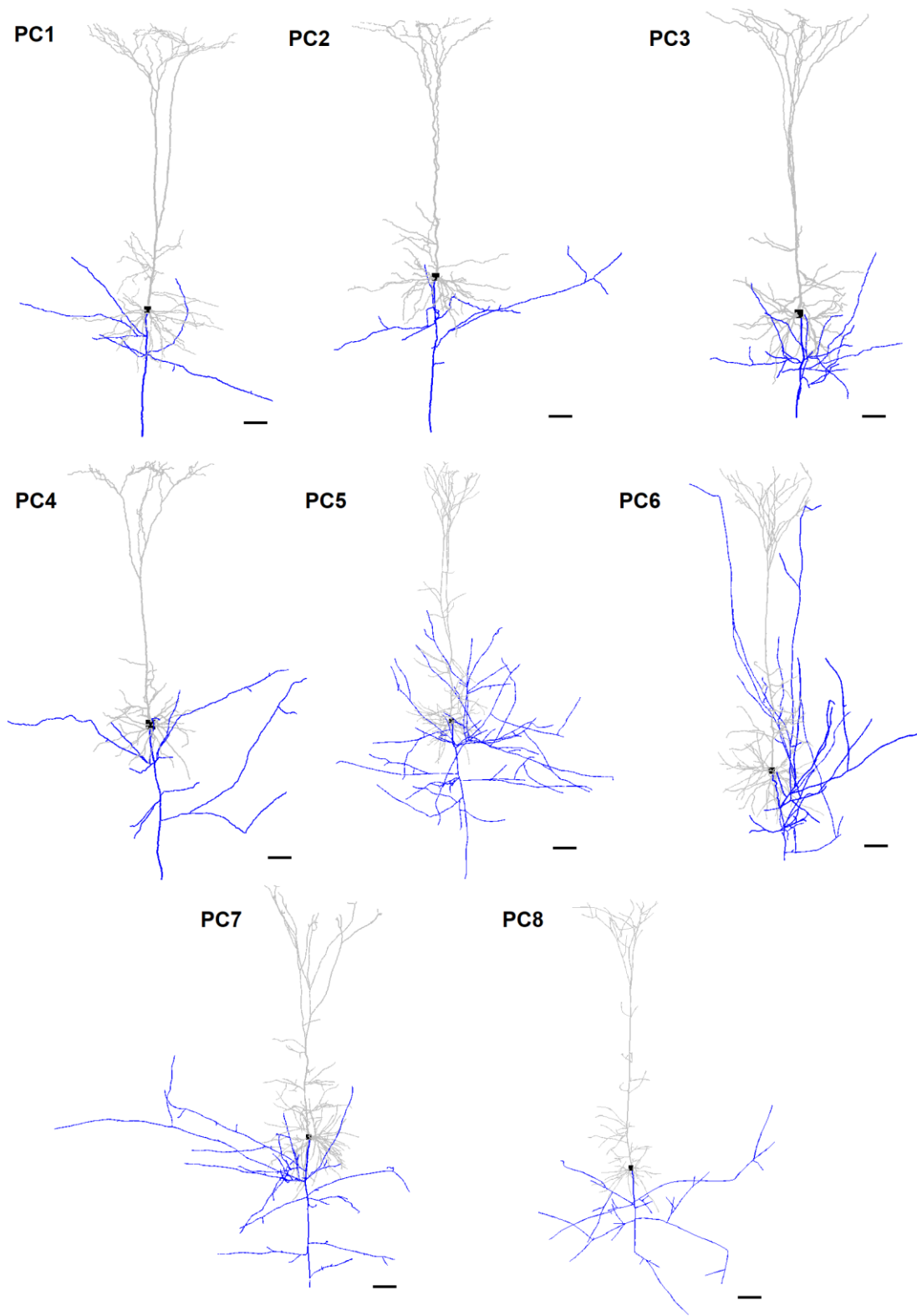


Figure 5.2. Investigated PC model neurons (PC1-PC8). Dendrites in gray, soma in black, and axons in blue. Scale bars represent 100 μm .

Die approbierte gedruckte Originalversion dieser Dissertation ist an der TU Wien Bibliothek verfügbar.
The approved original version of this doctoral thesis is available in print at TU Wien Bibliothek.

5.2 Biophysical properties

5.2.1 PC

PCs were modeled based on a previous study (Almog and Korngreen, 2014), which recorded the membrane voltage from soma and dendrites of cortical neurons L5 of rat somatosensory region. Applying a pharmacological peeling method and a genetic algorithm, their model could predict many mechanisms known in pyramidal cells, such as AP (back)propagation and generation of the dendritic spike. This thesis uses the exact mechanisms for ionic channels and the conductivity values from cell 5 in the original study (Table 5.1). Following mechanisms and channels are used in the PC model.

Intracellular $[Ca^{2+}]_i$

The intracellular Ca^{2+} is simulated based on (Destexhe et al., 1993).

$$[Ca]_i = -\left(\frac{I_{Ca}}{2Fd}\right) + \frac{[Ca^{2+}]_{rest} - [Ca^{2+}]_i}{\tau} \quad (5.1)$$

With $[Ca^{2+}]_i$ in millimoles and the unit conversion of $k = 10000$ for I_{Ca} ($\mu A/cm^2$), $F = 96489$ C/mol being the Faraday constant, $d = 0.1 \mu m$ being the depth of the shell under the membrane, $[Ca^{2+}]_{rest} = 10^{-5}$ mM is the intracellular calcium concentration at rest and $\tau = 80$ ms is the rate of calcium removal adapted for cortical neurons from (Schaefer et al., 2003)

Na^+ channel

The sodium channel were modeled using HH-type model and based on recordings from nucleated patches from L5 neocortical pyramidal neurons (Keren et al., 2005).

$$g_{Na} = \bar{g}_{Na} m^3 h \quad (5.2)$$

$$m_{\infty} = \frac{1}{1 + \exp\left(-\frac{(V_m + 38)}{10}\right)} \quad \tau_m = 0.058 + 0.114 \exp\left(-\left(\frac{V_m + 36}{28}\right)^2\right) \quad (5.3)$$

$$h_{\infty} = \frac{1}{1 + \exp\left(\frac{(V_m + 66)}{6}\right)} \quad \tau_m = 0.28 + 16.7 \exp\left(-\left(\frac{V_m + 60}{25}\right)^2\right) \quad (5.4)$$

Fast inactivating K^+ channel

Both slow and fast inactivating K^+ channels were based on nucleated patch recordings from (Almog and Korngreen, 2009).

$$g_{Kf} = \bar{g}_{Kf} a^4 b \quad (5.5)$$

$$a_\infty = \frac{1}{1 + \exp\left(-\frac{(V_m + 47)}{29}\right)} \quad \tau_a = 0.34 + 0.92 \exp\left(-((V_m + 71)/59)^2\right) \quad (5.6)$$

$$b_\infty = \frac{1}{1 + \exp\left(\frac{(V_m + 66)}{10}\right)} \quad \tau_b = 8 + 49 \exp(-((V_m + 73)/23)^2) \quad (5.7)$$

Slow inactivating K^+ channel

$$g_{Ks} = \bar{g}_{Ks} r^2 (0.5S_1 + 0.5S_2) \quad (5.8)$$

$$\alpha_r = \frac{0.0052(V_m - 11.1)}{1 - \exp\left(-\frac{(V_m - 11.1)}{13.1}\right)} \quad \beta_r = 0.02 \exp\left(-\frac{(V_m + 1.27)}{71}\right) - 0.005 \quad (5.9)$$

$$r_\infty = \frac{\alpha_r}{(\alpha_r + \beta_r)} \quad \tau_r = \frac{1}{(\alpha_r + \beta_r)} \quad (5.10)$$

$$S_{1\infty} = S_{2\infty} = \frac{1}{1 + \exp\left(\frac{(V_m + 58)}{11}\right)} \quad (5.11)$$

$$\tau_{S_1} = 360 + (1010 + 23.7(V_m + 54)) \exp\left(-\left(\frac{(V_m + 75)}{48}\right)^2\right) \quad (5.12)$$

$$\tau_{S_2} = 2350 + 1380 \exp(-0.011V_m) - 210 \exp(-0.03V_m) \quad (5.13)$$

Hyperpolarization-activated cation current (I_h) channel

The hyperpolarization activated cation channel was modeled based on cell attached somatic and dendritic recordings from (Williams and Stuart, 2000; Berger et al., 2001).

$$g_{Ih} = \bar{g}_{Ih} O \quad (5.14)$$

$$O_{\infty} = \frac{1}{1 + \exp\left(\frac{(V_m + 91)}{6}\right)} \quad \tau_o = \frac{1}{(0.0004 \exp(-0.025V_m) + 0.088 \exp(0.062V_m))} \quad (5.15)$$

High voltage activated (HVA) Ca^{2+} channel

Both HVA and medium voltage activated (MVA) channels were modeled based on nucleated patches (Almog and Korngreen, 2009) and the whole-cell recording experiments (Foehring et al., 2000; Magistretti et al., 2000) with the equations based on the Goldman-Hodgkin-Katz equation.

$$P_{CaHVA} = \bar{P}_{CaHVA} \alpha_{\infty}^2 \beta_{\infty} \quad (5.16)$$

$$\alpha_{\infty} = \frac{1.1}{(1 + \exp(-\frac{(V_m + 14)}{10}))} \quad \tau_{\alpha} = \frac{0.97}{\cosh(0.032(V_m + 26))} \quad (5.17)$$

$$\beta_{\infty} = \frac{0.75}{(1 + \exp(\frac{(V_m + 23)}{7}))} \quad \tau_{\beta} = \frac{70}{\cosh(0.047(V_m - 20))} \quad (5.18)$$

Medium voltage activated (MVA) Ca^{2+} channel

$$P_{CaMVA} = \bar{P}_{CaMVA} \alpha_{\infty}^2 \beta_{\infty} \quad (5.19)$$

$$\alpha_{\infty} = \frac{1}{(1 + \exp(-\frac{(V_m + 23)}{7}))} \quad \tau_{\alpha} = \frac{5.5}{\cosh(0.032(V_m + 23))} \quad (5.20)$$

$$\beta_{\infty} = \frac{1}{(1 + \exp(\frac{(V_m + 79)}{8}))} \quad \tau_{\beta} = \frac{771}{\cosh(0.047(V_m + 79))} \quad (5.21)$$

Small conductance Ca^{2+} gated K^+ (K_{SK}) channel

Both calcium gated potassium channel kinetics were based on whole-cell recordings from experimental studies (Khaliq et al., 2003; Sun et al., 2003; Akemann and Knöpfel, 2006; Mercer et al., 2007; Deister et al., 2009).

$$G_{SK} = \bar{G}_{SK} \alpha_{\infty} \quad (5.21)$$

$$\alpha_{\infty} = \frac{1.3^4 [Ca^{2+}]_i^4}{(1.3^4 [Ca^{2+}]_i^4 + 0.06)} \quad \tau_{\alpha} = \frac{1}{(1.3^4 [Ca^{2+}]_i^4 + 0.06)} \quad (5.22)$$

Large conductance Ca^{2+} gated K^+ (K_{BK}) channel

$$G_{BK} = \bar{G}_{BK} \alpha_{\infty}^3 \gamma^2 \beta_{\infty} \quad (5.23)$$

$$\alpha_{\infty} = \frac{1}{(1 + \exp(-\frac{(V_m + 29)}{6.2}))} \quad \tau_{\alpha} = \frac{1000.505}{(\exp(-\frac{(V_m + 86)}{-10}))} \quad (5.24)$$

$$\gamma_{\infty} = \frac{1}{(1 + \frac{0.001}{[Ca^{2+}]_i})} \quad \tau_{\gamma} = 1 \quad (5.25)$$

$$\beta_{\infty} = \frac{0.085 + (1 - 0.085)}{(1 + \exp(-\frac{(V_m + 32)}{-6}))} \quad \tau_{\beta} = \frac{1001.9}{\exp(-\frac{(V_m + 49)}{13})} \quad (5.26)$$

The axon model was adapted from (Mainen and Sejnowski, 1996). The same gating kinetics as in Equations (5.2-5.13) were applied for the sodium, slow, and fast inactivating K^+ channels. Table 5.1 shows all maximum conductivities used in the axon, soma, and dendrites in PCs, which are constant. Additionally, the apical values can be calculated through exponential equations as explained in the table caption and can be found in the original study by (Almog and Korngreen, 2014). The model temperature was set to 34 °C.

Biophysical properties

Param.	Unit	Soma	Dendrite	AXON				
				Hill	AIS	Non-my	NoR	IN
ρ_i	k Ω .cm	0.12	0.12	0.12	0.12	0.12	0.12	0.12
C_m	$\mu\text{F}/\text{cm}^2$	0.6	0.6	0.6	0.6	0.6	0.6	0.04
g_{pas}	$\text{pS}/\mu\text{m}^2$	0.39	0.39	0.39	0.39	0.39	0.02	0.39
g_{Na}	$\text{pS}/\mu\text{m}^2$	352	56	6000	30000	1000	30000	352
Na_{dist}	μm	-	481	-	-	-	-	-
$g_{k,slow}$	$\text{pS}/\mu\text{m}^2$	206	3.79	1500	1500	206	1500	206
$K_{slow,slope}$	$1/\mu\text{m}$	-	-0.092	-	-	-	-	-
$g_{k,fast}$	$\text{pS}/\mu\text{m}^2$	332	28	1000	1000	332	1000	332
$K_{fast,slope}$	$1/\mu\text{m}$	-	-0.012					
g_{iH}	$\text{pS}/\mu\text{m}^2$	2.51	118					
$I_{h,x1/2}$	μm	-	352					
$I_{h,slope}$	$1/\mu\text{m}$	-	-0.014					
p_{HVA}	$\mu\text{m}/\text{s}$	0.93	1.56					
$Ca_{HVA,dist}$	μm	-	10					
p_{MVA}	$\mu\text{m}/\text{s}$	31.5	4.9					
$Ca_{MVA,dist}$	μm	-	925					
g_{bk}	$\text{pS}/\mu\text{m}^2$	0.64	1.23					
BK_{dist}	μm	-	28					
g_{sk}	$\text{pS}/\mu\text{m}^2$	3.18	0.52					
SK_{dist}	μm	-	239					

None

Table 5.1. Parameter values were obtained from (Almog and Korngreen, 2014). ρ_i , C_m , and g_{pas} represent the intracellular conductivity, the specific membrane capacitance, and passive conductivity, respectively. The distance parameter is the dendritic pipette distance to the soma. The apical dendrite conductance gradient was calculated using exponential gradients that use the somatic and dendritic values:

$$G_{Ih}(x) = G_{Ih,soma} + \frac{G_{Ih,dend}}{\left(1 + \exp\left(I_{h,slope}(x - I_{h,x1/2})\right)\right)}$$

where the x stands for the distance between soma and dendritic pipette.

$$G_{Ks}(x) = G_{Ks,dend} + G_{Ks,soma}(\exp(K_{slow,slope} \cdot x))$$

The same equation was used to calculate the $G_{Kf}(x)$.

$$G_{Na}(x) = G_{Na,soma} + x \frac{(G_{Na,dend} - G_{Na,soma})}{Na_{dist}}$$

The same formula was used to calculate the apical permeability gradient of Ca_{HVA} and Ca_{MVA} .

5.2.2 RGC

Biophysical properties in RGCs are based on (Fohlmeister et al., 2010; Werginz et al., 2020) similar to the rat type II model in Fohlmeister et al., 2010, which has the same ion channels and kinetic equations as the cat beta model (see section 4.1). The maximum conductivities, however, are different between the two models. Table 5.2 shows all conductivities used in the RGC model neurons. The leak conductivity, intracellular resistivity, and specific membrane capacitance were set to 2.5 pS/ μm^2 , 143 $\Omega\cdot\text{cm}$, and 1 $\mu\text{F}/\text{cm}^2$, respectively. The model temperature was set to 33 $^{\circ}\text{C}$.

	Unit	SOMA	DEND	AXON		
				Hill	AIS	Non-my
gNa1.2	pS/ μm^2	650	650	1625	0	1000
gNa1.6	pS/ μm^2	0	0	0	1625	0
gK1.2	pS/ μm^2	350	350	625	0	700
gK1.6	pS/ μm^2	0	0	0	625	0
gCa	pS/ μm^2	15	15	15	15	15
gK,Ca	pS/ μm^2	1.5	1.5	1.5	1.5	1.5

Table 5.2. Maximum conductivities in RGC models based on data from (Fohlmeister et al., 2010; Werginz et al., 2020).

5.3 PC model validation

PCs receive thousands of synaptic inputs from numerous cells, integrate them into dendrites and soma to create outputs in the shape of APs that reach the axonal end and travel to the next processing units. Active and passive properties of dendrites generate these synaptic inputs. Therefore several functions, such as AP backpropagation from the soma into the dendritic tree (Stuart and Sakmann, 1994), as well as complex regenerative Ca^{2+} , and Na^+ spike generated by dendrites (Schiller et al., 1997; Magee, 1999; Martina et al., 2000; Migliore and Shepherd, 2002; Johnston, 2003), are crucial in the simulated cells to mimic the real cell functions. We examined some of these baseline properties, such as backpropagation of the AP through the dendritic arborization and generation of Ca^{2+} spikes in the reconstructed investigated PCs (n=8).

Figure 5.3 shows these evaluations in one of the neuron models (PC1). In the first experiment (Figure 5.3B), an EPSP-like current ($I_{max}=1.6$ nA) was injected into one of the apical branches indicated by the red cross. The membrane voltage at five positions along the cell showed subthreshold fluctuations. In the next step (Figure 5.3C), a rectangular (monophasic) anodic pulse ($I=0.6$ nA) was injected into the soma. The V_m traces show an AP that is first generated in the soma and backpropagated into the dendritic tree. Finally, the combination of the two pulses with a decrease of 25% of the current amplitude is injected into the cell. Figure 5.3D shows the Na^+ spike is generated first in the soma and (back)propagated to the axon and proximal dendrite. In contrast, the apical dendrite generated a Ca^{2+} spike.

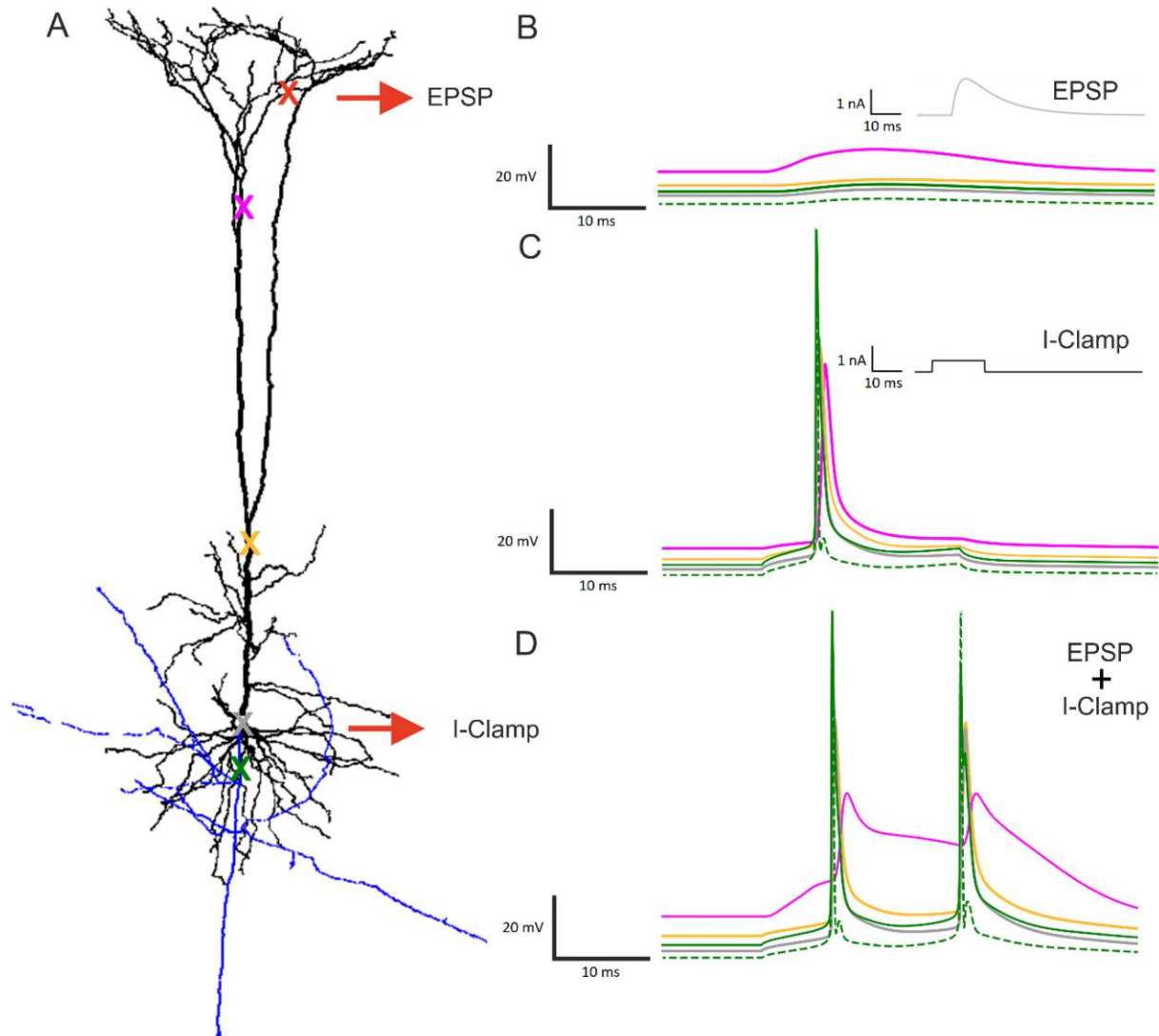


Figure 5.3. Reproducing backpropagation activated Ca^{2+} spikes. **(A)** Reconstruction of an L5 pyramidal neuron model (PC1). **(B)** Membrane voltage responses of an EPSP-like current with a maximum current of 1.6 nA (rising =2 ms, declining =10 ms) injected through the apical branch indicated by the red cross and red arrow. Membrane voltage responses over time **(B-D)** are indicated with the same colors as shown with crosses in on the shape plot neuron in **(A)**: pink=distal apic, orange=proximal apic, gray=soma, green = AIS. (i) The AIS is shown by a solid line, (ii) the first node of Ranvier by the dashed line. **(C)** Membrane voltage in response to an injection of a rectangular current of 0.6 nA through the soma depicted by the gray cross and red arrow. The action potential generated at the soma backpropagated along the apical dendrite. Color-coded as **(B)**. **(D)** Responses to the combination of the two stimuli with a 25% decrease, used in **(B)** and **(C)**. A backpropagation activated Ca^{2+} spike is generated at the distal apical dendrite.

5.4 Soma impact on thresholds

In the next step, the contribution of soma in the excitation and blockage of the cells was investigated. Therefore, the soma was modeled either as a single sphere or divided into 41 truncated cones with the axis orientated toward the electrode to study the electric field gradient along the somatic membrane. Figure 5.4A shows the activating function (Rattay, 1999) for both soma configurations of a RGC model neuron in response to a monophasic cathodic stimulus with an amplitude of 1 μA . For stimulating the soma with cathodic pulses, the transmembrane voltage was depolarized at the compartments in the hemisphere close to the electrode (red area). The compartments from the opposite side were hyperpolarized (blue).

In contrast, the membrane voltage changes were significantly small during the stimulus in the single compartment configuration, and the AF was close to zero (white). Small AF, in single compartment soma, resulted from a poor reflection of the extracellular gradient in the somatic transmembrane voltage.

Figure 5.4B-C demonstrates the computed LTs ('o') and UTs ('+') for PC (n=8) and RGC (n=34) model neurons using a point source approach. Thresholds were evaluated for electrode distances of 15, 30, 45, 60, 100, and 200 μm to the soma center for the single vs. multi-compartment soma configurations in pink and blue. The LTs and UTs increased slightly by increasing the electrode distance in both cell types. Computed LTs are in the same ranges in RGCs and PCs for all distances; for instance, in the smallest distance of 15 μm , both cells had mean LT $\sim 1 \mu\text{A}$.

On the other hand, Both cells showed substantial differences in UTs, with PCs having significantly higher UTs by almost ten-fold larger values. For example, at the smallest and largest distance of 15 and 200 μm , the mean UT in PCs were 100 μA and 10 mA, respectively, whereas in RGC, for sliced soma, UT means were 15 μA and 1 mA, respectively.

In addition, no significant difference between two soma configurations was observed either in LT or in UT in PC stimulation. In contrast, in RGCs, LTs in the sliced soma were significantly lower than the single-compartment model (p-value < 0.001) in the three shortest electrode distances (15-45 μm). Furthermore, a significant difference (p-value < 0.05) was observed between two soma configurations at 60 μm electrode distance.

On the other hand, in UTs, significant differences between different soma configurations were only observed in the two shortest electrode distances (p-value < 0.001) in RGCs. Observation of significant differences resulted from a high contribution of soma in RGC excitations, which only occurred when the electrode was located close to the soma surface. In comparison, the

results implied a negligible soma contribution in PCs for both threshold values even at electrode locations close to the soma.

In the next step of the analysis, threshold ratios (UT/LT) were calculated and demonstrated for multi and single compartment soma for both groups of the cells in blue and pink, respectively (Figure 5.4D-E). In PCs, for electrode distances up to 60 μm , an ascending trend was observed. However, in larger electrode distances, the threshold ratios decreased. No significant difference was found in ratios between both soma configurations at any investigated electrode distance. In RGCs, the threshold ratios increased monotonically with increasing electrode distance. A significant difference (p -value < 0.001) was observed only for the closest electrode distances for multi- vs. single compartment soma. Moreover, we found that the threshold ratios were noticeably higher (by magnitude up to 10 fold) in PCs, which resulted from significantly higher UTs.

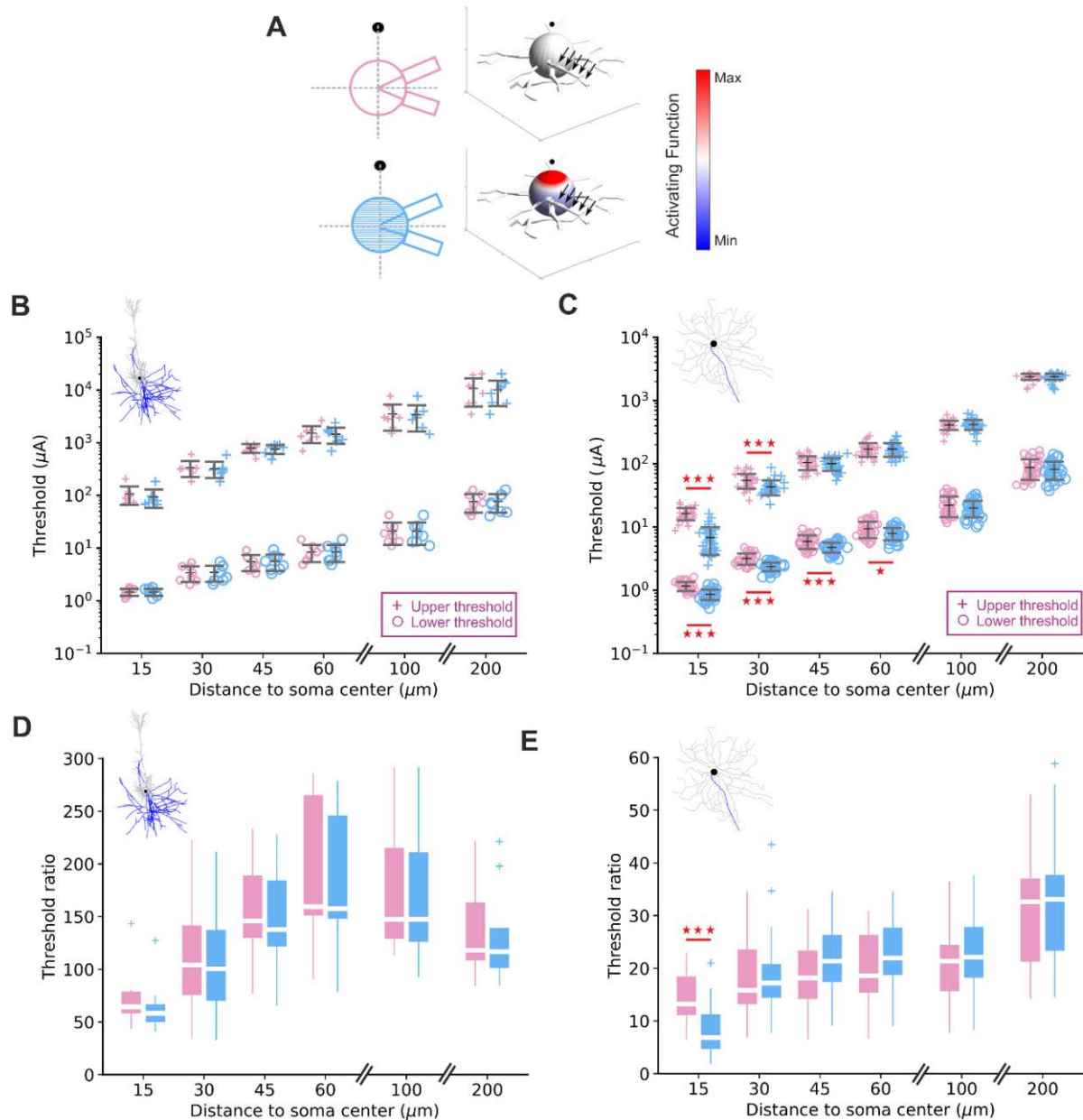


Figure 5.4. The lower and upper thresholds in RGC and PC models – **(A)** The soma was once modeled as a single spherical compartment (top, pink) and once as a sliced sphere containing 41 truncated cones (bottom, blue). Activating function (AF) has been shown for both soma configurations (for one model RGC) in a color-coded manner for each compartment in reaction to a $1 \mu\text{A}$ cathodic pulse. Note that one compartment soma has a small AF (appeared white). The electrode position is displayed with black circles, and black arrows indicate the axon. **(B)** For both soma structures, the Lower ('o') and upper ('+') thresholds were computed at increasing electrode distances for 8 PC model neurons and shown in pink and blue for single and multi-compartment soma, respectively. **(C)** Same as **(B)** for 34 RGC model neurons. **(D)** The upper and lower threshold ratios were computed for PCs in both soma configurations with the same color code. **(E)** Same as **(D)** for RGC model neurons. In **(B-D)**, the electrode was

positioned above the soma with electrode distance to the soma center ranging from 15 to 200 μm . Significant differences in (C) and (E) are shown with three, two, and one star for p-values less than 0.001, 0.01, and 0.05, respectively. Figure adapted from (Sajedi et al., 2021).

For the next step, the correlation between threshold and geometric features of both groups of cells was studied. Table 5.3 shows the r^2 values at each electrode distance for a single feature, namely: the lengths of AIS, non-myelinated axon, total axon, and dendrite as well as the areas of the axon and dendrite for PCs; The soma diameter, hillock, and AIS length, as well as dendritic field, length, and areas in RGCs. No correlation between thresholds and the investigated anatomical feature was found, except in PCs for dendrite area and LTs (Figure 5.5).

Moreover, as previously observed, we found some correlations between AIS length and LT, UT, and UT/LT only for small electrode distances (Jeng et al., 2011; Werginz et al., 2020). However, the overall result of this section demonstrated that single morphological parameters did not determine the thresholds and threshold ratios, and they incorporated multiple parameters such as geometry, biophysics, axonal arrangement, and electrode location.

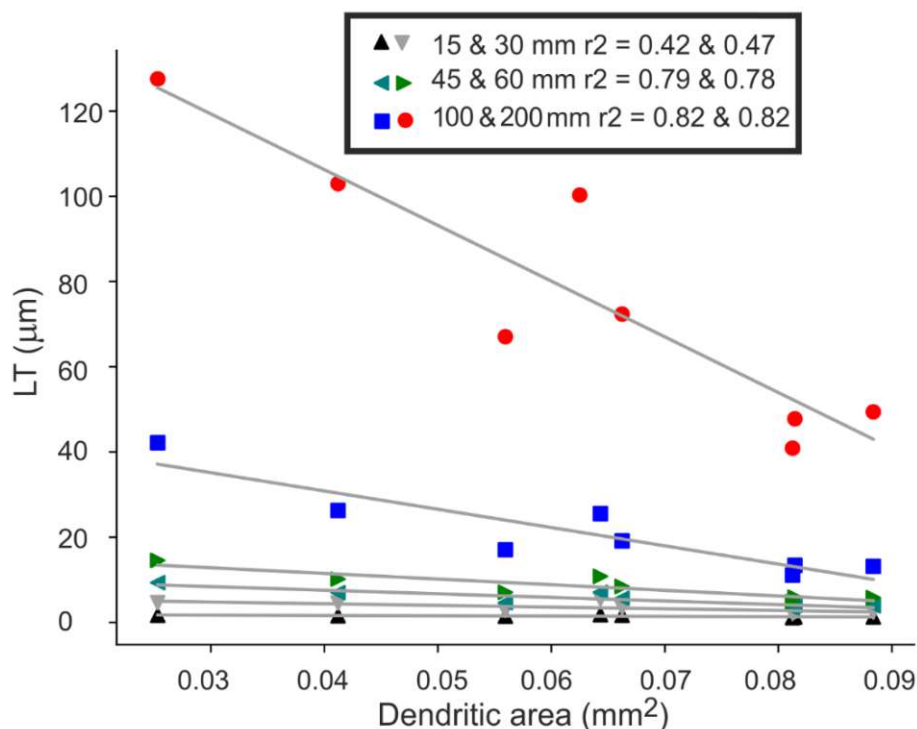


Figure 5.5. Lower threshold (LT) in PC models vs. dendrite diameter. LT values have been shown for each PC model in the investigated electrode distances. In larger electrode distance ($>45 \mu\text{m}$), LT decreases with increasing dendritic area. The goodness of linear fit was almost high for the last

Soma impact on thresholds

four investigated distances ($>45 \mu\text{m}$), and the highest slop occurred for the largest electrode distance of $200 \mu\text{m}$ (red circles) with $r^2=0.82$.

Distance to soma center (μm)	15	30	45	60	100	200
AIS_len_LT	0.21	0.33	0.29	0.30	0.30	0.38
AIS_len_UT	0.34	0.05	0.00	0.00	0.03	0.12
AIS_len_ratio	0.16	0.01	0.29	0.37	0.18	0.04
Non-my._len_LT	0.01	0.01	0.05	0.07	0.11	0.06
Non-my._len_UT	0.04	0.04	0.08	0.00	0.00	0.04
Non-my._len_ratio	0.04	0.02	0.02	0.00	0.01	0.04
Axon_len_LT	0.21	0.29	0.16	0.13	0.10	0.26
Axon_len_UT	0.28	0.10	0.31	0.44	0.55	0.46
Axon_len_ratio	0.09	0.01	0.04	0.00	0.17	0.08
Axon_area_LT	0.04	0.00	0.00	0.01	0.02	0.00
Axon_area_UT	0.64	0.46	0.22	0.08	0.06	0.01
Axon_area_ratio	0.44	0.14	0.02	0.01	0.04	0.00
Dend._len_LT	0.17	0.05	0.36	0.39	0.45	0.28
Dend._len_UT	0.02	0.00	0.23	0.09	0.00	0.03
Dend._len_ratio	0.06	0.04	0.44	0.39	0.18	0.04
Dend._area_LT	0.42	0.47	0.79	0.78	0.82	0.82
Dend._area_UT	0.03	0.01	0.00	0.03	0.33	0.39
Dend._area_ratio	0.00	0.14	0.61	0.33	0.03	0.01
Soma_diam_LT	0.02	0.13	0.03	0.01	0.01	0.03
Soma_diam_UT	0.67	0.09	0.00	0.01	0.01	0.00
Soma_diam_ratio	0.43	0.0	0.01	0.00	0.02	0.07
Hill._len_LT	0.06	0.23	0.20	0.18	0.23	0.36

AP initiation sites

Hill_len_UT	0.09	0.00	0.04	0.01	0.05	0.02
Hill_len_ratio	0.03	0.05	0.15	0.05	0.10	0.21
AIS_len_LT	0.28	0.19	0.28	0.28	0.27	0.15
AIS_len_UT	0.26	0.38	0.12	0.03	0.01	0.08
AIS_len_ratio	0.37	0.39	0.25	0.24	0.21	0.13
Dend_field_LT	0.00	0.04	0.00	0.00	0.00	0.00
Dend_field_UT	0.37	0.03	0.03	0.02	0.02	0.00
Dend_field_ratio	0.27	0.00	0.02	0.01	0.00	0.00
Dend_len_LT	0.02	0.00	0.04	0.07	0.09	0.05
Dend_len_UT	0.20	0.15	0.00	0.03	0.05	0.00
Dend_len_ratio	0.18	0.11	0.01	0.00	0.02	0.03
Dend_area_LT	0.01	0.00	0.02	0.04	0.06	0.03
Dend_area_UT	0.23	0.15	0.00	0.00	0.02	0.00
Dend_area_ratio	0.19	0.08	0.01	0.01	0.01	0.01

Table 5.3. r^2 values for correlations between multiple geometric parameters and LT, UT, as well as threshold ratio (UT/LT). Top section: PCs, bottom section: RGCs. r^2 values larger than 0.5 are indicated in red. AIS=Axon Initial Segment; Non-my (non-myelinated axon); Hill=hillock.

5.5 AP initiation sites

Subsequently, AP initiation sites in both cell groups were computed and analyzed using a monophasic cathodic pulse for the closest electrode position to the soma (15 μm) incorporating multi-compartment soma (41 compartments). The spike initiation site (SSI) was considered as the first compartment with membrane voltage crossing the 0 V. Figure 5.6A and Figure 5.6C shows the membrane voltage over time for somatic compartments (salmon), AIS (purple), and axon (light blue). A schematic illustration of the cells is displayed on top.

Taking the AF into account, the somatic compartments in the hemisphere close to the electrode are depolarized (blue arrow) during the pulse (red square). In contrast, compartments in the other hemisphere were hyperpolarized (red arrow). However, despite high depolarization in the upper somatic hemisphere, the AP always initiated at the AIS because of the high sodium

channel density, as previously reported for PC and RGC stimulations (Rattay and Wenger, 2010; Werginz et al., 2014).

The SSIs are shown vs. the distance between the end of AIS to soma border (AIS length + hillock length) in Figure 5.6B and Figure 5.6D for the investigated electrode distances of 15, 30, 45, 60, 100, and 200 μm . Regardless of electrode distance, the AP was again initiated within the AIS. The black curve indicates the best logistic regression fit with a high goodness of fit of 0.91 and 0.74 for PCs and RGCs, respectively.

Overall, the results of this experiment indicated that APs always initiated at the AIS distal end except for cells with longer AIS in which the SSI was shifted toward the center of AIS.

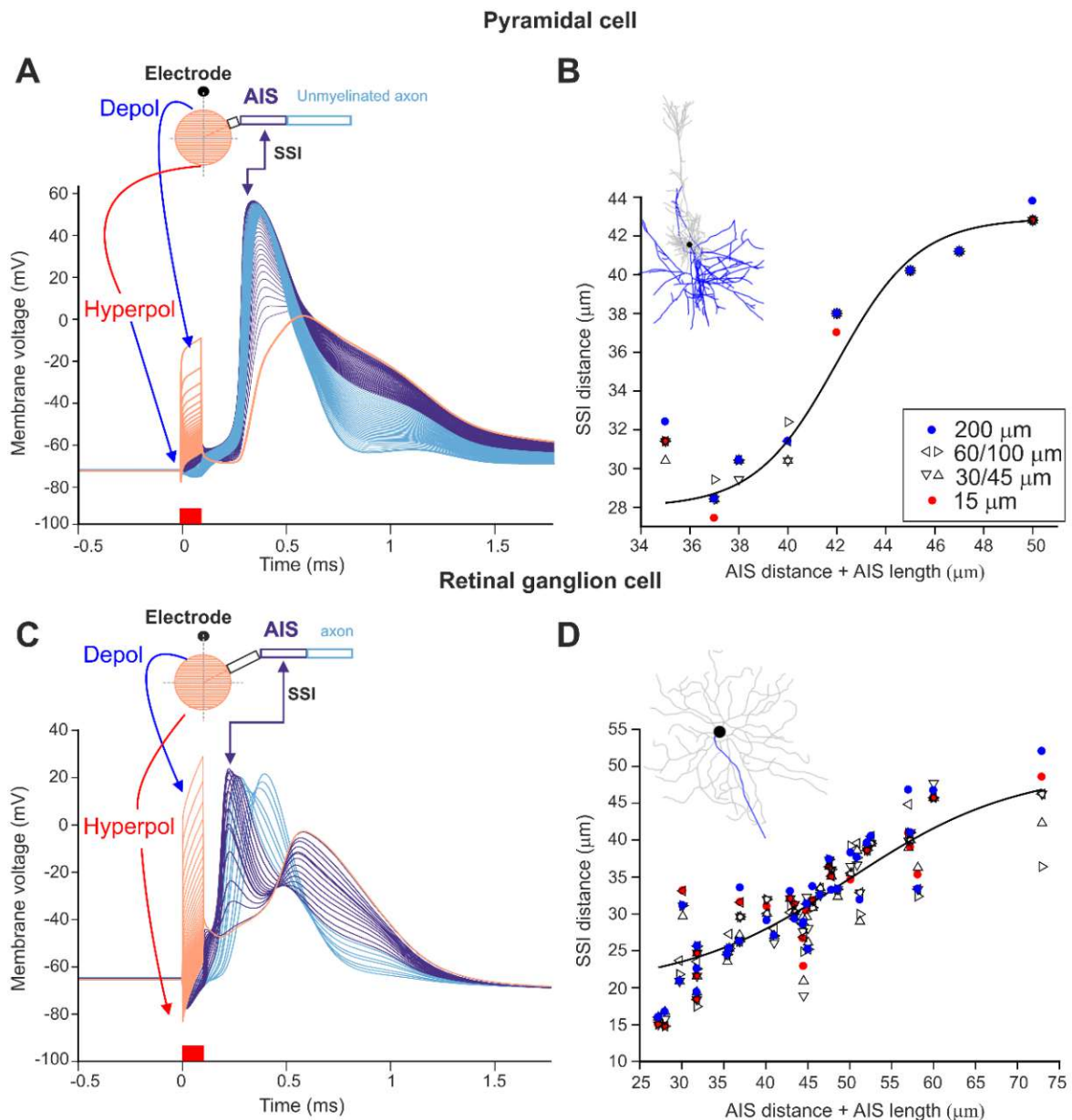


Figure 5.6. AIS is the AP initiation site in RGCs and PCs. **(A)** Descriptive response of a PC model neuron to stimulation 15 μm above the soma. Membrane voltage of 41 soma compartments (thick salmon lines), as well as AIS (purple) and non-myelinated compartments (light blue), is plotted over time. The purple kinked arrow indicates the approximate site of spike initiation (SSI). The blue and red arrows show the location of soma compartments which are de- and hyperpolarized most strongly. Stimulus duration (0.1 ms, cathodic) is shown at the bottom, in red. **(B)** For each PC model neuron ($n=8$), the distance between the soma and the site of spike initiation is plotted versus the distance between the soma border and the distal end of the AIS (i.e., AIS length + hill length). Electrode to soma distance ranged from 15-200 μm . The black curve indicates the best-fit logistic regression ($r^2=0.91$). **(C)** Same as **(A)** for a RGC model neuron. AIS compartments are purple, and the axon is light blue. **(D)** Same as **(B)** for 34 RGC model neurons. The black curve indicates the best-fit logistic regression ($r^2=0.74$). Figure adapted from (Sajedi et al., 2021).

5.6 Partial upper threshold in PCs

AP detection sites were set to the distal axon in RGC as the only output pathway, whereas, for PCs with a complex axon geometry and numerous axon collaterals, there were various possibilities to set a site for detecting the excitability status. Therefore, the AP detection site was considered at the first node of Ranvier, located at the end of the myelinated axon where the bifurcations started. This point was approximately 100-150 μm away from the soma in PCs.

However, during the UT detection experiment in PCs, we observed that the AP stopped being generated at parts of the cell such as dendrite, soma, proximal axon, and some axon collateral, whereas other parts of the axons were still actively propagating AP. Figure 5.7A-D demonstrates the cell excitability status for one PC model neuron (PC7) as an example during various stimulus amplitudes: at LT, 50% UT, UT, and 150% UT.

At LT (Figure 5.7A), the spike initiated at AIS and (back) propagated to most parts of the cell except some basal terminals (gray) and also very distal apical branches (not shown). Setting the pulse amplitude to 50% of the UT (Figure 5.7B), the AP initiated at the axon and did not propagate back to the soma and dendrites (somatic blockage). Figure 5.7C shows the cell excitability at UT, where most parts were blocked, yet some axonal branches were spiking. The strong hyperpolarization during the stimulus can be observed in black curves representing the membrane voltage over time for the areas indicated with a cross. However, by increasing the amplitude up to 150% UT, the AP was still generated in two branches, while other cell parts were blocked or not excited at all (Figure 5.7D).

The partial spiking in PCs was additionally investigated in the axon collaterals for all model neurons by calculating the percentage of the spiking nodes for strong amplitudes increasing from LT up to 700LT. The result of this investigation is demonstrated in Figure 5.8. Following the smallest distance (solid blue curve), the node percentage reduced drastically at 50LT, and the mean values dropped down to $\sim 40\%$ of nodes at 100LT. For the higher distances, though, the spiking percentage decreased gradually to about 25%, where it plateaued at stimulus > 500 LT. However, a total block was not possible in PCs for the investigated distances, and the AP blockage was mostly observed for the regions with strong hyperpolarization due to the strong stimulus. We believe the partial blocking resulted from an inhomogeneous reflection of electric field on the axonal membrane voltage that is branched in various directions and resulted in an inhomogeneous driving force or activating function.

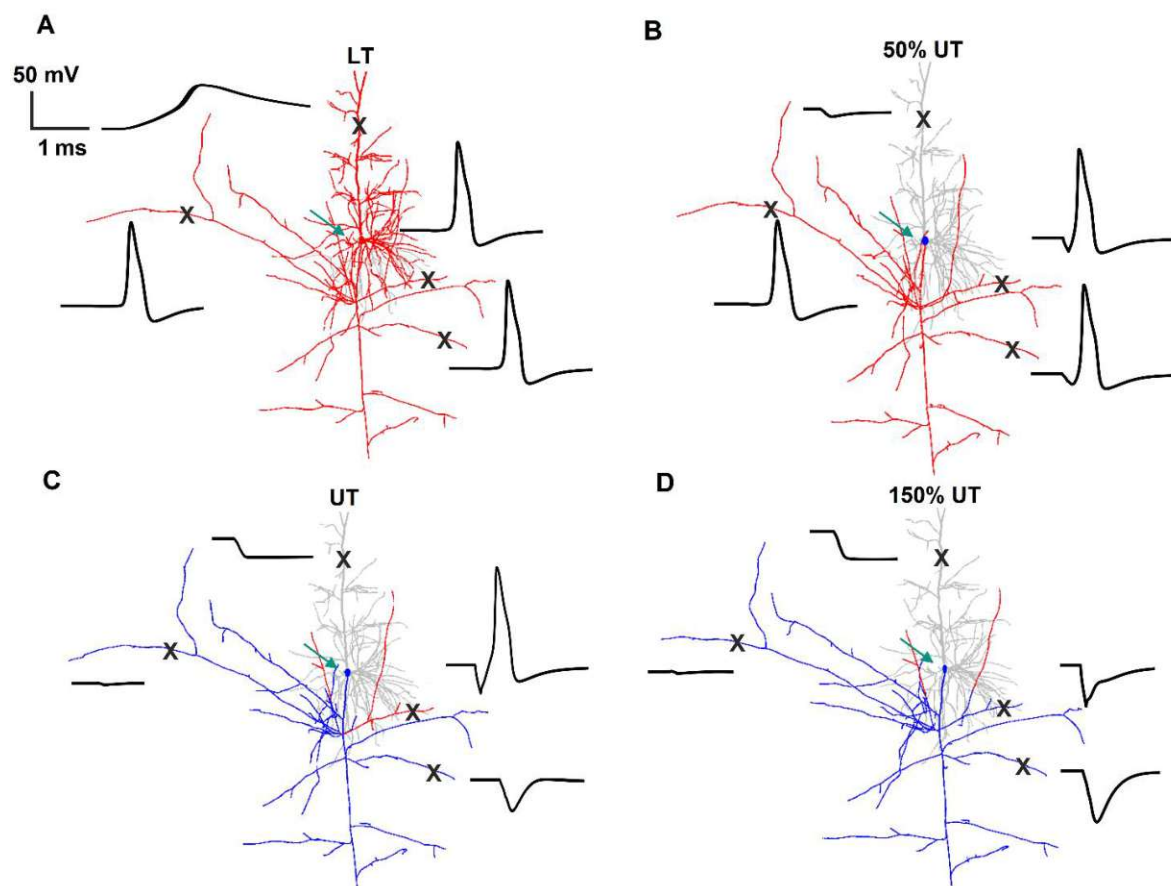


Figure 5.7. PC excitation during various amplitude. **(A)** At LT stimulation: Neuron shape plot representing neural portions generated an AP (red) and not excited portions (gray). The membrane voltage over time (black) is shown for four locations indicated by ('X'). **(B-D)** Similar layout as **(A)** for amplitudes of **(B)** 50% UT, **(C)** UT, and **(D)** 150% UT, respectively. Regions with an AP are red, regions without an AP, gray (dendrites), or blue (axon and soma). Green arrows indicate the electrode location of 15 μm . Figure adapted from (Sajedi et al., 2021)

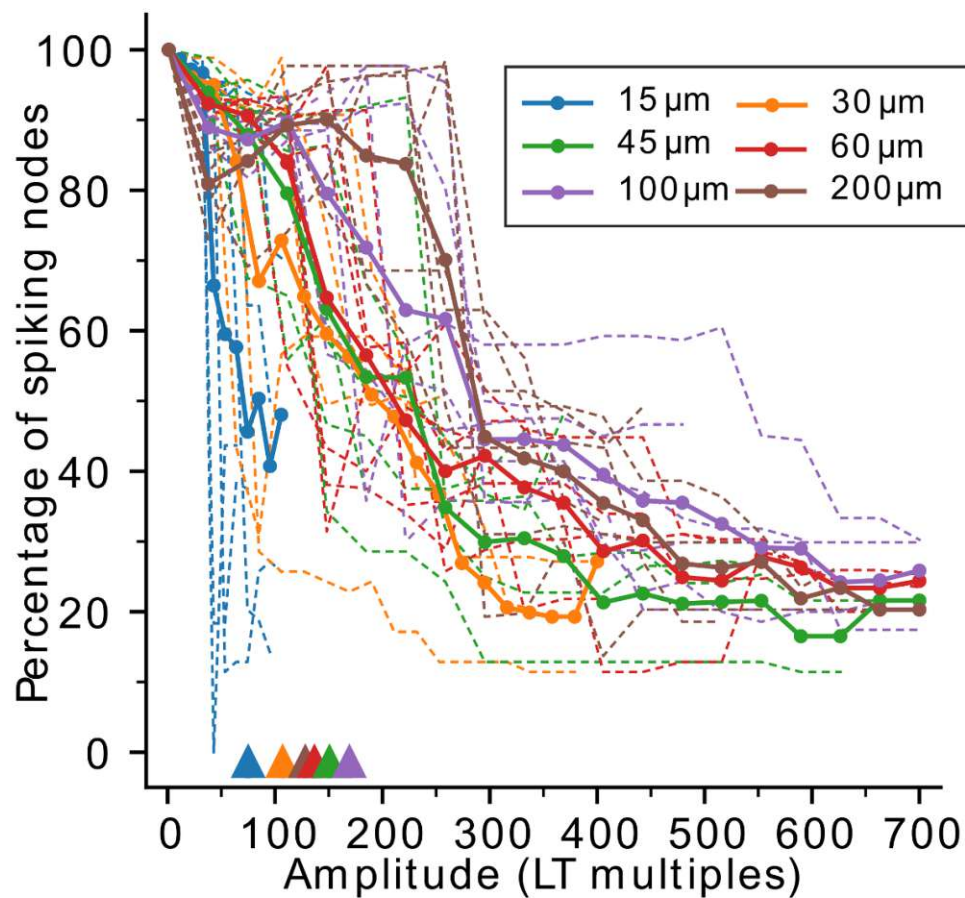


Figure 5.8. Spiking nodes percentage. The spiking percentage of nodes of Ranvier is plotted against stimulus amplitude (in multiples of LT) for the investigated electrode distances. Dashed lines indicate the spiking node percentage for single-cell, thick lines indicate population means. Triangles indicate mean thresholds ratios for different electrode distances. Figure adapted from (Sajedi et al., 2021).

5.7 Impact of stimulus parameters on threshold

5.7.1 PCs

Selective stimulation of a specific group of cortical neurons with microelectrodes is challenging, and the exact location cannot be obtained during surgery; the inserted array is therefore placed randomly relative to soma positions. In this experiment, the effect of various electrode positioning around the PC soma on the thresholds is investigated for six-point source locations (Figure 5.9A, circles) with an equal distance of $15\ \mu\text{m}$ to the soma center. Figure 5.9B demonstrates the LTs and UTs for each model PC. An outlier in every cell for an electrode position causes significantly smaller thresholds. For more details, thresholds were evaluated

for the electrode distance to the hillock or soma border. The analysis showed that the outliers were related to the hillock's closest positions, as demonstrated in Figure 5.9C, salmon ellipse. Finally, the threshold ratios were computed and compared for each PC model neuron for the six investigated electrode positions (Figure 5.9D). The medians ranged from 40 to 80, which was similar to the threshold ratios of the previous experiment (Figure 5.4D) for the same electrode distance of 15 μm .

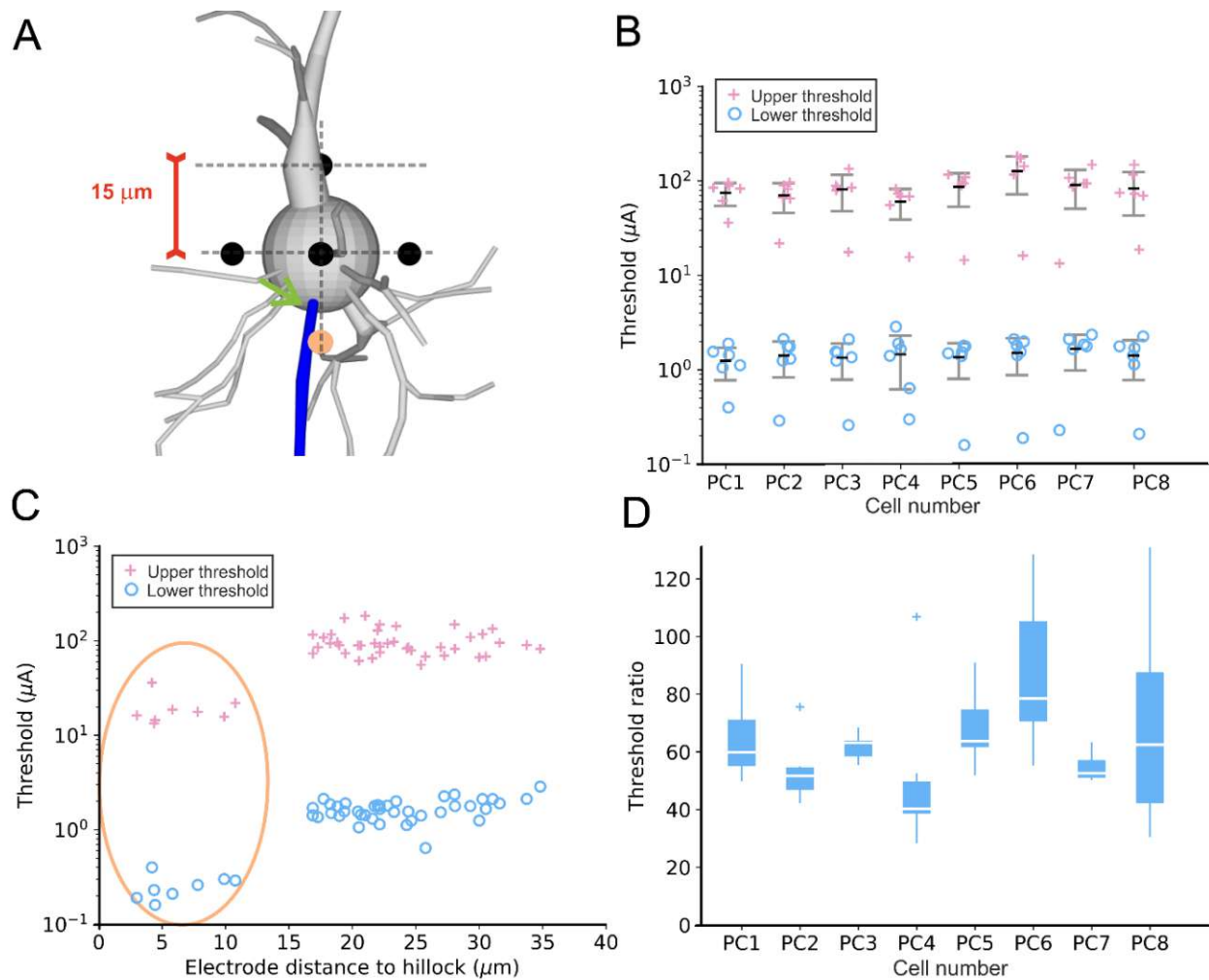


Figure 5.9. Thresholds for different electrode positions around the PC soma. **(A)** Six electrode positions (black and salmon circles) at a distance of 15 μm to the soma center were investigated for the 8 PC model neurons. The salmon circle indicates the electrode positions closest to the hillock (green arrow). **(B)** LTs ('o') and UTs ('+') are shown for individual cells. **(C)** LTs ('o') and UTs ('+') are plotted as a function of electrode distance to the hillock. Points within the ellipse correspond to the same colored electrode location in (A). **(D)** Threshold ratios for the investigated PCs (n=8) in the investigated electrode locations. Figure adapted from (Sajedi et al., 2021).

5.7.2 RGCs

Up to now, the stimulation parameters were limited to a point source approach with a monophasic pulse. However, such parameters are not possible in neural implants due to hardware/software problems, high energy consumption, and tissue damage. In epiretinal implants, the electrode array is usually placed on the epiretinal surface to have a close and direct impact on RGCs. As the RGCs have a planar dendritic configuration, the disk electrodes are used in these neural prosthetic devices. Additionally, using monophasic pulses is not possible due to charge accumulation, and consequently, tissue damage may occur (see section 1.1). Therefore, we were interested in the impact of disk electrode diameter on RGC excitations for an electrode distance of 15 μm , as this distance has the strongest effect on somatic membrane voltage (Figure 5.4E).

Figure 5.10A shows the impact of increasing disk diameters on the threshold ratios for all RGC model neurons. The result showed an increase of ratios for diameters larger $< 50 \mu\text{m}$. The maximum median threshold ratio (15 vs. ~ 6 for point source) was observed for the disk diameter of 50 μm . Interestingly, for the largest electrode diameter (200 μm), the threshold ratios were again similar to the points source approach.

In the next step of the analysis, the effect of pulse shape (mono vs. biphasic) was studied. For this experiment, cathodic leading biphasic pulses with a constant cathodic phase duration of 0.1 ms were applied. However, the anodic phase increased from 0.1 to 1 ms, resulting in a phase duration ratio ($D_{\text{cat}}/D_{\text{ano}}$) of 1 to 0.1, respectively. The threshold ratios were compared with the monophasic pulse used in our previous experiment (Figure 5.10B). This experiment demonstrated higher threshold ratios (up to three-fold) for pulse ratios > 0.6 . However, the effect becomes similar to a monophasic pulse for pulses with a longer charge balancing phase (anodic phase).

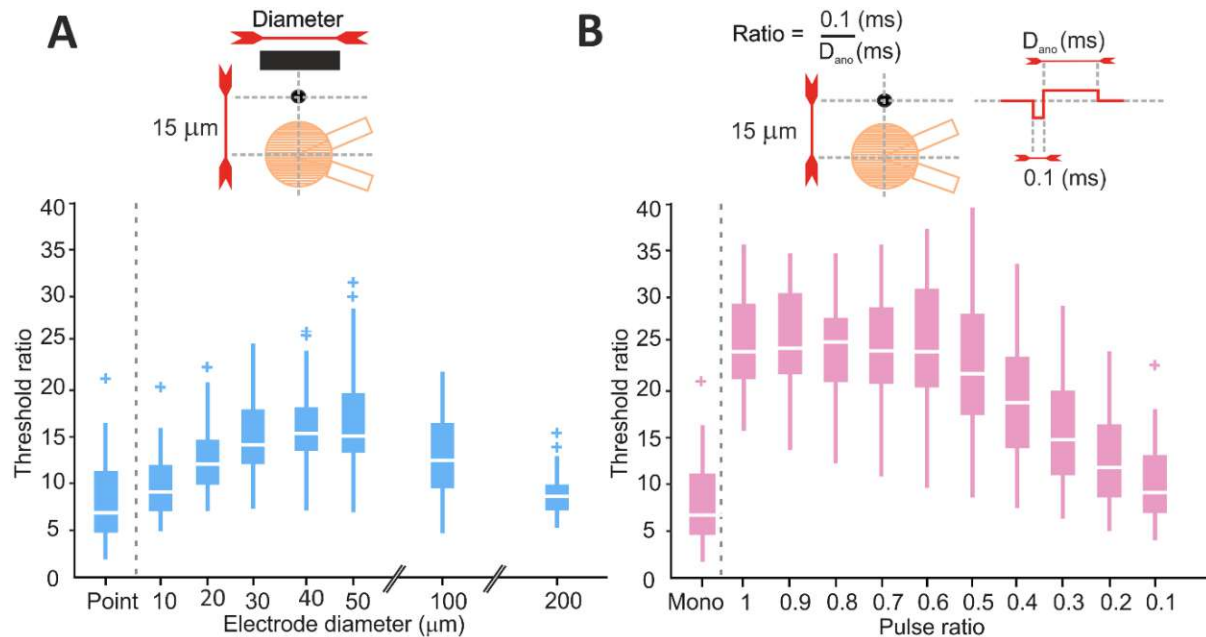


Figure 5.10. Effect of electrode diameter and pulse shape on threshold ratios in RGC model neurons. **(A)** Threshold ratio against disk diameters ranging from 10-200 μm . **(B)** Threshold ratio of monophasic compared with charge-balanced biphasic pulses vs. the ratio $0.1/D_{\text{ano}}$. Figure adapted from (Sajedi et al., 2021).

5.8 Discussion

An axon has been found the most excitable part of the cell in extracellular stimulation, as previously seen by other studies (Porter, 1963; Nowak and Bullier, 1998; Rattay and Wenger, 2010). Early investigations on straight fibers showed that cathodic pulses usually need intensities five times lower than the intensity in anodic pulse (BeMent and Ranck, 1969; Rattay, 1990). Therefore, for lower energy consumption in prosthetic devices such as deep brain or spinal cord stimulation, pseudo-monophasic cathodic leading pulses are usually applied.

An upper limit for axonal stimulation with cathodic pulses has been detected, and a value of 3 was reported for threshold ratio (UT/LT) in an early investigation (Katz and Miledi, 1965). Other studies investigating the same phenomenon in myelinated axons reported a ratio of 8 to 10 in the spinal cord fibers (Roberts and Smith, 1973; Ranck, 1975). Our results demonstrated significantly larger values for the myelinated PC axon due to axonal complicated branching forms and geometric variations compared with the previous investigations, primarily on giant straight axons.

AP initiation is difficult in soma and dendrites because of low sodium channel densities in RGC and PCs (Gasparini et al., 2004; Rattay and Wenger, 2010; Rattay et al., 2012). In RGCs, the increased sodium conductances caused the soma to play an active role because (i) depolarization of the upper hemisphere activated the low threshold sodium channels in the proximal AIS; however, it was not enough to start the AP at the soma. (ii) Strong AF in the RGC soma influenced the UTs. However, the primarily depolarized region is always smaller than half of the somatic surface (Fellner et al., 2019).

In an experimental study by Boinagrov et al., 2012, stimulation of isolated RGC somata with a micro-electrode 25 μm away from the soma have resulted in a UT/LT ratio of about six. If both thresholds (LT and UT) are specified by the rule of 50% of the pulse causing AP, the ratio is larger, e.g., 10 for stronger pulses. The same ranges were found for the RGC neuron models in this study. Additionally, with increasing the distance, the threshold ratios increased (Figure 5.4E).

In the first set of experiments, the soma was considered once a single compartment with almost no reflection of electric field (AF ~ 0) and once divided into 41 compartments always pointing toward the stimulating electrode. The threshold ratios were compared for both soma configurations. The LTs, UTs, and threshold ratios had no significant difference for both somas in the case of PC neuron models (Figure 5.4B and Figure 5.4D). Whereas, in RGC models, there were significant differences for LTs, UTs, and threshold ratios for distances smaller than 60, 30, and 15 μm , respectively (Figure 5.4C & Figure 5.4E).

As there are not enough experimental UT studies on PCs, a complete interpretation from the result was not possible for the different soma contributions in PC vs. RGC. However, the only explanation could be the anatomical differences between two somata to our knowledge. So firstly, in PCs, many dendrites have to be maintained by PC soma with intracellular current flow through a somatic excitation. Secondly, the axon has a very complex configuration with branches in different variations in the case of PC model neurons. The LTs, UTs, and threshold ratios were analyzed for further investigation based on various anatomical features such as AIS, dendrite, axonal length, and areas, etc. (Table 5.3). No direct correlation between a single feature and the thresholds was found except for the LTs and dendritic area in the PC model neuron (Figure 5.5). Overall, a single parameter did not define the thresholds and threshold ratios. In contrast, a combination of parameters such as geometrical and electrophysiological features and the distribution of electric fields might impact the threshold ratios.

Several investigations indicated that the AIS is the most sensitive part of the cell in electric stimulation (Fried et al., 2009; Jeng et al., 2011; Werginz et al., 2020). In agreement with previous studies that mostly used intracellular stimulation or synaptic excitation (Palmer and

Stuart, 2006; Shu et al., 2007; Yu et al., 2008; Bender and Trussell, 2012), our result demonstrated that AP was always initiated within the AIS in both cell groups. Although in this investigation, the stimulation was always applied in the vicinity of the soma and not above the AIS, somatic depolarization led to depolarizing axial current flow into AIS and consequently initiated the AP within the AIS because of high sodium channel density. Contrary to an experimental study which reported that the AIS end (~35 μm) was the site of AP initiation in PC (Palmer and Stuart, 2006), we demonstrated that with increasing the AIS length, the AP initiation site shifted toward the AIS center for both cell types (Figure 5.6).

Our result demonstrated that a complete block did not occur in the PC model neurons due to the complex cell geometry of PCs (Figure 5.7 and Figure 5.8). The partial blockage happened in our investigations for all PC neuron models when stimulating the cell around the soma. We observed that this partial block was related to complex axonal arrangement and the electrode distances from the axonal branches (Figure 5.7). These observations are in line with previously noted by Nowak and Bullier, 1996 who used extracellular stimulation of cortical neurons and reported axon branches fired AP while the soma, dendrites, AIS, and the first node of Ranvier were artificially blocked (Nowak and Bullier, 1996). In RGCs, in contrast, a complete UT always occurred either due to somatic UT in close electrode distances and consequently lower threshold ratios (up to 15) or due to anodal surround block of the axon for larger electrode distances with higher threshold ratios (up to 60).

Stimulating PCs close to axon hillock resulted in significantly smaller LTs and UTs. In contrast, threshold ratios appeared similar or in close ranges (Figure 5.9B-C vs. Figure 5.9D). In RGCs, increasing disk diameters to 50 μm caused almost three-fold larger threshold ratios. Surprisingly, for the largest electrode disk diameter of 200 μm , the ratios dropped close to those in point source stimulation. Monophasic and pseudo-monophasic pulses resulted in similar threshold ratios in RGC model neurons. In contrast, symmetric or close to symmetric pulses resulted in 3.5-4 times larger threshold ratios.

From the experimental point of view, it is essential to know which stimulus parameter maximizes the threshold ratios. When the ratio is small undesirable blocks will occur during micro-stimulation and causes blockage of the cells in the region of interest. In RGCs, our results suggested that stimulation from the largest electrode distance of 200 μm with a disk diameter of 50 μm and applying symmetric biphasic pulse increase the threshold ratio to its maximum values. However, the ratios were already significant in PCs, but the electrode distance of 60 μm resulted in the highest threshold ratio. Overall, we observed that UTs and ratios strongly depended on axonal branches and arrangement in PCs. Therefore, making a general statement about PCs is more complicated and needs more investigation.

Nevertheless, the model neurons were all detailed in geometry and biophysics in our investigation. We used PCs with highly branched complex axons, which were used for the first time in a computer study to our knowledge. The biophysical properties were used from the latest and most famous kinetics available for these cells. However, some limitations were considered in this three-dimensional investigation, such as simplifying extracellular medium, which was assumed to be homogeneous, whereas neural tissue is shown to be heterogeneous and leads to distorted electric field (see section 2.5 and Figure 2.7).

However, we believe heterogeneity does not substantially affect the results of the small electrode to cell distances. Another limitation was using the point source approach in most experiments except only in one part for RGCs. Nevertheless, electric fields produced by disk electrodes with an electrode to cell distances larger than electrode diameter becomes very similar to the point source approach (Werginz et al., 2020).

Overall, the upper threshold phenomenon was detected for PCs and RGCs. Whether the UT has practical implications is still questionable. We showed low UT/LT ratios (~ 5) for the small electrode to cell distances (Figure 5.4E) in RGCs. In PCs, on the other hand, ratios ranged from ~ 50 to ~ 300 (Figure 5.4D); therefore, we believe the UT has no practical implications in cortical tissue stimulation.

However, the significant differences between UTs and threshold ratios between two cell types were curious. Therefore, the next chapter is dedicated to investigating thresholds and threshold ratios in myelinated and non-myelinated axons using different geometrical features and kinetic models.

Chapter 6

Anodal surround block in axon models

So far, three different cells have been studied for the threshold window and the block phenomena were discussed in detail for both simplified 2D and realistic 3D structures. The following section aims to analyze the excitation window in myelinated and non-myelinated axon models exclusively. The lower (LT) and upper thresholds (UT) have been calculated, and the blockage at UT was compared for the investigated axons at the investigated electrode locations.

6.1 Axon models

Four myelinated and two non-myelinated axon models were used: (i) A myelinated axon, named 10HH, with 10-fold HH kinetic, in nodal area. This axon mimics the AP propagation in human SGCs based on (Rattay et al., 2001b), and details about the model can be found in section 3.1. (ii) A myelinated axon with kinetics from Mainen and Sejnowski, 1996, called Mainen, is commonly used in axons of cortical neurons to mimic the AP propagation (see section 5.2.1, and Table 5.1, also (Mainen and Sejnowski, 1996)). (iii) A myelinated axon with CRRSS kinetic from (Chiu et al., 1979; Sweeney et al., 1987), called CRRSS, and finally (iv) a myelinated axon applying MRG model from (McIntyre et al., 2002), called MRG, that is being commonly used for AP propagation of myelinated neurons of mammalian axons. The MRG and CRRSS models are explained in the following section. For non-myelinated axons, (i) A RGC axon was used with biophysical properties based on (Fohlmeister et al., 2010; Werginz et al., 2020). Details on this model can be found in section 5.2.2 and Table 5.2. (ii) The second non-myelinated axon was performed with classical HH kinetics using a temperature factor of $k=12$ to replicate the mammalian axons (Hodgkin and Huxley, 1952; Rattay and Aberham, 1993). More details on the HH gating kinetics can be found in section 2.2.

All axons were modeled in a 2D configuration along the x-axis with a multi-compartment model (see section 2.3). The fibers length was set to 1 mm for non-myelinated axons and 10 mm in myelinated axons, except for large electrode distances and high stimulus intensities in myelinated fibers to avoid AP initiation at the axonal end (ending effect), fiber length was extended to 20 mm. Two fiber diameters were investigated for all models (except in MRG), a thin and a thick fiber with a diameter of 1 and 5.7 μm (MRG model is defined for diameters from 5.7 to 16 μm), respectively. In the myelinated axons, nodes and internodes lengths were set to 1 μm and $100 \times$ fiber diameter, respectively. Compartment lengths were set to 1 μm in the non-myelinated axons as well as in nodes of Ranvier, which consist of a single compartment. Compartment lengths of internodes were set to about 20 μm in electrode distances $< 50 \mu\text{m}$. Intra and extracellular resistivities and membrane capacitance were set to 70 and 300 $\Omega\cdot\text{cm}$ and 1 ($\mu\text{F}/\text{cm}^2$), respectively.

First, AP conduction and velocity were tested in all axons by injecting an intracellular current at the first compartment. A point source electrode was set along the z-axis, in the middle of the non-myelinated axons, and above a node of Ranvier in myelinated axons to investigate cell membrane responses to extracellular stimulations. LTs, UTs, and threshold ratios were computed for electrode distances of 5, 10, 20, 50, 100, 200, 500, and 1000 μm to the center of fibers applying a monophasic cathodic pulse with pulse durations of 0.1 and 0.2 ms. However, in non-myelinated axons, only the first six electrode distances (5-200) were investigated due to the huge computational cost. The extracellular potentials were calculated by a point source approach in a homogeneous infinite medium (see section 2.5).

6.1.1 The CRRSS model

The CRRSS axon model was introduced by (Sweeney et al., 1987), which was based on data from (Chiu et al., 1979) and frequently used to simulate mammalian nerves. Similar to SGC and Mainen axon, this model consists of nodes of Ranvier (active) and internodal (passive) compartments. The passive conductivity and capacitance are calculated by dividing the original values ($g_m=1$ and $C_m=1$) by the number of myelin sheath layers N (similar to the SGC model). Active membrane ionic current, temperature factors, and the model gating kinetics are used in the model as in the following. Similar to the HH model, the voltage values assumed in the CRRSS model (Table 6.1) are given in a reduced way, where the steady-state value of the membrane voltage is 0. The physically correct value is $V_m = V + V_{rest}$, with $V_{rest} = -80 \text{ mV}$.

Biophysical properties

Passive membrane conductivity, passive (mS/cm ²)	g_m	1
Number of myelin sheath layers	N	$40 \times \text{fiber diameter } (\mu\text{m})$
Sodium channel conductivity (mS/cm ²)	\bar{g}_{Na}	1445
Leak channel conductivity (mS/cm ²)	g_L	128
Equilibrium potential for sodium channels (mV)	E_{Na}	115
Equilibrium potential for leakage conductance (mV)	E_L	-0.01
Temperature (°C)	T	37

Table 6.1. Biophysical parameters used in the CRRSS model, based on (Chiu et al., 1979; Sweeney et al., 1987).

$$i_{ion} = \bar{g}_{Na} m^2 h (V_m - E_{Na}) \quad k = 3^{(0.1T - 3.7)}$$

$$\alpha_m = \frac{97 + 0.363V_m}{1 + \exp\left(\frac{31 - V_m}{5.3}\right)} \quad \beta = \frac{\alpha_m}{\exp\left(\frac{V_m - 23.8}{4.17}\right)}$$

$$\beta_h = \frac{15.6}{1 + \exp\left(\frac{24 - V_m}{10}\right)} \quad \alpha_h = \frac{\beta_h}{\exp\left(\frac{V_m - 5.5}{5}\right)}$$

6.1.2 The MRG model

The MRG axon is modeled as a double cable structure (Figure 6.1) which is developed based on experimental data from mammalian myelinated axons (McIntyre et al., 2002), and the model has been demonstrated as a good model to predict myelinated axon excitation in warm blooded animals (Takahashi et al., 2007; Kuhn et al., 2009; Wongsarnpigoon et al., 2010).

Biophysical properties

Myelin capacitance ($\mu\text{F}/\text{cm}^2$)	c_m	0.1
Nodal and internodal capacitance ($\mu\text{F}/\text{cm}^2$) [*]	c_n, c_i	1
Axoplasmic resistivity ($\Omega\cdot\text{cm}$)	ρ_a	70
Periaxonal resistivity ($\Omega\cdot\text{cm}$)	ρ_p	70
Myelin conductance (S/cm^2)	g_m	0.001
MYSA conductance (S/cm^2)	g_a	0.001
FLUT conductance (S/cm^2)	g_f	0.0001
STIN conductance (S/cm^2)	g_i	0.0001
Sodium channel conductivity (S/cm^2)	g_{Na_f}	3
Potassium channel conductivity (S/cm^2)	g_{K_s}	0.08
Persistent sodium conductivity (S/cm^2)	g_{Na_p}	0.01
Nodal leakage conductivity (S/cm^2)	g_L	0.007
Equilibrium potential for sodium channels (mV)	E_{Na}	50
Equilibrium potential for potassium channels (mV)	E_K	-90
Equilibrium potential for leakage conductance (mV)	E_L	-90
Rest potential (mV)	V_{rest}	-80

Table 6.2. Biophysical parameters used in the MRG model. MYSA, STIN, and FLUT stand for the myelin attachment segment, stereotyped internodal region, and the paranodal main segment. All parameter values were based on the original study (McIntyre et al., 2002) with slight adaptation in *.

The MRG model includes fast and persistent sodium channels, slow potassium, and a leakage channel in the nodal area. In contrast, the internodal area has a passive membrane structure. Model gating kinetics of the active membrane (nodal area) is used as in the following.

Fast sodium current

$$I_{Naf} = g_{Naf} m^3 h (V_m - E_{Na})$$

$$\alpha_m = \frac{6.57(V_m + 21.4)}{1 - \exp\left(\frac{-V_m - 21.4}{10.3}\right)} \quad \beta_m = \frac{0.304(-V_m - 25.7)}{1 - \exp\left(\frac{V_m + 25.7}{9.16}\right)}$$

$$\alpha_h = \frac{0.34(-V_m - 114)}{1 - \exp\left(\frac{V_m + 114}{11}\right)} \quad \beta_h = \frac{12.6}{1 - \exp\left(\frac{-V_m - 31.8}{13.4}\right)}$$

Persistent sodium current

$$I_{Nap} = g_{Naf} p^3 (V_m - E_{Na})$$

$$\alpha_p = \frac{0.0353(V_m + 27)}{1 - \exp\left(\frac{-V_m - 27}{10.2}\right)} \quad \beta_p = \frac{0.000883(-V_m - 34)}{1 - \exp\left(\frac{V_m + 34}{10}\right)}$$

Slow potassium current

$$I_{Ks} = g_{Ks} s (V_m - E_K)$$

$$\alpha_s = \frac{0.3}{1 - \exp\left(\frac{V_m + 53}{-5}\right)} \quad \beta_s = \frac{0.03}{1 - \exp\left(\frac{V_m + 90}{-1}\right)}$$

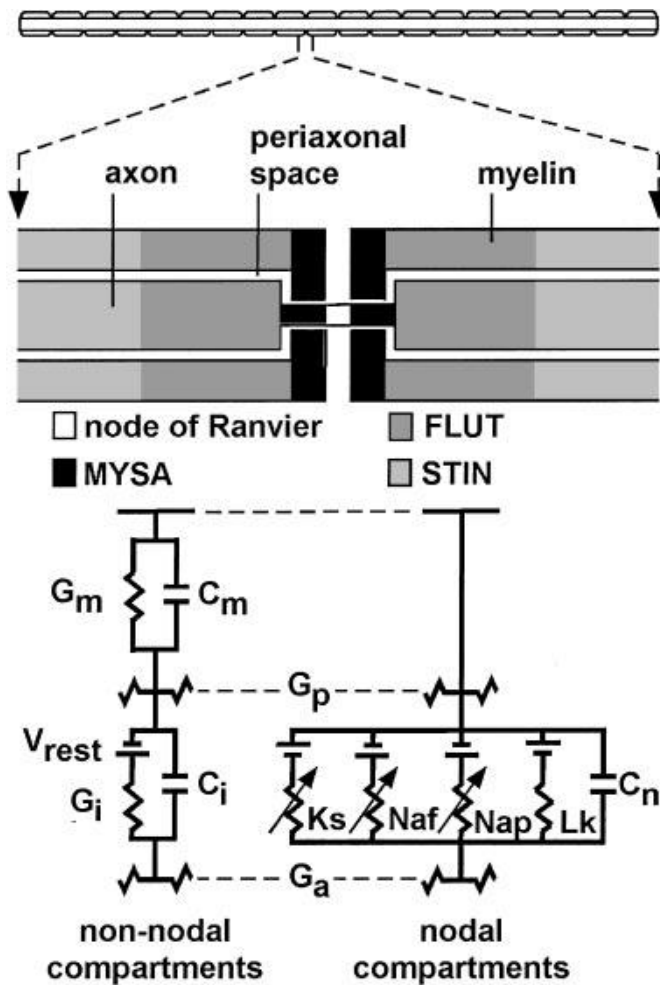


Figure 6.1. Multi-compartment double cable model of MRG axon. Each internodal section of the model consisted of 2 paranodal myelin attachment segments (MYSA), 2 paranodal main segments (FLUT), and 6 internodal segments (STIN). The nodal membrane dynamics included fast and persistent sodium, slow potassium, and linear leakage conductances parallel with the nodal capacitance (C_n). The internodal segments were represented by a double cable structure of linear conductances with an explicit representation of the myelin sheath (G_m in parallel with C_m) and the internodal axolemma (G_i in parallel with C_i). Figure and caption from (McIntyre et al., 2002).

6.2 Threshold windows in myelinated fibers

Figure 6.2 shows a model comparison of LT and UT for 1 μm (left traces) versus 5.7 μm (right) fibers, stimulated with 100 μs (top) versus 200 μs (bottom) cathodic pulses.

LTs and UTs versus electrode distance to the center of fibers with a fiber diameter $d = 1 \mu\text{m}$ and pulse duration of 0.1 ms are plotted in Figure 6.2A. The 10HH axon possessed the lowest LTs by mean values of 36.70% and 49.31% to CRRSS and Mainen axons, respectively. In contrast, the highest UTs were observed in the Mainen model, with mean differences of 88.72% and 92.98% compared with the 10HH and CRRSS models, respectively. However, due to numeric overflow in the applied computational framework, in the CRRSS model extracting the UT values were not possible for the electrode to fiber distances $> 50 \mu\text{m}$, and the same problem was also observed in the Mainen model for the largest investigated electrode distance of 1 mm. Moreover, the CRRSS model demonstrated a narrow threshold window for the four calculated distances (5, 10, 20, and 50 μm) with a maximum threshold ratio of 3.1 at 50 μm .

Figure 6.2B demonstrates threshold windows for the axon diameter of 5.7 μm in four models (Mainen, 10HH, CRRSS, and MRG) again with a pulse duration of 0.1 ms. The LTs are in a similar range in three axon models of CRRSS, 10HH, and MRG. However, the Mainen model possessed the highest LTs compared with CRRSS, 10HH, and MRG models with mean values of 48.56%, 58.69%, and 57.21%, respectively. In UTs, the highest values can be observed for the MRG and Mainen axons by an average difference of 32.67%. In addition, the CRRSS had the smallest UTs for the computed electrode distances (5-200 μm).

By increasing fiber diameter to 5.7 μm , when the shorter pulse was applied, LTs noticeably decreased by a mean value of 31.52%, 41.76%, and 31.20% in the Mainen, CRRSS, and 10 HH, respectively, as previously seen, thick fibers are easier to stimulate than thin ones (Ranck, 1975; Rattay, 1986, 1999). Additionally, UTs decreased in thicker fibers compared with their corresponding fiber diameter of 1 μm as follows: (i) in the Mainen model, UTs decreased by a mean value of 70.70% (49.15% in the smallest electrode distance and about 96.49% at the largest computed distance of 500 μm). (ii) In CRRSS, the UTs decreased averagely 29.47% (6.25% at the smallest electrode distance and about 67.31% at the highest computed electrode distance of 50 μm) and finally (ii) in the 10HH model, the UTs decreased with a mean value of 51.96% (7.92% at the smallest distance of 5 μm and approximately 91.76% at the highest investigated electrode distance of 1 mm).

In the next set of calculations, LTs and UTs were computed for 0.2 ms pulse duration and $d = 1 \mu\text{m}$ (Figure 6.2C). Interestingly, the CRRSS axon was not excitable for the first two electrode

distances (5 and 10 μm), and at the next possible distance of 20 μm , an extremely narrow threshold window with a threshold ratio of only 1.34 was observed. Moreover, again 10HH axon possessed the lowest LTs compared with Mainen and CRRSS models with mean reductions of 51.58% and 62.53%, respectively. The highest UTs were observed for the Mainen model, as previously seen with the shorter pulse, compared with the 10HH and CRRSS with a mean increase of 84.14% and 95.14%, respectively.

Figure 6.2D shows the thresholds for $d = 5.7 \mu\text{m}$ and a 0.2 ms pulse. Due to lower UTs compared with previous cases (smaller pulse duration and diameter), there were no numeric overflow issues, and all UTs were possible to be extracted in the investigated distances. The LTs were in a very similar range in the three axon models MRG, 10HH, and CRRSS, with mean differences of 1.27% to 10HH and CRRSS (almost overlapped) and a mean difference of 2.45% to the 10HH and MRG model. Like the shorter pulse duration, the Mainen model possessed the highest LTs with a mean increase of 58.44% to 10HH and CRRSS and 55.84% to MRG axon. In contrast, UTs in the CRRSS and 10HH models became overlapped (solid green and gray) with a mean difference of 2.05%. The Mainen and MRG axons possessed the highest UTs; more specifically, for electrode distances up to 200 μm , the highest UTs were observed in the Mainen model with an average increase of 41.83% compared with MRG, and they become smaller in MRG axon for the last two distances of 500 μm and 1 mm for approximately 44.16% and 72.72%, respectively.

By increasing fiber diameter to 5.7 μm , when the longer pulse was applied, LTs decreased significantly, in Mainen, CRRSS with mean values of 62.09% and 72.64%, respectively, while in 10 HH axon, LTs decreased more slightly with a mean value of 27.52%. Additionally, by applying the longer pulse, increasing the diameter decreased UTs as follows: (i) in the Mainen model, UTs decreased by a mean value of 63.47% (41.18% in the smallest electrode distance and about 96.73% at the largest computed distance of 500 μm). (ii) In CRRSS, the UTs decreased averagely 77.19% (96.54% at the highest computed electrode distance of 1 mm), and finally (ii) in the 10HH model, the UTs decreased with a mean value of 50.22% (3.36% at the smallest distance of 5 μm and approximately 92.53% at the highest investigated electrode distance of 1 mm).

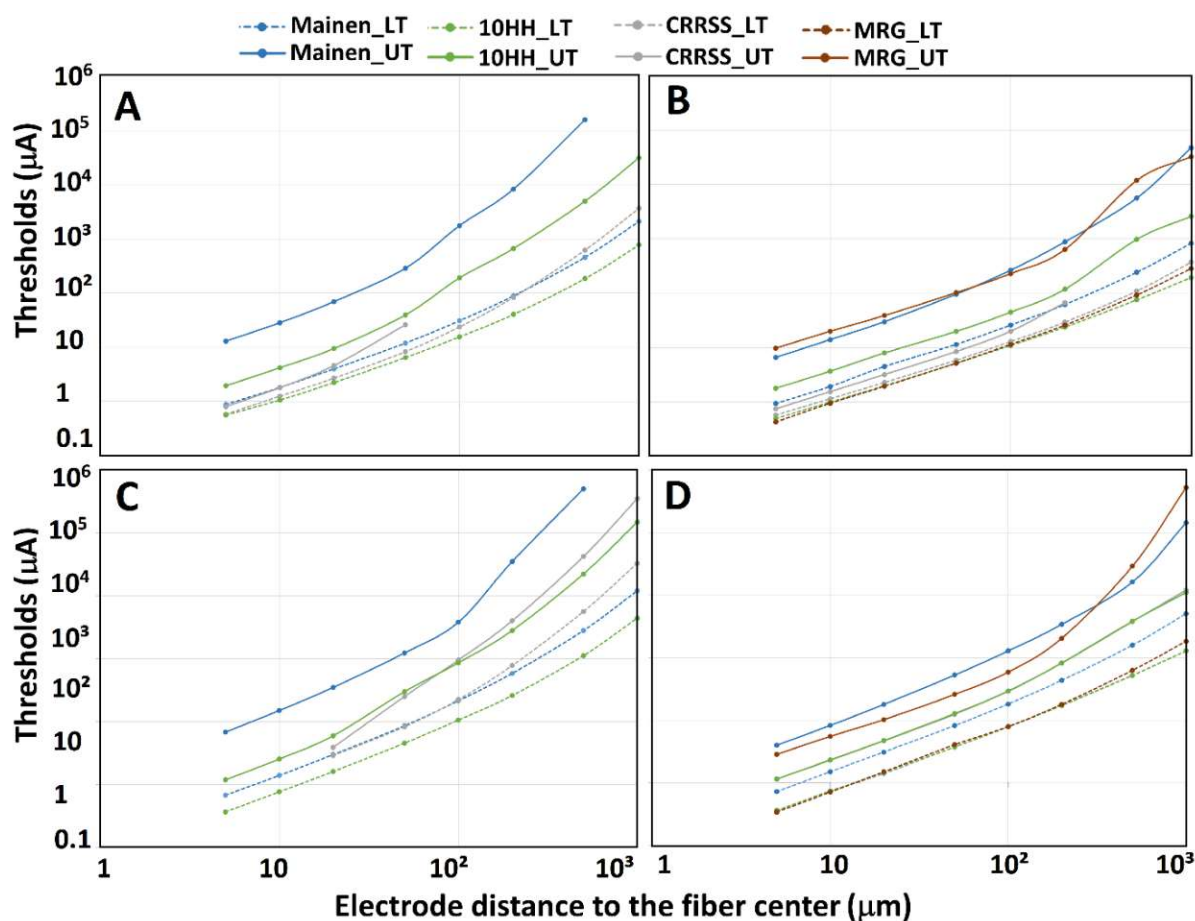


Figure 6.2. Lower (LT) and upper thresholds (UT) for myelinated axon models. LTs (dashed lines) and UTs (solid lines) were plotted versus the electrode distance to the fiber center for a monophasic cathodic pulse with a duration of 0.1 ms with axon diameters of (A) 1 µm and (B) 5.7 µm. Same layout as (A-B) with pulse duration of 0.2 ms for axon diameter of (C) 1 µm and (D) 5.7 µm. Note that the CRRSS LTs and UTs are overlapped with LTs and UTs of 10HH in (D). Due to numeric overflow UTs were not possible to be calculated for the Mainen axon at the highest distance of 1 mm (A & C), same effects for CRRSS model with a diameter of 1 µm at distances > 50 µm (A), and for the CRRSS axon with a diameter of 5.7 µm at distances >200 µm (B).

6.3 Threshold ratios in myelinated fibers

Figure 6.3 demonstrates the UT/LT threshold ratios for the investigated axon models with two diameters for the two investigated pulse durations. In this set of experiments, the effect of pulse duration and diameter were analyzed and discussed in the following.

6.3.1 The MRG model

The MRG model has been studied with the smallest possible diameter of 5.7 μm . By increasing the electrode distance to fiber to 200 μm , threshold ratios slightly changed, whereas at the last two investigated electrode distances (500 μm and 1 mm), ratios were increased up to 5.2 and 6.36-folds in pulse duration of 0.1 and 0.2 ms, respectively (Figure 6.3A-B, orange bars). However, by doubling the pulse duration, threshold ratios decreased with an average of 62.87% for all electrode distances except at the largest electrode distance, with the ratio increasing 60.63% (Figure 6.3A vs. Figure 6.3B, orange bars).

6.3.2 10HH model

In the 10HH axon (Figure 6.3A vs. Figure 6.3B, green & green hatch bars), by increasing the electrode distance, regardless of pulse duration, the threshold ratios have increased but more slightly in fiber with the larger diameter, specifically for the first six electrode to fiber distances (5-200 μm).

Doubling pulse duration in the thinner axons decreased threshold ratios in all distances with an average of 21.40%, except at a distance of 50 μm , in which ratios increased approximately 6.87%. However, in the case of larger diameter, when the pulse duration is doubled, the ratios slightly decreased at distances < 200 μm with a mean value of 11.18%, whereas for the two largest electrode distances, the ratios decreased significantly (up to 42.84%).

By increasing the axon diameter ($\times 5.7$), when the shorter pulse was applied, the threshold ratios decreased slightly at the first three electrode distances (5, 10, 20 μm) and more sharply for larger distances with an overall average of 43.68% (Figure 6.3A, green vs. green hatch bars). A similar trend was observed in the case of the longer pulse; the ratios decreased slightly for the first three electrode distances and decreased significantly at higher electrode distances with an average decrease of 39% (Figure 6.3B, green vs. green hatch bars). Moreover, the highest decrease in threshold ratios was observed in the axon with the largest diameter stimulated with the longer pulse duration of 0.2 ms, which caused a decrease in ratios with an average of 48.48%.

6.3.3 The CRRSS model

The effect of pulse lengthening was studied in the CRRSS axon, and surprisingly in the thick axon model, the ratios increased by a mean value of 56.97% by doubling the pulse duration

(Figure 6.3A vs. Figure 6.3B, gray bars). In the case of the thinner axon, because of the axon model not being excitable in small distances and overflow issue in large electrode distances, the effect of elongating the pulse duration could only be studied for two electrode distances of 20 and 50 μm at which the ratios decreased 21.36% and 3.73%, respectively (Figure 6.3A vs. Figure 6.3B, gray hatch bars).

By increasing the axon diameter ($\times 5.7$), threshold ratios decreased by an average of 21.31% in the shorter pulse duration. In contrast, by using the longer pulse, the ratios increased for the first two possible electrode distances of 20 and 50 μm up to 59.94% and 9.64%, respectively, and decreased for the remained investigated distances with an average of 8.68% (Figure 6.3B gray vs. gray hatch bars).

6.3.4 The Mainen model

In the Mainen axon, regardless of pulse duration, threshold ratios enhanced with increasing the electrode distance and more significantly in the thinner axon (Figure 6.3A-B, blue hatch bars).

By doubling the pulse duration, the threshold ratios decreased with a mean value of 41.89% in the thinner axon (Figure 6.3A vs. Figure 6.3B, blue hatch bars), and a mean value of 30.07% in the axon with a diameter of 5.7 μm (Figure 6.3A vs. Figure 6.3B, blue bars).

By increasing the axon diameter ($\times 5.7$), the threshold ratios decreased with an average of 70.61% when stimulating with the pulse duration of 0.1 ms and an average of 62.68% by applying the longer pulse (Figure 6.3A-B, blue vs. blue hatch bars). Finally, the most changes in threshold ratios were observed when axon diameter and pulse ratios increased simultaneously, which resulted in an average decrease in ratios by a mean value of 77.66%.

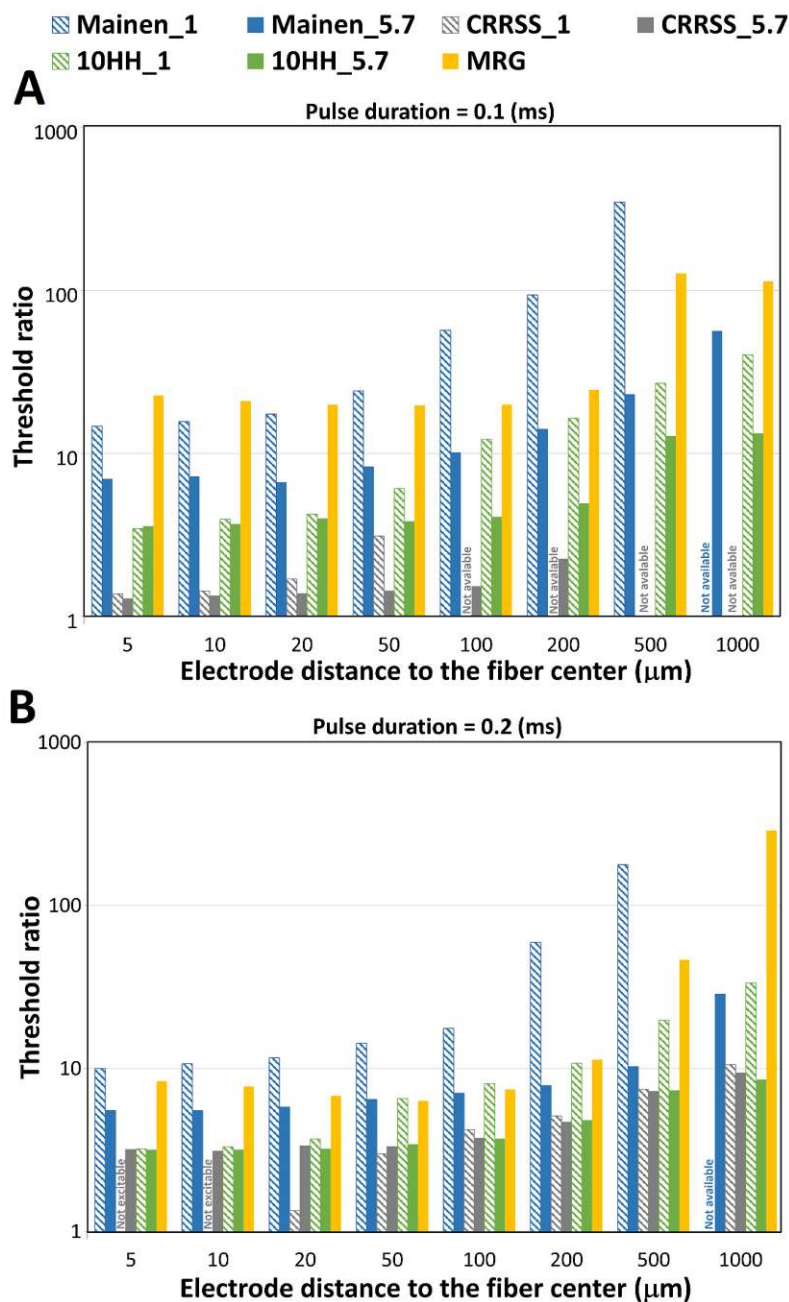


Figure 6.3. Threshold ratios (UT/LT) of the investigated myelinated axon models. Threshold ratios were plotted versus the electrode distance to the fiber center with a diameter of 1 μm and 5.7 μm stimulated with a monophasic cathodic pulse with a duration of (A) 0.1 ms and (B) 0.2 ms. Note that due to a numeric overflow, the UT values were not available for the CRRSS model with a diameter of 1 μm for electrode distances $>50 \mu\text{m}$ and with a diameter of 5.7 μm for electrode distances $>200 \mu\text{m}$ in shorter pulse. In the Mainen model, again due to numeric overflow, the UTs were not calculated for the largest electrode distance in case of shorter pulse duration. However, when the longer pulse was applied, the CRRSS model was not excitable with the smaller diameter (1 μm) for electrode distances closer than 20 μm .

6.4 Threshold windows in non-myelinated fibers

In the next step, the same lower and upper thresholds computations were applied to non-myelinated axon models HH and RGC. Figure 6.4A demonstrates the threshold windows for diameters (1 μm vs. 5.7 μm) and 0.1 ms pulse. The LTs are in very similar ranges, with a mean difference of approximately 12.8% for thin (light blue and red dashed lines) and approximately 11.84% for thick fiber diameters (dark blue and pink dashed lines). On the other hand, increasing the fiber diameter ($\times 5.7$) led to lower the LTs by an average of 29.94% (with a maximum of 54.55% at the largest electrode distance) in HH axon and 34.32% (with a maximum of 56.36% at the largest electrode distance) in RGC axon.

Moreover, high UTs were primarily observed in thin axons (light blue and red), and the RGC model with a diameter of 1 μm possessed the largest UTs. The UTs, however, in thin (light blue and solid red lines) and thick axons (dark blue and solid pink lines), are slightly distinct between the two axon models in small electrode distances and more significantly different in larger electrode distances with a mean difference of 35.92% in thinner axon and 31.09% in the thicker axon. By increasing the fiber diameter ($\times 5.7$), UTs have reduced 58.33% (with a maximum of 78.23% at the largest electrode distance) in the HH axon and 57.7% (with a maximum of 81.33% at the largest electrode distance) in the RGC axon.

Figure 6.4B displays the thresholds for 0.2 ms cathodic pulses. Again, thick fibers possessed lower LTs, and the LTs were in the same ranges in both axon models with mean differences of 10.85% and 6.43% in the case of thinner fiber (light blue and red dashed lines) and thicker fibers (dark blue and pink dashed lines), respectively. Moreover, when the fiber diameter is increased ($\times 5.7$), similar to shorter pulse, LTs decreased 36.07% (with a maximum of 50.83% at the largest electrode distance) in HH axon and 28.92% (with a maximum of 50.83% at the largest electrode distance) in the RGC axon.

As previously observed in the shorter pulse, thin fibers possessed higher UTs, and again, the highest UTs were observed in the RGC axon with a diameter of 1 μm . In addition, comparing UTs between the two axon models, the thin (light blue and solid red lines) and thick axons (dark blue and solid pink lines), were slightly different in close electrode to fiber distances and more significantly different in larger distances, with an overall mean difference of 44.35% in fiber diameter of 1 μm and 36.62% in fiber diameter of 5.7 μm . Furthermore, by increasing the fiber diameter ($\times 5.7$), the UTs have reduced 54.43% (with a maximum of 77.19% at the largest electrode distance) in the HH axon and 44.13% (maximum of 80.28% at the largest electrode distance) in the RGC axon.

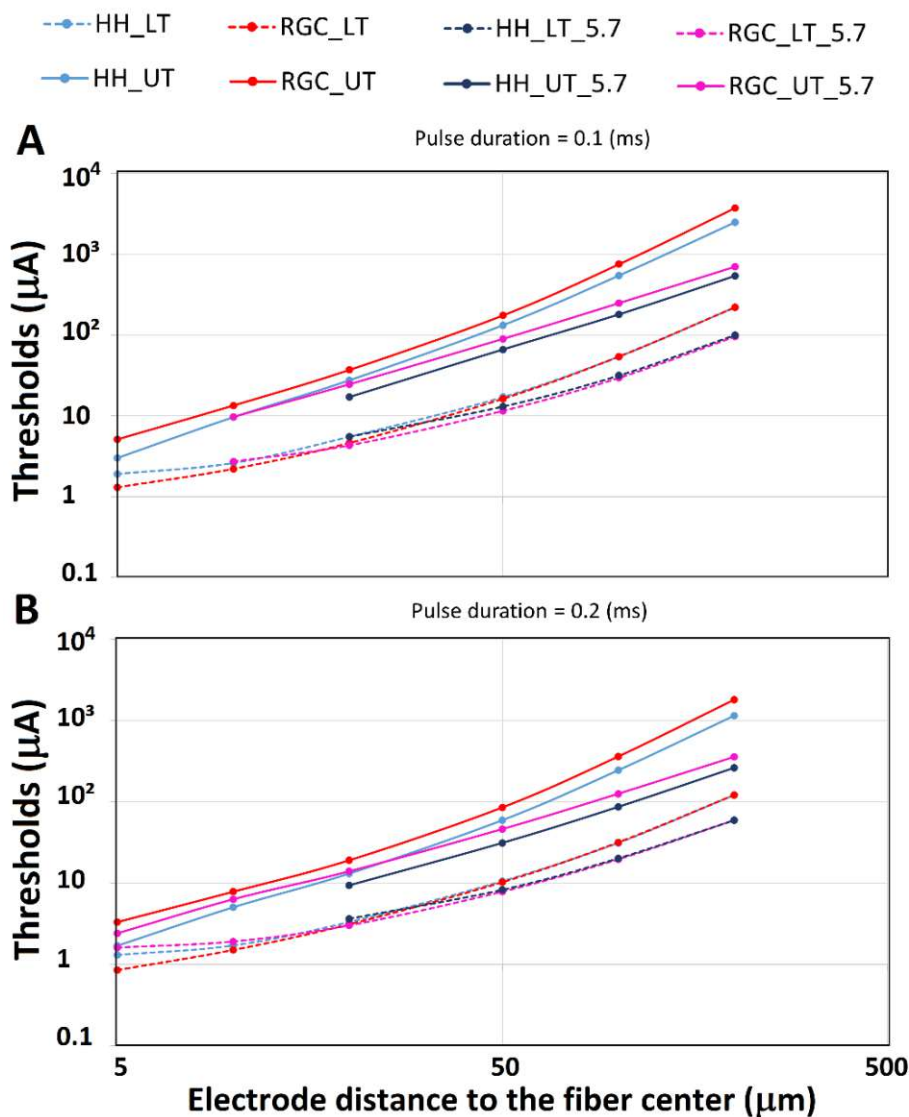


Figure 6.4. Lower (LT) and upper thresholds (UT) for non-myelinated axon models. LTs (dashed lines) and UTs (solid lines) were plotted versus the electrode distance to the fiber center, for axon diameters of 1 μm (light blue and red) and 5.7 μm (dark blue and pink) stimulated with a monophasic cathodic pulse with a duration of (A) 0.1 ms and (B) 0.2 ms pulse duration. The thicker HH and RGC axons were not excitable in electrode distance to fibers < 20 (for both pulse durations) and < 10 μm (for longer pulse), respectively.

6.5 Threshold ratios in non-myelinated fibers

In this set of experiments, the effects of pulse duration and diameter are discussed in detail (Figure 6.5). First, by applying the shorter pulse, the largest ratios were observed for thinner RGC axon with a mean difference of 47.79% compared with the thin HH axon (Figure 6.5A,

red hatch vs. blue hatch bars). In both thin axon models, the UT/LT ratio increased significantly by increasing the electrode to fiber distance. However, this effect was observed only slightly at the small distances (5-20 μm) in thicker axons. Additionally, axons with larger diameters (5.7 μm) were not excitable for the electrode to fiber distances $< 20 \mu\text{m}$ and $< 10 \mu\text{m}$ in HH and the RGC models, respectively.

Moreover, by stimulating the axons with a pulse duration of 0.2 ms, similar effects were observed, and again largest ratios were found for thinner RGC axons with a mean difference of 53.36% compared with the thin HH axon (Figure 6.5B, red vs. blue hatch bars). As previously seen, in thin axon models, the ratios increased significantly by increasing the electrode distance, whereas, in thicker axons, the effect was only noted at the small distances (5-20 μm). Thin HH axon was not excitable for the electrode to fiber distances $< 20 \mu\text{m}$.

Nevertheless, doubling the pulse duration resulted in a slight decrease in ratios in all investigated axons by mean values 20.88% and 21.28 in thin and thick HH axons, respectively, (Figure 6.5A vs. Figure 6.5B, hatch blue and blue bars), 15.41%, and 18.43% in thin and thick RGC axon, respectively (Figure 6.5A vs. Figure 6.5B, hatch red and red bars). Increasing the fiber diameter ($\times 5.7$) resulted in a reduction in ratios in all investigated axons by mean values 58.33% and 42.04% in HH axons by applying the shorter and longer pulse durations, respectively, (Figure 6.5A, hatch blue vs. blue bars), as well as 42.04%, and 38.97% in RGC axon for shorter and longer pulse, respectively (Figure 6.5B, hatch red vs. red bars).

For the last set of experiments, the effect of pulse and diameter have been investigated simultaneously in both axon models. By doubling the pulse duration and increasing the diameter to 5.7-fold, the ratios have decreased more significantly in both axon models with similar mean values of 54.46% and 52.32% in the HH and RGC models, respectively.

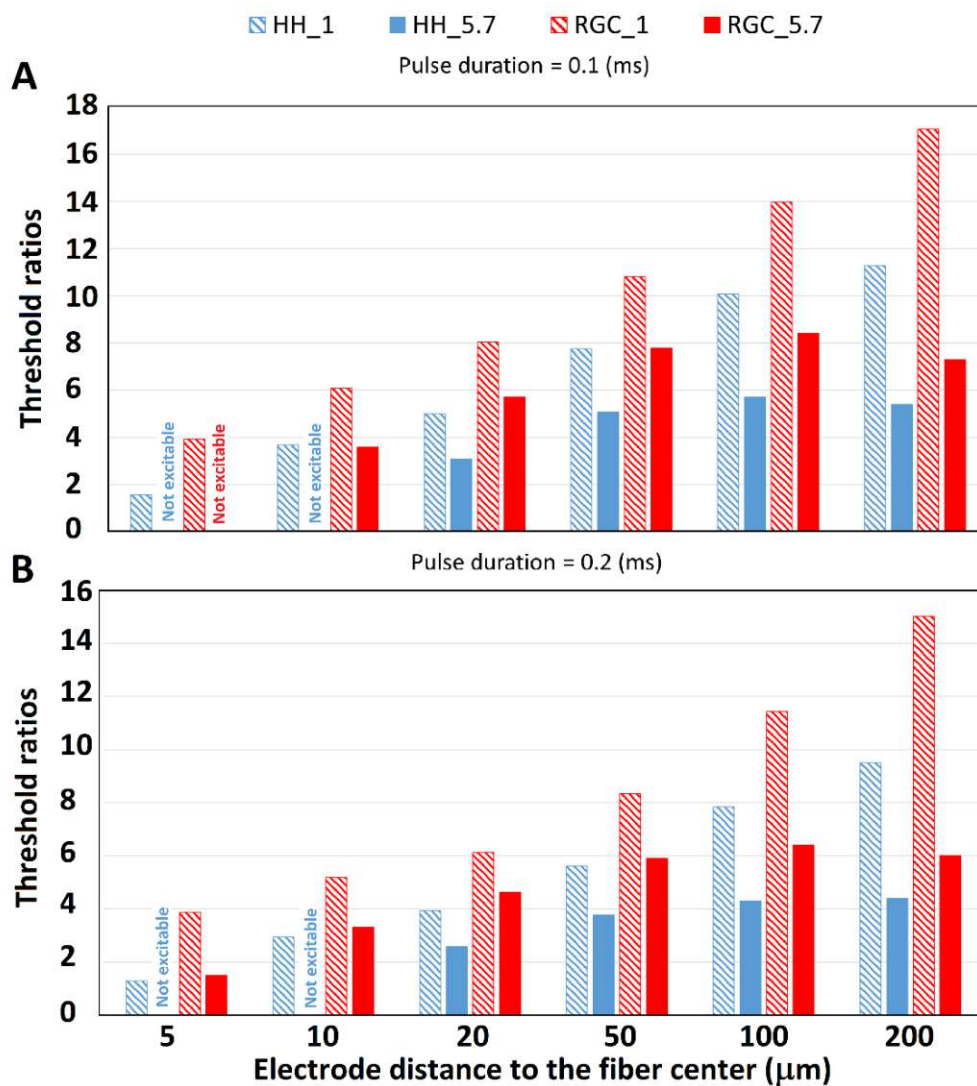


Figure 6.5. Threshold ratios (UT/LT) of the investigated non-myelinated axon models. Threshold ratios were plotted versus the electrode distance to the fiber center with a diameter of 1 μm (hatch colors) and 5.7 μm stimulated with a monophasic cathodic pulse with a duration of (A) 0.1 ms and (B) 0.2 ms.

6.6 Discussion

Katz and Miledi (Katz and Miledi, 1965) reported a small ratio of two or three for close electrode spots to the motor nerve fiber of the frog and explained the blockage phenomenon caused by the anodal surround in cathodic stimuli, resulting from hyperpolarization of the neighboring regions. Other early investigations from experimental studies have also demonstrated that a monophasic cathodic pulse can stimulate an axon within a range possessing a lower and upper limit (BeMent and Ranck, 1969; Jankowska and Roberts, 1972; Armstrong et al., 1973; Jankowska and Smith, 1973; Roberts and Smith, 1973; Abzug et al., 1974). These data have been collected and represented in a review study by Ranck (Ranck, 1975), who has reported that a UT/LT ratio > 8 may cause AP blockage in myelinated axons.

In addition, a computational study by Rattay and Aberham (Rattay and Aberham, 1993) used four kinetic membranes of CRRSS, Franken-Haeuser-Huxley or FH model (Frankenhaeuser and Huxley, 1964), Schwarz-Eikhof or SE model (Schwarz and Eikhof, 1987), and HH models, showed that by increasing the electrode to fiber distance, the UT/LT ratios increased in the FH, SE, and CRRSS models. They also reported that by applying short pulses, extremely high stimuli are required for producing AP blockage, which causes cellular damage. This effect was previously seen in an experimental study by Fang and Mortimer (Fang and Mortimer, 1987).

However, due to the complexity of neural tissue and issues such as artifacts during the recording of neural responses, highly dense structures, the unknown anatomy of the investigated cell, and not identifying which part of the cell is initiating an AP, there are not enough data from experimental studies that are current-distance or current-duration related for either myelinated or non-myelinated axons.

6.6.1 Myelinated fibers

The first part of this chapter investigated the threshold windows with four myelinated axon models: (i) the Mainen, (ii) the MRG, (iii) the 10-fold HH, and (iv) the CRRSS models. In summary, the following effects were observed in this investigation:

- (i) Highest UTs were observed in the Mainen axon when stimulating the thin fibers in both pulse durations. When stimulating fibers with a larger diameter, Mainen and MRG possessed the highest UT values regardless of pulse duration.
- (ii) The thin 10HH axon possessed the smallest LTs in both pulse durations. In contrast, in fibers with larger diameters, similar LTs were identified for MRG, CRRSS, and 10HH.

On the other hand, regardless of fiber diameter and pulse duration, the Mainen axon always possessed the highest LTs.

- (iii) When the pulse duration was set to 0.1 ms, increasing in diameter led to decreasing LTs with similar mean values of approximately 32%, 42%, and 31% in the Mainen, CRRSS, and 10 HH, respectively, as also previously seen that thick fibers are easier to stimulate (Ranck, 1975; Rattay, 1986, 1999).
- (iv) Applying the longer pulse (0.2 ms) by increasing the fiber diameter LTs decreased with mean values of almost two-fold, approximately 62% in Mainen and 73% in CRRSS. In the 10HH axon, however, the effect was very similar to the shorter pulse with a slightly smaller mean value of ~28%.
- (v) When applying pulse duration of 0.1 ms, increasing the fiber diameter led to smaller UTs by mean values of approximately 71%, 29%, and 52% in the Mainen, CRRSS, and 10HH models, respectively. In pulse duration of 0.2 ms, increasing the fiber diameter decreased UTs with mean values of approximately 63%, 77%, and 50% in the Mainen, CRRSS, and 10HH models, respectively.
- (vi) By increasing the stimulation distance threshold ratios increased significantly in all axon models, especially in thinner axon with an exception for MRG model, in which the ratios were almost constant for the first six electrode distances (5-200 μm), in the last two investigated distances, however, ratios increased significantly.
- (vii) By two-fold increasing the pulse duration, the threshold ratios decreased in all fibers and more significantly in thinner axons, except for the thick CRRSS fiber, in which, surprisingly, the ratios increased by a mean value of approximately 57%. By increasing the fiber diameter ($\times 5.7$), the threshold ratios decreased in all axon models (for all investigated distances) for both pulse duration with a small exception of the first two distances in the CRRSS model for a pulse duration of 0.2 ms.

Overall, in consistence with the reported data from previous studies (Ranck, 1975; Rattay and Aberham, 1993), threshold ratios < 10 was observed for most investigated myelinated axon models when the pulse duration was set to 0.2 ms except for the thin Mainen and MRG models in electrode to fiber distances > 20 and electrode to fiber distances $> 200 \mu\text{m}$, respectively.

6.6.2 Non-myelinated fibers

In the second part, two non-myelinated axon models were studied for threshold windows and threshold ratios: (i) The RGC axon and (ii) the classical HH axon using temperature factor $k = 12$ to simulate AP propagation in the mammalian axon. In summary, the following results were obtained from this set of investigations:

- (i) A similar range in LTs was observed in both (HH and RGC) for thick axons (5.7 μm), possessing the lowest LTs, regardless of pulse duration. In contrast, the highest UTs were observed in thin fibers, specifically in the thin RGC axon, for both investigated pulse durations.
- (ii) Increasing the fiber diameter resulted in a reduction in LTs with a mean value of approximately 30% and 34% in HH and RGC, respectively, when the pulse duration was set to 0.1 ms. In longer pulse, LTs reduced averagely 36% and 29% in HH and RGC models, respectively.
- (iii) Increasing the diameter to 5.7-fold reduced the UTs by a mean value of approximately 57% in both axon models in the case of the shorter pulse; in longer pulse, UTs decreased about 54% and 44% in HH and RGC axons, respectively. The highest threshold ratios for thin RGC axons were observed with a mean difference of approximately 48% and 53% compared with the thin HH axon for pulse durations of 0.1 and 0.2 ms, respectively.
- (iv) Regardless of pulse duration, by increasing the electrode to fiber distance, threshold ratios increased significantly in thin fibers (HH and RGC), whereas in thick fibers, the effect was noted only slightly at small electrode distances (5-20 μm).
- (v) Doubling the pulse durations reduced ratios by a similar mean value of approximately 21% in thin and thick HH axons and mean values of 15% and 18% in thin and thick RGCs, respectively.
- (vi) Increasing fiber diameter to 5.7-fold reduced threshold ratios by mean values of approximately 58% and 42% in HH axon for pulse durations of 0.1 and 0.2 ms, respectively. Subsequently, ratios reduced averagely 42% and 39% in RGC axon for the shorter and longer pulse, respectively, when the fiber diameter increased.

Overall, threshold ratios were extremely smaller in non-myelinated fibers compared with myelinated ones, which may result from significantly higher ion channel densities, specifically sodium ions, in the nodal area. However, more investigation is needed in both experimental and computational studies to study this effect. Some effects were repeated in both axons (myelinated vs. non-myelinated) such as: (i) By increasing the fiber diameter LTs, UTs and threshold ratios decrease. (ii) Increasing the pulse duration results in decreasing the threshold ratios. (iii) By increasing the stimulation distance, threshold ratios increase. (iv) Thinner fibers have higher UT values and higher threshold ratios, especially when stimulated with short pulses.

Chapter 7

Conclusion

Extracellular stimulation of neural tissue had substantial successful applications in recent decades. Neuroprosthetics bypass the impaired neural pathway to treat or restore lost functions. Employing micro-arrays in small dense areas and using miniaturized electronic components facilitate the effective excitation of a single target cell. However, neurons are excitable only within a range called a stimulation window that includes a lower threshold as the smallest amount of the current needed to elicit a neural response and an upper threshold above which the action potential is prevented from generating or propagation. In some cases, such as at close electrode-neuron distances, the threshold window is small, and therefore, stimulation of the region of interest can lead to an undesirable block in the same area, which is of concern.

A block can be generated either arbitrarily to inhibit a neural activation or unpleasantly due to an increased stimulus. This thesis has studied and discussed the two important block phenomena. The somatic block occurs due to high stimulus currents in close electrode-soma distances. Due to the spherical shape, two hemispheres become oppositely polarized when stimulating a soma. So if a cathodic pulse is used, the hemisphere close to the electrode is depolarized partly, and the rest become hyperpolarized. It has been demonstrated that several mechanisms are involved in this process, such as an inverse sodium current (Boinagrov et al., 2012), inactivating sodium channels, and strong potassium currents (Fellner et al., 2019). The threshold ratio (UT/LT) in the case of a somatic block is shown to be small (< 8). However, if the electrode is in the axonal excitation range, the axon elicits the AP, and therefore the cell is not in a complete blockage anymore (Rattay, 2014; Meng et al., 2018).

Another undesirable neural inactivation is an anodal block that mostly appears in the axonal membrane due to intense cathodic stimulus (Katz and Miledi, 1965; Jankowska and Roberts, 1972; Roberts and Smith, 1973; Rattay and Aberham, 1993). A cathodic stimulus generates a depolarized area in the cellular membrane close to the electrode and two hyperpolarized regions in the surrounding flanks (Figure 2.8A, blue trace). Cathodic stimuli are usually easier and

require fewer amplitudes to excite a cell (Ranck, 1975; Rattay, 1986, 1999), and therefore they are frequently used in neuroprosthetics with a following balanced phased of the opposite polarity to avoid charge accommodations. Moreover, due to strong stimulus intensity, AP initiated in the depolarized area is trapped within the hyperpolarized neighbors and cannot propagate further. Axons are essential in neural signaling and communication as they are the final part of the cells which pass the signal to the next processing neighbors. In addition, axons are usually the largest part of the cells and possess a high amount of sodium channels (usually a sodium band), making them the easiest and most excitable part of the cell (Porter, 1963; Nowak and Bullier, 1998; Rattay and Wenger, 2010). Therefore, blockage in the axon can cause the cell's final blockage state, mostly occurring with higher threshold ratios than in the somatic block, depending on the axon geometry and type.

A 2D investigation has been carried out for calculating LTs, UTs, and threshold ratios in three cell types of a SGC, a RGC, and a PC with similar linear geometries with an electrode positioned above the multi-compartment soma using 100 μs and 1 ms cathodic pulses. The most important findings in this investigation were: (i) despite the same somatic geometries, the soma was not excitable with a shorter pulse (100 μs) in PC, due to low sodium conductance of 8 in PC, vs. 69.4 and 120 mS/cm^2 in RGC and SGC. (ii) Profoundly degenerated SGC soma was not excitable for electrode distance closer than 4 μm , (iii) a clear limit was found in whole-cell stimulation where the cell excitation was governed by soma (electrode to cell distance <40 μm in SGC, <20 μm in RGC and PC, Figure 4.7) and for larger electrode distances the axon dominates the cell. (iv) PC possessed substantially higher (up to 8-fold) UTs and threshold ratios than RGC and SGC.

However, 2D model neurons lacked a real cell geometry by neglecting the complex structure of dendrites (in RGC & PC) and axon collaterals (in PC) as well as the simplified kinetics in some cases. Therefore, in the next part, the investigations were extended to a 3D model reconstructed RGC (n=34) and PC group neurons (n= 8) by applying cathodic pulses (mostly 100 μs monophasic pulses) in the vicinity of the soma (5-200 μm). The main findings of this investigation were: (i) soma played almost no role in PC excitation. In contrast, for stimulating RGCs in the soma vicinity, soma may mostly rule the cell excitation, and at these distances, UT occurs due to somatic block in RGC. (ii) At LT levels, APs always initiated at AIS in both cell types; in cells with short AIS, the AP site was close to the distal part of AIS, whereas, in cells with longer AIS, the initiation site shifted towards the center of AIS. (iii) PCs possessed extremely high UTs, and (iv) no complete block was observed in PCs. (v) The arrangement of axon collaterals in PCs significantly impacted UTs while almost no impact on LTs.

Interestingly, in the 3D investigation again, PCs possessed significantly higher threshold ratios of 5 to 10-fold depending on the electrode to cell distance. On the other hand, in some comparable distances such as at electrode distances of 50-60 μm from the soma, ratios were significantly higher in the 3D model PCs compared with the 2D PC, which could result from the appearance of dendrite and complex axon collaterals in the 3D PC which was neglected in the 2D model.

Another curious point is that in the 2D investigation, we observed that the PC soma was not excitable for short pulses (100 μs), and similarly, the results from complex 3D structure PCs showed that soma played no role in cell excitation by comparing the single- vs. multi-compartment soma with the same pulse. We concluded that highly branched dendrite and axons may have resulted in PC somata having a passive role. However, compared with the situation in the 2D investigation, an additional factor for this effect is the low sodium conductance (80 vs. 690 $\text{pS}/\mu\text{m}^2$ in 2D PC vs. 2D RGC, 350 vs. 650 $\text{pS}/\mu\text{m}^2$ in 3D PC vs. 3D RGC); although the sodium conductance was still larger (~ 4 times) in the 3D model PC, a larger somatodendritic area in 3D may compensate for the sodium conductance differences.

Moreover, the behavior was almost similar and comparable in the 2D and 3D RGC models. In both investigations for stimulating RGCs in the soma vicinity, soma may mostly rule the cell excitation, and at these distances, UT occurred due to somatic block, whereas at large stimulus distances, cell blockage was more related to the axonal anodal block.

However, the most curious finding was the partial blockage in 3D PCs that were not observed in the 2D model and neither of RGCs. As this effect was more linked to the complex axon structure, it was encouraging to investigate the axonal excitation window and ratios, which was carried out in the final part of this thesis. For this investigation, different kinetics of myelinated and non-myelinated fibers with a thin and thick diameter were studied in a range of electrode to fiber distance applying a 100 and 200 μs cathodic rectangular pulse. For myelinated fibers, the main findings were: (i) highest UTs were observed for thin and thick Mainen model (which was used in 3D PC myelinated axons) and MRG model. (ii) Increasing fiber diameter decreased UTs and threshold ratios in the investigated axon models. (iii) Increasing the pulse duration caused decreasing the UTs and threshold ratios and most significantly in thin fibers. In non-myelinated fibers, significant findings were: (i) highest UTs and threshold ratios were found for thin fibers, and UTs and threshold ratios decreased by increasing the diameter. (ii) Increasing pulse duration decreased UTs and threshold ratios as previously observed in myelinated fibers.

One of the pure axon investigation highlights was that thin fibers always possessed the highest thresholds and threshold ratios. This effect was stronger when these fibers were stimulated with

Conclusion

short cathodic pulses. In agreement with this finding, previous experimental studies also reported that while electrical currents can block thick and large axons, small axons can still conduct APs (Whitwam and Kidd, 1975; Bhadra and Kilgore, 2004). However, these results can also explain why no complete block was occurred in our 3D PCs even by applying very high current intensities as they possessed numerous laterals with extremely thin branches and terminals.

Arbitrary generation of blocks can be used for successful and selective control of fibers which can have many clinical applications in the future, such as treating pain, hypertension, and chronic nausea. In addition, selective and smart excitation in micro-stimulation can benefit from deliberately using block by inactivating only a specific cell or a group of cells. However, to apply blocks selectively and deliberately, a complete understanding of the mechanisms involved in blocks is necessary.

References

Abzug, C., Maeda, M., Peterson, B.W., Wilson, V.J., Bean, C.P., 1974. Cervical branching of lumbar vestibulospinal axons: With an Appendix. *J. Physiol.* 243, 499–522.

Akemann, W., Knöpfel, T., 2006. Interaction of Kv3 potassium channels and resurgent sodium current influences the rate of spontaneous firing of Purkinje neurons. *J. Neurosci.* 26, 4602–4612.

Almog, M., Korngreen, A., 2014. A quantitative description of dendritic conductances and its application to dendritic excitation in layer 5 pyramidal neurons. *J. Neurosci.* 34, 182–196.

Almog, M., Korngreen, A., 2009. Characterization of voltage-gated Ca²⁺ conductances in layer 5 neocortical pyramidal neurons from rats. *PLoS One* 4, e4841.

Amthor, F.R., Takahashi, E.S., Oyster, C.W., 1989. Morphologies of rabbit retinal ganglion cells with complex receptive fields. *J. Comp. Neurol.* 280, 97–121.

Armstrong, D.M., Harvey, R.J., Schild, R.F., 1973. The spatial organisation of climbing fibre branching in the cat cerebellum. *Exp. brain Res.* 18, 40–58.

Ascoli, G.A., 2006. Mobilizing the base of neuroscience data: the case of neuronal morphologies. *Nat. Rev. Neurosci.* 7, 318–324.

Baccus, S.A., Ölveczky, B.P., Manu, M., Meister, M., 2008. A retinal circuit that computes object motion. *J. Neurosci.* 28, 6807–6817.

Bakondi, G., Pór, A., Kovacs, I., Szűcs, G., Rusznák, Z., 2009. Hyperpolarization-activated, cyclic nucleotide-gated, cation non-selective channel subunit expression pattern of guinea-pig spiral ganglion cells. *Neuroscience* 158, 1469–1477.

Barlow, H., Hill, R.M., Levick, W.R., 1964. Retinal ganglion cells responding selectively to direction and speed of image motion in the rabbit. *J. Physiol.* 173, 377–407.

Barlow, H.B., Levick, W.R., 1965. The mechanism of directionally selective units in rabbit's retina. *J. Physiol.* 178, 477–504.

BeMent, S.L., Ranck Jr, J.B., 1969. A quantitative study of electrical stimulation of central myelinated fibers. *Exp. Neurol.* 24, 147–170.

Bender, K.J., Trussell, L.O., 2012. The physiology of the axon initial segment. *Annu. Rev. Neurosci.* 35, 249–265.

Berger, T., Larkum, M.E., Lüscher, H.-R., 2001. High I_h channel density in the distal apical dendrite of layer V pyramidal cells increases bidirectional attenuation of EPSPs. *J. Neurophysiol.* 85, 855–868.

Bhadra, N. and Kilgore, K.L., 2004. Direct current electrical conduction block of peripheral nerve. *IEEE Transactions on Neural Systems and Rehabilitation Engineering*, 12(3), pp.313-324.

Bierer, J.A., Faulkner, K.F., 2010. Identifying cochlear implant channels with poor electrode-neuron interface: partial tripolar, single-channel thresholds and psychophysical tuning curves. *Ear Hear.* 31, 247.

Bierer, J.A., Litvak, L., 2016. Reducing Channel Interaction Through Cochlear Implant Programming May Improve Speech Perception, in: *Trends in Hearing*. doi:10.1177/2331216516653389

References

- Black, R.C., Clark, G.M., Tong, Y.C., Patrick, J.F., 1983. CURRENT DISTRIBUTIONS IN COCHLEAR STIMULATION. *Ann. N. Y. Acad. Sci.* doi:10.1111/j.1749-6632.1983.tb31626.x
- Boiko, T., Rasband, M.N., Levinson, S.R., Caldwell, J.H., Mandel, G., Trimmer, J.S., Matthews, G., 2001. Compact myelin dictates the differential targeting of two sodium channel isoforms in the same axon. *Neuron* 30, 91–104.
- Boiko, T., Van Wart, A., Caldwell, J.H., Levinson, S.R., Trimmer, J.S., Matthews, G., 2003. Functional specialization of the axon initial segment by isoform-specific sodium channel targeting. *J. Neurosci.* 23, 2306–2313.
- Boinagrov, D., Pangratz-Fuehrer, S., Suh, B., Mathieson, K., Naik, N., Palanker, D., 2012. Upper threshold of extracellular neural stimulation. *J. Neurophysiol.* 108, 3233–3238.
- Boisvert, I., Reis, M., Au, A., Cowan, R., Dowell, R.C., 2020. Cochlear implantation outcomes in adults: A scoping review. *PLoS One* 15, e0232421.
- Briaire, J.J., Frijns, J.H.M., 2005. Unraveling the electrically evoked compound action potential. *Hear. Res.* doi:10.1016/j.heares.2005.03.020
- Brummer, S.B., Turner, M.J., 1977. Electrochemical considerations for safe electrical stimulation of the nervous system with platinum electrodes. *IEEE Trans. Biomed. Eng.* 59–63.
- Buitenweg, J.R., Rutten, W.L.C., Marani, E., 2002. Extracellular stimulation window explained by a geometry-based model of the neuron-electrode contact. *IEEE Trans. Biomed. Eng.* 49, 1591–1599.
- Butson, C.R., Cooper, S.E., Henderson, J.M., McIntyre, C.C., 2007. Patient-specific analysis of the volume of tissue activated during deep brain stimulation. *Neuroimage* 34, 661–670.
- Caldwell, J.H., Daw, N.W., 1978. New properties of rabbit retinal ganglion cells. *J. Physiol.* 276, 257–276.
- Caldwell, J.H., Schaller, K.L., Lasher, R.S., Peles, E., Levinson, S.R., 2000. Sodium channel Nav1. 6 is localized at nodes of Ranvier, dendrites, and synapses. *Proc. Natl. Acad. Sci.* 97, 5616–5620.
- Cameron, T., 2004. Safety and efficacy of spinal cord stimulation for the treatment of chronic pain: a 20-year literature review. *J. Neurosurg. Spine* 100, 254–267.
- Carnevale, N.T., Hines, M.L., 2006. *The NEURON book*. Cambridge University Press.
- Castagnola, V., 2014. Implantable microelectrodes on soft substrate with nanostructured active surface for stimulation and recording of brain activities.
- Catterall, W.A., Goldin, A.L., Waxman, S.G., 2005. International Union of Pharmacology. XLVII. Nomenclature and structure-function relationships of voltage-gated sodium channels. *Pharmacol. Rev.* 57, 397–409.
- Cayce, J.M., Friedman, R.M., Chen, G., Jansen, E.D., Mahadevan-Jansen, A., Roe, A.W., 2014. Infrared neural stimulation of primary visual cortex in non-human primates. *Neuroimage* 84, 181–190.
- Chen, C., 1997. Hyperpolarization-activated current (I_h) in primary auditory neurons. *Hear. Res.* 110, 179–190.
- Chen, J., Poulaki, V., Kim, S.-J., Eldred, W.D., Kane, S., Gingerich, M., Shire, D.B., Jensen, R., DeWalt, G., Kaplan, H.J., 2020. Implantation and extraction of penetrating electrode arrays in minipig retinas. *Transl. Vis. Sci. Technol.* 9, 19.
- Chen, W.C., Xue, H.Z., Hsu, Y.L., Liu, Q., Patel, S., Davis, R.L., 2011. Complex distribution patterns of voltage-gated calcium channel α -subunits in the spiral ganglion. *Hear. Res.* 278, 52–68.
- Chiu, S.Y., Ritchie, J.M., Rogart, R.B., Stagg, D., 1979. A quantitative description of membrane currents in rabbit myelinated nerve. *J. Physiol.* 292, 149–166.

References

- Chow, A.Y., Chow, V.Y., 1997. Subretinal electrical stimulation of the rabbit retina. *Neurosci. Lett.* 225, 13–16.
- Cleland, B.G., Levick, W.R., 1974. Brisk and sluggish concentrically organized ganglion cells in the cat's retina. *J. Physiol.* 240, 421–456.
- Coffey, R.J., 2001. Deep brain stimulation for chronic pain: results of two multicenter trials and a structured review. *Pain Med.* 2, 183–192.
- Cogan, S.F., 2008. Neural stimulation and recording electrodes. *Annu. Rev. Biomed. Eng.* 10, 275–309.
- Cogan, S.F., Ludwig, K.A., Welle, C.G., Takmakov, P., 2016. Tissue damage thresholds during therapeutic electrical stimulation. *J. Neural Eng.* 13, 21001.
- Cohen, Lawrence T and Xu, Jin and Xu, Shi Ang and Clark, G.M., 1996. Improved and simplified methods for specifying positions of the electrode bands of a cochlear implant array. *Sci. Publ.* 9.
- Cohen, C.C.H., Popovic, M.A., Klooster, J., Weil, M.-T., Möbius, W., Nave, K.-A., Kole, M.H.P., 2020. Saltatory conduction along myelinated axons involves a periaxonal nanocircuit. *Cell* 180, 311–322.
- Colbert, C.M., Johnston, D., 1996. Axonal action-potential initiation and Na⁺ channel densities in the soma and axon initial segment of subicular pyramidal neurons. *J. Neurosci.* 16, 6676–6686.
- Colbert, C.M., Pan, E., 2002. Ion channel properties underlying axonal action potential initiation in pyramidal neurons. *Nat. Neurosci.* 5, 533–538.
- Coombs, J.S., Curtis, D.R., Eccles, J., 1957. The generation of impulses in motoneurons. *J. Physiol.* 139, 232.
- Craner, M.J., Lo, A.C., Black, J.A., Waxman, S.G., 2003. Abnormal sodium channel distribution in optic nerve axons in a model of inflammatory demyelination. *Brain* 126, 1552–1561.
- Crank, J., Nicolson, P., 1947. A practical method for numerical evaluation of solutions of partial differential equations of the heat-conduction type, in: *Mathematical Proceedings of the Cambridge Philosophical Society*. Cambridge University Press, pp. 50–67.
- Crawford, A.C., Fettiplace, R., 1985. The mechanical properties of ciliary bundles of turtle cochlear hair cells. *J. Physiol.* 364, 359–379.
- Cullinan, W.E., Herman, J.P., Helmreich, D.L., Watson Jr, S.J., 1995. A neuroanatomy of stress.
- Curtiss, C.F., Hirschfelder, J.O., 1952. Integration of stiff equations. *Proc. Natl. Acad. Sci. U. S. A.* 38, 235.
- Davis, R.L., Liu, Q., 2011. Complex primary afferents: what the distribution of electrophysiologically-relevant phenotypes within the spiral ganglion tells us about peripheral neural coding. *Hear. Res.* 276, 34–43.
- Deister, C.A., Chan, C.S., Surmeier, D.J., Wilson, C.J., 2009. Calcium-activated SK channels influence voltage-gated ion channels to determine the precision of firing in globus pallidus neurons. *J. Neurosci.* 29, 8452–8461.
- Deschênes, M., Paradis, M., Roy, J.P., Steriade, M., 1984. Electrophysiology of neurons of lateral thalamic nuclei in cat: resting properties and burst discharges. *J. Neurophysiol.* 51, 1196–1219.
- Destexhe, A., Babloyantz, A., Sejnowski, T.J., 1993. Ionic mechanisms for intrinsic slow oscillations in thalamic relay neurons. *Biophys. J.* 65, 1538–1552.
- Dhande, O.S., Estevez, M.E., Quattrochi, L.E., El-Danaf, R.N., Nguyen, P.L., Berson, D.M., Huberman, A.D., 2013. Genetic dissection of retinal inputs to brainstem nuclei controlling image stabilization. *J. Neurosci.* 33, 17797–17813.
- Do, M.T.H., Yau, K.-W., 2010. Intrinsically photosensitive retinal ganglion cells. *Physiol. Rev.*

References

- Duke, A.R., Jenkins, M.W., Lu, H., McManus, J.M., Chiel, H.J., Jansen, E.D., 2013. Transient and selective suppression of neural activity with infrared light. *Sci. Rep.* 3, 1–8.
- Duke, A.R., Lu, H., Jenkins, M.W., Chiel, H.J., Jansen, E.D., 2012. Spatial and temporal variability in response to hybrid electro-optical stimulation. *J. Neural Eng.* 9, 36003.
- Eckmiller, R., 1997. Learning retina implants with epiretinal contacts. *Ophthalmic Res.* 29, 281–289.
- Eickenscheidt, M., Zeck, G., 2014. Action potentials in retinal ganglion cells are initiated at the site of maximal curvature of the extracellular potential. *J. Neural Eng.* doi:10.1088/1741-2560/11/3/036006
- Ellis, T.-M., Foote, K.D., Fernandez, H.H., Sudhyadhom, A., Rodriguez, R.L., Zeilman, P., Jacobson IV, C.E., Okun, M.S., 2008. Reoperation for suboptimal outcomes after deep brain stimulation surgery. *Neurosurgery* 63, 754–761.
- Famiglietti, E. V., Kaneko, A., Tachibana, M., 1977. Neuronal architecture of on and off pathways to ganglion cells in carp retina. *Science* (80-.). 198, 1267–1269.
- Famiglietti, E. V., Kolb, H., 1976. Structural basis for ON-and OFF-center responses in retinal ganglion cells. *Science* (80-.). 194, 193–195.
- Fang, Z.P., Mortimer, J.T., 1987. A method for attaining natural recruitment order in artificially activated muscles, in: *Proc. 9th Annu. Conf. IEEE Eng. Med. Biol. Soc.* pp. 657–658.
- Fatt, P., 1957. Sequence of events in synaptic activation of a motoneurone. *J. Neurophysiol.* 20, 61–80.
- Felder, E., Kanonier, G., Scholtz, A., Rask-Andersen, H., A Schrott-Fischer, A., 1997. Quantitative evaluation of cochlear neuronal and computer-aided three-dimensional reconstruction of spiral ganglion cells in humans with a peripheral loss of nerve fibres. *Hear. Res.* doi:10.1016/S0378-5955(96)00209-2
- Feldmeyer, D., 2015. Functional and Structural Diversity of Pyramidal Cells.
- Fellner, A., Stiennon, I., Rattay, F., 2019. Analysis of upper threshold mechanisms of spherical neurons during extracellular stimulation. *J. Neurophysiol.* 121, 1315–1328.
- Finley, C.C., Wilson, B.S., White, M.W., 2011. Models of Neural Responsiveness to Electrical Stimulation, in: *Cochlear Implants.* doi:10.1007/978-1-4612-3256-8_5
- Foehring, R.C., Mermelstein, P.G., Song, W.-J., Ulrich, S., Surmeier, D.J., 2000. Unique properties of R-type calcium currents in neocortical and neostriatal neurons. *J. Neurophysiol.* 84, 2225–2236.
- Fohlmeister, J.F., Cohen, E.D., Newman, E.A., 2010. Mechanisms and distribution of ion channels in retinal ganglion cells: using temperature as an independent variable. *J. Neurophysiol.* 103, 1357–1374.
- Fohlmeister, J.F., Coleman, P.A., Miller, R.F., 1990. Modeling the repetitive firing of retinal ganglion cells. *Brain Res.* 510, 343–345.
- Fohlmeister, J.F., Miller, R.F., 1997. Impulse encoding mechanisms of ganglion cells in the tiger salamander retina. *J. Neurophysiol.* 78, 1935–1947.
- Frankenhaeuser, B., Huxley, A.F., 1964. The action potential in the myelinated nerve fibre of *Xenopus laevis* as computed on the basis of voltage clamp data. *J. Physiol.* 171, 302–315.
- Fried, S.I., Lasker, A.C.W., Desai, N.J., Eddington, D.K., Rizzo 3rd, J.F., 2009. Axonal sodium-channel bands shape the response to electric stimulation in retinal ganglion cells. *J. Neurophysiol.* 101, 1972–1987.
- Frijns, J.H.M., de Snoo, S.L., Schoonhoven, R., 1995. Potential distributions and neural excitation patterns in a rotationally symmetric model of the electrically stimulated cochlea. *Hear. Res.* doi:10.1016/0378-5955(95)00090-Q
- Fryatt, A.G., Vial, C., Mulheran, M., Gunthorpe, M.J., Grubb, B.D., 2009. Voltage-gated sodium channel expression in rat spiral ganglion neurons. *Mol. Cell. Neurosci.* 42, 399–407.

References

- Fuortes, M.G.F., Frank, K., Becker, M.C., 1957. Steps in the production of motoneuron spikes. *J. Gen. Physiol.* 40, 735–752.
- Garnhamt, C.W., Barker, A.T., Freeston, I.L., 1995. Measurement of the activating function of magnetic stimulation using combined electrical and magnetic stimuli. *J. Med. Eng. Technol.* 19, 57–61.
- Gasparini, S., Migliore, M., Magee, J.C., 2004. On the initiation and propagation of dendritic spikes in CA1 pyramidal neurons. *J. Neurosci.* 24, 11046–11056.
- Goldman, D.E., 1943. Potential, impedance, and rectification in membranes. *J. Gen. Physiol.* 27, 37–60.
- Guo, C., Peng, J., Zhang, Y., Li, A., Li, Y., Yuan, J., Xu, X., Ren, M., Gong, H., Chen, S., 2017. Single-axon level morphological analysis of corticofugal projection neurons in mouse barrel field. *Sci. Rep.* 7, 1–9.
- Guo, T., Tsai, D., Bai, S., Morley, J.W., Suaning, G.J., Lovell, N.H., Dokos, S., 2014. Understanding the retina: A review of computational models of the retina from the single cell to the network level. *Crit. Rev. Biomed. Eng.* 42.
- Gutman, G.A., Chandy, K.G., Adelman, J.P., Aiyar, J., Bayliss, D.A., Clapham, D.E., Covarriubias, M., Desir, G. V, Furuichi, K., Ganetzky, B., 2003. International Union of Pharmacology. XLI. Compendium of voltage-gated ion channels: potassium channels. *Pharmacol. Rev.* 55, 583–586.
- Hanekom, T., 2001. Three-dimensional spiraling finite element model of the electrically stimulated cochlea. *Ear Hear.* doi:10.1097/00003446-200108000-00005
- Hattar, S., Liao, H.-W., Takao, M., Berson, D.M., Yau, K.-W., 2002. Melanopsin-containing retinal ganglion cells: architecture, projections, and intrinsic photosensitivity. *Science* (80-.). 295, 1065–1070.
- Hattar, S., Lucas, R.J., Mrosovsky, N., Thompson, S., Douglas, R.H., Hankins, M.W., Lem, J., Biel, M., Hofmann, F., Foster, R.G., 2003. Melanopsin and rod–cone photoreceptive systems account for all major accessory visual functions in mice. *Nature* 424, 75–81.
- Häusser, M., Spruston, N., Stuart, G.J., 2000. Diversity and dynamics of dendritic signaling. *Science* (80-.). 290, 739–744.
- Hay, E., Schürmann, F., Markram, H., Segev, I., 2013. Preserving axosomatic spiking features despite diverse dendritic morphology. *J. Neurophysiol.* 109, 2972–2981.
- Henderson, D., Miller, R.F., 2007. Low-voltage activated calcium currents in ganglion cells of the tiger salamander retina: experiment and simulation. *Vis. Neurosci.* 24, 37–51.
- Henne, J., Pöttering, S., Jeserich, G., 2000. Voltage-gated potassium channels in retinal ganglion cells of trout: A combined biophysical, pharmacological, and single-cell RT-PCR approach. *J. Neurosci. Res.* 62, 629–637.
- Heshmat, A., Sajedi, S., Chacko, L.J., Fischer, N., Schrott-Fischer, A., Rattay, F., 2020. Dendritic Degeneration of Human Auditory Nerve Fibers and Its Impact on the Spiking Pattern Under Regular Conditions and During Cochlear Implant Stimulation. *Front. Neurosci.* 14.
- Heshmat, A., Sajedi, S., Schrott-Fischer, A., Rattay, F., n.d. Polarity sensitivity of human auditory nerve fibers based on pulse shape, cochlear implant stimulation strategy and array. *Front. Neurosci.* 1624.
- Hochmair, I., Hochmair, E., Nopp, P., Waller, M., Jolly, C., 2015. Deep electrode insertion and sound coding in cochlear implants. *Hear. Res.* doi:10.1016/j.heares.2014.10.006
- Hodaie, M., Wennberg, R.A., Dostrovsky, J.O., Lozano, A.M., 2002. Chronic anterior thalamus stimulation for intractable epilepsy. *Epilepsia* 43, 603–608.
- Hodgkin, A.L., Huxley, A.F., 1952. A quantitative description of ion currents and its applications to conduction and excitation in nerve. *J Physiol.* doi:10.1113/jphysiol.1952.sp004764

References

- Hodgkin, A.L., Rushton, W.A.H., 1946. The electrical constants of a crustacean nerve fibre. *Proc. R. Soc. London. Ser. B-Biological Sci.* 133, 444–479.
- Höltje, M., Brunk, I., Grosse, J., Beyer, E., Veh, R.W., Bergmann, M., Grosse, G., Ahnert-Hilger, G., 2007. Differential distribution of voltage-gated potassium channels Kv 1.1–Kv1. 6 in the rat retina during development. *J. Neurosci. Res.* 85, 19–33.
- Hossain, W.A., Antic, S.D., Yang, Y., Rasband, M.N., Morest, D.K., 2005. Where is the spike generator of the cochlear nerve? Voltage-gated sodium channels in the mouse cochlea. *J. Neurosci.* doi:10.1523/JNEUROSCI.0123-05.2005
- Hu, W., Tian, C., Li, T., Yang, M., Hou, H., Shu, Y., 2009. Distinct contributions of Na v 1.6 and Na v 1.2 in action potential initiation and backpropagation. *Nat. Neurosci.* 12, 996–1002.
- Hudspeth, A.J., 1989. How the ear's works work. *Nature* 341, 397–404.
- Huguenard, J.R., Prince, D.A., 1992. A novel T-type current underlies prolonged Ca (2+)-dependent burst firing in GABAergic neurons of rat thalamic reticular nucleus. *J. Neurosci.* 12, 3804–3817.
- Huguenard, J.R., Prince, D.A., 1991. Slow inactivation of a TEA-sensitive K current in acutely isolated rat thalamic relay neurons. *J. Neurophysiol.* 66, 1316–1328.
- Humayun, M.S., De Juan, E., Dagnelie, G., Greenberg, R.J., Propst, R.H., Phillips, D.H., 1996. Visual perception elicited by electrical stimulation of retina in blind humans. *Arch. Ophthalmol.* 114, 40–46.
- Humayun, M.S., de Juan Jr, E., Weiland, J.D., Dagnelie, G., Katona, S., Greenberg, R., Suzuki, S., 1999. Pattern electrical stimulation of the human retina. *Vision Res.* 39, 2569–2576.
- Inda, M.C., DeFelipe, J., Muñoz, A., 2006. Voltage-gated ion channels in the axon initial segment of human cortical pyramidal cells and their relationship with chandelier cells. *Proc. Natl. Acad. Sci.* 103, 2920–2925.
- Jahn, K.N., Arenberg, J.G., 2019. Polarity Sensitivity in Pediatric and Adult Cochlear Implant Listeners. *Trends Hear.* doi:10.1177/2331216519862987
- Jankowska, E., Roberts, W.J., 1972. An electrophysiological demonstration of the axonal projections of single spinal interneurons in the cat. *J. Physiol.* 222, 597–622.
- Jankowska, E., Smith, D.O., 1973. Antidromic activation of Renshaw cells and their axonal projections. *Acta Physiol. Scand.* 88, 198–214.
- Jansen, H., 1984. Ionic basis for the electroresponsiveness and oscillatory properties of guinea-pig thalamic neurons in vitro. *J Physiol* 349, 227–247.
- Javel, E., Shepherd, R.K., 2000. Electrical stimulation of the auditory nerve. III. Response initiation sites and temporal fine structure. *Hear. Res.* doi:10.1016/S0378-5955(99)00186-0
- Jeng, J., Tang, S., Molnar, A., Desai, N.J., Fried, S.I., 2011. The sodium channel band shapes the response to electric stimulation in retinal ganglion cells. *J. Neural Eng.* 8, 36022.
- Jezernik, S., Craggs, M., Grill, W.M., Creasey, G., Rijkhoff, N.J.M., 2002. Electrical stimulation for the treatment of bladder dysfunction: current status and future possibilities. *Neurol. Res.* 24, 413–430.
- Johnston, D., 2003. Christie BR, Frick A, Gray R, Hoffman DA, Schexnayder LK, Watanabe S, and Yuan LL. Act. dendrites, potassium channels synaptic Plast. *Philos Trans R Soc L. B Biol Sci* 358, 667–674.
- Johnston, D., Christie, B.R., Frick, A., Gray, R., Hoffman, D.A., Schexnayder, L.K., Watanabe, S., Yuan, L.-L., 2003. Active dendrites, potassium channels and synaptic plasticity. *Philos. Trans. R. Soc. London. Ser. B Biol. Sci.* 358, 667–674.
- Kalkman, R.K., Briare, J.J., Dekker, D.M.T., Frijns, J.H.M., 2014. Place pitch versus electrode location in a realistic computational model of the implanted human cochlea. *Hear. Res.* doi:10.1016/j.heares.2014.06.003

References

- Kameneva, T., Meffin, H., Burkitt, A.N., 2011. Modelling intrinsic electrophysiological properties of ON and OFF retinal ganglion cells. *J. Comput. Neurosci.* 31, 547–561.
- Kampa, B.M., Letzkus, J.J., Stuart, G.J., 2007. Dendritic mechanisms controlling spike-timing-dependent synaptic plasticity. *Trends Neurosci.* 30, 456–463.
- Kaneda, M., Kaneko, A., 1991. Voltage-gated sodium currents in isolated retinal ganglion cells of the cat: relation between the inactivation kinetics and the cell type. *Neurosci. Res.* 11, 261–275.
- Kaneko, Y., Watanabe, S.-I., 2007. Expression of Nav1. 1 in rat retinal AII amacrine cells. *Neurosci. Lett.* 424, 83–88.
- Kaniasus, E., 2012. Biomedical signals and sensors I: Linking physiological phenomena and biosignals. Springer Science & Business Media.
- Katz, B., Miledi, R., 1965. Propagation of electric activity in motor nerve terminals. *Proc. R. Soc. London. Ser. B. Biol. Sci.* 161, 453–482.
- Kay, J.N., Chu, M.W., Sanes, J.R., 2012. MEGF10 and MEGF11 mediate homotypic interactions required for mosaic spacing of retinal neurons. *Nature* 483, 465–469.
- Keren, N., Peled, N., Korngreen, A., 2005. Constraining compartmental models using multiple voltage recordings and genetic algorithms. *J. Neurophysiol.*
- Khaliq, Z.M., Gouwens, N.W., Raman, I.M., 2003. The contribution of resurgent sodium current to high-frequency firing in Purkinje neurons: an experimental and modeling study. *J. Neurosci.* 23, 4899–4912.
- Kilgore, K.L., 2015. Introduction and fundamental requirements of neuroprostheses, in: *Implantable Neuroprostheses for Restoring Function*. Elsevier, pp. 3–11.
- Kim, Y.-H., Holt, J.R., 2013. Functional contributions of HCN channels in the primary auditory neurons of the mouse inner ear. *J. Gen. Physiol.* 142, 207–223.
- Kirkpatrick, S., Gelatt, C.D., Vecchi, M.P., 1983. Optimization by simulated annealing. *Science (80-)*. 220, 671–680.
- Kole, M.H.P., Ilschner, S.U., Kampa, B.M., Williams, S.R., Ruben, P.C., Stuart, G.J., 2008. Action potential generation requires a high sodium channel density in the axon initial segment. *Nat. Neurosci.* 11, 178–186.
- Kole, M.H.P., Letzkus, J.J., Stuart, G.J., 2007. Axon initial segment Kv1 channels control axonal action potential waveform and synaptic efficacy. *Neuron* 55, 633–647.
- Komada, M., Soriano, P., 2002. β IV-spectrin regulates sodium channel clustering through ankyrin-G at axon initial segments and nodes of Ranvier. *J. Cell Biol.* 156, 337–348.
- Kuffler, S.W., 1953. Discharge patterns and functional organization of mammalian retina. *J. Neurophysiol.* 16, 37–68.
- Kuhn, A., Keller, T., Lawrence, M., Morari, M., 2009. A model for transcutaneous current stimulation: simulations and experiments. *Med. Biol. Eng. Comput.* 47, 279–289.
- Kuhn, J., Gründler, T.O.J., Lenartz, D., Sturm, V., Klosterkötter, J., Huff, W., 2010. Deep brain stimulation for psychiatric disorders. *Dtsch. Arztebl. Int.* 107, 105.
- Kuncel, A.M., Grill, W.M., 2004. Selection of stimulus parameters for deep brain stimulation. *Clin. Neurophysiol.* 115, 2431–2441.
- Laback, B., Egger, K., Majdak, P., 2015. Perception and coding of interaural time differences with bilateral cochlear implants. *Hear. Res.* doi:10.1016/j.heares.2014.10.004
- Learning, L., 2021. Hearing and Equilibrium | Anatomy and Physiology [WWW Document]. URL <https://courses.lumenlearning.com/nemcc-ap/chapter/special-senses-hearing-audition-and-balance/> (accessed 11.15.21).

References

- Ledergerber, D., Larkum, M.E., 2010. Properties of layer 6 pyramidal neuron apical dendrites. *J. Neurosci.* 30, 13031–13044.
- Lee, S.C., Hayashida, Y., Ishida, A.T., 2003. Availability of low-threshold Ca²⁺ current in retinal ganglion cells. *J. Neurophysiol.* 90, 3888–3901.
- Letierrier, C., 2018. The axon initial segment: an updated viewpoint. *J. Neurosci.* 38, 2135–2145.
- Levick, W.R., 1967. Receptive fields and trigger features of ganglion cells in the visual streak of the rabbit's retina. *J. Physiol.* 188, 285–307.
- Lieberman, M.C., 2020. Hidden hearing loss: Primary neural degeneration in the noise-damaged and aging cochlea. *Acoust. Sci. Technol.* 41, 59–62.
- Lieberman, M.C., Oliver, M.E., 1984. Morphometry of intracellularly labeled neurons of the auditory nerve: correlations with functional properties. *J. Comp. Neurol.* 223, 163–176.
- Limousin, P., Speelman, J.D., Gielen, F., Janssens, M., 1999. Multicentre European study of thalamic stimulation in parkinsonian and essential tremor. *J. Neurol. Neurosurg. Psychiatry* 66, 289–296.
- Litovsky, R.Y., Parkinson, A., Arcaroli, J., 2009. Spatial hearing and speech intelligibility in bilateral cochlear implant users. *Ear Hear.* doi:10.1097/AUD.0b013e3181a165be
- Liu, Q., Lee, E., Davis, R.L., 2014a. Heterogeneous intrinsic excitability of murine spiral ganglion neurons is determined by Kv1 and HCN channels. *Neuroscience* 257, 96–110.
- Liu, Q., Manis, P.B., Davis, R.L., 2014b. Ih and HCN channels in murine spiral ganglion neurons: tonotopic variation, local heterogeneity, and kinetic model. *J. Assoc. Res. Otolaryngol.* 15, 585–599.
- Long, C.J., Holden, T.A., McClelland, G.H., Parkinson, W.S., Shelton, C., Kelsall, D.C., Smith, Z.M., 2014. Examining the electro-neural interface of cochlear implant users using psychophysics, CT scans, and speech understanding. *JARO - J. Assoc. Res. Otolaryngol.* doi:10.1007/s10162-013-0437-5
- Lopez, I., Ishiyama, G., Acuna, D., Ishiyama, A., Baloh, R.W., 2003. Immunolocalization of voltage-gated calcium channel $\alpha 1$ subunits in the chinchilla cochlea. *Cell Tissue Res.* 313, 177–186.
- Lothet, E.H., Shaw, K.M., Lu, H., Zhuo, J., Wang, Y.T., Gu, S., Stolz, D.B., Jansen, E.D., Horn, C.C., Chiel, H.J., 2017. Selective inhibition of small-diameter axons using infrared light. *Sci. Rep.* 7, 1–8.
- Lv, P., Kim, H.J., Lee, J.-H., Sihm, C.-R., Gharai, S.F., Mousavi-Nik, A., Wang, W., Wang, H.-G., Gratton, M.A., Doyle, K.J., 2014. Genetic, cellular, and functional evidence for Ca²⁺ inflow through Cav1. 2 and Cav1. 3 channels in murine spiral ganglion neurons. *J. Neurosci.* 34, 7383–7393.
- Lv, P., Sihm, C.-R., Wang, W., Shen, H., Kim, H.J., Rocha-Sanchez, S.M., Yamoah, E.N., 2012. Posthearing Ca²⁺ currents and their roles in shaping the different modes of firing of spiral ganglion neurons. *J. Neurosci.* 32, 16314–16330.
- Macherey, O., Carlyon, R.P., Van Wieringen, A., Deeks, J.M., Wouters, J., 2008. Higher sensitivity of human auditory nerve fibers to positive electrical currents. *JARO - J. Assoc. Res. Otolaryngol.* doi:10.1007/s10162-008-0112-4
- Magee, J.C., 1999. Dendritic Ih normalizes temporal summation in hippocampal CA1 neurons. *Nat. Neurosci.* 2, 508–514.
- Magistretti, J., Brevi, S., De Curtis, M., 2000. A blocker-resistant, fast-decaying, intermediate-threshold calcium current in palaeocortical pyramidal neurons. *Eur. J. Neurosci.* 12, 2376–2386.
- Mainen, Z.F., Sejnowski, T.J., 1996. Influence of dendritic structure on firing pattern in model neocortical neurons. *Nature* 382, 363–366.
- Mangado, N., Pons-Prats, J., Coma, M., Mistrík, P., Piella, G., Ceresa, M., Ballester, M.Á.G., 2018. Computational evaluation of cochlear implant surgery outcomes accounting for uncertainty and parameter variability. *Front Physiol.* doi:10.3389/fphys.2018.00498

References

- Martina, M., Vida, I., Jonas, P., 2000. Distal initiation and active propagation of action potentials in interneuron dendrites. *Science* (80-.). 287, 295–300.
- Masland, R.H., 2012. The neuronal organization of the retina. *Neuron* 76, 266–280.
- Mathieson, K., Loudin, J., Goetz, G., Huie, P., Wang, L., Kamins, T.I., Galambos, L., Smith, R., Harris, J.S., Sher, A., 2012. Photovoltaic retinal prosthesis with high pixel density. *Nat. Photonics* 6, 391–397.
- Matic, A.I., Robinson, A.M., Young, H.K., Badofsky, B., Rajguru, S.M., Stock, S., Richter, C.-P., 2013. Behavioral and electrophysiological responses evoked by chronic infrared neural stimulation of the cochlea. *PLoS One* 8, e58189.
- Mayberg, H.S., Lozano, A.M., Voon, V., McNeely, H.E., Seminowicz, D., Hamani, C., Schwalb, J.M., Kennedy, S.H., 2005. Deep brain stimulation for treatment-resistant depression. *Neuron* 45, 651–660.
- Mazzoni, F., Novelli, E., Strettoi, E., 2008. Retinal ganglion cells survive and maintain normal dendritic morphology in a mouse model of inherited photoreceptor degeneration. *J. Neurosci.* 28, 14282–14292.
- McCORMICK, D.A., Pape, H.-C., 1990. Properties of a hyperpolarization-activated cation current and its role in rhythmic oscillation in thalamic relay neurones. *J. Physiol.* 431, 291–318.
- McCreery, D.B., Agnew, W.F., Bullara, L.A., 2002. The effects of prolonged intracortical microstimulation on the excitability of pyramidal tract neurons in the cat. *Ann. Biomed. Eng.* 30, 107–119.
- McCreery, D.B., Agnew, W.F., Yuen, T.G.H., Bullara, L., 1990. Charge density and charge per phase as cofactors in neural injury induced by electrical stimulation. *IEEE Trans. Biomed. Eng.* 37, 996–1001.
- McCreery, D.B., Yuen, T.G.H., Agnew, W.F., Bullara, L.A., 1994. Stimulus parameters affecting tissue injury during microstimulation in the cochlear nucleus of the cat. *Hear. Res.* 77, 105–115.
- McCreery, D.B., Yuen, T.G.H., Bullara, L.A., 2000. Chronic microstimulation in the feline ventral cochlear nucleus: physiologic and histologic effects. *Hear. Res.* 149, 223–238.
- McHanwell, S., Brenner, E., Chirculescu, A.R.M., Drukker, J., van Mameren, H., Mazzotti, G., Pais, D., Paulsen, F., Plaisant, O., Caillaud, M.M., Laforêt, E., Riedere, B.M., Sañudo, J.R., Bueno-López, J.L., Doñate-Oliver, F., Sprumont, P., Teofilovski-Parapid, G., Moxham, B.J., 2008. The legal and ethical framework governing Body Donation in Europe - A review of current practice and recommendations for good practice. *Eur. J. Anat.*
- McIntyre, C.C., Richardson, A.G., Grill, W.M., 2002. Modeling the excitability of mammalian nerve fibers: influence of afterpotentials on the recovery cycle. *J. Neurophysiol.* 87, 995–1006.
- McNeal, D.R., 1976. Analysis of a model for excitation of myelinated nerve. *IEEE Trans. Biomed. Eng.* 329–337.
- Meng, K., Fellner, A., Rattay, F., Ghezzi, D., Meffin, H., Ibbotson, M.R., Kameneva, T., 2018. Upper stimulation threshold for retinal ganglion cell activation. *J. Neural Eng.* 15, 46012.
- Mercer, J.N., Chan, C.S., Tkatch, T., Held, J., Surmeier, D.J., 2007. Nav1. 6 sodium channels are critical to pacemaking and fast spiking in globus pallidus neurons. *J. Neurosci.* 27, 13552–13566.
- Middlebrooks, J.C., Snyder, R.L., 2008. Intraneural stimulation for auditory prosthesis: modiolar trunk and intracranial stimulation sites. *Hear. Res.* 242, 52–63.
- Migliore, M., Shepherd, G.M., 2002. Emerging rules for the distributions of active dendritic conductances. *Nat. Rev. Neurosci.* 3, 362–370.
- Mitchell, M., 1998. An introduction to genetic algorithms. MIT press.
- Mohs, R., Bloom, F.E., Kupfer, D.J., 2000. *Psychopharmacology: 4th Generation of Progress.*
- Montgomery Jr, E.B., 1999. Deep brain stimulation reduces symptoms of Parkinson disease. *Cleve. Clin. J. Med.* 66, 9–11.

References

- Morgan, J., Wong, R., 2007. Development of cell types and synaptic connections in the retina. *Webvision Organ. Retin. Vis. Syst.* [Internet].
- Motz, H., Rattay, F., 1986. A study of the application of the Hodgkin-Huxley and the Frankenhaeuser-Huxley model for electrostimulation of the acoustic nerve. *Neuroscience*. doi:10.1016/0306-4522(86)90064-3
- Nernst, W., 1888. Zur kinetik der in lösung befindlichen körper. *Zeitschrift für Phys. Chemie* 2, 613–637.
- Newman, J., 1966. Resistance for flow of current to a disk. *J. Electrochem. Soc* 113, 501–502.
- Nguyen, H.T., Tangutooru, S.M., Rountree, C.M., Kantzos, A.J., Tarlochan, F., Yoon, W.J., Troy, J.B., 2016. Thalamic visual prosthesis. *IEEE Trans. Biomed. Eng.* 63, 1573–1580.
- Nowak, L.G., Bullier, J., 1998. Axons, but not cell bodies, are activated by electrical stimulation in cortical gray matter II. Evidence from selective inactivation of cell bodies and axon initial segments. *Exp. brain Res.* 118, 489–500.
- Nowak, L.G., Bullier, J., 1996. Spread of stimulating current in the cortical grey matter of rat visual cortex studied on a new in vitro slice preparation. *J. Neurosci. Methods* 67, 237–248.
- Oak, M.-H., Yi, E., 2014. Voltage-gated K⁺ channels contributing to temporal precision at the inner hair cell-auditory afferent nerve fiber synapses in the mammalian cochlea. *Arch. Pharm. Res.* 37, 821–833.
- Okun, M.S., Rodriguez, R.L., Foote, K.D., Sudhyadhom, A., Bova, F., Jacobson, C., Bello, B., Zeilman, P., Fernandez, H.H., 2008. A case-based review of troubleshooting deep brain stimulator issues in movement and neuropsychiatric disorders. *Parkinsonism Relat. Disord.* 14, 532–538.
- Okun, M.S., Tagliati, M., Pourfar, M., Fernandez, H.H., Rodriguez, R.L., Alterman, R.L., Foote, K.D., 2005. Management of referred deep brain stimulation failures: a retrospective analysis from 2 movement disorders centers. *Arch. Neurol.* 62, 1250–1255.
- Ota, C.Y., Kimura, R.S., 1980. Ultrastructural study of the human spiral ganglion. *Acta Otolaryngol.* doi:10.3109/00016488009127108
- Overmyer, K.M., Pearce, J.A., DeWitt, D.P., 1979. Measurements of temperature distributions at electro-surgical dispersive electrode sites.
- Palmer, L.M., Stuart, G.J., 2006. Site of action potential initiation in layer 5 pyramidal neurons. *J. Neurosci.* 26, 1854–1863.
- Panda, S., Sato, T.K., Castrucci, A.M., Rollag, M.D., DeGrip, W.J., Hogenesch, J.B., Provencio, I., Kay, S.A., 2002. Melanopsin (Opn4) requirement for normal light-induced circadian phase shifting. *Science* (80- .). 298, 2213–2216.
- Pang, J.-J., Gao, F., Wu, S.M., 2003. Light-evoked excitatory and inhibitory synaptic inputs to ON and OFF α ganglion cells in the mouse retina. *J. Neurosci.* 23, 6063–6073.
- Pape, H.-C., 1996. Queer current and pacemaker: the hyperpolarization-activated cation current in neurons. *Annu. Rev. Physiol.* 58, 299–327.
- Pereda, A.E., 2014. Electrical synapses and their functional interactions with chemical synapses. *Nat. Rev. Neurosci.* 15, 250–263.
- Perlmutter, J.S., Mink, J.W., 2006. Deep brain stimulation. *Annu. Rev. Neurosci.* 29, 229–257.
- Pollard, C.E., Crunelli, V., 1988. Intrinsic membrane currents in projection cells of the cat and rat lateral geniculate nucleus. *Neurosci Lett* 32, S39.
- Pollock, N.S., Ferguson, S.C.D., McFarlane, S., 2002. Expression of voltage-dependent potassium channels in the developing visual system of *Xenopus laevis*. *J. Comp. Neurol.* 452, 381–391.
- Porter, R., 1963. Focal stimulation of hypoglossal neurones in the cat. *J. Physiol.* 169, 630.

References

- Potrusil, T., 2013. Human cochlear nerve model: data collection and simulation.
- Potrusil, T., Heshmat, A., Sajedi, S., Wenger, C., Chacko, L.J., Glueckert, R., Schrott-Fischer, A., Rattay, F., 2020. Finite Element Analysis and Three-Dimensional Reconstruction of Tonotopically Aligned Human Auditory Fiber Pathways: A Computational Environment for Modeling Electrical Stimulation by a Cochlear Implant based on micro-CT. *Hear. Res.* 108001. doi:<https://doi.org/10.1016/j.heares.2020.108001>
- Potrusil, T., Wenger, C., Glueckert, R., Schrott-Fischer, A., Rattay, F., 2012. Morphometric classification and spatial organization of spiral ganglion neurons in the human cochlea: Consequences for single fiber response to electrical stimulation. *Neuroscience*. doi:[10.1016/j.neuroscience.2012.03.033](https://doi.org/10.1016/j.neuroscience.2012.03.033)
- Qiu, X., Kumbalasiri, T., Carlson, S.M., Wong, K.Y., Krishna, V., Provencio, I., Berson, D.M., 2005. Induction of photosensitivity by heterologous expression of melanopsin. *Nature* 433, 745–749.
- Ranck, J.B., 1975. Which elements are excited in electrical stimulation of mammalian central nervous system: A review. *Brain Res.* doi:[10.1016/0006-8993\(75\)90364-9](https://doi.org/10.1016/0006-8993(75)90364-9)
- Rattay, F., 2014. On the upper threshold phenomenon of extracellular neural stimulation. *J. Neurophysiol.* 112, 2664–2665.
- Rattay, F., 2008. Current distance relations for fiber stimulation with point sources. *IEEE Trans. Biomed. Eng.* doi:[10.1109/TBME.2008.915676](https://doi.org/10.1109/TBME.2008.915676)
- Rattay, F., 1999. The basic mechanism for the electrical stimulation of the nervous system. *Neuroscience*. doi:[10.1016/S0306-4522\(98\)00330-3](https://doi.org/10.1016/S0306-4522(98)00330-3)
- Rattay, F., 1990. Electrical Nerve Stimulation: Theory, Experiments, and Applications - Back Matter, in: *Electrical Nerve Stimulation: Theory, Experiments, and Applications*.
- Rattay, F., 1989. Analysis of models for extracellular fiber stimulation. *IEEE Trans. Biomed. Eng.* 36, 676–682.
- Rattay, F., 1986. Analysis of Models for External Stimulation of Axons. *IEEE Trans. Biomed. Eng.* doi:[10.1109/TBME.1986.325670](https://doi.org/10.1109/TBME.1986.325670)
- Rattay, F., Aberham, M., 1993. Modeling Axon Membranes for Functional Electrical Stimulation. *IEEE Trans. Biomed. Eng.* doi:[10.1109/10.250575](https://doi.org/10.1109/10.250575)
- Rattay, F., Bassereh, H., Fellner, A., 2017. Impact of Electrode Position on the Elicitation of Sodium Spikes in Retinal Bipolar Cells. *Sci. Rep.* doi:[10.1038/s41598-017-17603-8](https://doi.org/10.1038/s41598-017-17603-8)
- Rattay, F., Danner, S.M., 2014. Peak I of the human auditory brainstem response results from the somatic regions of type I spiral ganglion cells: evidence from computer modeling. *Hear. Res.* 315, 67–79.
- Rattay, F., Danner, S.M., Hofstoetter, U.S., Minassian, K., 2014. Finite Element Modeling for Extracellular Stimulation.
- Rattay, F., Greenberg, R.J., Resatz, S., 2003. „Neuron Modeling“, in: *Handbook of Neuroprosthetic Methods*, eds. Finn WE, LoPresti PG.
- Rattay, F., Leao, R.N., Felix, H., 2001a. A model of the electrically excited human cochlear neuron. II. Influence of the three-dimensional cochlear structure on neural excitability. *Hear. Res.* doi:[10.1016/S0378-5955\(00\)00257-4](https://doi.org/10.1016/S0378-5955(00)00257-4)
- Rattay, F., Lutter, P., Felix, H., 2001b. A model of the electrically excited human cochlear neuron I. Contribution of neural substructures to the generation and propagation of spikes. *Hear. Res.* doi:[10.1016/S0378-5955\(00\)00256-2](https://doi.org/10.1016/S0378-5955(00)00256-2)
- Rattay, F., Paredes, L.P., Leao, R.N., 2012. Strength–duration relationship for intra-versus extracellular stimulation with microelectrodes. *Neuroscience* 214, 1–13.
- Rattay, F., Wenger, C., 2010. Which elements of the mammalian central nervous system are excited by low current stimulation with microelectrodes? *Neuroscience* 170, 399–407.

References

- Reijntjes, D.O.J., Pyott, S.J., 2016. The afferent signaling complex: regulation of type I spiral ganglion neuron responses in the auditory periphery. *Hear. Res.* 336, 1–16.
- Riederer, B.M., Bolt, S., Brenner, E., Bueno-López, J.L., Circulescu, A.R.M., Davies, D.C., De Caro, R., Gerrits, P.O., McHanwell, S., Pais, D., Paulsen, F., Plaisant, O., Sendemir, E., Stabile, I., Moxham, B.J., 2012. The legal and ethical framework governing Body Donation in Europe - 1st update on current practice. *Eur. J. Anat.*
- Rizzo III, J.F., Wyatt, J., 1997. REVIEW ■: prospects for a visual prosthesis. *Neurosci.* 3, 251–262.
- Roberts, W.J., Smith, D.O., 1973. Analysis of Threshold Currents during Myostimulation of Fibres in the Spinal Cord. *Acta Physiol. Scand.* 89, 384–394.
- Roehm, P.C., Xu, N., Woodson, E.A., Green, S.H., Hansen, M.R., 2008. Membrane depolarization inhibits spiral ganglion neurite growth via activation of multiple types of voltage sensitive calcium channels and calpain. *Mol. Cell. Neurosci.* 37, 376–387.
- Rosa, M.A., Lisanby, S.H., 2012. Somatic treatments for mood disorders. *Neuropsychopharmacology* 37, 102–116.
- Rose, T.L., Robblee, L.S., 1990. Electrical stimulation with Pt electrodes. VIII. Electrochemically safe charge injection limits with 0.2 ms pulses (neuronal application). *IEEE Trans. Biomed. Eng.* 37, 1118–1120.
- Roska, B., Meister, M., 2014. 13 The Retina Dissects the Visual Scene. *new Vis. Neurosci.* 163.
- Ruben, P.C., Ilschner, S.U., Williams, S.R., Stuart, G.J., 2003. Distribution and properties of sodium channels in the axon initial segment of layer 5 cortical pyramidal neurons, in: *Soc Neurosci Abstr.*
- Rubinstein, J.T., Rubinstein, J.T., 1993. Axon Termination Conditions for Electrical Stimulation. *IEEE Trans. Biomed. Eng.* doi:10.1109/10.237695
- Rushton, W.A.H., 1951. A theory of the effects of fibre size in medullated nerve. *J. Physiol.* 115, 101–122.
- Russell, T.L., Werblin, F.S., 2010. Retinal synaptic pathways underlying the response of the rabbit local edge detector. *J. Neurophysiol.* 103, 2757–2769.
- Rusznák, Z., Szűcs, G., 2009. Spiral ganglion neurones: an overview of morphology, firing behaviour, ionic channels and function. *Pflügers Arch. J. Physiol.* 457, 1303–1325.
- S., B., J., Encke, M., O.-L., R., W., F., S., J., Eberharter, F., B., W., H., 2019. Electrical Stimulation in the Human Cochlea: A Computational Study Based on High-Resolution Micro-CT Scans. *Front. Neurosci.*
- Sackeim, H.A., Rush, A.J., George, M.S., Marangell, L.B., Husain, M.M., Nahas, Z., Johnson, C.R., Seidman, S., Giller, C., Haines, S., 2001. Vagus nerve stimulation (VNSTM) for treatment-resistant depression: efficacy, side effects, and predictors of outcome. *Neuropsychopharmacology* 25, 713–728.
- Sajedi, S., Fellner, A., Stiennon, I., Rattay, F., 2020. Cathodic microelectrode stimulation window for spike initiation in the soma. *Fed. Eur. Neurosci. Soc.*
- Sajedi, S., Fellner, A., Werginz, P., Rattay, F., n.d. Block phenomena during electric micro-stimulation of pyramidal cells and retinal ganglion cells. *Front. Cell. Neurosci.* 492. <https://doi.org/10.3389/fncel.2021.771600>
- Sakmann, B., Neher, E., 1984. Patch clamp techniques for studying ionic channels in excitable membranes. *Annu. Rev. Physiol.* 46, 455–472.
- Sanes, J.R., Masland, R.H., 2015. The types of retinal ganglion cells: current status and implications for neuronal classification. *Annu. Rev. Neurosci.* 38, 221–246.
- Schachter, M.J., Oesch, N., Smith, R.G., Taylor, W.R., 2010. Dendritic spikes amplify the synaptic signal to enhance detection of motion in a simulation of the direction-selective ganglion cell. *PLoS Comput. Biol.* 6, e1000899.

References

- Schachter, S.C., Saper, C.B., 1998. Vagus nerve stimulation. *Epilepsia* 39, 677–686.
- Schaefer, A.T., Larkum, M.E., Sakmann, B., Roth, A., 2003. Coincidence detection in pyramidal neurons is tuned by their dendritic branching pattern. *J. Neurophysiol.* 89, 3143–3154.
- Schiller, J., Schiller, Y., Stuart, G., Sakmann, B., 1997. Calcium action potentials restricted to distal apical dendrites of rat neocortical pyramidal neurons. *J. Physiol.* 505, 605–616.
- Schiller, P.H., 2010. Parallel information processing channels created in the retina. *Proc. Natl. Acad. Sci.* 107, 17087–17094.
- Schmidt, E.M., Bak, M.J., Hambrecht, F.T., Kufta, C. V, O’rourke, D.K., Vallabhanath, P., 1996. Feasibility of a visual prosthesis for the blind based on intracortical micro stimulation of the visual cortex. *Brain* 119, 507–522.
- Schwarz, J.R., Eikhof, G., 1987. Na currents and action potentials in rat myelinated nerve fibres at 20 and 37 C. *Pflügers Arch.* 409, 569–577.
- Shannon, R. V, 2012. Advances in auditory prostheses. *Curr. Opin. Neurol.* 25, 61.
- Sheasby, B.W., Fohlmeister, J.F., 1999. Impulse encoding across the dendritic morphologies of retinal ganglion cells. *J. Neurophysiol.* 81, 1685–1698.
- Shu, Y., Duque, A., Yu, Y., Haider, B., McCormick, D.A., 2007a. Properties of action-potential initiation in neocortical pyramidal cells: evidence from whole cell axon recordings. *J. Neurophysiol.* 97, 746–760.
- Shu, Y., Yu, Y., Yang, J., McCormick, D.A., 2007b. Selective control of cortical axonal spikes by a slowly inactivating K⁺ current. *Proc. Natl. Acad. Sci.* 104, 11453–11458.
- Silbernagl, S., Despopoulos, A., 2007. *Taschenatlas Physiologie*. Georg Thieme Verlag.
- Soltesz, I., Lightowler, S., Leresche, N., Jassik-Gerschenfeld, D., Pollard, C.E., Crunelli, V., 1991. Two inward currents and the transformation of low-frequency oscillations of rat and cat thalamocortical cells. *J. Physiol.* 441, 175–197.
- Spelman, F.A., Pfungst, B.E., Sutton, D., 1980. Operating ranges for cochlear implants. *Ann. Otol. Rhinol. Laryngol.*
- Spoendlin, H., 1972. Innervation densities of the cochlea. *Acta Otolaryngol.* doi:10.3109/00016487209138937
- Spoendlin, H., Schrott, A., 1989. Analysis of the human auditory nerve. *Hear. Res.* doi:10.1016/0378-5955(89)90056-7
- Spoendlin, H., Schrott, A., 1988. The spiral ganglion and the innervation of the human organ of corti. *Acta Otolaryngol.* doi:10.3109/00016488809119493
- Stone, J., Fukuda, Y., 1974. Properties of cat retinal ganglion cells: a comparison of W-cells with X-and Y-cells. *J. Neurophysiol.* 37, 722–748.
- Stuart, G., Schiller, J., Sakmann, B., 1997. Action potential initiation and propagation in rat neocortical pyramidal neurons. *J. Physiol.* 505, 617–632.
- Stuart, G.J., Sakmann, B., 1994. Active propagation of somatic action potentials into neocortical pyramidal cell dendrites. *Nature* 367, 69–72.
- Suesserman, M.F., Spelman, F.A., 1993. Lumped-Parameter Model for In Vivo Cochlear Stimulation. *IEEE Trans. Biomed. Eng.* doi:10.1109/10.216407
- Sun, W., Deng, Q., Levick, W.R., He, S., 2006. ON direction-selective ganglion cells in the mouse retina. *J. Physiol.* 576, 197–202.

References

- Sun, X., Gu, X.Q., Haddad, G.G., 2003. Calcium influx via L-and N-type calcium channels activates a transient large-conductance Ca²⁺-activated K⁺ current in mouse neocortical pyramidal neurons. *J. Neurosci.* 23, 3639–3648.
- Sweeney, J.D., Mortimer, J.T., Durand, D., 1987. Modeling of mammalian myelinated nerve for functional neuromuscular stimulation, in: *IEEE 9th Annual Conference of the Engineering in Medicine and Biology Society*. pp. 1577–1578.
- Takahashi, H., Nakao, M., Kaga, K., 2007. Selective activation of distant nerve by surface electrode array. *IEEE Trans. Biomed. Eng.* 54, 563–569.
- Talley, E.M., Cribbs, L.L., Lee, J.-H., Daud, A., Perez-Reyes, E., Bayliss, D.A., 1999. Differential distribution of three members of a gene family encoding low voltage-activated (T-type) calcium channels. *J. Neurosci.* 19, 1895–1911.
- Thomson, W., 1856. Iii. on the theory of the electric telegraph. *Proc. R. Soc. London* 382–399.
- Tong, W., Meffin, H., Garrett, D.J., Ibbotson, M.R., 2020. Stimulation strategies for improving the resolution of retinal prostheses. *Front. Neurosci.* 14, 262.
- Undurraga, J.A., Carlyon, R.P., Macherey, O., Wouters, J., Van Wieringen, A., 2012. Spread of excitation varies for different electrical pulse shapes and stimulation modes in cochlear implants. *Hear. Res.* 290, 21–36.
- Undurraga, J.A., Carlyon, R.P., Wouters, J., Van Wieringen, A., 2013. The polarity sensitivity of the electrically stimulated human auditory nerve measured at the level of the brainstem. *JARO - J. Assoc. Res. Otolaryngol.* doi:10.1007/s10162-013-0377-0
- van den Honert, C., Stypulkowski, P.H., 1987. Temporal response patterns of single auditory nerve fibers elicited by periodic electrical stimuli. *Hear. Res.* doi:10.1016/0378-5955(87)90168-7
- Van Wart, A., Trimmer, J.S., Matthews, G., 2007. Polarized distribution of ion channels within microdomains of the axon initial segment. *J. Comp. Neurol.* 500, 339–352.
- Van Wyk, M., Taylor, W.R., Vaney, D.I., 2006. Local edge detectors: a substrate for fine spatial vision at low temporal frequencies in rabbit retina. *J. Neurosci.* 26, 13250–13263.
- Vanier, M.C., Bower, J.M., 1999. A comparative survey of automated parameter-search methods for compartmental neural models. *J. Comput. Neurosci.* 7, 149–171.
- Velasco, M., Velasco, F., Velasco, A.L., 2001. Centromedian–thalamic and hippocampal electrical stimulation for the control of intractable epileptic seizures. *J. Clin. Neurophysiol.* 18, 495–513.
- Wan, G., Corfas, G., 2017. Transient auditory nerve demyelination as a new mechanism for hidden hearing loss. *Nat. Commun.* 8, 1–13.
- Wässle, H., 2004. Parallel processing in the mammalian retina. *Nat. Rev. Neurosci.* 5, 747–757.
- Wässle, H., Peichl, L., Boycott, B.B., 1981. Morphology and topography of on-and off-alpha cells in the cat retina. *Proc. R. Soc. London. Ser. B. Biol. Sci.* 212, 157–175.
- Wässle, H., Riemann, H.J., 1978. The mosaic of nerve cells in the mammalian retina. *Proc. R. Soc. London. Ser. B. Biol. Sci.* 200, 441–461.
- Weiland, J.D., Anderson, D.J., Humayun, M.S., 2002. In vitro electrical properties for iridium oxide versus titanium nitride stimulating electrodes. *IEEE Trans. Biomed. Eng.* 49, 1574–1579.
- Weitz, A.C., Nanduri, D., Behrend, M.R., Gonzalez-Calle, A., Greenberg, R.J., Humayun, M.S., Chow, R.H., Weiland, J.D., 2015. Improving the spatial resolution of epiretinal implants by increasing stimulus pulse duration. *Sci. Transl. Med.* 7, 318ra203-318ra203.
- Wells, J., Kao, C., Mariappan, K., Albea, J., Jansen, E.D., Konrad, P., Mahadevan-Jansen, A., 2005. Optical stimulation of neural tissue in vivo. *Opt. Lett.* 30, 504–506.

References

- Weng, S., Sun, W., He, S., 2005. Identification of ON-OFF direction-selective ganglion cells in the mouse retina. *J. Physiol.* 562, 915–923.
- Werginz, P., Fried, S.I., Rattay, F., 2014. Influence of the sodium channel band on retinal ganglion cell excitation during electric stimulation—a modeling study. *Neuroscience* 266, 162–177.
- Werginz, P., Raghuram, V., Fried, S.I., 2020. The relationship between morphological properties and thresholds to extracellular electric stimulation in α RGCs. *J. Neural Eng.* 17, 45015.
- Werginz, P., Rattay, F., 2016. The impact of calcium current reversal on neurotransmitter release in the electrically stimulated retina. *J. Neural Eng.* 13, 46013.
- Werginz, P., Rattay, F., 2014. Past, present, future: a review on visual prostheses. *Minerva Med.* 106, 65–77.
- West, R.M.E., 1996. On the development and interpretation of parameter manifolds for biophysically robust compartmental models of CA3 hippocampal neurons. University of Minnesota.
- Whitwam, J.G. and Kidd, C., 1975. The use of direct current to cause selective block of large fibres in peripheral nerves. *British journal of anaesthesia*, 47(11), pp.1123-1132.
- Wiley, J.D., Webster, J.G., 1982. Analysis and control of the current distribution under circular dispersive electrodes. *IEEE Trans. Biomed. Eng.* 381–385.
- Williams, S.R., Stuart, G.J., 2000. Site independence of EPSP time course is mediated by dendritic I_h in neocortical pyramidal neurons. *J. Neurophysiol.* 83, 3177–3182.
- Wilson, B.S., Dorman, M.F., 2008. Cochlear implants: a remarkable past and a brilliant future. *Hear. Res.* 242, 3–21.
- Wollner, D.A., Catterall, W.A., 1986. Localization of sodium channels in axon hillocks and initial segments of retinal ganglion cells. *Proc. Natl. Acad. Sci.* 83, 8424–8428.
- Wongsarnpigoon, A., Woock, J.P., Grill, W.M., 2010. Efficiency analysis of waveform shape for electrical excitation of nerve fibers. *IEEE Trans. Neural Syst. Rehabil. Eng.* 18, 319–328.
- y Cajal, S.R., 1888. Estructura de los centros nerviosos de las aves.
- Yamagata, M., Sanes, J.R., 2012. Expanding the Ig superfamily code for laminar specificity in retina: expression and role of contactins. *J. Neurosci.* 32, 14402–14414.
- Yamagata, M., Sanes, J.R., 2008. Dscam and Sidekick proteins direct lamina-specific synaptic connections in vertebrate retina. *Nature* 451, 465–469.
- Yi, E., Roux, I., Glowatzki, E., 2010. Dendritic HCN channels shape excitatory postsynaptic potentials at the inner hair cell afferent synapse in the mammalian cochlea. *J. Neurophysiol.* 103, 2532–2543.
- Yonehara, K., Ishikane, H., Sakuta, H., Shintani, T., Nakamura-Yonehara, K., Kamiji, N.L., Usui, S., Noda, M., 2009. Identification of retinal ganglion cells and their projections involved in central transmission of information about upward and downward image motion. *PLoS One* 4, e4320.
- Yu, Y., Shu, Y., McCormick, D.A., 2008. Cortical action potential backpropagation explains spike threshold variability and rapid-onset kinetics. *J. Neurosci.* 28, 7260–7272.
- Zrenner, E., Miliczek, K.-D., Gabel, V.P., Graf, H.G., Guenther, E., Haemmerle, H., Hoefflinger, B., Kohler, K., Nisch, W., Schubert, M., 1997. The development of subretinal microphotodiodes for replacement of degenerated photoreceptors. *Ophthalmic Res.* 29, 269–280.

Curriculum Vitae

Profile

Sogand Sadat Sajedi

Innsbrucker Strasse 1/13a
6060 Hall in Tirol, Austria

Email: sogand.sajedi@tuwien.ac.at

Date of Birth: 20.02.1987



Education

Since 04/19	Doctoral student (Dr. techn., PhD) - <i>Engineering Sciences</i> Vienna University of Technology
10/15 – 11/18	Master's degree (Dipl.-Ing., MSc) - <i>Biomedical Engineering</i> Vienna University of Technology
07/12 – 07/15	Pre-Master - <i>German language and Biomedical Engineering</i> Vienna University of Technology
10/05 – 10/10	Bachelor's degree (BA) - <i>Electrical Engineering</i> Islamic Azad University

Work Experience

- Since 11/18 Project Assistant (Austrian Science Fund). Vienna University of Technology, Institute for Analysis and Scientific Computing
- Since 04/19 Cooperation with Medical University of Innsbruck, Laboratory for Inner Ear Biology, Department of Otorhinolaryngology
-

Papers in Peer-reviewed Journals

- 2021 **Sajedi, S.**, Fellner, A., Werginz, P., and Rattay, F., (2021) *Block phenomena during electric micro-stimulation of pyramidal cells and retinal ganglion cells*. *Frontiers in Cellular Neuroscience*, 492. <https://doi.org/10.3389/fncel.2021.771600>
- 2021 Heshmat A, **Sajedi S**, Schrott-Fischer A and Rattay F., (2021) *Polarity Sensitivity of Human Auditory Nerve Fibers Based on Pulse Shape and Cochlear Implant Stimulation Strategy and Array*. *Frontiers in Neuroscience*. 15:751599. <https://doi.org/10.3389/fnins.2021.751599>
- 2020 Heshmat, A., **Sajedi, S.**, Chacko, L. J., Fischer, N., Schrott-Fischer, A., and Rattay, F., (2020). *Dendritic Degeneration of Human Auditory Nerve Fibers and Its Impact on the Spiking Pattern Under Regular Conditions and During Cochlear Implant Stimulation*. *Frontiers in Neuroscience*, 14. <https://doi.org/10.3389/fnins.2020.599868>
- 2020 Potrusil, T., Heshmat, A., **Sajedi, S.**, Wenger, C., Chacko, L. J., Glueckert, R., Schrott-Fischer, A., and Rattay, F., (2020). *Finite element analysis and three-dimensional reconstruction of tonotopically aligned human auditory fiber pathways: a computational environment for modeling electrical stimulation by a cochlear implant based on micro-CT*. *Hearing Research*, 393, 108001. <https://doi.org/10.1016/j.heares.2020.108001>
-

Papers in Conference Contributions / Poster Presentations

- 2021 Heshmat, A., **Sajedi, S.**, Schrott-Fischer, A., and Rattay, F., (2021). *Impact of peripheral degeneration of human cochlear nerve fibers on the spiking pattern and cochlear implant performance*. Conference on Implantable Auditory Prostheses (CIAP) USA.
- 2021 Tanzer, T., **Sajedi, S.**, Heshmat, A., and Rattay, F., (2021). *Impact of auditory nerve fiber's diameter on the dynamic range during stimulation with a cochlear implant*. Conference on Implantable Auditory Prostheses (CIAP) USA.
- 2021 Tanzer, T., **Sajedi, S.**, and Rattay, F., (2021). *Impact of electrode placement on spiking probability of a stimulated human auditory nerve fiber*. Organization For Computational Neurosciences.
- 2020 Heshmat, A., **Sajedi, S.**, Schrott-Fischer, A., and Rattay, F., (2020). *Dendritic degeneration of human cochlear ganglion neurons type I and its impact on the spiking pattern*. Bernstein Conference 2020. <https://doi.org/10.12751/nncn.bc2020.0087>
- 2020 **Sajedi, S.**, Heshmat, A., Schrott-Fischer, A., and Rattay, F., (2020). *Effects of dendritic degeneration of human cochlear ganglion neurons type I on cochlear implant performance*. Bernstein Conference 2020. <https://doi.org/10.12751/nncn.bc2020.0214>
- 2020 Heshmat, A., **Sajedi, S.**, Schrott-Fischer, A., and Rattay, F., (2020). *Comparison of extracellular voltage distribution in cochlear implant systems with and without carrier: a computational study based on micro-CT images of a human cochlea*. 2nd Annual Computational Data Neuroscience Symposium, Harvard University.
- 2020 Potrusil, T., Heshmat, A., **Sajedi, S.**, Wenger, C., Chacko, L.J., Glueckert, R., Schrott-Fischer, A. and Rattay, F., (2020). *Simulated nerve responses to cochlear implant stimulation based on three-dimensional micro-CT reconstruction of human auditory nerve*. Association for Research in Otolaryngology (ARO) - 43rd Annual MidWinter Meeting Conference.

- 2020 **Sajedi, S.**, Fellner, A., Stiennon, I and Rattay, F., (2020). *Cathodic microelectrode stimulation window for spike initiation in the soma*. The Federation of European Neuroscience Societies (FENS) Conference.
- 2020 Heshmat, A., **Sajedi, S.**, Schrott-Fischer, A., and Rattay, F., (2020). *Polarity sensitivity from electrical stimulation of degenerated human cochlear neurons*. The Federation of European Neuroscience Societies (FENS) Conference.
- 2019 **Sajedi, S.**, Heshmat, A., Schrott-Fischer, A. and Rattay, F., (2019). *Cochlear implants for cat and man & what we learn from a modeling study*. Vienna young Scientists Symposium (VSS) Conference.
-

Teaching

- 2019W - 2021W Rattay F., Fellner A., **Sajedi S.**, Computer Simulation in Medicine, Lecture with demonstrations (VU 101.498, 3 ECTS), Vienna University of Technology